# HIGH CADENCE ASTRONOMICAL POLARIMETRY FOR TIME DOMAIN ASTRONOMY ON THE LIVERPOOL TELESCOPE

Doug Arnold

A thesis submitted in partial fulfilment of the requirements of
Liverpool John Moores University
for the degree of
Doctor of Philosophy.
June 13, 2017

# Declaration

The work presented in this thesis was carried out at the Astrophysics Research Institute, Liverpool John Moores University. Unless otherwise stated, it is the original work of the author.

While registered as a candidate for the degree of Doctor of Philosophy, for which submission is now made, the author has not been registered as a candidate for any other award. This thesis has not been submitted in whole, or in part, for any other degree.

Doug Arnold
Astrophysics Research Institute
Liverpool John Moores University
ic2, Liverpool Science Park
146 Brownlow Hill
Liverpool, L3 5RF
UK

JUNE 13, 2017

# Abstract

Gamma-ray bursts are the most violent of known astrophysical events, with up to $10^{53}$ ergs of energy released on the order of seconds. These extreme explosions, first observed in 1960s, form a fast moving field of research within astrophysics which relies on multi-wavelength observations of these transient events to probe the early-time ($\lesssim$15 minutes) parameter space of these events. In the optical regime, follow-up observations to the prompt emission are ideally suited to the 2.0 metre Liverpool Telescope (LT), situated at an altitude of 2363m on the Observatorio Roque de las Muchachos (ORM), La Palma, Canary Islands. The LT is fully robotic and able to respond automatically to triggers of new gamma-ray burst (GRB) events, starting within 2-3 minutes of the detection of the prompt emission.

The observed radiation from GRBs is released from relativistic jets. Launched from a black hole central engine, the energy within the jets is converted to the observed radiation predominantly through a synchrotron process, which can produce highly linearly polarised radiation. Polarimetric observations of this radiation are a key resource to infer the magnetic field structure of the emission region and distinguish between baryonic and magnetic models of jet physics. For this reason, the Liverpool Telescope has hosted the RINGO series of polarimeters which use a novel design to enable early-time polarimetric measurements of these highly variable optical sources.

RINGO was mounted on the LT in 2005, and observed GRB 090102A providing a measure of 10.2 $\pm$ 1.3% average linear polarisation in the period of 160-220 s post

burst. RINGO2, mounted in June 2009 improved on the original design utilising a triggered electron multiplying CCD system. Both RINGO and RINGO2 were single band instruments. The development of RINGO3 extended the design of RINGO2 into a simultaneous 3 band polarimeter.

This work focuses on the characterisation of RINGO2 and analysing the sample of GRB observations made during its lifetime. The observations of GRB 120308A provide measurements with a high confidence, inferring the existence of stable, ordered magnetic fields within the jet. Analysis of other GRB afterglows observed with RINGO2 provides confidence in this result and confirm that jets can be highly magnetised, with the majority of energy being contained in magnetic field recombination and not through kinetic energy of baryonic matter.

RINGO3, a multi-band extension to RINGO2, was developed and tested within the Astrophysics Research Institute labs before being commissioned on the Liverpool Telescope in November 2012. Lab tests of instrument throughput with calculations of the signal to noise ratio across the operating wavelength defined the optimal cut-offs of the 3 wavelength bands. This instrument was then characterised using similar methods to RINGO2, and whilst not an ideal instrument was found to be within the required performance for the prime science goal of early-time GRB afterglow observations.

# Publications

In the course of completing the work presented in this thesis, the contents of Chapter 6 have been submitted and accepted for publication in a refereed journal:

Mundell, C. G., Kopač, D., Arnold, D. M., Steele, I. A., Gomboc, A., Kobayashi, S., Harrison, R. M., Smith, R. J., Guidorzi, C., Virgili, F. J., Melandri, A. & Japelj, J., 2013, 'Highly polarized light from stable ordered magnetic fields in GRB 120308A' *Nature*, 504, pp. 119-121

The contents of Chapter 2 were published as an unrefereed paper in conference proceedings:

Arnold, D. M., Steele, I. A., Mottram, C. J., & Smith, R. J. 2012, 'RINGO3: a multicolour fast response polarimeter' *Proc. SPIE*, Vol. 8446, Ground-based and Airborne Instrumentation for Astronomy

During the course of studies contributions were made to the following refereed journal papers:

Kopač, D., Mundell, C. G., Japelj, J., Arnold, D. M., Steele, I. A., Guidorzi, C., Dichiara, S., Kobayashi, S., Gomboc, A., Harrison, R. M., Lamb, G. P., Melandri, A., Smith, R. J., Virgili, F. J., Castro-Tirado, A. J., Gorosabel, J., Jarvinen, A., Sanchez-Ramirez, R., Oates, S. R., Jelinek, M. 2015, 'Limits on Optical Polarization during the Prompt Phase of GRB 140430A' *The Astrophysical Journal*, 813, pp. 14

Melandri, A., Virgili, F. J., Guidorzi, C., Bernardini, M. G., Kobayashi, S., Mundell, C. G., Gomboc, A., Dintinjana, B., Hentunen, V.-P., Japelj, J., Kopač, D., Kuroda, D., Morgan, A. N., Steele, I. A., Quadri, U., Arici, G., Arnold, D., Girelli, R., Hanayama, H., Kawai, N., Miku, H., Nissinen, M., Salmi, T., Smith, R. J., Strabla, L., Tonincelli, M., Quadri, A. 2014, 'The nature of the late achromatic bump in GRB 120326A' *Astron. & Astrophysics* 572, pp.A55

# Acknowledgements

I would firstly like to thank the ARI and Liverpool John Moores University, for maintaining a fantastic working environment and facilities which provided much scientific opportunity during the PhD. Also to all of my colleagues and friends from The Isaac Newton Group, the Nordic Optical Telescope and the ORM observatory in La Palma. Thanks especially to Lillian Dominguez, Ovidiu Vadesvescu and Chris Benn for much support and mentoring during my year at the Isaac Newton Group.

Academically I wish to thank all of the Liverpool Telescope GRB team, and also all who work so hard to maintain such an excellent observational facility. I'm especially indebted to Drejc Kopač for his friendship, enthusiasm and scientific collaboration, especially when I was in situations where I was not able to offer much in return.

I'm very grateful to my supervisors, Carole Mundell and Iain Steele. I have had an especially enjoyable time working with Iain and his understanding and support have been much appreciated.

Finally I wish to thank my parents who provided much needed support during this period of my life.

DOUG ARNOLD JUNE 13, 2017


*'Bernard of Chartres used to compare us to [puny] dwarfs perched on the shoulders of giants. He pointed out that we see more and farther than our predecessors, not because we have keener vision or greater height, but because we are lifted up and borne aloft on their gigantic stature'"*

- John of Salisbury, 1159

# Contents

# List of Tables

# List of Figures

# List of changes

# Chapter 1

# Introduction

The fully robotic Liverpool Telescope, situated on the island of La Palma is specifically designed for making observations in the field of time domain astrophysics. With its robotic capabilities it is an ideal observing platform for probing the early-time ($\lesssim$15 minutes) phase of gamma-ray burst afterglows. One of the distinct features of the Liverpool Telescope in making these observations at these early times is its polarimetric capability, provided by the RINGO series of polarimeters.

This introduction establishes the theory, applications and considerations of polarimetry as an observational method. Then a short history of gamma-ray burst science is presented, from initial discovery through to the era of rapid multi-band followup. Finally the Liverpool Telescope and the polarimetric capabilities provided through the design and commissioning of the RINGO series of polarimeters are introduced.

## 1.1 Polarimetry in astronomy

Light, or more precisely, electromagnetic radiation, is the carrier by which most of our knowledge of the universe outside the Earth's atmosphere has been inferred. Until recently, the field of observational astronomy has been entirely built upon the capture

and categorisation of the properties of electromagnetic waves. Due to the quantum nature of electromagnetic radiation, it defies being described fully as either a wave or a particle, having properties of both. However, in the field of polarimetry, the properties of polarisation are explained purely in the electromagnetic wave view.

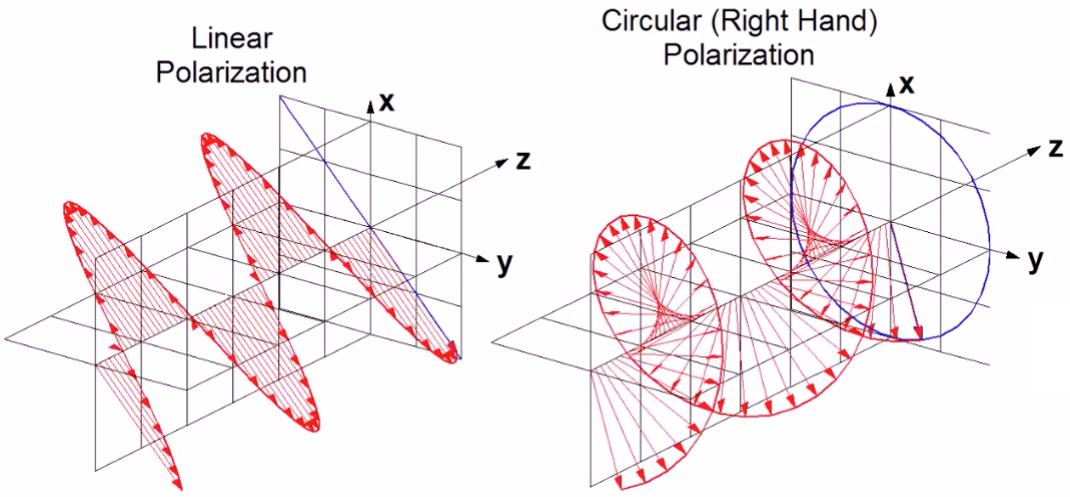


Figure 1.1: The property of polarisation is defined as the movement of the electronic field vector ($\vec{E}$, shown in red) in a fixed plane orthogonal to the propagation direction of the electromagnetic wave (blue traces). The two boundary conditions of polarisation are shown above, namely linear and circular polarisation. The time dependent $\vec{E}$ vector is described as the resultant of two perpendicular electric field components, $e_x$ and $e_y$ which oscillate sinusoidally with time and equal frequency. For linear polarisation the oscillations of $e_x$ and $e_y$ are in phase. When these components are out of phase by $\pi/2$, and oscillating with equal magnitude, then 100% circular polarisation exists with the $\vec{E}$ tracing a circle on the fixed plane with time. With other phase differences, elliptical polarisation is observed.

An electromagnetic wave is a transverse oscillating wave of conjoined electric and magnetic fields, where the oscillations of the fields are perpendicular to the direction of propagation (z). At any point the electric and magnetic field vectors ($\vec{E}$,$\vec{B}$) are orthogonal. By convention, however, the property of polarisation is described by only considering the $\vec{E}$ component of the wave.

By considering a static plane perpendicular to the electromagnetic wave propagation (z), through which the wave passes, the property of polarisation is the shape which the $\vec{E}$ vector traces on the plane as a function of time. Figure 1.1 shows this plane and the pattern of the electric field vector traces as the wave propagates through.

$$\vec{E}(z,t) = \begin{bmatrix} e_x \\ e_y \\ 0 \end{bmatrix} e^{i(kz-\omega t)} \tag{1.1}$$

Equation 1.1 describes a 100% linearly polarised wave. $\vec{E}$ is a function of position ($z$) and time ($t$), where wavenumber $k = 2\pi/\lambda$ ($\lambda$ is wavelength in metres) and angular frequency $\omega = 2\pi f$ (f is frequency in hertz). The vector matrix contains 3 components, $e_x$, $e_y$ and $0$. These are the Cartesian components of the oscillation in x, y and z axes. This shows that $\vec{E}$ cannot have a z component and is always orthogonal to the direction of propagation. $e_x$ and $e_y$ are the x and y components of the oscillation and their ratio defines the angle of polarisation (i.e. $e_x$ = 0, $e_y$ = 1 will describe an $\vec{E}$ oscillation in the y plane only).

In equation 1.1 the components of electric field oscillation are constrained to be in phase with each other, however in nature there is no such constraint. For example, in optics, a phase difference can be imparted between the $e_x$ and $e_y$ components using a birefringent crystal aligned in such a way that the refractive indices (and hence propagation velocities) differ for the two components. A quarter wave plate is a common optical element, which is tuned to a specific frequency of radiation. It will take 100% linearly polarised radiation and impart a quarter wave phase difference between the electric field components. In this situation, the $\vec{E}$ will now trace out a circular path on the fixed plane, orthogonal to the direction of propagation, as shown on the right image in Figure 1.1. This special case is referred to as circular polarisation.

For a single electromagnetic wave, linear polarisation occurs when the $e_x$ and $e_y$ components are in phase, circular polarisation occurs when they are out of phase by

$\lambda/4$ and equal (with the direction of phase shift determining either left hand or right hand circular polarisation). In all other cases the electric field vector will trace an ellipse producing elliptical polarisation.

Unpolarised monochromatic radiation can be viewed of a large number of superposition of in phase, 100% linearly polarised waves which have electrical field oscillations with no preference for any one angle. In Astrophysical situations a true monochromatic electromagnetic wave is a rarity with radiation of many different wavelengths making up the radiation. Over very short periods of time (on the order of wavelengths), the movement of the electrical field vector on the fixed plane will trace patterns denoting linear and circular polarisation as different components move in and out of phase, however the overall polarisation of the radiation must be taken as a time averaged motion of the electrical field vector (Tinbergen, 2005).

This thesis is based around a series of polarimeters which measure the level of linear polarisation. Therefore the majority of discussion relates purely to this type of polarisation.

### 1.1.1 Polarisation mechanisms

One of the most common sources of observed optical radiation in the universe is thermal emission via black body radiation (Planck, 1901) from the photosphere of stars. Early measurements of stellar polarisation did find significant levels of polarisation ($\sim 10\%$). However what was observed was that stars with higher levels of extinction (light attenuated my intervening Galactic material), had more significant levels of polarisation, aligned in angle across the field, and across different spectral types (Hall & Mikesell, 1949; Hiltner, 1949).

The explanation for this is that the vast majority of stellar sources are essentially unpolarised (showing less than 1% polarisation) as reported by Hall & Mikesell (1950),

and that measured polarisation is due to the effect of intervening material.

In the next sections we look at three mechanisms which produce polarised radiation. Two of these mechanisms involve unpolarised ($\lesssim$1%) thermal radiation from stellar sources being polarised by intervening material. The third involves a mechanism which produces polarised radiation at source.

Presented first is absorption and scattering by the interstellar medium (ISM) and how this process is able to polarise the radiation received by the observer. This process forms a large part of this thesis as it is the mechanism by which standard polarimetric sources gain their observed polarisations. These objects are the main tools in determining and calibrating a polarimeter and have observed polarisations of up to $\sim$10 %.

The second mechanism of polarisation is that of Rayleigh scattering, specifically within the earth's atmosphere. This process has been used in this work to deduce the polarimetric response of the imagers across the field of view, also providing a highly polarised source (up to 85 %) for observation.

The final mechanism of observed polarisation forms the scientific goal of this thesis. Differing from thermal emission with its isotropic mechanisms, synchrotron emission is a highly orientation dependent process, involving charge acceleration due to strong magnetic fields and energised plasma. The radiation from this process can be highly polarised on levels of $\sim$70 %

**Absorption and scattering by the interstellar medium**

The interstellar medium (ISM) is the matter existing between stellar sources within a galaxy. It is mainly comprises of neutral and molecular hydrogen gas, helium, plus other heavier molecules such as oxygen. A component of the ISM is also interstellar dust, formed of irregular shaped composites of silicon, carbon and ice. Having particle

sizes on the order of ∼400nm, dust has a considerable impact on optical radiation propagating through the ISM.

$$\frac{dN}{dx} = -Nn\sigma \tag{1.2}$$

The radiation is affected by the cross section, $\sigma$, of the medium. This is the sum of separate scattering and absorption cross sections. Equation 1.2 shows how a monochromatic stream of photons with number $N$, are scattered as they travel through the medium along direction $x$, where $n$ is the number density of particles per unit volume. $\sigma$ is a function of wavelength and increases as wavelength decreases. This leads to the cross section being larger for shorter wavelengths. The phenomena of reddening is commonly observed, where radiation which passes through the ISM has a larger proportion of shorter wavelengths being scattered, thus the remaining radiation is 'reddened'.

When polarised stellar sources were initially observed (Hall & Mikesell, 1949; Hiltner, 1949), it was noted that areas of sky with polarised sources correlated to areas with observed reddening. Further to this, the angles of linear polarisation were seen to be in general alignment for stellar sources in the same field. This evidence pointed towards the fact that the inter stellar dust was polarising the starlight observed.

Work by Davis & Greenstein (1951) explained a mechanism which would produce the observed polarised radiation through models. Their calculations looked at how rapidly spinning dust grains (angular velocities of $10^5 \rightarrow 10^6$ rad/sec) of around 12 % iron align their axis of rotation with local magnetic fields. Further to this the non spherical dust grains align with their short axis parallel to the magnetic field lines due to paramagnetic relaxation. The time frame of this process was found to be on order of $10^{13}$ seconds, and the process balanced by bombardment of the grains by interstellar gas, resetting their alignment and spin.

With the dust grains showing a tendency alignment of rotation and short axis they present two different cross sections to orthogonally polarised electromagnetic waves, one aligned with the magnetic field. The cross section $\sigma_{\parallel} < \sigma_{\perp}$, leading to a larger proportion of the polarised radiation perpendicular to the field lines being scattered or absorbed. The net effect of this is that the radiation will be linearly polarised with the angle of polarisation parallel to the magnetic field lines.

The exact mechanisms of grain alignment are not simple (Roberge, 1996), and there is still some debate as to the exact mechanism of alignment. However, the mechanism of polarising radiation is well understood and modelled and allows polarisation measurements of stellar sources, viewed through dichroic dust, to characterise both the dust properties and the Galactic magnetic field structure (Roberge & Whittet, 1996).

In this work the polarising properties of dichroic dust are exploited in the observations of polarimetric standard stars. Observations of these sources are used extensively in Chapter 5 for the characterisation of the polarimeters on the Liverpool Telescope.

**Rayleigh scattering**

Scattering within the Earth's atmosphere can be explained by the process presented by Lord Rayleigh in the latter part of the 19th century (Strutt, 1871). The process that bears his name is a special form of elastic scattering whereby the dimensions of the scattering particles are much smaller than the wavelength of the light being scattered. Rayleigh's breakthrough in explaining atmospheric scattering came from the application of Maxwell's equations of Electromagnetism.

In this model incident radiation induces dipole oscillations in the scattering particle. In the Earth's atmosphere the particles are predominantly Nitrogen and Oxygen molecules of size $1.5 \times 10^{-10}$ m. From the induced dipole oscillations, the emitted radiation in all directions was explained by Equation 1.3 from Meyer-Arendt (1989),

where an observer at scattering angle $\theta$ and distance $R$ will observe and intensity of $I$. In this equation, $\alpha$ is the polarisability (tendency of the particle to have its charges displaced by an electric field) and $N$ is the number of scattering particles. The visualisation of this equation is shown in Figure 1.2.

$$I = I_0 \frac{8\pi^4 N \alpha^2}{\lambda^4 R^2}(1 + \cos^2\theta) \tag{1.3}$$

From this equation, as also seen in the ISM, we can see that scattering is highly wavelength dependent with the scattering cross section being proportional to $\lambda^{-4}$. This was empirically observed by Rayleigh Hey (1983), but took many years for him to deduce the mechanism of this. In the power radiated by a dipole, this term is observed due to the angular frequency of dipole oscillation.

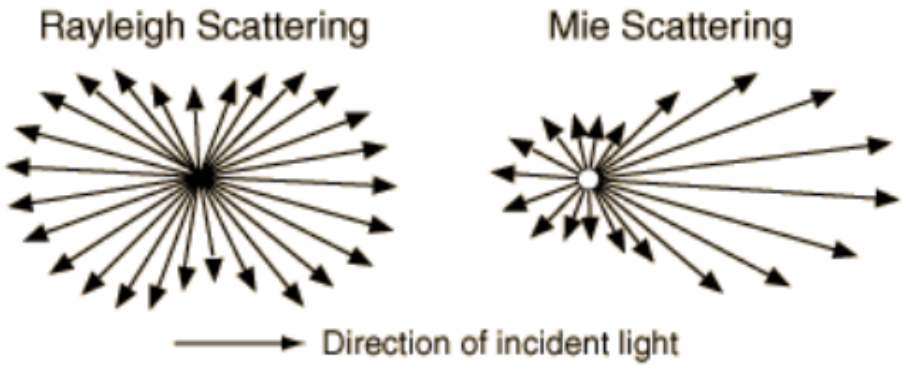


Figure 1.2: Intensity of Rayleigh and Mie scattering at different angles. In Mie scattering where the particle size is on order or larger than the wavelength of scattered radiation a predominant front lobe occurs. In Rayleigh scattering scenarios, where the scattering particle size is $<$ 1/10th of the wavelength of radiation, the intensity of radiation at different viewing angles is described by Equation 1.3. Taken from Meyer-Arendt (1989)

When incident radiation induces dipole oscillation in a molecule, the oscillation can be generally said to be constrained to the plane perpendicular to the direction of propagation. The dipole will radiate in all directions due to this oscillation, however

there is a strong effect of linear polarisation for emitted radiation dependant on angle. As the dipole oscillations are constrained to the plane, radiation emitted at 90°to the incident radiation will only present electric field oscillations aligned with the plane and hence is highly polarised. Figure 1.3 shows this effect graphically.

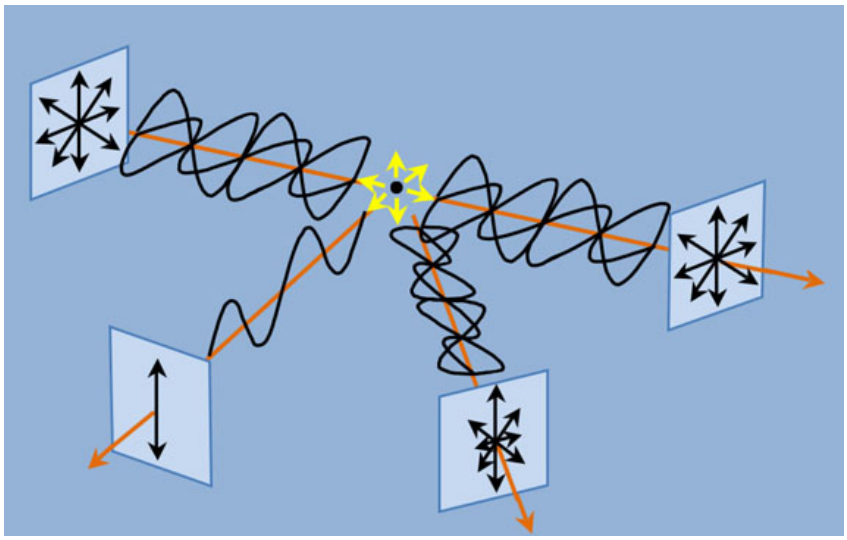

Figure 1.3: When unpolarised radiation is scattered, it becomes linearly polarised dependent on the scattering angle, due to the induced dipole oscillations being constrained to a plane perpendicular to the direction of propagation of the incoming radiation. The maximum level of linear polarisation occurs with a 90 degree scattering angle. The level of linear polarisation is given in Equation 1.4 from Bradbury & Vehrencamp (1998)

$$p = p_{max} \times \frac{\sin^2 \theta_s}{1 + \cos^2 \theta_s} \tag{1.4}$$

In physical situations of an extended scattering medium, 100% linearly polarised radiation is not observed, with scattered radiation inducing more complex dipole oscillations, which tend towards the perpendicular plane, but are not fully constrained to it. In this scenario the linear polarisation is described as in Equation 1.4, where $\theta$ is the scattering angle and $p_{max}$ is the maximum linear polarisation observed at $\theta = 90°$.

### Synchrotron emission

Non-thermal emission processes result in a spectral energy distribution (SED) that differs greatly from the Plank distributions that thermal sources such as stars produce via black body radiation. Synchrotron radiation (also known as magnetobremsstrahlung radiation) first identified by Elder et al. (1947), is a non-thermal emission process which occurs in plasmas. These contain free electrons with enough kinetic energy to be moving relativistically in strong magnetic fields (Ginzburg & Syrovatskii, 1965). The path of the electron spirals around the strong magnetic field lines, resulting in an electric charge which is constantly under acceleration. This, in turn, leads to the system emitting radiation.

The relativistic speeds involved are best described by the Lorentz Factor (Equation 1.5) and lead to the phenomenon of relativistic beaming, where the opening angle of the cone of radiation can be approximated by Equation 1.6 (Westfold, 1959). This also leads to increase in both flux and frequency of the spectrum compared to the rest frame of the electron due to Doppler effects.

$$\Gamma = (1 - \frac{v^2}{c^2})^{-\frac{1}{2}} \tag{1.5}$$

$$\theta \sim \frac{1}{\Gamma} \tag{1.6}$$

For a single electron orbiting in a plane perpendicular to the magnetic field vector which has no transverse motion along the magnetic field, the radiation will be highly polarised (see Figure 1.4). The type of polarisation will depend on the viewing angle. Observers at the edge of the cone of the beaming will see highly elliptical polarisation. However 100 % linear polarisation is possible if the observer is directly within the orbital plane of the electron. This situation is a special case, however, as the electron would be expected to have motion along the magnetic field line and hence describe a

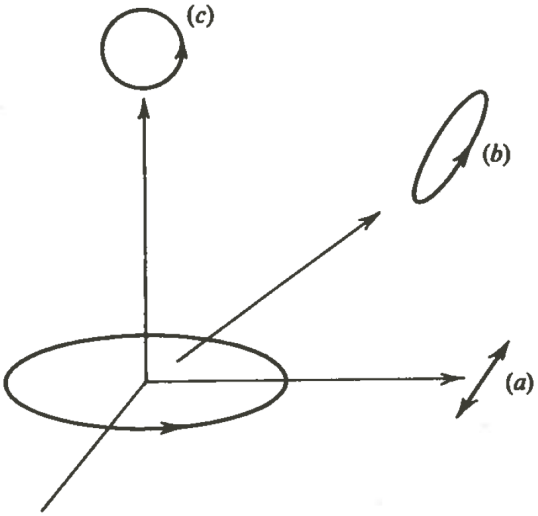


Figure 1.4: An electron orbiting in a fixed plane will produce radiation which will be polarised. When viewed in the orbital plane, the emission will be 100 % linearly polarised (a). When viewed normal to the plane the emission will be circularly polarised (c) and at angles in between will be elliptically polarised (b). Note that the diagram is in the perspective of the rest frame of the electron before the effects of relativistic beaming. Taken from Lyne & Graham-Smith (2006)

helical path.

For a distribution of electrons with differing kinetic energy vectors in a uniform magnetic field, the observed circular polarisation will be negligible. This occurs because electrons with opposite transverse motions along the magnetic field will spiral in opposite directions and the net radiation will be unpolarised circularly.

Due to the mechanisms involved, measuring the polarisation properties of Synchrotron emission, " is the most direct method of detecting magnetic fields" (Tinbergen, 2005). This is the core scientific aim of this thesis.

### 1.1.2 Photometric measurements for polarimetry

To distinguish the polarisation state of radiation, the magnitude of the oscillations (or the intensity) of the electromagnetic radiation needs to be sampled as a function

of angle. To do this in the optical regime, a polarising filter can be used which will transmit radiation with an aligned orientation and attenuate radiation of an orthogonal orientation. By taking four intensity measurements with a polarising filter at different angles, it is possible to deduce the level and orientation of linear polarisation.

At this point it is worth noting that rotational degeneracy occurs in the orientation of the linear polarisation of an electromagnetic wave. Orientations separated by 180°are physically identical and are unable to be distinguished. The same is true for polarising filters. For this reason the angle of rotation, $\beta$, is limited to $0° \leq \beta < 180°$.

The four optimal angles to take measurements are 0°, 45°, 90°and 135°. Two values are made by comparing the intensities of orthogonal filter angles (e.g. $I_{0^\circ}$ & $I_{0^\circ}$). This is explained in the thesis of de Juan Ovelar (2013) through Equations 1.7 and also through similar notation in Kitchin (2003). Note that the angles of -45°and 135°are identical for the purposes of polarimetric measurements.

$$Q = (I_{0^\circ} - I_{90^\circ}) \tag{1.7a}$$

$$U = (I_{45^\circ} - I_{-45^\circ}) \tag{1.7b}$$

Both Q and U are measures of the anisotropy of intensity of radiation as a function of angle. From these the full linear polarisation state of the radiation can be calculated.

**Imaging Photometry**

The core reduction method for imaging polarimetry is that of differential photometry. In its simplest form, this comprises the making of photometric measurements on 4 observations, each taken with the polaroid at angles differing by 45°. In addition to the normal photometric measurements and calibrations, a set of polarimetric calibrations needs to be made which is, arguably, more complicated than for those of simple

photometry.

Photometry is the method of measuring the flux received at Earth of a celestial source. In the CCD era, this is a very standard process in optical astronomy, and a backbone of observational astrophysics. Flux is a function of wavelength and is commonly measured as $F_\lambda$ in units of $Wm^{-2}nm^{-1}$. Astronomical observations generally use optical filters which have a certain wavelength width and response (or transmission) profile over this width, blocking any photons of wavelength outside this wavelength 'band'.

When capturing imaging data through a telescope, the CCD can be thought of as a grid of photon counters. Images of point sources (which describes all stellar sources and GRB afterglows) do not fall onto a single pixel of the CCD chip owing to a number of effects. We consider two of those here: Diffraction and Atmospheric turbulence.

$$\theta = 1.22 \times \frac{\lambda}{d} \tag{1.8}$$

The effect of telescope diffraction is to spread the flux of a point source over a 2-dimensional pattern on the CCD. This diffraction pattern is shown in Figure 1.5, where the Airy disk is the zeroth order, central diffraction spike. The width of this is expressed as an angle ($\theta$), at a certain wavelength for a telescope of diameter d (see Equation 1.8.

The second effect, that of atmospheric turbulence, makes the contribution of the Airy disk and the 2-dimensional diffraction pattern negligible. Atmospheric turbulence creates the effect known as seeing by which the turbulent column of atmosphere, through which the telescope is observing, spreads the flux from stellar sources across the CCD chip. This creates a 2-dimensional (2D) distribution which can be approximated by a Gaussian. Seeing is expressed as the full width half maximum (FWHM) of the distribution in angular terms.

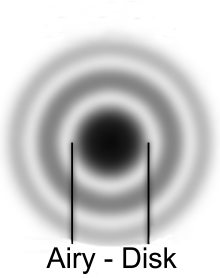


Figure 1.5: The 2-dimensional diffraction pattern produced by a circular telescope aperture. The diameter of the Airy disk is given in angular terms by $\theta$ in Equation 1.8

### Analysis

To count the number of photons, an aperture (often circular) is used to surround the source which is being measured. The number of counts within this circular aperture are summed to produce the source aperture counts. A measurement of the background levels are also taken from an annulus around the source. This is then subtracted from the source aperture counts (both scaled for the number of pixels or area that the source circle and background annulus contain) to leave a remainder which is the counts from the source. Lastly, a gain value must be applied as one photoelectron captured at the CCD is not relative to one count. The analogue to digital unit (ADU) of the CCD chip scales the charge received into an 16-bit value which can have the range of 0 to 65535 ($2^{16}$) in most CCD systems. To ensure a good dynamic range, a gain value is applied by the ADU which is measured in photoelectrons per count ($e^{-}$/ADU).

This system will accurately reconstruct the number of photons which were detected by the CCD chip from a source. However there are uncertainties in this measurement which are essential to calculate and state as part of a complete photometric measurement.

### Error calculation

Error, or uncertainty on a photometric measurement, is created by various sources of noise which are inherent in the process of observation with CCD cameras. The major

sources can be defined as Poisson counting errors on both source and sky background levels (in number of photoelectrons, $Ne^-$), dark noise (D) created from thermally induced charge in CCD pixels (i.e. not created by incident photon impacts), and the read noise (RN) which is again a stochastic effect at the ADU stage of readout of the CCD. This is generally given as an RMS value. As these noises are per photon counter (i.e. pixel) each term for noise is dependent on the number of pixels used ($N_{pix}$) which is dictated by the size and shape of the aperture used for photometric measurement.

$$\sigma_{RN} = \sqrt{N_{pix} \times RN^2} \tag{1.9a}$$

$$\sigma_{dark} = \sqrt{D \times N_{pix} \times t} \tag{1.9b}$$

$$\sigma_{sky} = \sqrt{N_{pix} \times Ne^-_{sky}} \tag{1.9c}$$

$$\sigma_{source} = \sqrt{N_{pix} \times Ne^-_{source}} \tag{1.9d}$$

Further discussion on photometric error and it's applicability to the RINGO series of polarimeters in contained in Section 4.1 within Chapter 4.

### Mathematical representation of polarisation

Polarisation of radiation is expressed in mathematical terms using Stokes vectors. The full polarisation state of incoming radiation, S, can be explained by the 4-vector shown in Equation 1.10, where I represents the total incoming radiation, Q and U express the radiation contained within linear polarisation (calculated as in Equation 1.7) and V represents the circular polarisation of incoming radiation. In order to deduce the level of linear polarisation, the Stokes parameters of Q and U need to be normalised against the total intensity, I. This produces the normalised Stokes parameters q and u as shown in Equation 1.11.

$$S = \begin{bmatrix} I \\ Q \\ U \\ V \end{bmatrix} \tag{1.10}$$

$$q = Q/I \tag{1.11a}$$

$$u = U/I \tag{1.11b}$$

The normalised Stokes parameters are the Cartesian values which represent the polar quantity of polarisation which has a magnitude and angle. The q-u plane (Figure 1.6 provides a useful visualisation of polarisation and is the basis for much analysis presented in this thesis.

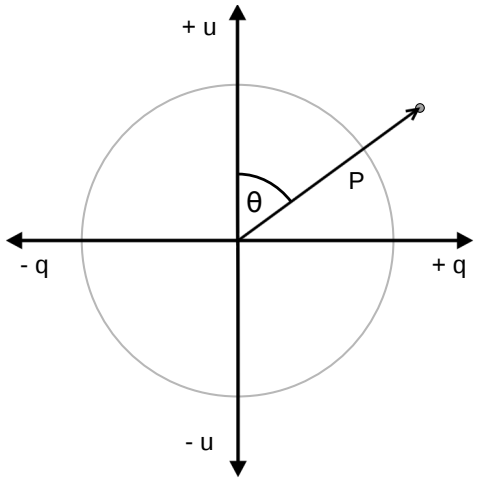


Figure 1.6: The q-u plane in which measurements of linear polarisation are plotted based on the normalised Stokes parameters q and u. The level of linear polarisation, P, is denoted by the vector length from the origin to this point. The angle of polarisation is denoted by $\beta$ which is $\theta/2$ (see equations 1.12 and 1.13)

Final values of linear polarisation are calculated using the simple Cartesian-Polar transformations given in equations 1.12 and 1.13

$$p = \sqrt{q^2 + u^2} \tag{1.12}$$

$$\beta = \frac{atan\left(\frac{u}{q}\right)}{2} \tag{1.13}$$

**Uncertainties on polarimetric measurements**

The errors on the final values of polarisation ($p$ and $\beta$) can be due to systematic and non-systematic effects. Systematic effects in the optical regime include that of the mirrors of the telescope. They will modify the polarisation state of radiation before it is measured by the polarimeter. Non systematic sources of uncertainty are in the noise of the initial measurement of I, Q and V of a source (Poisson counting noise, CCD readout noise etc.). These lead to uncertainty values on the normalised Stokes parameters, q and u.

Non-systematic sources of noise need to be quantified, but due to their nature cannot be corrected. Chapter 4, being focused on data reduction, explains the origins of noise and how determining this noise provides uncertainties on the polarisation measurement, requiring Monte Carlo methods. The systematic sources of uncertainty can be characterised for various situations, and if the modelling of these systemic effects is good enough, then corrections can be applied to remove them. The bulk of work undertaken in this thesis was on developing systems and tests to create models of systematic uncertainty for the polarimetric systems on the Liverpool Telescope. This is presented in Chapter 5, which looks extensively at methods, challenges and limitations in the characterisation of the Liverpool Telescope's polarimetric systems.

### Astronomical formalisms on linear polarisation

Often studies will provide normalised Stokes parameters that are received at the instrument, but these need to be converted to an on-sky reference to enable comparison with other observations. The orientations of the Stokes parameters obtained by a polarimetric measurement are dependent on a number of physical factors. On an altitude-azimuth (alt-az) telescope (common for 2-metre class and larger telescopes, including the Liverpool Telescope) there is first the sky angle, which changes dependent on the pointing and position in the sky of the object over time. After that point will often be a Cassegrain or Nasmyth rotator which will change the orientation of the instrument in relationship to the telescope, and is often used to de-rotate the field during tracking on an (alt-az) mounted telescope.

For cross referencing angles of polarisation between different studies, linear polarisation follows the convention of being expressed both as a percentage and an angle in degrees, which is the angle on the sky counter-clockwise (towards East) from North. This convention was decided upon in 1973 at the IAU XVth General Assembly.

### Conventions used in this thesis

Linear polarisation values derived from the normalised Stokes parameters are expressed as a percentage, with the angle in degrees. This percentage could just as easily be expressed as a decimal value between 0 and 1.

Similarly the normalised Stokes parameters (q and u) can be expressed as a decimal value between 0 and 1, or as a percentage between 0 % and 100 %. Unfortunately for the reader, one expression is not used exclusively throughout the thesis. Certain plots are labelled numerically, but the convention is to attempt to express all normalised Stokes parameters, and polarisations as percentages.

In any case, the conversions are very simple. For clarity, an example q value of 0.213, could just as easily be expressed as 21.3 %.

## 1.2 Gamma-ray bursts

### 1.2.1 Initial detection and characterisation

First discovered by the Vela satellites in 1960s (Bloom, 2011), the nomenclature of gamma-ray bursts is due to the initial observations of these phenomena. A number of events were detected in which a high-energy, short duration flash (on order of seconds) was observed. With the Vela network of satellites being primarily concerned with detecting breaches of the Nuclear Test Ban Treaty (1963), they happened to be a serendipitous tool of detection, but not one of useful characterisation. From 1969 to 1972 the satellites detected sixteen bursts, with durations ranging from 0.1s to 30s (Klebesadel et al., 1973). By analysing the timing of detection from 2 satellites, it was possible to define an annulus on the sky from where the burst could have occurred. If detected by 3 satellites, two annuli were produced. The burst direction could then be determined to one of the two points where the annuli overlap. From this relatively crude form of localisation it was possible to eliminate the Earth or the Sun as the sources of this strange radiation signature.

Due to the short time scales of the events, it was apparent that the source of gamma-ray bursts must be compact, with the short light crossing time of emission region. The high levels of flux ($\sim 10^{-5}$ ergs / cm$^{-2}$ to $\sim 2 \times 10^{-4}$ ergs / cm$^{-2}$) gave a constraint on an energy distance relation. Either they were Galactic events of moderate energy, or cosmological events of extreme energy. In the discussion of Klebesadel et al. (1973) the timings of the detections were cross correlated with optically observed transient events, such as supernovae and galactic novae. This yielded no temporal or spatial connections with these objects, leaving the origin and progenitors of gamma-ray bursts (GRBs) a mystery.

In the 15 years post detection, most theoretical work focused on the assumption that GRBs were galactic sources. Work proceeded on possible models of energy release from neutron stars that would provide the observed short-lived radiation. In 1991 the Compton Gamma-Ray Observatory (CGRO) was launched (Gehrels et al., 1992) with its sensitive Burst and Transient Source Experiment (BATSE) which could detect and accurately localise ($\sim$ 10 degrees) a large number of bursts. Within a year Meegan et al. (1992) showed directional isotropy within statistical limits on a sample of 153 bursts.

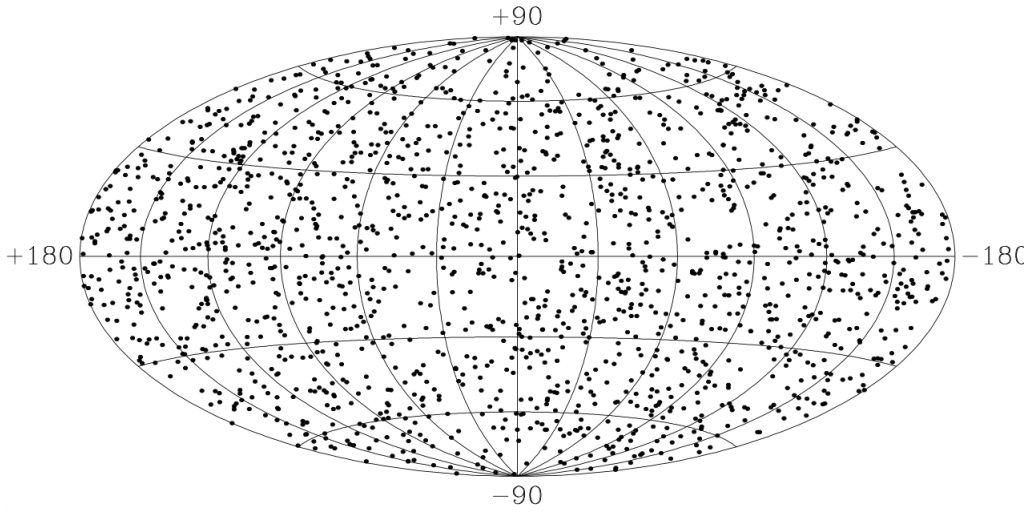


Figure 1.7: A diagram of the spatial distribution of 1637 gamma-ray bursts detected by the BATSE instrument and published in the 4Br catalogue (Paciesas et al., 1999). The Aitoff-Hammer projection gives a spatially correct representation and is projected in galactic coordinates. The isotropic nature of the events with no bias towards the plane of our own galaxy or nearby galaxies was strong evidence for GRBs occurring at cosmological distances. Taken from Paciesas et al. (1999)

Over the lifetime of CGRO the sample of 2704 localisations from BATSE revealed an isotropic distribution (Figure 1.7), with no preference for the Milky Way galactic plane, or that of any nearby galaxies, such as Andromeda. This, along with the narrower than expected flux distributions that would occur for events on galactic scales, provided strong evidence that these events originated at cosmological distances. How-

ever, this placed a constraint on the amount of energy required. To produce the observed flux, the events would require huge amounts of energy (up to $\sim 10^{52} - 10^{54}$ ergs) to be released on second time scales (Mészáros, 2002).

### Long and Short GRBs

By using the metric of $T_{90}$ (time in which 90 % of the burst fluence is detected), it was noticed that the sample of GRBs from BATSE fell into two non-distinct categories. The bimodal distribution of $T_{90}$ for the BATSE samples (Figure 1.8) points at two classes of GRBs, which were defined as long and short GRBs, with a $T_{90}$ of 2s being the dividing line between the populations.

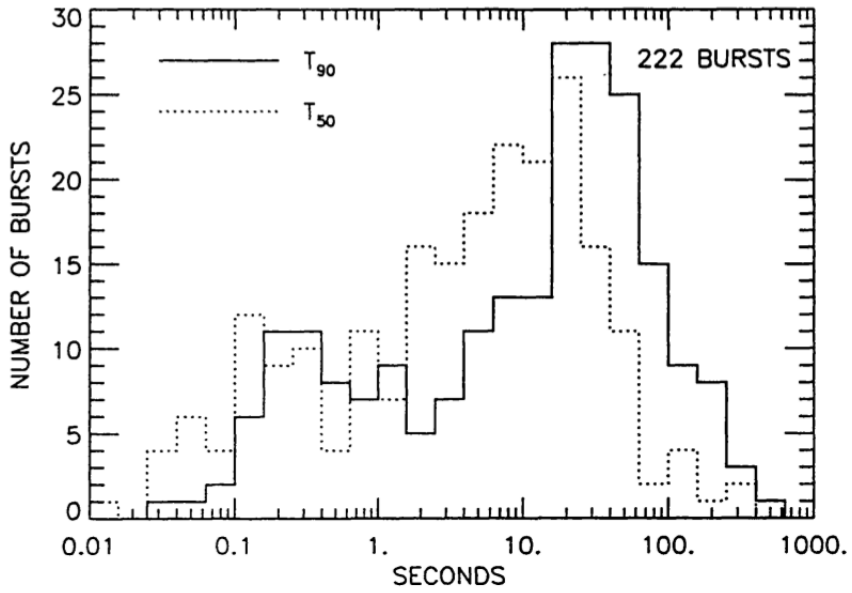


Figure 1.8: The $T_{90}$ and $T_{50}$ durations of 222 GRBs observed with BATSE. The $T_{90}$ (time of 90 % of the total burst fluence) shows a bimodal distribution with a separation near 2s. This indicates (along with a $T_{90}$ vs Spectral hardness anti-correlation) that there are two non-discrete types of event and hence at least two progenitor types. Taken from Fishman & Meegan (1995)

Supplementing the evidence for two populations of GRBs, was a link with spectral hardness. An anti-correlation between $T_{90}$ and spectral harness was found by Kouveliotou et al. (1993), meaning that long bursts had a peak gamma-ray fluence at a lower (softer) frequency than the short bursts.

#### Cosmological confirmation from GRB 970508A

The cosmological distance of GRBs was confirmed in 1997 when the Dutch-Italian satellite BeppoSAX (Piro, 1996) detected GRB 970508A. Counterparts for this burst were found in both radio and optical observations, fading over a period of weeks. These observations were of a component separate from the long finished gamma ray prompt emission, and were the first observations of a GRB afterglow.

Ground based optical spectroscopic follow-up gave constraints that the burst originated from an event at a redshift of $0.835 \leq z \lesssim 2.3$ (Metzger et al., 1997) deduced from the absorption lines of intervening gas and the upper limits of non detection of the Lyman-alpha forest. This was further constrained to $z = 1.09^{+0.14}_{-0.41}$ (Reichart, 1998). Detailed analysis of the radio observations taken over a number of weeks was in agreement with a relativistically expanding fireball with an isotropic energy of $\sim 10^{52}$ ergs (Waxman et al., 1998).

### 1.2.2 Progenitors

In order to satisfy the energy requirements to generate the observed gamma-ray fluence at cosmological distances, progenitors need to be able to deposit vast amounts of energy into a small area (confirmed by the light crossing time). If the emission were to be isotropic, an energy of $\lesssim 10^{54}$ erg would be liberated from a region of $\lesssim 100$ km within a time scale on the order of seconds (Mészáros, 2002). Woosley (1993) gave a theory of such a situation occurring in massive 'failed' core collapse supernova, where a Wolf-Raylet type star (of $\sim 15 M_{\odot}$ a collapse) forms a black hole (BH) rather than a

Neutron Star (NS). These deaths of large stars, which form a black hole can be called collapsars. With a spinning black hole and enough local material to form an accretion disk, there is a central engine with enough energy density to create the observed flux. Furthermore, the emission would not be isotropic, but in the form of 'a pair fireball' originating from the poles of the black hole rotation.

The first discovery of GRB-SNe coincidence which had eluded Klebesadel in 1973 was from the coincidence of GRB 980425A and SNIb/IC 1998bw (Bloom et al., 1999; Wang & Wheeler, 1998). This event gave the first observational support of the collapsar model of GRBs. Seven years later, Woosley & Bloom (2006) reviewed the evidence from other events and found that these GRB-SNe were of higher energy than that of normal SNe. Whilst there was a large amount of diversity in the small sample, the GRBs associated with supernovae were of the long duration, soft spectral hardness population.

The findings of dual populations of GRBs by Fishman & Meegan (1995) suggest that there is more than one progenitor method. For the shorter, and harder, GRBs the progenitors are believed to be neutron star mergers, NS-NS, (Eichler et al., 1989) or the merger of a neutron star with a black hole, NS-BH, (Mochkovitch et al., 1993).

Both of these progenitor types (collapsars or compact mergers) are expected to form a black hole of a few solar masses, surrounded by a torus of material to power the engine. For both cases the energy requirements are within one order of magnitude (Mészáros et al., 1999) and both form a viable black hole and material torus central engine from which the GRB is powered.

### 1.2.3 The fireball model and jets

Over the past 20 years, much has been determined about the origin and mechanisms of GRBs. However Ghisellini (2010) provides a review of our 'Pillars of knowledge'

regarding GRBs, and whilst they are well constrained, they are also few. Ghisellini commits only to the facts that GRBs are cosmological, have large bulk Lorentz factors ($\Gamma \gtrsim 1000$), contain prompt and afterglow phases, have two non-distinct populations of long and short and have a connection with core collapse (Type Ic) supernovae.

Despite this progress, the main challenge for any model of GRBs is to explain the conversion of the vast input energy deposited into a small volume (on order of Schwarzschild radii) into the observed high energy radiation. The fireball (or blast wave) theory of gamma-ray bursts, developed by Mészáros & Rees (1994) provided a viable and testable mechanism for conversion of energy to radiation. In this model, the central engine accelerates material into a relativistic 'wind' in the form of expanding shells of plasma in a jet structure. The more erratic prompt gamma-ray emission occurs from within the expanding jet, as shells with different bulk Lorentz factors collide, whilst at later times, the smoother afterglow emission in x-ray, radio and optical wavelengths occurs as the jet collides with the denser interstellar medium (ISM). In both of these emissions, collisionless shocks lead to non-thermal emissions (Mészáros et al., 1994).

The conversion of energy from the central engine into the bulk motion of the relativistic jet, and its subsequent conversion into radiation is proven through observation. The greatest uncertainty is the composition of the energy within the jet. The Mészáros & Rees model proposes a baryonic fireball, where an acceleration of matter to high Lorentz factors occurs due to huge internal pressure against the opaque electron-positron pairs created by the huge energy density of the central engine.

An alternative model championed strongly by Lyutikov & Blandford (2003) allows for a matter free fireball, where the energy of the spinning black hole engine is removed in an electromagnetically-dominated outflow. A relativistic magnetic bubble 'cold fireball' is created, which then releases the observed electromagnetic emission due to electromagnetic instabilities and recombination in a free force plasma (Poynting-Flux).

In either the baryonic model (Mészáros & Rees) or magnetic recombination model (Lyutikov & Blandford), the final conversion of the energy from the central engine to the observed afterglow radiation happens owing to the synchrotron emission process, where free electrons spiral around magnetic fields, converting their kinetic energy into electromagnetic radiation. It is also noteworthy that these two theories are not exclusive of one another, in that the energy of a GRB fireball could be magnetically dominated, but still contain baryonic matter. This is discussed later in this section.

**Afterglow emission**

Whilst the prompt gamma-ray emission from GRBs can provide a great deal of information about the energy source, the flash is often very short lived and observations are constrained by the specifications of the satellite mounted instruments. The afterglow phase, however, provides a much longer window of observation in a number of wavebands. For terrestrial observers, the onset of the afterglow phase occurs within minutes of the prompt emission, and can be visible for a timescale of days (optical emission) to months (radio emission).

Distinct from the prompt emission, the afterglow occurs as the relativistic jet from the central engine is slowed by a denser interstellar medium (ISM). As the Lorentz factor of the jet decreases the bulk energy is converted into a shock front, providing a huge amount of kinetic energy to the plasma material at the boundary. The radiative cooling of this 'forward shock' is the observed afterglow.

In hydrodynamic simulations of a baryonic jet such as Kobayashi et al. (1999) (Figure 1.9), the forward shock can produce a short lived reverse shock which will propagate back down the jet, producing a separate emitting region from within the jet.

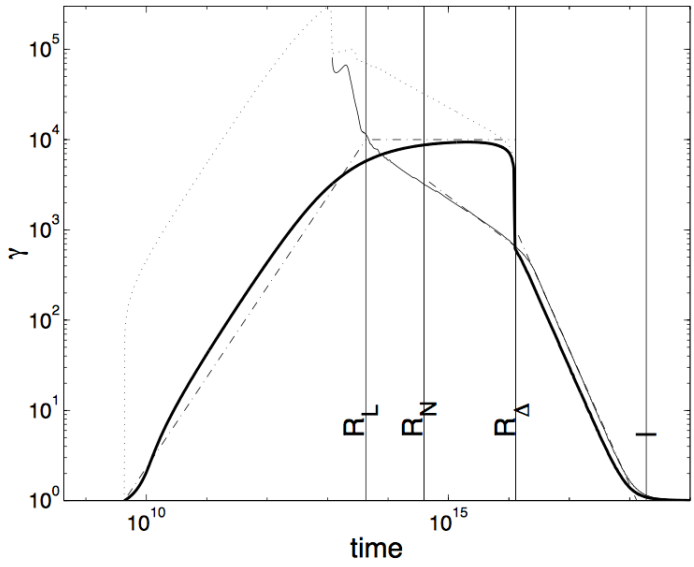


Figure 1.9: Hydrodynamical simulation of the bulk Lorentz factor, $\gamma$, of a baryonic jet vs time. $R_L$, $R_N$ and $R_\Delta$ are the radius of coasting, radius of reverse shock and radius of external shock respectively. Taken from Kobayashi et al. (1999)

### Synchrotron spectrum

In synchrotron radiation, an accelerating charge produces electromagnetic radiation. For a single electron, spiralling around a magnetic field, the radiation would be observed as a series of pulses of radiation at the same wavelength. The wavelength is dependent on the (kinetic) energy of the electron, where $\nu \propto KE^2$. However, with synchrotron radiation in astrophysical situations, there are a huge number of free electrons and the resultant radiation is characterised by the energy distribution of the population.

$$N(E)dE \propto E^{-k}dE \tag{1.14}$$

Equation 1.14 gives the approximate energy distribution, $N(E)$, for a population of electrons, where $k \simeq 2$ . This leads to a smooth distribution whereby the number of electrons with a certain energy decreases as energy increases. In a uniform magnetic field the radiation will form the characteristic power law spectrum of synchrotron radiation, which is easily distinguishable from that of thermal emission (Figure 1.10).

Also, the linear polarisation of this radiation will be $\sim 70\,\%$, as the angular momenta of the electrons will all have aligned axes.

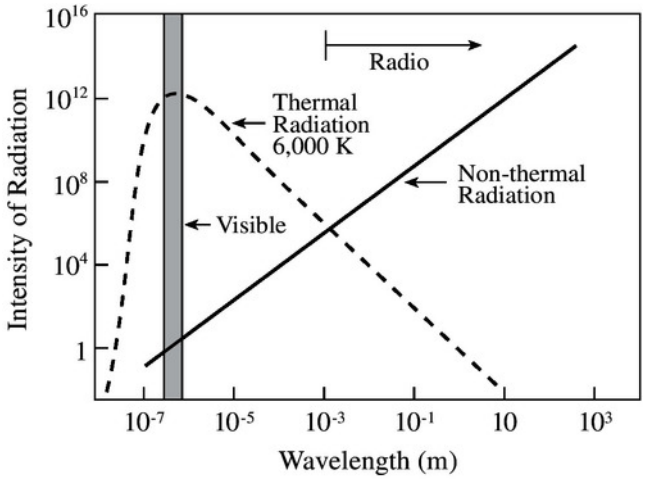


Figure 1.10: Basic diagram showing the different spectra provided by both thermal and non-thermal (synchrotron) radiation. From Lang (2013)

In the case of GRB afterglows, the relativistic jet collides with the ISM, transferring bulk kinetic energy of the jet (Baryonic jet model) into the kinetic energy of the electrons, through collisionless shocking. In the case of a single input of energy, the emission from the electrons will change with time, as they lose energy in the form of radiation. Viewed simplistically (in the absence of any other effects or absorption), the observed flux from a gamma-ray burst afterglow follows Equation 1.15 (Sari et al., 1998), where $\alpha$ and $\beta$ are positive, producing a transient lightcurve that decays with time. Despite its simplicity, values of $\alpha$ and $\beta$ are used as a metric to characterise GRB afterglows.

$$F(\nu) \propto t^{-\alpha}\nu^{\beta} \tag{1.15}$$

### Synchrotron cooling

Sari et al. (1998) provides a much more detailed model of the spectra for GRB afterglows, showing the synchrotron cooling of shocked material (Figure 1.11). This deals with a number of effects such as synchrotron self absorption, occurring below $\nu_a$, and the cooling frequency. This is defined as the frequency of the orbit of an electron spiralling in the magnetic fields, which cools in a time frame equal to the current hydrodynamical time, $t_{hyd}$. These spectra provide 4 different power law segments which move across the spectrum as the environment of the shocked material changes. Fast cooling occurs when the typical (or peak) synchrotron frequency ($\nu_m$) is higher than the cooling frequency ($\nu_c$). As the material cools, $\nu_c$ drops below that of $\nu_m$ and from this point the material is in the slow cooling phase.

The significance of the shape of the cooling spectra is apparent in its impact on observed optical lightcurves. As $\nu_m$ or $\nu_c$ move through the observing band, the lightcurve will experience a 'break' where the steepness of decay ($\alpha$) will change. This break in the lightcurve would also be joined by a change in spectral index (colour) if observing lightcurves in multiple bands. With high cadence, multi-band photometry it could even be possible to observe the lightcurve breaks occur at different moments in different bands.

### Reverse shocks and compound lightcurves

Reverse shocks are a feature of GRBs that cannot occur in the scenario of a purely magnetic, matter free fireball, and for that reason have been a prized phenomena for astronomers to observe. As reverse shocks are short lived, they require ground based optical observations to commence within hours, if not minutes, of the detection of the prompt emission.

GRB 990123A was widely observed by a number of ground based facilities and provided evidence of the cooling break ($\nu_c$) passing through the optical wavebands at

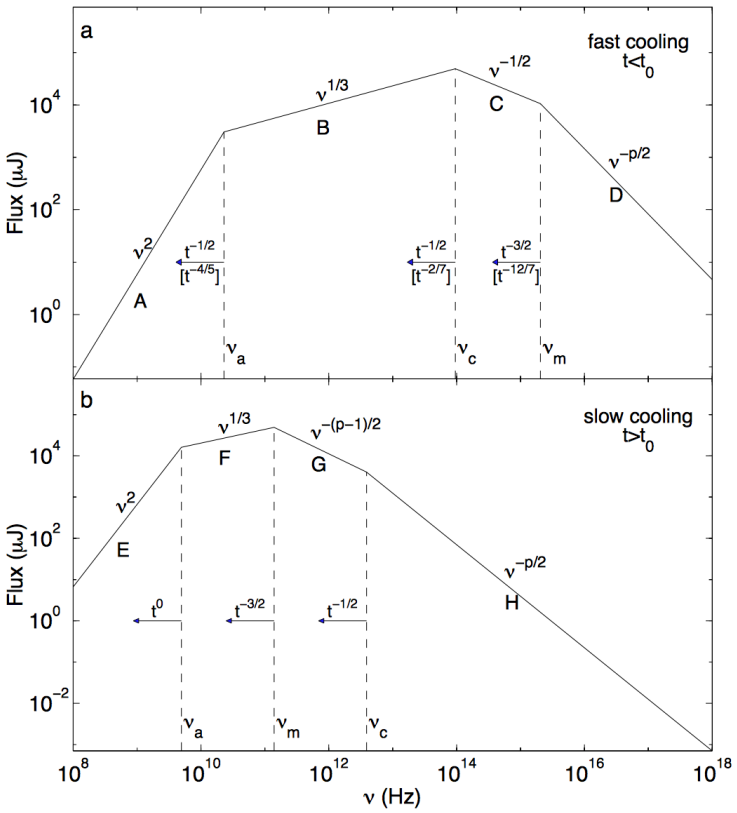


Figure 1.11: Synchrotron cooling spectra of a relativistic shock. The case of fast cooling (a) is expected at early times ($t < t_0$), whereas slow cooling (b) occurs at later times ($t > t_0$). The frequencies, $\nu_m$, $\nu_c$ and $\nu_a$ are the 'typical' synchrotron frequency, the cooling frequency and the self absorption frequency respectively. These decrease over time as indicated. Taken from Sari et al. (1998)

around 1 day (Castro-Tirado et al., 1999). In addition to this, the fast small follow-up telescope ROTSE-I (Marshall et al., 1997) was able to view the 8.86 magnitude burst at early times (Gisler et al., 1999) and an optical 'flash' was observed that could be interpreted as a reverse shock (Mészáros & Rees, 1999; Wang et al., 2000).

GRB 021004A was also well observed by both ground based and space based optical facilities, producing very detailed lightcurves. A number of bright deviations were observed to the expected cooling decay lightcurve over the first 24 hours of the observations (Mirabal et al., 2002; Pandey et al., 2003).

A prime explanation for these bright deviations in both bursts and also in GRB 021211A was given as the presence of reverse shocks (Kobayashi & Zhang, 2003; Zhang et al., 2003). This led to the categorisation of characteristic afterglow lightcurves based on the relative strengths and timings of the forward and reverse shock emissions (Figure 1.12).

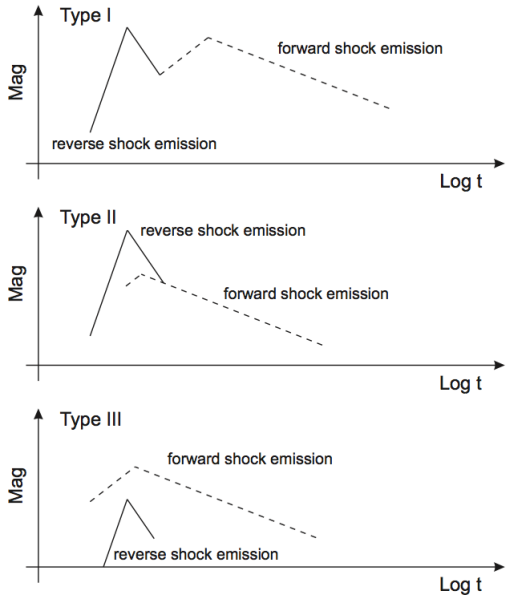


Figure 1.12: Illustration of forward and reverse shock components forming compound lightcurves. Reverse shock emission decays at a higher rate to the forward shock emission. A classification introduced by Zhang et al. (2003) gives a Type I lightcurve, where two peaks will be observed, or a Type II, where there is a single peak and an early time break in the lightcurve decay as the forward shock becomes dominant. In Type 3 situations the presence of a weak reverse shock contribution will be hard to distinguish just from the temporal features of a lightcurve. Taken from Mundell et al. (2010)

To constrain the characteristics of an optical lightcurve, multiple photometric measurements are required with a high cadence. Single band observations (e.g. Sloan r') with a high enough signal to noise ratio (small photometric errors) will be able to provide good sampling of the lightcurve to identify forward and reverse shock components. However, with forward and reverse shocks also having distinct spectral evolution, it is desirable to have multi-band photometry which will help further distinguish

the energetics of the forward and reverse shocks.

An important point to note is that the forward shock emits radiation at the jet boundary, whereas the reverse shock emitting region is from within the jet.

**Fireball magnetisation and polarisation**

The magnetisation of the fireball is the metric which distinguishes between a baryonic or magnetic dominated outflow. The metric is the ratio of magnetic to kinetic energy (Equation 1.16). For a baryonic jet where the energy is almost entirely contained in the kinetic energy of the relativistic material, $\sigma \ll 1$. In the case of a matter free fireball where the energy is contained exclusively in the advected magnetic field from the central engine (Poynting-Flux), then $\sigma \to \infty$.

$$Magnetisation\,(\sigma) = \frac{Magnetic\,Energy}{Kinetic\,Energy} \tag{1.16}$$

Magnetohydrodynamical (MHD) simulations of relativistic energy outflows of differing magnetisations provide predictions for the observed afterglow lightcurves in both temporal and spectral evolution Zhang & Kobayashi (2005). However it is polarisation of the radiation which is a key factor for distinguishing the magnetic field structure and hence the magnetisation of the jet.

In the baryonic model, there is expected to be no large scale order to the magnetic fields in the jet, leading to low levels of polarisation for any radiation produced from within the jet. In the Poynting-Flux model, large scale magnetic fields are expected to exist within the jet leading to high levels of linear polarisation (Lyutikov, 2009).

To probe the magnetic field structure of the jets through optical polarimetric measurements, the burst must have a reverse shock component which dominates that of the forward shock. Any period where this is the case will be at early-times, short lived,

and at a point where the lightcurve is highly variable. To make significant polarimetric measurements requires a high cadence polarimeter, mounted on a telescope that can react quickly to bursts.

### 1.2.4 The era of rapid GRB follow-up

At the start of the millennium, a new era of observational gamma-ray research was required to further the understanding of GRB processes and test the models being proposed. This era had to turn follow-up of GRBs into a routine task, rather than the patchy and disparate chance observations around the turn of the millennium. The observational parameter spaces which would provide the largest scientific gain were in the early-time afterglow onset phase (occurring minutes after the prompt emission) and in dense sampling of this period of a burst with observations across a large number of wavelengths from X-ray to radio. To enable these observations a low latency trigger mechanism signalling a burst detection was needed, together with a large network of global observatories responding simultaneously.

A drive for instruments specifically designed for GRB follow-up has led to innovative developments, such as the simultaneous 7-band imager GROND (Greiner et al., 2008) and the RINGO series of polarimeters. These instruments have been essential for the realisation of science findings in the era of rapid follow-up.

#### *Swift*, Integral and the GCN

The 2004 launch of the NASA *Swift* satellite (Wells & Gehrels, 2004) is heralded as the start of the era of rapid ground based follow-up for GRBs. With the Burst Alert Telescope (BAT), *Swift* was specifically developed to monitor half the sky and be able to provide a 2-sigma positioning error circle to ground based instruments of $\sim$4 arcmins. This happens within a minute of the detection, giving a trigger to ground based observatories through the Gamma-ray Coordination Network (GCN) (Barthelmy

et al., 1998).

*Swift* also has the XRT, X-Ray Telescope, (Burrows et al., 2003), and the UVOT uv-optical instrument (Nousek et al., 1999). Once the BAT has detected a burst, *Swift* will rapidly slew to the location providing X-ray and UV-optical coverage. Upon identification of the X-ray counterpart, localisation of arcsecond accuracy can then be passed through the GCN network. The network is monitored by a wide number of observing facilities globally. These facilities often have override procedures to normal scheduled observing to perform follow-up observations. Upon identification and measurements of the optical (or radio) counterparts, the GCN acts as a real time communications network for publishing observations which will inform future actions of larger facilities. These, in turn, may make deeper observations over a number of days following the initial trigger.

The INTEGRAL satellite is another space based gamma-ray observatory which predates the launch of *Swift*, and provides a contribution to the GCN network in the form of triggers. However whilst the detection rate of *Swift* is on the order of $\sim 3$ per week, INTEGRAL's Burst Alert System, IBAS, has a detection rate that is approximately the same number within a month. The positional accuracy and latency of transmission of INTEGRAL triggers on the GCN network are broadly comparable to that of *Swift*, being measured in a few arcminutes and tens of seconds respectively.

**The Liverpool and Faulkes Telescopes**

To exploit the low latency of the GCN triggers, ground based response has to be equally fast. Human telescope operators will lose valuable time in the process of starting follow-up observations, compared to an automated system. The Liverpool and Faulkes telescopes are 2.0 metre class robotic observatories which have a Robotic Control System (RCS), eliminating the need for an onsite or even remote observer. Based in La Palma, Hawaii and Western Australia, these telescopes provide good global cov-

erage to be able to respond to GRB triggers.

The Liverpool Telescope with its fully autonomous operation has been at the forefront of fast optical follow-up of GRBs (Mundell et al., 2010). An automated response (Guidorzi & et al, 2006) to triggers from the *Swift* satellite has enabled observations to start as little as 90 seconds after the burst trigger. This early-time response has enabled the Liverpool collaborators to probe the characteristics of the initial burst, by catching the optical transient (OT) before the peak of the light curve. At these early times, energy is still being injected into the system from the central engine of the GRB and the onset of the afterglow phase can be directly observed.

**GRB 061126A**

A breakthrough follow-up operation occurred with GRB 061126A, which was the epitome of the scientific realisation of the rapid follow-up era. Observed from 26 minutes post trigger to 20 days in the X-ray and from 258s to 15 days in the optical, with gamma-ray and ultraviolet observations from *Swift* BAT and UVOT, the afterglow of this burst was extremely well observed temporally and spectrally (Gomboc et al., 2008).

With use of the GCN for communications, optical photometric observations of this bright burst were taken from the Faulkes Telescope North & Gemini North (Hawaii), The Liverpool Telescope & Isaac Newton Telescope (La Palma), Tautenburg Schmidt Telescope (Germany), SARA observatory (USA), Sampurnanand Telescope & Himalaya Telescope (India), plus other smaller observatories. This was the first realisation of true global coverage for observations of a GRB event.

The well sampled multi-colour lightcurve (Figure 1.13) gave good constraints on the temporal decay in the reverse shock ($\alpha_r = 1.69 \pm 0.09$) and forward shock ($\alpha_f = 0.78 \pm 0.04$). From the various models of jet physics, the values obtained for the tem-

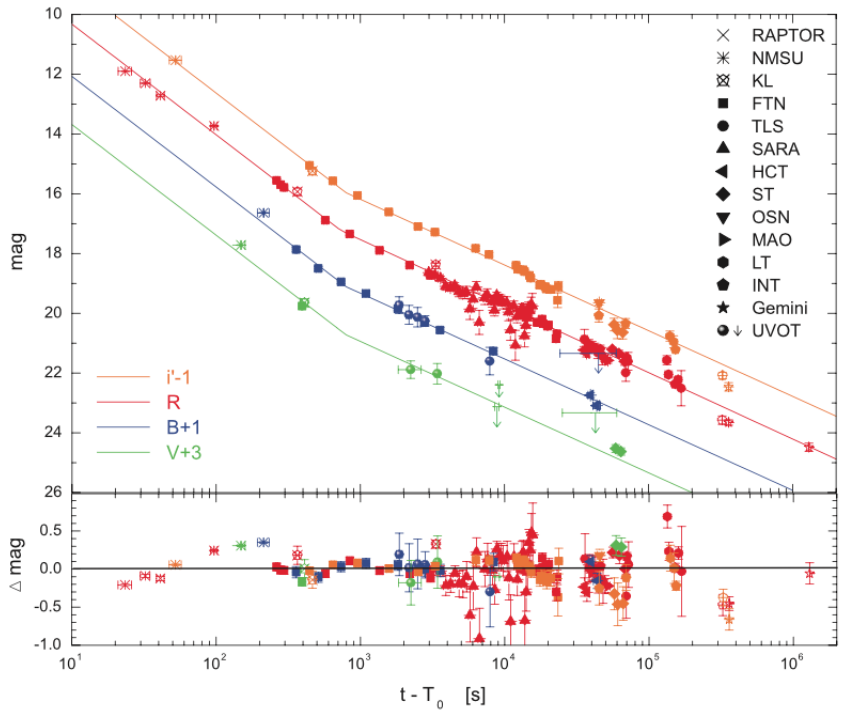


Figure 1.13: The well sampled, multi-band optical lightcurve of GRB 061126A. This burst epitomised how the co-ordinated efforts in ground based optical follow-up could lead to high sampling of the lightcurve over a long period to enable accurate characterisation of the afterglow parameters. The obvious break in the lightcurve at $\sim$ 900 s shows that there are both forward and reverse shock components contributing to the lightcurve at early times, and that the burst is of a Type II burst from Figure 1.12. Taken from Gomboc et al. (2008)

poral decay were interpreted thus: The jet has much higher magnetic energy density than at the point of the fireball deceleration. Despite this the jet is expected to be baryonically dominated. The observations and findings are presented in Gomboc et al. (2008)

To deduce the magnetic properties of the emission regions of the forward and reverse shock, and confirm the models from which the interpretation was based, would have required accurate polarimetric measurements occurring within the period of $10^2$ s to $10^4$ s.

### 1.2.5 Early-time polarimetric measurements of GRBs

Polarimetric measurements had been performed on a handful of GRB afterglows (Greiner et al., 2003; Hjorth et al., 1999; Wiersema et al., 2012) before the era of rapid follow-up. These measurements showed a low polarisation ($\lesssim 2\,\%$) and high variability in polarisation angle. In these late time measurements the emission is coming from the shock front region where no ordered magnetic fields are expected to occur, and the low values of polarisation are consistent with this expectation. One exception to this was GRB 020405A which was observed with a V-band polarisation of 9.9 % , as late as 1.9 days post burst (Bersier et al., 2003).

One promising observation was a measurement of polarisation in the prompt gamma-ray emission of GRB 021206A (Coburn & Boggs, 2003) by the RHESSI satellite (Lin, 2000). With the prompt emission showing extremely high polarisation, there was strong evidence of the uniform magnetic fields which support the Poynting-Flux theory of relativistic jets (Lyutikov et al., 2003). This generated vast discussion. However, reanalysis of the RHESSI data found that the original claims were based on errors of data reduction and that there were no constraints on the prompt emission polarisation which could be deduced from the data set (Wigger et al., 2005).

#### Breakthrough measurements with the Liverpool Telescope

The Liverpool telescope made the first early-time polarimetric measurement of a GRB afterglow with the original RINGO polarimeter. GRB 060418A was observed 203s after the prompt emission and provided an upper limit of 8 % polarisation at a time when the forward and reverse shocks were providing equal amounts of radiation (Mundell C.G. et al, 2007). GRB 090102A provided a measure of $10.2 \pm 1.3$ % (Steele et al., 2009), which was the first early-time confirmation of this level of polarisation. This was the average measure of a 60 second exposure, during which time the polarisation could have been higher and changed angles. The event could have been modelled by any of the 3 jet structures found in figure 1.14.

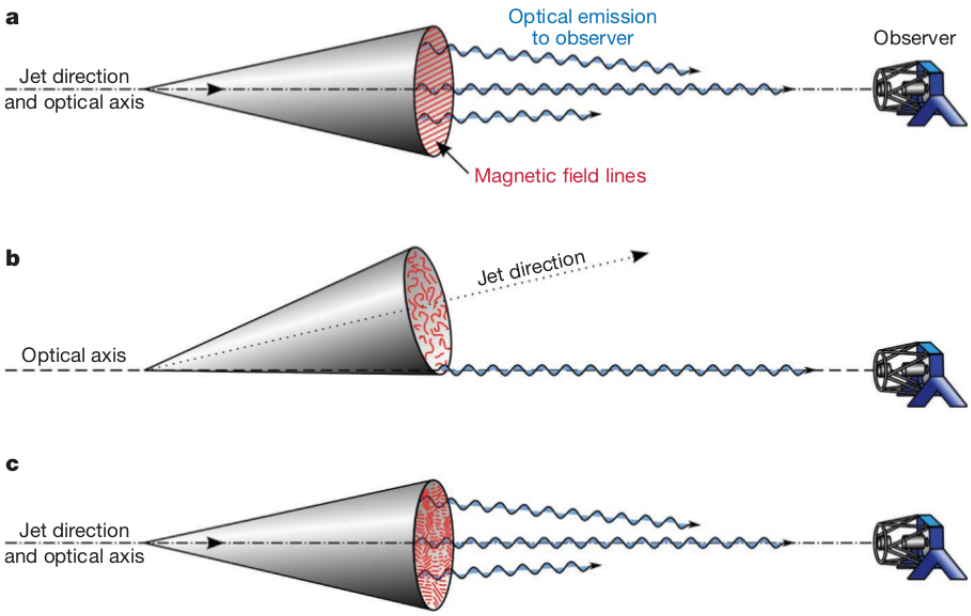


Figure 1.14: Possible models of jet magnetic fields and orientations which would explain the observations of GRB 090102A. A high degree of polarisation is predicted in the case of a large scale ordered magnetic field (a) with a constant polarisation angle. A high degree of polarisation could also be seen in the case of a disordered, tangled magnetic field if we are viewing the jet off axis (b). In this situation it is expected that the degree and angle of polarisation should fluctuate on small time scales (on order of minutes). A compromise between the two models would be patches of ordered magnetic field structure (c), in which stochastic fluctuation in the ordered magnetic field patches would provide smaller degrees of varying polarisation, with possible changes in polarisation angle. RINGO3 continues and improves the work of RINGO2 in being able to distinguish between these models with high cadence polarimetry.

RINGO2 used a new design, which is able to provide greater temporal structure to the measurements of GRBs. The first observing success was in the observation of GRB 110205A (Cucchiara et al., 2011), where two measurements were made at early-times, giving a 3-sigma upper limit of 16 % with an observation starting 243s after the trigger and then a 2-sigma upper limit of 3.6 % at 56 minutes post trigger.

Work undertaken in this thesis deals with the data analysis of all other GRB afterglows observed during the life of the RINGO2 instrument.

## 1.3 Polarimeters on the Liverpool Telescope

Having dealt only with the physics and results of polarimetric observations of GRB afterglows in Section 1.2, this section will address in much greater detail the concept, engineering and observing properties of the Liverpool Telescope and the RINGO series of instruments. Being developed by Liverpool John Moores University, the RINGO series of polarimeters have been exclusively mounted on the 2 metre Liverpool Telescope (LT).

### 1.3.1 Liverpool Telescope

At the end of the last century, as the Gemini Telescopes (Mauma Kea, Hawaii; Cerro Pachon, Chile) and the Very Large Telescope (Cerro Paranal, Chile) heralded the 8-metre era, the LT with its 2.0 metre aperture could look like an outdated development. However, the LT was developed specifically to excel in a niche area of time domain astronomy in which other facilities could not compete. The key to this was enabling robotic observation, bringing in new observing structures for remote observers. This enabled detection and monitoring of bright transient sources, such as supernovae, novae, galactic microquasars, microlensing events, transiting extrasolar planets and of course gamma-ray bursts.

The Liverpool Telescope (Steele et al., 2004) saw first light in July 2003, and was rapidly developed to become the world's largest fully autonomous telescope. The LT is situated at the Observatorio del Roque de los Muchachos (ORM), at an altitude of 2363m, on the island of La Palma. With a latitude of $\sim 28^{\circ}$, the ORM is one of the best Northern Hemispheric observation sites in the world.

#### Optical Design

The LT's design is a 2.0 metre, $f/10$, Ritchey–Chrétien telescope, on an Alt-Az mounting. It has a Cassegrain focus which is managed by an Acquisition and Guidance

(A&G) unit, with a single straight through instrument port and 8 available side ports. The telescope beam can be very quickly directed to any of these ports, via the insertion and rotation of a 45°plane science fold mirror. This setup allows the LT to have a rich instrument suite, with fast changes between instruments.

The dome is of a novel 'clam shell' design, which folds away completely when open. This allows the telescope to slew quickly ($\sim 2^{\circ}\,s^{-1}$) to any part of the sky without a large dome to rotate. The benefit is that observations can start immediately from the point when the telescope starts tracking, without having to wait for the rotating dome to 'catch up'. This is essential to maximise observing time for a telescope that will be observing a large number of objects and pointings over an observing night. A drawback to this design is that the dome does not protect the telescope from wind buffeting which can produce vibrations / oscillations in pointing leading to blurred images (extended point spread functions).

**Instrumentation suite**

The instrumentation suite of the LT is constantly being upgraded. However, it has generally hosted a standard optical imaging camera (RATcam, IO-O), a near infrared imager (SupIRCam, IO:I), a fibre fed integral-field spectrograph (FRODOspec), a long slit spectrograph (Meaburn Spectrometer, SPRAT) plus a polarimeter (RINGO, RINGO2, RINGO3). In addition to these instruments the LT has hosted a number of specialist instruments for specific areas of time domain astronomy. A list of instruments which have been permanently mounted on the LT is presented in Table 1.1.

This rich instrumentation suite allows observations for many diverse proposals to be observed on the same night. This provides long term monitoring and also rapid response facilities to observers, all of which is enabled by the unique autonomous observing functionality.

| Instrument | Type | Description |
|---|---|---|
| IO-O | Optical imager | $10 \times 10'$ FOV |
| IO-I | Near infra-red imager | $6.27 \times 6.27'$ FOV |
| RISE | Fast readout imager for transiting exoplanet research | $9.2 \times 9.2'$ FOV |
| RINGO3 | Simultaneous 3 band high cadence polarimeter | $\sim 4 \times 4'$ FOV |
| SPRAT | Low dispersion spectrograph | 4.6 Angstrom/pixel dispersion |
| LOTUS | Ultraviolet spectrograph | 320-630nm range |
| FRODOSpec | Dual arm fibre fed integral field spectrograph | Blue arm 390-570nm, Red arm 580-940nm |
| RATcam | Optical imager | $4.6 \times 4.6'$ FOV, replaced by IO-O in February 2014 |
| RINGO2 | Single band high cadence polarimeter | $\sim 4 \times 4'$ FOV, replaced by RINGO3 in October 2012 |
| RINGO | Novel ring polarimeter | $\sim 4 \times 4'$ FOV, replaced by RINGO2 in June 2009 |
| SupIRcam | Near infra-red imager | Decomissioned in July 2010 |

Table 1.1: List of instruments which have been mounted on the Liverpool Telescope.

### Autonomous operation

The autonomous operation of the LT is enabled by the Robotic Control System (RCS) developed by Fraser & Steele (2002). On conventional telescopes with an observer, there is the Telescope Control System (TCS) which controls pointing and tracking of the instrument and then an Instrument Control System (ICS) which manages exposures and data acquisition. The RCS takes the place of the observer by controlling the TCS and ICS to make observations.

The RCS was designed with two key drivers, reliability and efficiency. The Liverpool Telescope with its own weather station is able to operate completely autonomously, and whilst remote support astronomers monitor the start up of the telescope each night, the human intervention in the telescope operations is rarely required.

To drive efficiency the RCS makes real time decisions on observations based on current observational conditions. This is done using a scheduler which is constantly performing scoring of observations and selecting the next candidate observations from the accepted observing blocks. The observations have a priority and a number of user defined observing constraints (i.e. maximum airmass, moon distance, etc). Based on these priorities and constraints, the RCS works its way through observations over an observing semester.

The RCS can also handle overide requests, which is an esential part of the Liverpool Telescope GRB follow up operations. Upon notification of a GRB trigger, with observable co-ordinates the telescope is able to cease the current observation and respond to this request.

Anecdotally, it is claimed that when installed, the RCS doubled the efficiency of the LT compared to a human observer. However at that time the human observers were doing 2 week shifts in a small noisy room, so it is hardly surprising.

**GRB Follow-up routine**

The LT-TRAP pipeline developed by Guidorzi & et al (2006) is an automated and autonomous response system to GCN triggers of new GRB detections from *Swift* / INTEGRAL. Upon a trigger the pipeline cross checks the location with known galactic soft gamma-ray repeaters (SGRs), which can produce an unwanted, non GRB trigger. If the source location is not known, LT-TRAP takes over control of the telescope from the RCS.

The pipeline performs a first response polarimeter observation of 200 $\rightarrow$ 600s, before switching to the imaging camera to take 3 Sloan $r'$ band exposures for object identification. Given that the error circle of the BAT trigger is $\sim 4$ arcmins, the pipeline tries to detect which, if any, object in the field is a good GRB candidate. By cross cor-

relating sources with known catalogues and analysing any magnitude difference within the three $r'$ band exposures, the pipeline can automatically detect the transient.

By this point an LT GRB team member, who has been alerted by text message, will be monitoring the pipeline and the decisions it makes. If an optical transient is found, and it is of adequate magnitude, polarimetric observations will be scheduled. If the magnitude is fainter than $r'$=17, then the quality of the polarimetric measurements will not be adequate, so the pipeline will image in Sloan $g'$, $r'$, $i'$, $z$ to obtain data of multi-colour lightcurve, and obtain constraints on redshift.

If no transient is found then the pipeline will take deeper exposures in $r'$ and $i'$ bands, to attempt to find a faint counterpart, and in the process give upper limits of the magnitude of the optical counterpart to the burst. With at least one team member observing GCN reports, the pipeline may be over ridden at any time to perform specific observations.

### 1.3.2 RINGO

Polarimetry of transient sources, such as supernovae and GRBs, complicates the measurment method of polarisation. These variable objects require that measurements of radiation intensity for a number of polaroid angles are obtained at a cadence which is much faster than the time scales of photometric variation. Due to this, the original RINGO instrument (Steele et al., 2004) was based on the design of Clarke & Neumayer (2002) which employs a rapidly rotating ($\sim$500 rpm) prism and polaroid to produce ringed images, within which the polarisation state was encoded (Figure 1.15). RINGO was a single band polarimeter with a wide band which encompassed both V and R bands.

To reduce the data from an exposure and make a polarisation measurement, the ring was split into 8 segments, from which the flux and error would be calculated. From

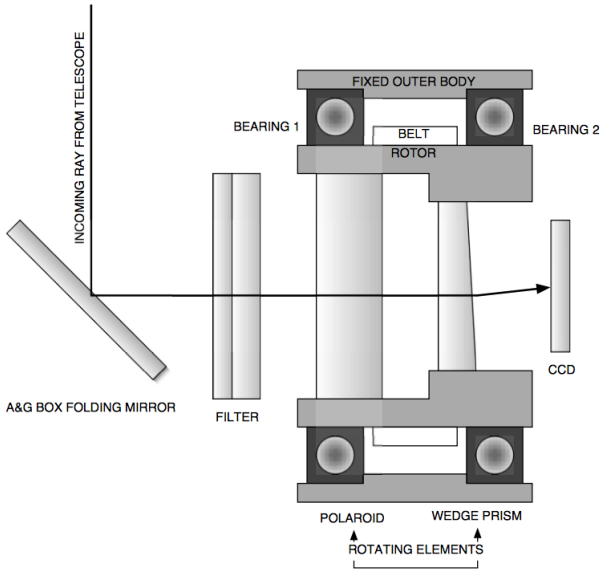


Figure 1.15: Cross-section of RINGO showing the rotator and prism which together produce the ringed images. As the ring rotates the polaroid will be modulating the flux, based on the level of linear polarisation, thus encoding the polarisation into the flux profile of the ring. From Steele et al. (2010).

these 8 measurements, simple and elegant calculations described by Clarke & Neumayer (2002) enable the normalised Stokes parameters of q and u to be determined. The equations are used for all the polarimetric calculations of all RINGO instruments and are covered in Chapter 4, which outlines the data reduction methods and considerations for RINGO2 and RINGO3.

The RINGO design had several drawbacks, however, which were all due to the ringed images. The spreading of the flux on the CCD into a ring of 40 pixel radius meant that both the read noise and sky noise for this was up to 200 times higher than a conventional non-ringed image. This limited polarimetry to $\sim$16th magnitude or brighter GRB optical afterglows, of whose observational occurrence is expected to be less than a couple per year. A second issue was that during a single integration only the average polarisation could be calculated. Any changes in polarisation magnitude or angle during the integration could not be measured. Lastly, the rings of sources which were close together could overlap and interfere with each other, posing data reduction issues and higher levels of uncertainty.

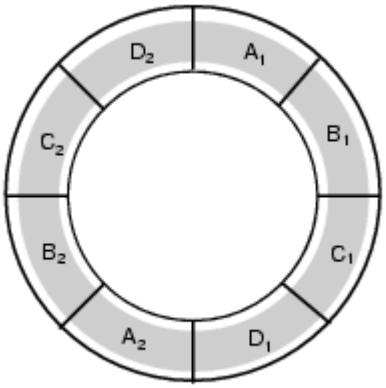


Figure 1.16: The Diagram from (Clarke & Neumayer, 2002) is showing the original RINGO ringed image split into 8 flux bins, which are synonymous with RINGO2's set of 8 non-ringed images. As linear polarisation is measured between 0 and 180 degrees, regions on opposite sides of the ring (i.e. A1 and A2) represent polaroid rotations which measure the flux at an identical angle of polarisation.

### 1.3.3 RINGO2

Mounted in July 2009, RINGO2 (Steele et al., 2010) used a new design exploiting a fast readout electron multiplying CCD (EMCCD), which was electro-mechanically triggered 8 times per rotation of a polaroid. With normal non-ringed imaging, this polarimeter was able to perform polarisation measurements down to $\sim$17th magnitude, and also enabled variable temporal analysis of polarisation over the duration of observations. Another benefit of RINGO2 was that accurate temporal photometry could also be determined from the data along with polarimetry, by stacking the 8 frames to provide the full flux in all orientations. This instrument enables both sampling of a light curve and polarimetric measurements in one observation.

The amount of data from RINGO2 is large with eight $512 \times 512$ pixel frames being produced per second for the single camera. A 700 second observation in raw data is around 6 GB for RINGO2. These files are automatically processed on site, the morning after observations. Each 125ms frame is stacked with frames of corresponding polaroid rotation, producing 8 FITS files for each observation. By performing photometry on each image, 8 fluxes are obtained which are synonymous with the 8 segments of the

ring in a RINGO observation. Each file corresponds to a 45 degree region of the rotating polaroid as shown in Figure 1.16.

At the commencement of this course of study (October 2011), RINGO2 was still mounted on the Liverpool Telescope and in active follow-up service, gaining excellent early time data of GRB afterglows. Details of these observations are in Chapter 6.

### 1.3.4 RINGO3

To extend the design of RINGO2, a multi-band version was envisaged, using 2 dichroic mirrors and 3 EMCCD cameras to enable simultaneous photometric and polarimetric measurements in 3 bands (Figure 1.18). RINGO3 (Arnold et al., 2012) had been almost fully designed by October 2011, with only minor design elements (e.g. specification of dichroic mirrors) to be determined. The instrument design, testing and commissioning form Chapters 2 and 3 of this thesis.

## 1.4 This work

This thesis covers the evolution and science successes of the Liverpool Telescope's polarimetric capabilities between October 2011 and September 2015. During this period RINGO2 was in active service in the rapid follow-up of gamma-ray bursts, whilst RINGO3 was being developed. RINGO3 was commissioned in November 2012, cannibalising the rotor mechanism and EMCCD detector of RINGO2 in the process.

The design of RINGO3 and the lab tests undertaken to deduce the specifications of the dichroic mirrors are covered by Chapter 2. The commissioning of the RINGO3 instrument on site, with results of first light analysis are presented in Chapter 3 with the details of post-commissioning optical issues experienced during 2013 and 2014.

Chapter 4 describes the data reduction principles of RINGO2 and RINGO3, including details of a number of investigations into optimal parameters for reduction. Also covered in this chapter are details of the data reduction pipeline developed during this PhD to enable consistent and flexible reduction of RINGO2 and RINGO3 data to produce large data sets to investigate instrumental characteristics.

Chapter 5 introduces the optical and observational issues which lead to inaccuracies in polarimetric measurements. By using the rich dataset of observations of polarimetric standard stars, along with some novel observations, the instrumental characteristics of both RINGO2 and RINGO3 are determined to provide correction factors which are necessary to obtain polarimetric values.

Finally, Chapter 6 looks at the analysis of 9 separate GRBs which were successfully observed with RINGO2. For these bursts the polarisation values are analysed. Of these bursts, GRB 120308A provided ground breaking early-time observations which formed the subject of a Nature paper (Mundell et al., 2013). The polarimetric reduction and statistical verifications that were done for this paper are presented along with the scientific findings.

Conclusions of the above work are presented in Chapter 7

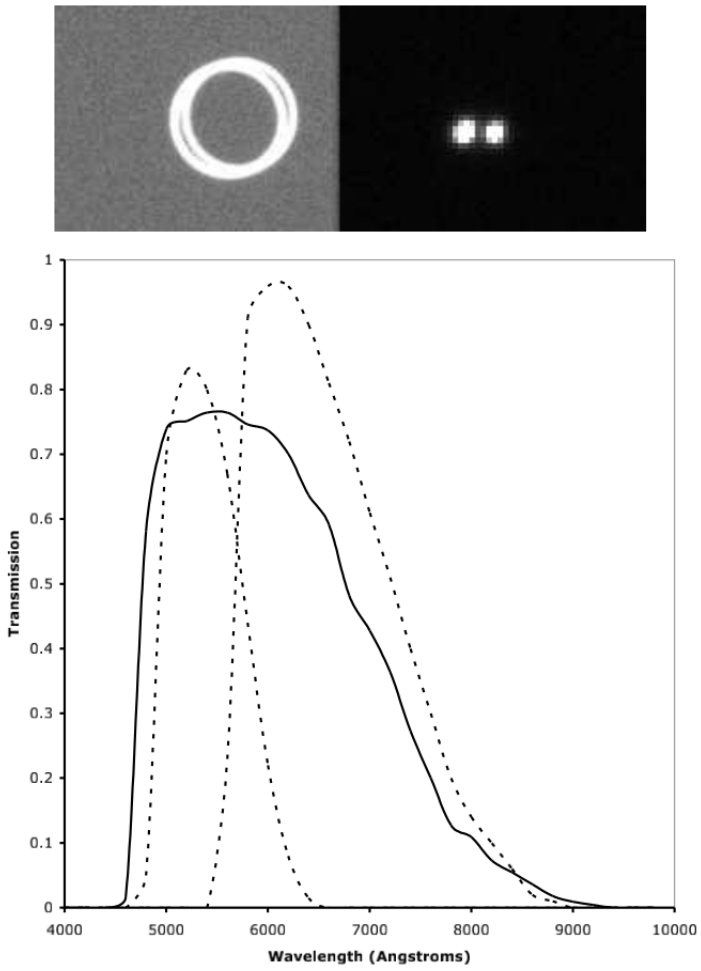


Figure 1.17: RINGO (top left) and RINGO2 (top right) observations of the zero-polarisation standard double star GD 319. The RINGO data are confused by the overlapping rings; a problem which does not affect RINGO2. Below is the throughput of the filter used for both RINGO and RINGO2 which is a hybrid 'V+R' filter, consisting of a 3mm Schott GG475 filter cemented to a 2mm KG3 filter. From Steele et al. (2010).

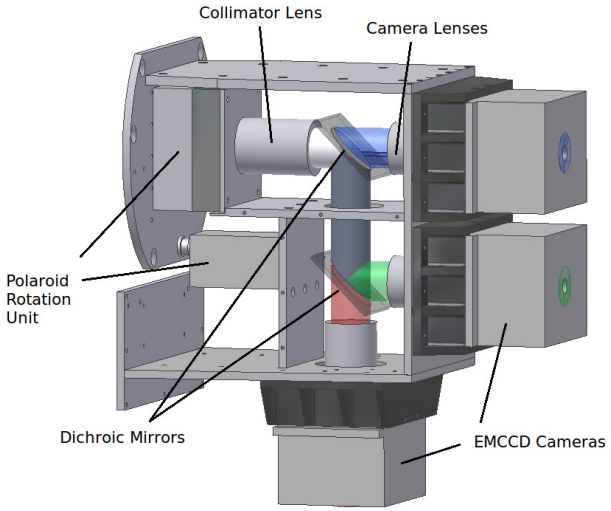


Figure 1.18: CAD diagram of RINGO3 design with sides removed, showing internal optics and light paths. 2 dichroic mirrors split the incoming radiation into 3 bands, which are simultaneously measured using 3 electron multiplying CCD cameras triggered by the rotation of the polaroid.

# Chapter 2

# RINGO3 design and development

## 2.1 RINGO3 design and specifications

### 2.1.1 The Liverpool Telescope development rationale

As described in Chapter 1, the Liverpool Telescope (LT) focuses on a specific time domain niche of astrophysics. This allows a small, versatile telescope to be scientifically competitive in the 8 metre era. The ongoing constraints of funding for smaller facilities impose limits on the resources available for operational and development activities.

Due to the specialism of research undertaken by the Liverpool Telescope, innovative instruments have to be produced to support the science goals. The RINGO series of instruments are a prime example of this, being unique in their ability to accurately measure the polarisation of a rapidly fading transient source. They have been produced economically and with short development cycles, necessitated by the fast moving field of GRB research. For RINGO3, the challenges were to develop an innovative, cost effective instrument on short time scales. The design and development of the instrument addressed the challenges in the following ways:

- **Reuse of existing RINGO2 technologies**

  RINGO3 has been designed to be an extension of the proven RINGO2 design, as opposed to a new instrument. This reduces risk in the design and leads to shorter development time scales, as the team is extending well understood technologies in terms of the triggering and data acquisition systems. There is also the obvious cost saving associated with reusing the majority of the RINGO2 equipment.

- **Pre-packaged, reliable EMCCD technology**

  The instrument relies on the fast readout and low noise capability of electron multiplying CCD detectors. The pre-packaged Andor iXon+ 897 cameras (which incorporate EMCCD chip, bias, readout, cooling and acquisition interface into a small unit) provide an integrated solution for imaging. The addition of the two iXon+ 897 cameras forms the major materials cost in RINGO3. However the technology allows for fast development and a high level of reliability.

- **Use of consumer optics**

  The camera and collimator lenses in the instrument are high end commercially available photographic lenses. These mass produced items are precision achromatic units, with good coatings. They represent a huge cost saving compared to bespoke optics. A major design saving is that a large number of optical elements are held in perfect alignment, with the ability of movement for focusing. The trade-off is that these lenses are designed to be achromatic with good throughput over the visible spectrum. RINGO3 has an operating wavelength of 400nm $\rightarrow$ 900nm and this exceeds the limits of the visible spectrum ($\sim$380nm $\rightarrow$ 700nm). The lenses' throughput and achromatic performance at the longer wavelengths above 700nm is not known and cannot be guaranteed to be sufficient.

### 2.1.2 RINGO3 design

As above, the design of RINGO3 was created, as much as possible, as an extension of RINGO2 into a simultaneous 3 band polarimeter. This necessitated the existing elements of RINGO2 being repackaged into a new instrument. The rotating polaroid

mechanism and electromechanical triggering mechanisms are reused, as are the lenses and the existing Andor fast readout electron-multiplying CCD (EMCCD) camera. The addition of two dichroic mirrors to split the wavebands and two further cameras constitutes the design. By using the same RINGO2 collimator and camera lenses in the optical setup, the $4\times4'$ field of view and $0.45''$/pixel scale remain unchanged.

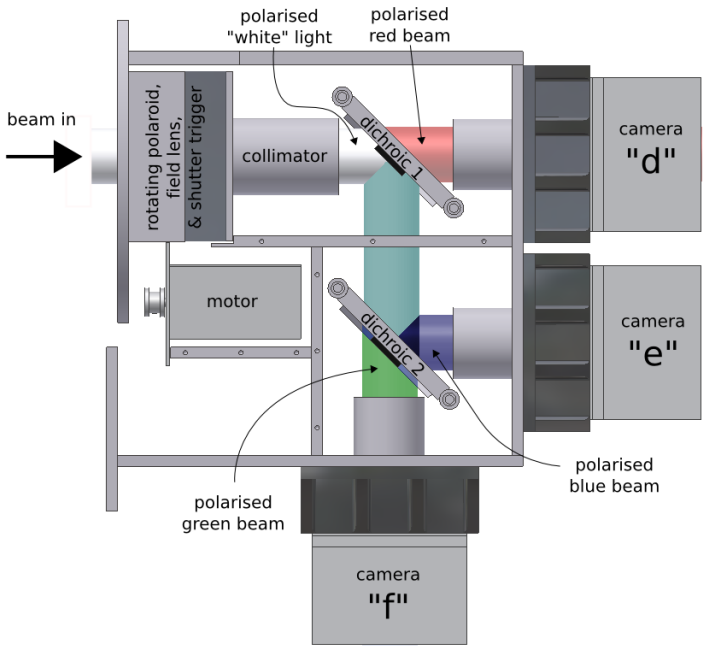


Figure 2.1: A cross section diagram of RINGO3 taken in the plane of the beams. The first optical element the beam hits is the polariser which linearly polarises the beam. The polariser is continuously rotated at one revolution per second by a brushless (to reduce electromagnetic interference during CCD readout) Creuzet high torque 24V DC motor (Steele et al., 2010). The beam passes through a collimator lens (Mamiya 150mm f/3.5) which creates a collimated beam of parallel rays for each field position. The dichroic mirrors act to split the incoming radiation into 3 different wavebands before camera lenses focus the beams onto the CCD camera units. After work to investigate instabilities of the instrument, a depolariser was fitted after the collimator lens to correct instrumental issues. Diagram by Stuart Bates

Mechanical design of RINGO3 was undertaken by the Liverpool Telescope development team and was close to finalisation before the commencement of this course of studies. Although there were many mechanical design considerations in the packaging

of the optical elements, these were in place before the commencement of the work presented here. However, some mechanical design considerations and the FEA (finite element analysis) of the instrument are discussed in Arnold et al. (2012). All design discussion hereafter relates purely to the optical performance of the instrument and electronic and computing requirements of the cameras.

The major design considerations arise from the extended operating wavelength compared to RINGO2, the selection of the 3 wavebands and the insertion of dichroic mirrors into the collimated beam section of the instrument.

| | |
|---|---|
| Operating Wavelength Range | $\sim 400 \rightarrow 900$ nm |
| Field of View | $4 \times 4'$ |
| CCD Size | 512 x 512 pixels |
| Pixel Scale | $0.45''$/pixel |
| Wavebands | 3 'flat' wavebands, with equal signal to noise ratios for a GRB event |

Table 2.1: RINGO3 Design Specifications. The $4 \times 4'$ field of view is optimal to match the 2-sigma error circle of the BAT detector on NASAs SWIFT satellite The 3 wavebands are defined by sharp cut-offs of the two dichroic mirrors. The wavelength of these transmission / reflection cut-offs were defined by calculating the instrumental throughput and selecting positions which gave equal signal to noise ratios in each band for a GRB event.

## 2.2 Instrument design

### 2.2.1 Polarising optics

As described in Chapter 1, the innovative part of the RINGO series of instruments is the use of a rapidly rotating linear polariser. This is essential for polarimetric measurements of highly variable sources on short time scales. A perfect polariser will transmit 100 % linearly polarised light of a transmitted intensity ($I$) based on the incident inten-

sity ($I_0$) and polarisation state of the incoming radiation. For incident, monochromatic radiation which is 100 % linearly polarised, the transmitted radiation is explained by Equation 2.1, where the angle $\theta$ is the difference between the polarisation angle and the angle of the linear polariser, and the throughput, $T(\lambda)$, is a function of wavelength.

$$I = I_0 \times T(\lambda) \times \cos^2(\theta) \tag{2.1}$$

For unpolarised radiation, it is easy to show that integrating a constant intensity present over the full range of angles ($0 \rightarrow \pi$ radians) yields a transmitted intensity of $0.5 \times T(\lambda)$. Hence the polariser will only transmit half of the incoming radiation, at best.

The properties required of the polarising optics can be summarised as,

- □ High throughput over operating wavelengths ($T(\lambda)$)
- □ High contrast ratio over operating wavelengths
- □ Consistent behaviour over the range of angles of incidence required (dictated by the field of view and telescope focal ratio)

The contrast ratio (or extinction ratio) is a measure of the efficiency of the polariser in polarising radiation. It is specified as the ratio of incident to transmitted intensity in the specific case that incident radiation ($I_0$) is 100 % linearly polarised, and that the polaroid is orientated at an angle of 90 degrees to the incoming polarised radiation (Equation 2.2). In the case of a perfect polariser in this set up, no radiation would be transmitted and its contrast ratio would be $\infty$. By analysing the existing RINGO2 polaroid (Meadowlark Optics precision linear polariser VIS) as shown in Figure 2.2, it is clear that the contrast ratio falls significantly above 750nm. At a contrast ratio of 10, the polariser will be transmitting up to 10 % of the radiation which is linearly polarised transversely to the polarisation angle that is being measured. This 'bleed'

will result in a washing out of the measured polarisation signal in the instrument. Due to the extended operating wavelength of RINGO3 a change in the polariser is required.

$$ContrastRatio(\lambda) = \frac{I_0(\lambda) \perp}{I(\lambda) \parallel} \tag{2.2}$$

The correct polariser to meet the requirements is the Meadowlark Optics Versalite VIS, with the performance shown on the lower plot in Figure 2.2. The Versalite series of polarisers utilise a chemical etching process to form a thin conducting wire grid on a glass substrate, as shown in Figure 2.3. They are optimised as polarising beamsplitters and have a high acceptance angle. The only drawback is the high reflectivity of the polariser (due to it being a beam splitter). It sends up to 50 % of the incident optical radiation back up the telescope. This could cause scattered light or ghosting in the images.

These two effects raise the background noise in images and reduce both photometric and polarimetric performance. In this case, one possible solution would be to tilt the Versalite polariser to direct the reflected beam into a circular baffle (as the reflected beam will trace an annulus in normal operation). However due to the position of the rotating polariser unit at the front of the instrument and its proximity to the A&G unit, it is more likely that the beam would be directed to trace out arcs around the A&G box mechanics. As could be imagined, this would produce confusing patterns of scattered light. Therefore the best starting situation is not to tilt the polaroid, but to send the reflected beam directly back up the telescope tube structure.

### 2.2.2 Camera triggering system

The rotator mechanism for RINGO2 incorporates 24 volt proximity sensors as described in Steele et al. (2010) which provide the triggering signals to the Andor iXon 897 units. There are two sensors: a ‘trigger’ and ‘home’ sensor. The trigger sensor detects 8 equally spaced magnetic markers positioned around the rotor barrel and per-

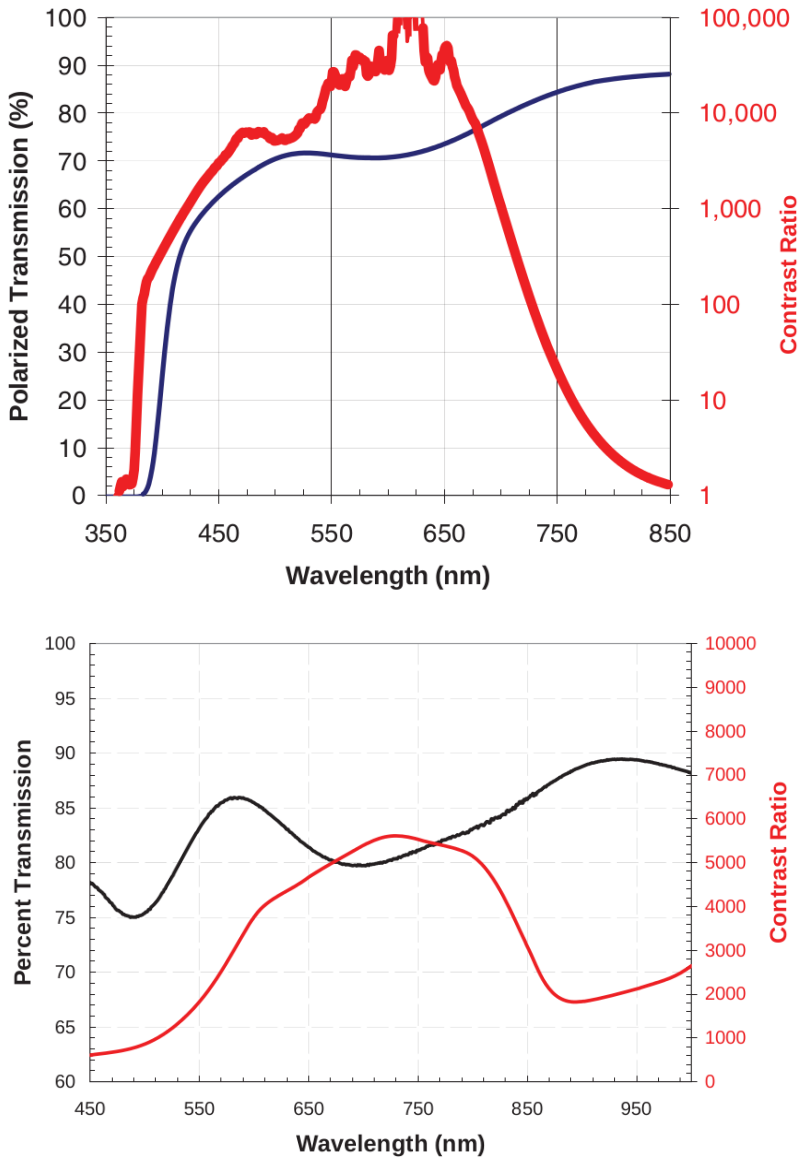


Figure 2.2: The specifications of the RINGO2 Meadowlark Optics precision linear polariser (above) and the polariser selected for RINGO3 Meadowlark Versalite VIS polariser (below). Contrast ratio is defined as the ratio of transmitted intensity through parallel polarisers to the transmitted intensity through crossed polarisers. The logarithmic scale on the upper plot for the contrast ratio is due to the high variability of this polariser across the wavelength range. The Versalite polariser for RINGO3, whilst not gaining a higher contrast ratio, has a much improved level of contrast ratio across the full operating wavelength range. Both plots taken from Meadowlark Optics datasheets

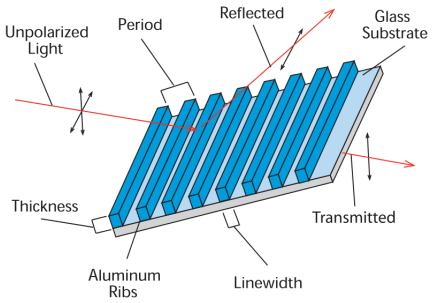


Figure 2.3: Diagram of wire grid polariser. Taken from Meadowlark Optics datasheet

forms the triggering of the 8 frames that constitute a polarimetric measurement. The home sensor detects one magnetic marker which specifies the start point of the rotor. The rotor is permanently running whilst the instrument is mounted on the telescope.

These proximity sensors require that the 24 volt signal is reduced to 5 volts for the Andor cameras. Also a small circuit is required to start the observations correctly. The schematic for this system is shown in Figure 2.4. The system is powered by the same 24 volt supply as the rotator mechanism, and uses a 24 volt to 5 volt power regulator. The trigger and home signals are transferred to 5 volt logic using an opto-isolator and a hex inverter (IC3, IC1 respectively in Figure 2.4)

When an observation is started from the Liverpool Telescope (LT) instrument control system (ICS), the control computers set up the three Andor cameras. These cameras each give a *shutter* signal to the triggering system, when they are ready to take exposures. This takes less than a second to initiate. These *shutter* signals are combined with AND logic in IC2 and when all 3 cameras are ready the signal goes to a simple 1 second delay circuit before becoming the input to a flip flop (IC2). The home signal provides the clock for the flip flop, so that this combined shutter signal is passed on only when the rotor reaches the home position. This ensures that the first exposure taken is always of the same rotor position.

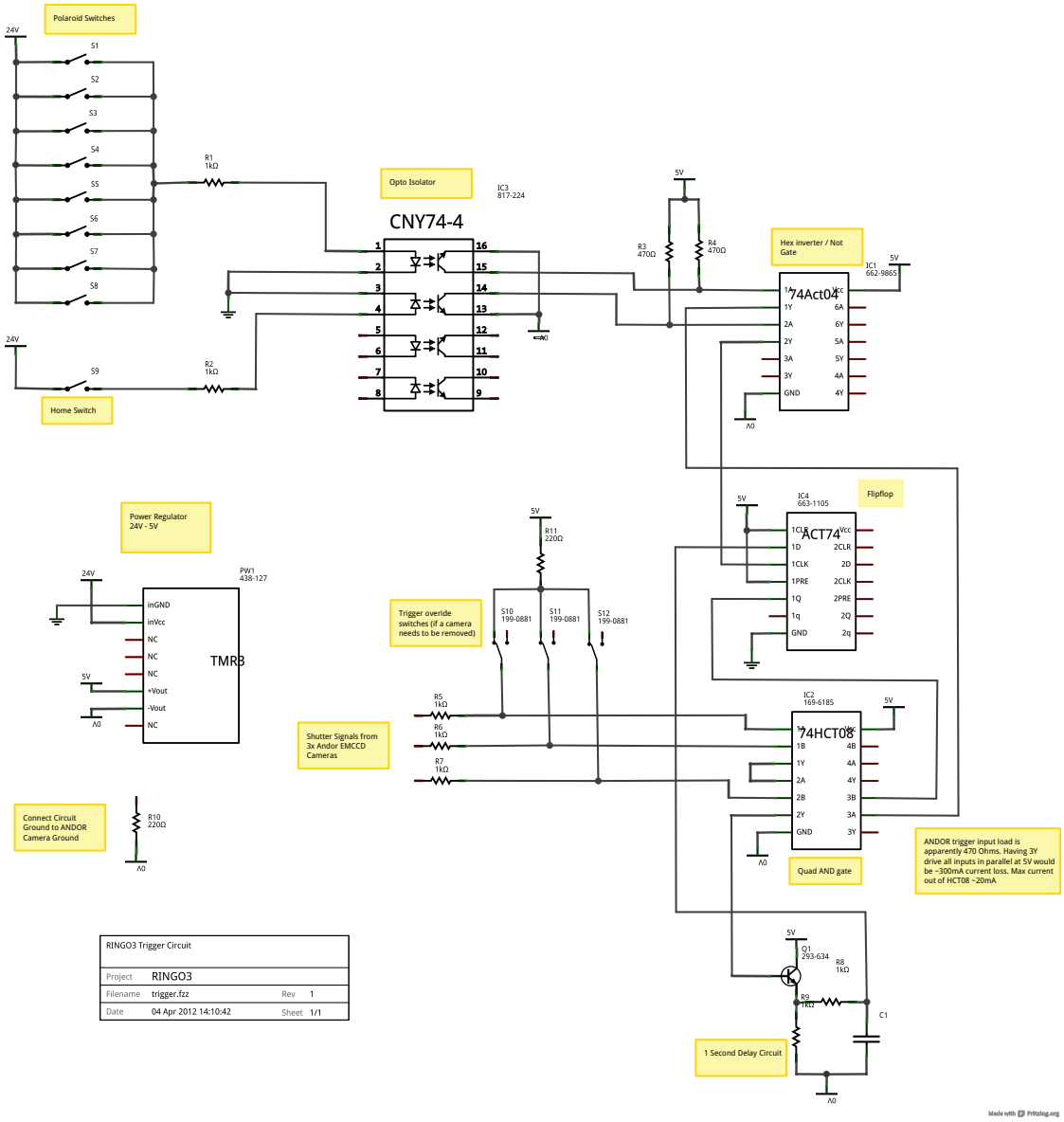


Figure 2.4: Electrical schematic of the RINGO3 camera triggering system. A trigger circuit existed previously for RINGO2 but was undocumented. The circuit was documented and extended using Fritzing software to take in 3 different *shutter* signals and combine with override switches should one of the cameras be taken out of the instrument.

AND logic in IC2 is then used to combine the now constantly high *shutter* signal passed from the flip flop and the trigger signal which provides 8 rising edge signals per rotation. The output of this AND logic is then fed to the *trigger* input of the 3 Andor cameras.

The only addition of note compared to the RINGO2 triggering system is that the *shutter* inputs from the cameras can be overridden by switches (S10, S11, S12). This enables RINGO3 to be operated with any of the cameras removed and their corresponding shutter outputs being forced high via a 220 Ω pull-up resistor (R11).

### 2.2.3 Collimator and camera lenses

The collimator and 3 camera lenses are high quality photographic lens units. The apertures on all lens units were checked and fixed to their largest settings. These lenses had been used successfully in RINGO2 to provide the $4\times4'$ field of view with no vignetting issues.

The collimator lens (Shown in Figure 2.1) is a Mamiya 150mm f/3.5 lens for a medium format camera used in reverse, and the focus of the telescope occurs at the position where the photographic film would have been. This is then focused to infinity, in order to provide a collimated beam into the instrument. It is in this collimated beam that the dichroic mirrors split the 3 wavebands to 3 separate camera lenses (Nikon AF-D 50mm f/1.4 lenses for 35mm cameras).

The Nikon camera lenses are attached to the Andor iXon EMCCD units using a simple adapter which converts the bayonet fitting of the lens to the screw fitting of the imaging unit. This adapter places the EMCCD chip closer than the intended focus of the lens unit. Consequently the focusing ring of the camera is not accurate for setting the focus to infinity (i.e. parallel rays convergence on CCD chip) for the input of the collimated beam. The whole issue of focusing the 3 bands in relation to each other can only be done using these camera lens focus rings. Focusing was undertaken when commissioning the instrument, and details of the procedure are included in Chapter 3.

### 2.2.4 Dichroic mirrors

Dichroic mirrors can be used in optical astronomy as wavelength dependent beam splitting devices (Velt & Tinbergen, 1981). These optical elements transmit radiation above a specified cut-off wavelength and reflect it below this. This allows simultaneous measurement in two bands or more (if multiple dichroics are used). By using the phenomenon of thin-film interference, dichroic mirrors layer up a number of films to create constructive interference in reflections below the cut-off wavelength. The ideal dichroic mirror will have a reflectivity of 100 % below the cut-off wavelength and a transmission of 100 % above, with a sharp transition between the two in the wavelength domain.

The transmission / reflection curves of the dichroic mirrors trace a profile describing a square wave created by a Fourier transform, with a less than vertical transition at the cut-off wavelength, small overshoot and minor oscillation at either side. The process of creating the dichroic mirror is by laying down numerous thin-film layers on the glass substrate. The thickness and refractive indices of each layer are tuned to provide constructive and destructive interference from reflections at each boundary, similar to terms in a Fourier series. The overall effect of these numerous layers gives the transmission profile shown.

#### Dichroic specifications and performance

Figure 2.5 shows the manufacturer's specifications of the dichroic mirrors. The unsmoothed higher order Fourier oscillations can be seen clearly around the transition. The determination of the cut-off wavelengths is discussed later in Section 2.4. The dichroics form the second most expensive part of the instrument after the Andor cameras and, whilst not perfect, they present adequate performance with little bleed of radiation between the bands. Lower wavelength radiation bleed (transmitted radiation that should have been reflected) is on the order of a few percent and the longer wavelength radiation being reflected only slightly higher. It is hoped that this radiation is

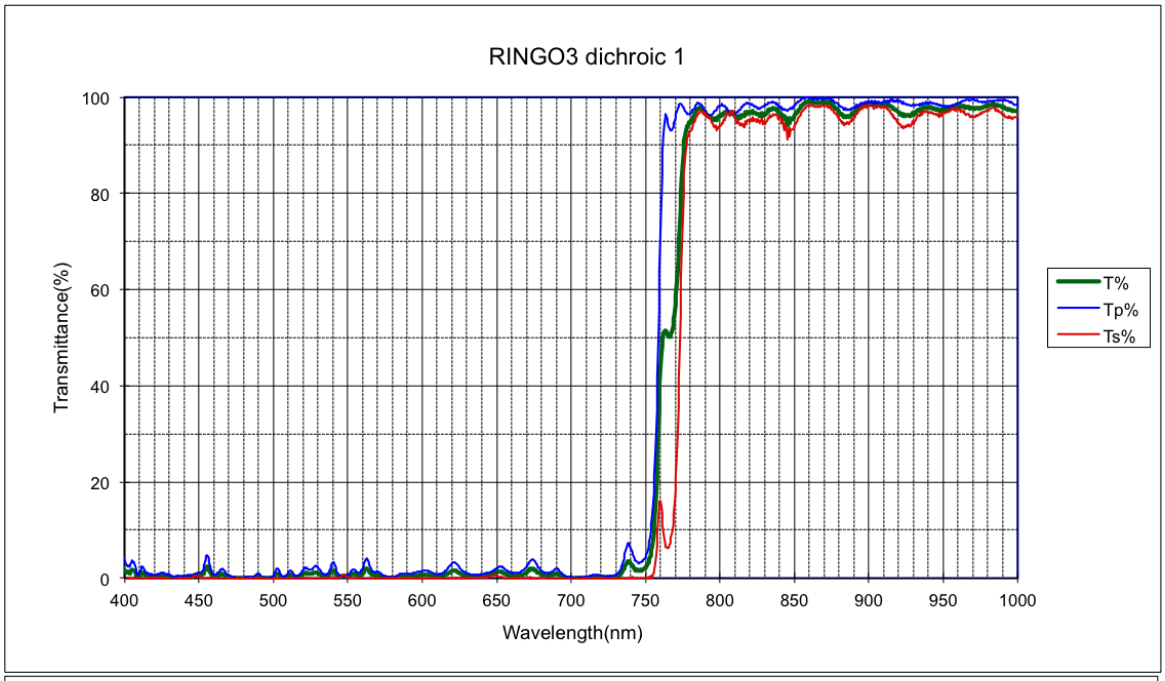


Figure 2.5: The transmittance curves of the two dichroic mirrors as tested by the supplier. The angle of incidence was 45°. Shown are the curves for unpolarised radiation (T %) as well as 100 % linearly polarised radiation parallel to the dichroic plane (Tp %) and perpendicular to this plane (Ts %).

attenuated rather than being incorrectly passed / reflected by the dichroic.

In terms of the efficiency of these optical elements, the throughput is very high and consistent across the wavebands. Other optical throughputs and effects, such as the lenses, polaroid and the quantum efficiency (QE) of the CCDs, play a much a bigger role in the throughput as described in Section 2.3.

The transition of the dichroic mirror, however, is less than perfect. For unpolarised radiation (T % curve) it can be seen that the transition occurs on the order of 30nm (750 $\rightarrow$ 780nm for dichroic 1, and 630 $\rightarrow$ 660nm for dichroic 2) which will give a bleed between bands. Provided that the variation of this bleed is consistent across spectral types and polarisations of sources, it can be calibrated for, and will have a minimal effect.

**Polarisation effects**

At all points in the instrument after the polariser, the polarisation state of the beam is unimportant. The only concern is the intensity of that radiation as a function of polariser angle. The collimated beam in which the dichroics sit can be assumed to be 100 % linearly polarised (by the polariser) with a constantly rotating angle of polarisation. The manufacturer tested this case for two polarisation angles, parallel and perpendicular to the plane of dichroic (Tp % and Ts % respectively in Figure 2.5). Whilst the transition is sharper for 100 % linearly polarised radiation, it can easily be seen that there is $\sim$10-15 nm difference in the position depending on the polarisation angle. Assuming that p and s (parallel and perpendicular) polarisation states represent the extremes of the transition wavelength, it is reasonable to expect that the transition wavelength of the dichroics will oscillate in this 10-15 nm zone with the polaroid rotation.

With an unpolarised source, the effect of the band transitions changing with polaroid angle can be accounted for. However, the effect that this will have on the measurement of polarised sources is not understood. The risks and options regarding the effect of the oscillating transition are discussed in Section 2.5.

### 2.2.5 Detectors

Ubiquitous in optical astronomy for the past 20 years, charged coupled devices (CCDs) are the most efficient, widely available detectors. Understandably these are used in the RINGO series of instruments. The requirements of the CCD detectors for RINGO3 remain unchanged compared with those of RINGO2. These requirements are:

- **Ability to take 8 exposures per second**

  The RINGO2/3 rotor is tuned to rotate at 60rpm, providing 8 equally spaced trigger signals to the cameras. This requires that the full acquisition system (CCD, readout, data storage) can readout, process and store one frame each 125ms.

- **Low bias and readout overheads**

  An exposure is being taken every 125ms. Therefore the time to set the bias level at the beginning of an exposure, and also the readout time must be negligible in order to maximise the integration time.

- **Low operating noise**

  The signal to noise (S/N) ratio determines the detection limit of astronomical measurements. Noise can occur from external sources (such as the Poisson counting error on-sky background) and also from the processes occurring on the CCD. The primary sources can be considered as dark noise (due to thermal effects on the CCD) and read noise, which occurs at the necessary amplification stage before the digitisation of the signal. The former source of noise can be reduced by cooling the CCD chip and the latter can be reduced by lowering readout speed.

□ **Detector area to provide a $4\times4'$ field**

The SWIFT BAT detector which provides the low latency (1 minute) trigger for GRB events has a $2\sigma$ error circle of $\sim3'$.

The above demands have conflicting requirements in the fast readout speed and low noise. Whilst normal CCD technology could not match these requirements, there are continuing developments in detector technology and the addition of an electron multiplication (EM) register between the CCD and gain amplifier allowing both of the above requirements to be met.

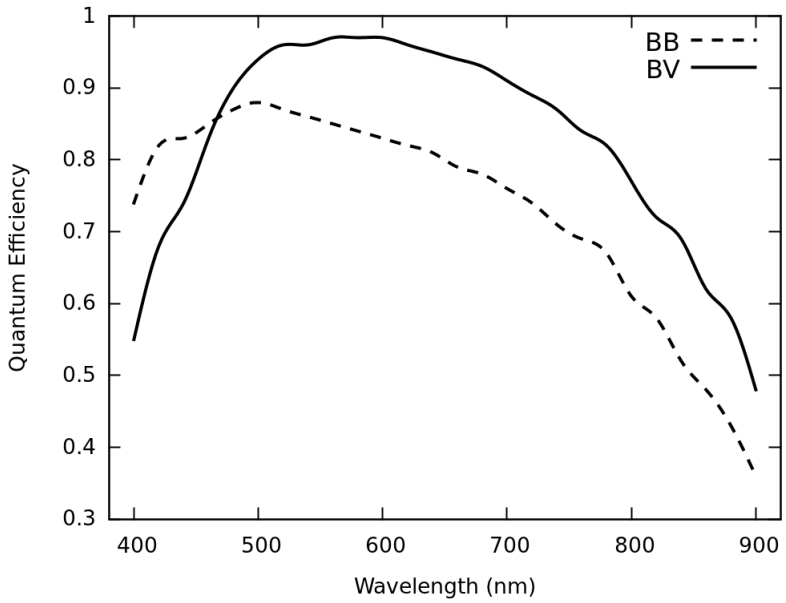


Figure 2.6: The quantum efficiency (QE) of the Andor iXon 897 electron EMCCD units. The BV units were selected for the mid to higher wavelength bands of the instrument, and a single BB camera was purchased to maximise throughput in the lower wavelength band of the instrument. Data from Andor specifications.

### Electron multiplying CCD technology

First developed by Andor Technology PLC in 2000 (Denvir & Conroy, 2003), EMCCD technology is a form of low light level CCD (L3CCD) technology, where due to

short exposures and/or faint illumination, the number of electrons generated in each pixel above the bias level is small. This poses a problem for the signal to noise ratio (SNR), which directly affects the errors on photometric measurements. In low light level conditions the number of electrons can be comparable to the RMS readout noise, which is added by the amplifier in order to allow the analogue to digital converter (ADC) to digitise the signal. RINGO2 and RINGO3 require high cadence observations which lead to short exposure times and hence benefit from L3CCD technology.

By placing the EM register before the readout amplifier, it is able to boost the signal and hence make the noise of output amplification and digitisation negligible. The EM register is a solid state register placed after the standard serial register. As charge is transferred through each stage, the phenomenon of impact ionisation is utilized to produce secondary electrons, and hence EM gain. When analysed by Basden & Haniff (2004) for astronomical use, EMCCD technology was found to be capable of subelectron effective readout noise, allowing for the detection of single photon events.

Equation 2.3 from Robbins & Hadwen (2003) shows the SNR of a conventional CCD and an EMCCD, where $S$, $D$ and $\sigma_r^2$ are the Signal, Dark Current and Read Noise, respectively. When the electron multiplication register is used the read noise is reduced by the square of the EM gain, $g$ and the term $F^2$ is based on the EM gain and the number of multiplication stages, $N_s$, of the EM register.

$$S/N_{conv} = \frac{S}{\sqrt{S + D + \sigma_r^2}} \tag{2.3a}$$

$$S/N_{EM} = \frac{S}{\sqrt{F^2 S + D + \frac{\sigma_r^2}{g^2}}} \tag{2.3b}$$

$$F^2 = 2(g-1)g^{-\frac{N_s-1}{N_s}} + \frac{1}{g} \tag{2.3c}$$

#### Electron multiplying CCD cameras

Andor provides a fully packaged unit in the iXon 897. The quantum efficiencies of the detectors for RINGO3 are shown in Figure 2.6. The existing BV model of RINGO2 was supplemented with one each of a BV and BB model, the latter being for the lowest wavelength band. The cameras provide all readout electronics (including the EM gain register), Peltier cooling (capable of -60°C, to reduce thermal dark noise) and ability to take exposures on external triggers. The cameras also interface to a data acquisition PC via a bespoke interface and PCIe card.

#### Control systems and software

Due to the addressing of cameras in the Andor software, a maximum of two cameras can be controlled by one control computer. For 3 cameras this means a requirement of at least two control computers. The existing software for RINGO2 was expanded by Rob Smith and Chris Mottram on the control PCs. Online pipelines for data reduction (described in Chapter 4) remained virtually unchanged.

Another consideration for the control computer which controls 2 cameras, was the processing load of data storage. This was lab tested by hooking up a simple signal generator to two cameras and measuring to ensure that there were no dropped frames.

### 2.2.6 Mechanical packaging of instrument elements

The mechanical packaging was designed in-house by Stuart Bates. The instrument design has undergone finite element analysis (FEA) for all the orientations on the sky. Casing design and camera mounting points have been iterated to reduce weight and provide the minimum amount of flexure. The areas of highest deformation are well within tolerances with deflection of less than 2 microns. This means that the instrument optics should be stable across the full range of telescope pointings and Cassegrain rotator angles.

The optical elements are fixed, except for the dichroic mirrors. A precision system of grub screws and springs can be used to allow tilt adjustment of the dichroic mirrors. This varies the beam angles entering the cameras and can be used to align the fields during commissioning. This is described further in Chapter 3.

## 2.3 Instrument throughput

A knowledge of the throughput efficiency (the ratio of detected to input photons across all operating wavelengths) is essential in predicting instrument performance. The throughput is also required in this case to create a model to analyse signal to noise ratios, so that the two cut-off wavelengths of the dichroic mirrors can be deduced. The throughputs of the polariser and quantum efficiencies of the cameras are known through manufacturer's specifications. However the commercial camera lenses do not have this information readily available.

Lab testing was undertaken to produce throughput data for the camera lenses, allowing an instrumental model to be constructed. This involved the use of a monochromator to provide the light source in various optical setups.

### 2.3.1 Monochromator instrument

A monochromator provides a narrowband optical output. The equipment in its simplest form comprises two slits and a rotatable prism. Input illumination passes through the input slit and, in turn, is split by the prism into beams of differing wavelengths. Using a graded rotation mechanism on the instrument the output wavelength can be selected.

The monochromator which was available for the testing was an old unit of unknown quality. The dial for selection of wavelength was of unknown calibration and was

assumed to be correct. Dependent on the spectrum of the illumination source, the monochromator will have a distinctive output spectrum, which needs to be characterised. The initial illumination was in the form of a 24 volts incandescent bulb, powered by a mains DC lab power supply which was set to 12 volts. This bulb had a poor output at shorter wavelengths, so a stable 5 volt blue LED was used for lower wavelength measurements (380 - 480nm).

To measure the output of the monochromator a single uncoated lab lens was used to focus the image of the slit onto the CCD camera. This lens was assumed to provide a near constant throughput over the wavelengths tested. The slit on the monochromator was set to its smallest value to provide the narrowest waveband. Three exposures were taken at each wavelength in the range 380 - 900nm using 20nm steps. The camera was set with EM gain set to 1 (inactive). The exposure time was 0.05s. These settings were deduced to ensure that no pixels were saturated at any wavelength of output.

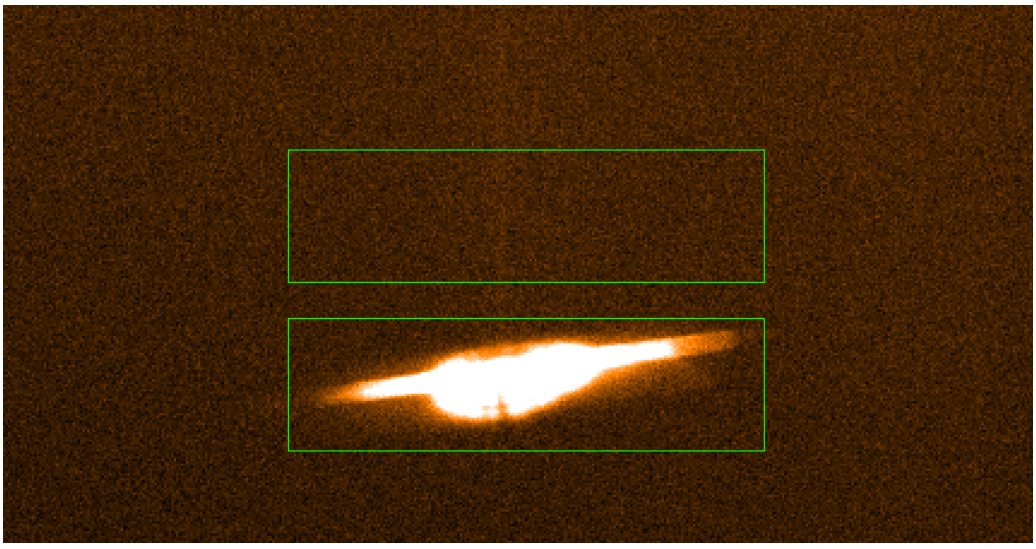

Figure 2.7: The image of the monochromator slit on the Andor iXon 897 camera taken with camera and collimator lenses at a wavelength setting of 550nm. For each run, the total counts in a rectangular aperture encompassing the whole slit were taken. A background value was obtained from the area above the slit with an aperture of identical dimensions.

Reduction of the data was performed using `imstat`, an example utility of the `cfitsio` library (Pence, 1999). This measured the total counts in a region of the image which encompassed the slit image. The fact that the lab lens is not achromatic was not an issue in this case, as a non sharp image of the slit is still fine for measurement, provided that the total flux falls within the measurement region. A background level was taken from a region above the slit with identical dimensions to the slit region as shown in Figure 2.7. By subtracting the background value from the slit value, the counts from the slit could be obtained. The images were not debiased prior to this analysis, as the method above automatically removes the bias level, which is included in both regions. The average of the 3 measurements was taken for each wavelength and due to the high levels of flux, the standard deviation of these measurements was less than 0.5 %.

The spectral output of the monochromator in Figure 2.8 has a linear metric labelled as 'Throughput'. This is the observed output (not absolute), as it has not been corrected for the quantum efficiency of the cameras.

### 2.3.2 Lens throughput measurements

The uncoated lab lens was replaced by the collimator lens and the camera lens was attached to the camera, replicating the single band setup of RINGO2. The procedure was followed as for the monochromator characterisation, with 3 exposures of each wavelength taken, and identical data reduction techniques used.

To calculate the lens throughput, the values obtained with the collimator and camera lenses were divided by the measured monochromator output. As both sets of measurements were taken with the QE effects of the Andor camera, this process removes any influence the camera has on throughput and gives the lens throughput values alone.

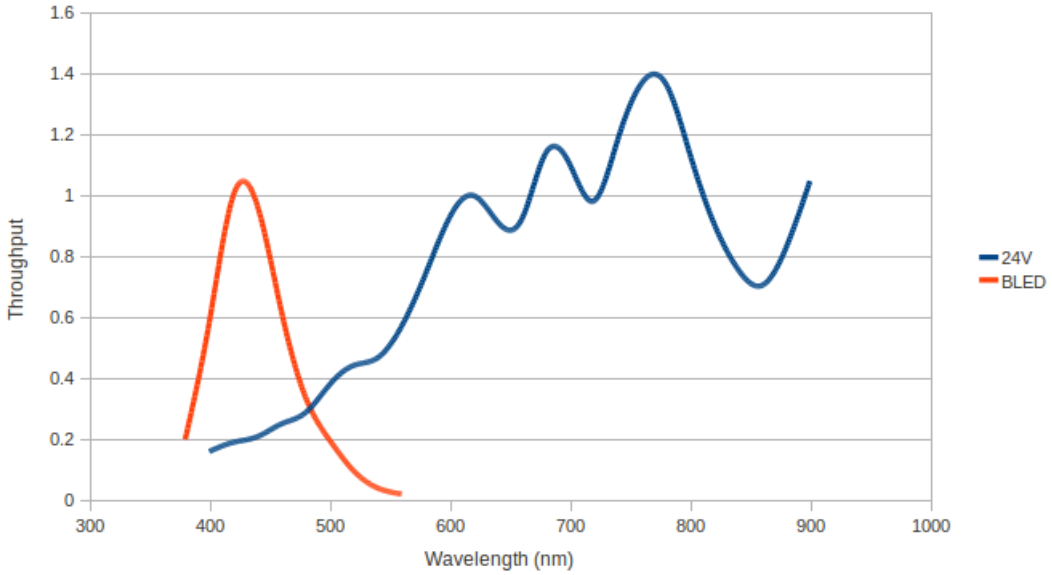


Figure 2.8: Measured output intensity of the monochromator with the 24V incandescent bulb (24V) and Blue LED (BLED). The output was measured using a single uncoated lab lens to focus the slit on the CCD camera. The curves are the observed output (not absolute) as they are not corrected for the quantum efficiency (QE) of the Andor iXon 897 camera.

### 2.3.3 Instrumental throughput

Instrumental throughput was calculated for the instrument by combining the throughput of the Versalite polariser, camera and collimator lenses and the QE of the cameras (Figure 2.13). Two models were created, one for each of the BB and BV type cameras with QE values as shown in Figure 2.6. The models do not contain the throughput values of the dichroic mirrors, as these were yet to be specified and manufactured. It was assumed that the dichroic mirrors have a high throughput / reflectance (better than 95 %), which is constant across the wavelength ranges at which they operate. Using this reasonable assumption, the effect of the mirrors on throughput is minimal compared to other optical elements and it can thus be safely omitted from the throughput model.

The throughput of the Liverpool Telescope was considered. However, with aluminium coated mirrors, the efficiency of reflectance is near flat across the operating wavelength of RINGO3 and hence was omitted from the model for waveband selec-

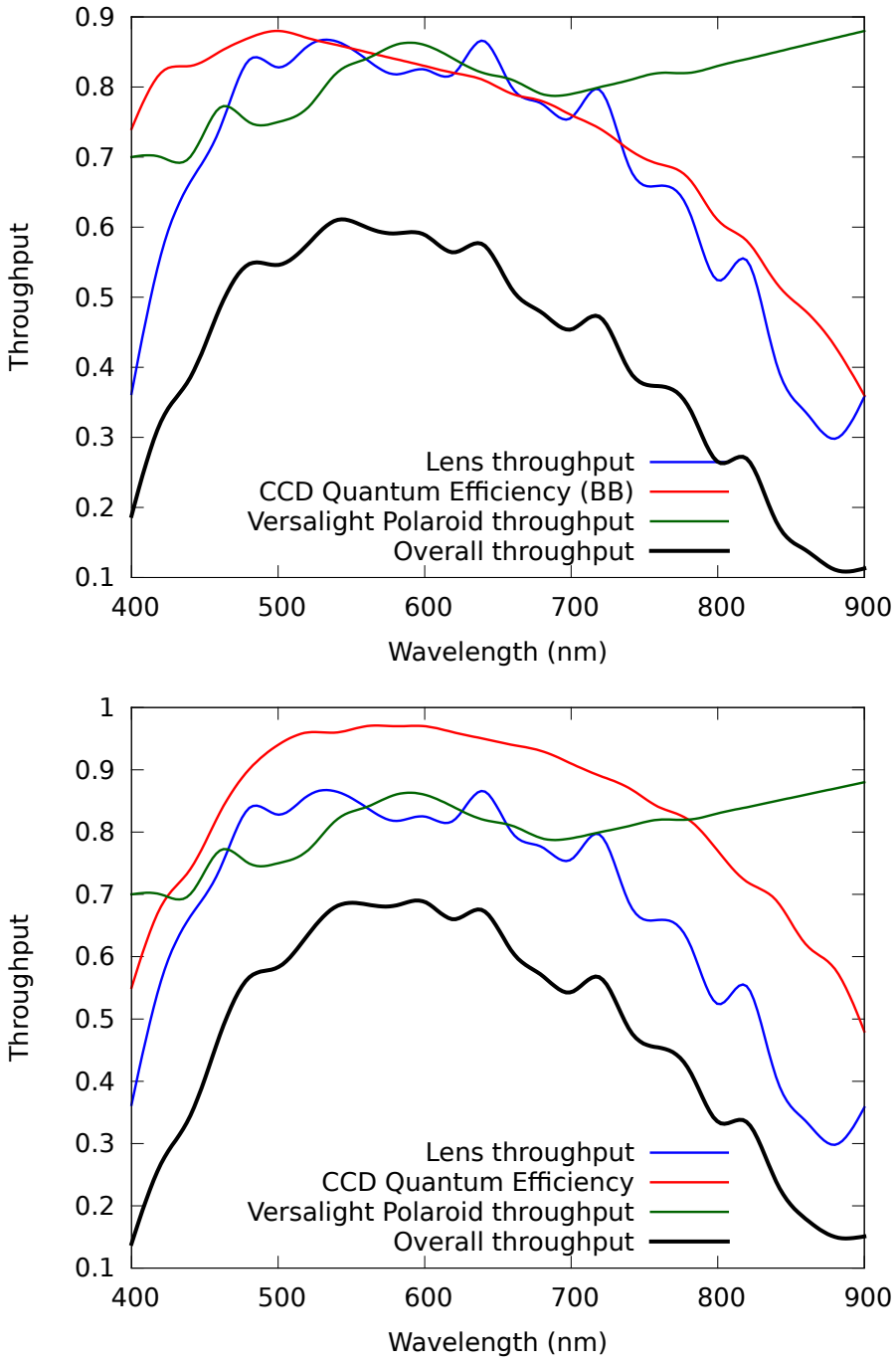


Figure 2.9: The instrumental throughput model of RINGO3 with the BB type camera (upper) and BV type camera (lower) quantum efficiency shown. The dominant elements in creating the profile are the lens throughputs and the camera quantum efficiency. The values taken for the Versalite polariser are from the Meadowlark optics specifications and are values which accept the previous 50 % flux reduction effect of a linear polariser.

tion.

## 2.4 Throughput modelling and waveband selection

The dichroic waveband cut-off wavelengths were selected to provide equal signal to noise ratios in all three bands for a 'typical' early-time GRB afterglow. To derive the cut-off wavelengths, spectra of the signal and the noise had to be passed through the instrumental throughput model. Various sources of noise, such as readout noise and Johnson noise, affect all wavebands equally. The low levels of these sources of noise in the Andor iXon 897 cameras mean that they were confidently omitted from analysis.

### 2.4.1 The La Palma sky spectra

The dominant source of noise in RINGO2 was shown to be due to the sky background. This is owing to the Poisson noise on the sky background, which is described as the square root of the sky signal. An optical spectrum of the Observatory Roque de las Muchachos (ORM) sky was measured by Benn & Ellison (1998) during dark time (unaffected by moon) using data from the Isaac Newton and Jacobus Kapteyn Telescopes. The full data for the plots was kindly supplied by Chris Benn of the Isaac Newton Group. The data was binned into 20nm wavelength bins, which were centred on the measurement wavelengths in the optical throughput tests. This data is shown in Figure 2.10

### 2.4.2 Optical spectrum of early-time GRB afterglow emission

Capturing an early-time ($\sim$ 15 minutes post trigger) spectra of a GRB has not yet been achieved. It is still a science goal of the Liverpool Telescope with the FRODOSpec instrument (Morales-Rueda et al., 2004; Mundell et al., 2010) or with the newer SPRAT spectrograph (Piascik et al., 2014). The theoretical output spectra are produced by synchrotron cooling as detailed in Sari et al. (1998). The spectra also

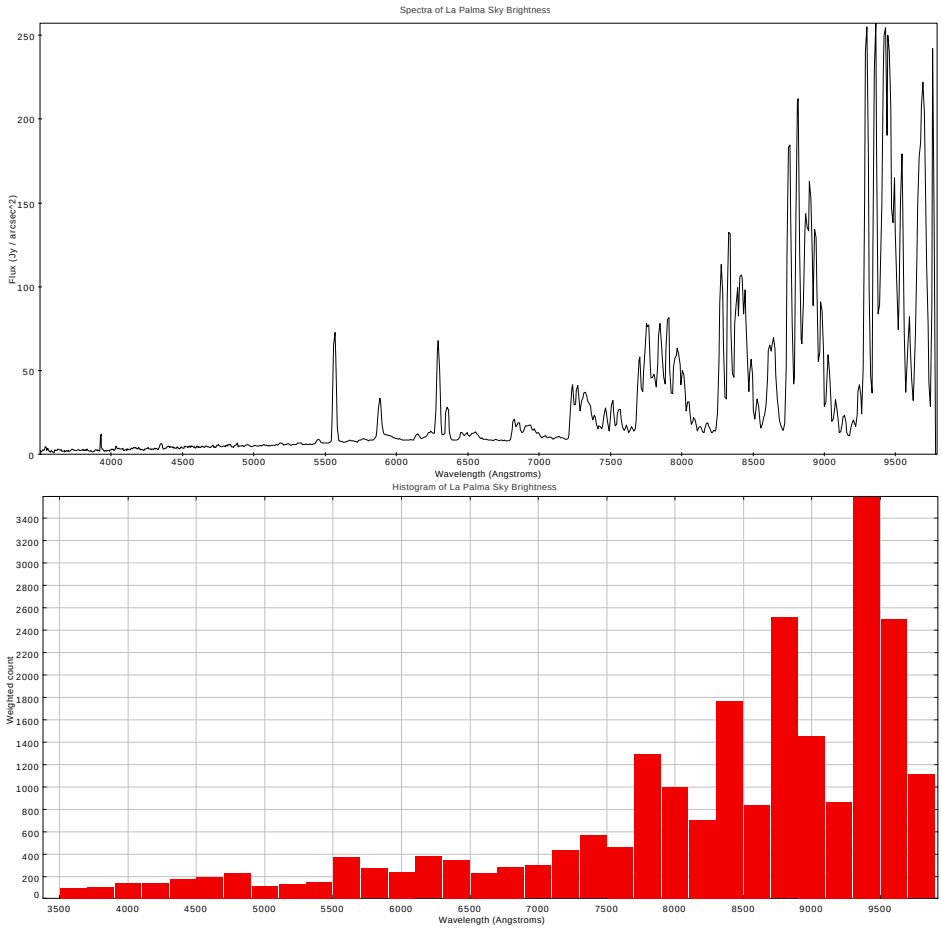


Figure 2.10: Raw and binned data of the La Palma sky spectrum taken from Benn & Ellison (1998)

evolve with time, with the peak of the synchrotron spectra moving to longer wavelengths. This occurs due to energy being lost from the emitting system (i.e. cooling) and the kinetic energy of individual electrons decreases, leading to longer wavelength emissions. Furthermore the spectra are affected by 3 aspects: the redshift of the burst (position of the Lyman-alpha dropout); any intervening galactic or extragalactic extinction; and absorption in the circumburst medium.

Despite all these issues, the knowledge that a simple synchrotron spectrum follows a power law, as described in Chapter 1, enables early-time multicolour photometric measurements to be used. These will create an observed spectrum, assuming that the evolution time of the spectrum is significantly longer than the period of observations.

RINGO3 in deployment will be able to provide simultaneous multi-band measurements and hence more accurate spectral analysis.

Early-time multi-band measurements were performed using the Liverpool Telescope and RATcam of the afterglow of GRB 050502A by Guidorzi et al. (2005). The lightcurves for these observations are shown in Figure 2.11. Observations were taken with the Liverpool Telescope in Sloan i' and r' bands plus Bessell B and V. By converting these measurements into arbitrary flux units (counts per Angstrom) across the width of each band, it is possible to gain four spectral points at the central wavelengths of each band. This 'back of an envelope' calculation yielded a synchrotron spectrum with a power law that sits below the fast and slow cooling regimes of Sari et al. (1998). It provides confidence that the observed spectra of GRB afterglows will not be far removed from the theoretical emission.

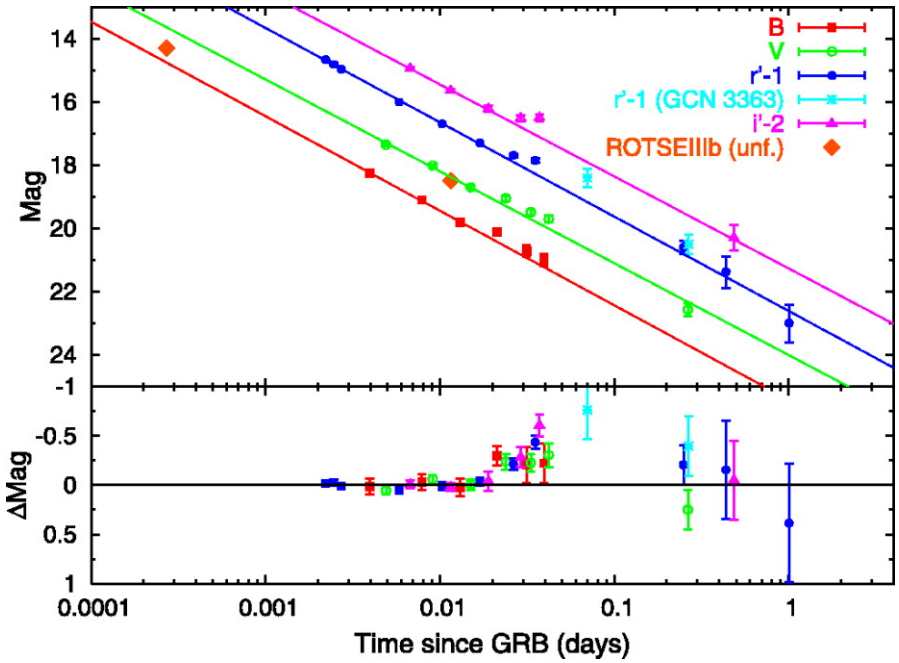


Figure 2.11: Early-time multi-band photometry by the Liverpool Telescope provides measurements by which a 'ballpark' synchrotron spectra can be inferred. It assumes that there are no major sources of extinction which would provide a more complex observed spectra. Guidorzi et al. (2005)

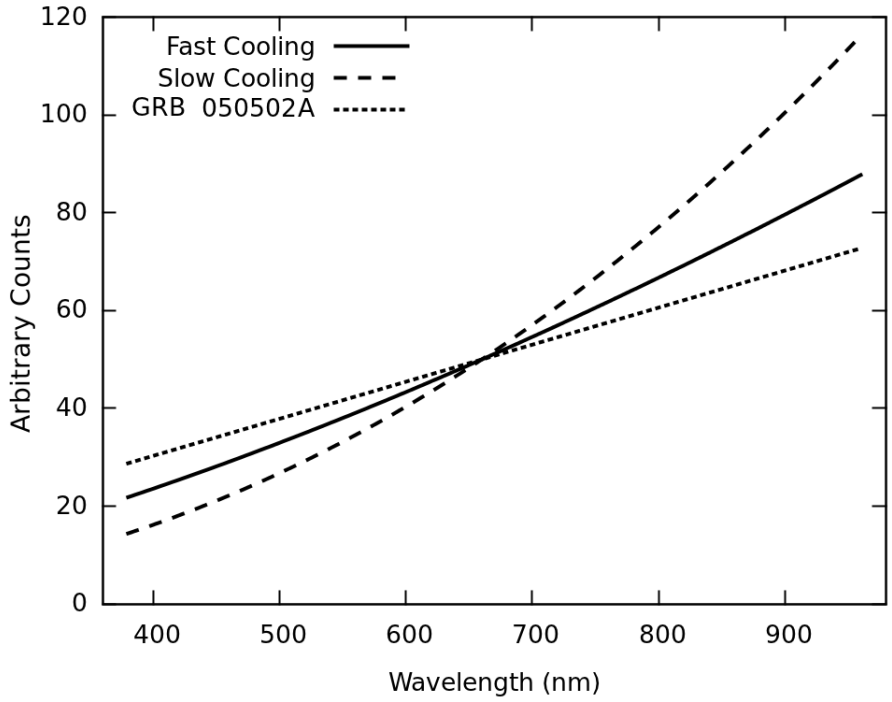


Figure 2.12: The fast and slow cooling emission spectra of Sari et al. (1998) and the 'ball-park' spectra of GRB 050502A inferred from photometric measurements of Guidorzi et al. (2005). Spectra were normalised at 650nm, representing the centre of the RINGO3 operating wavelength range.

### 2.4.3 Waveband boundaries

In order to calculate the waveband boundaries, an initial propagation of the signals (3 spectra in Figure 2.12) and the noise signal (Figure 2.10) were passed through the instrumental model (Figure 2.13). With the La Palma sky approximating well to a synchrotron spectra (increasing at higher wavelengths in the optical band) the wavelength boundaries for the signals are very close.

The waveband boundaries for the 4 spectra to gain equal signal in the 3 bands of RINGO3 are shown in Table 2.2. Weaker signals at lower wavelengths for GRB spectra, together with poor throughput of the instrument lead to a very wide lower wavelength band. When compared with the Sloan photometric bands (Fukugita et al., 1996), this 'BLUE' band equates to a composite $g'$+ $r'$ band. The higher bands approximate to $r'/i'$ and $i'/z'$ bands (Figure 2.14). Analysis of these bands led to the the decision of

cut-off wavelengths of the two dichroic mirrors to be 640nm and 760nm.

Due to the wide nature of the BV band, the BB camera was found to be less effective by $\sim$5 % as the turnover of the benefits in its quantum efficiency over the BV type camera occur at 450nm as shown in Figure 2.6. However, with the hardware already ordered the BB camera was still used.

| Input Spectrum | BV Band (nm) | R Band (nm) | I Band (nm) |
|---|---|---|---|
| GRB 050502A | 400-680 | 680-770 | 770-900 |
| Fast Cooling | 400-640 | 640-740 | 740-900 |
| Slow Cooling | 400-660 | 660-760 | 760-900 |
| La Palma Sky | 400-620 | 620-770 | 770-900 |

Table 2.2: The RINGO3 wavebands determined from equal signal at the detector when the 3 GRB spectra from figure 2.12 are put through the instrumental throughput model. The dominant source of noise is from the optical sky spectra of La Palma taken from Benn and Ellison 1998 (Benn & Ellison, 1998) and put through the instrumental throughput model.

## 2.5 RINGO3 risks and options

### 2.5.1 Polarising filter reflections

With the change to the Versalite polarising filter, which is designed as a beam splitter, highly polarised radiation is reflected back along the beam of the telescope. The polariser is mounted before the field lens, such that the beam is reflected back onto the M3 science fold mirror. This could lead to ghosting in the images, especially if the continuation of the telescope beam back into the A&G unit on the telescope leads the beam size to be larger than the science fold mirror. In this case there would be scattered light inside the A&G box, affecting measurements.

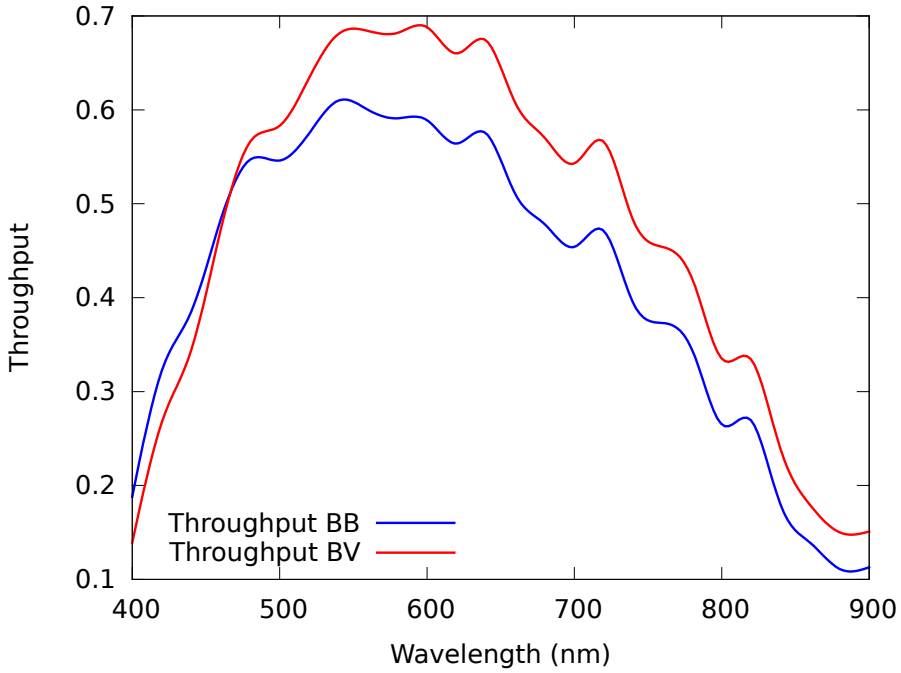


Figure 2.13: Comparison of the throughputs of RINGO3 across the full wavelength range with the quantum efficiencies of the BB and BV cameras. The decision to choose a camera with optimised quantum efficiency at shorter wavelengths seemed a sensible one. However with the wide e band (due to the synchrotron spectrum's influence), this was not a good choice with the turnover in efficiency occurring at 480nm, whilst the e band extends to 645nm. For obtaining the best amount of detection of radiation across this band a BV camera would have been preferential.

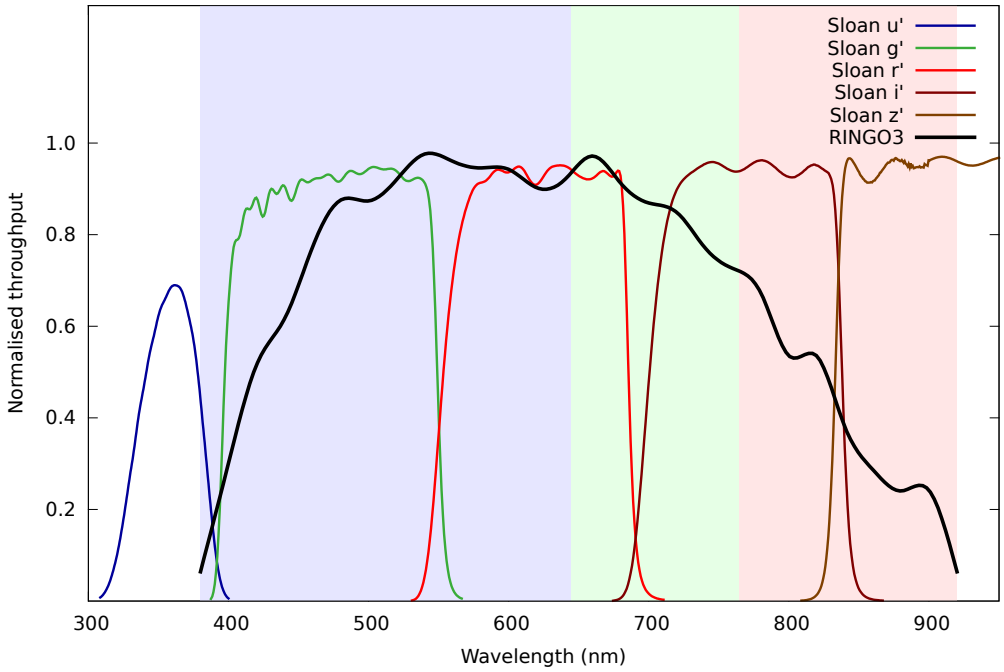


Figure 2.14: Comparison of RINGO3 bands and overall instrument throughput against the response curves of the Sloan photometric bands Fukugita et al. (1996).

If this is a visible issue in the data, it would be possible to tilt the polaroid so that the telescope beam has an angle of incidence of up to 45 degrees. This would then divert the reflected beam onto a circular baffle. The high angles of acceptance of the Versalite polaroid make this possible.

### 2.5.2 Instrument position on the Liverpool Telescope

As with RINGO2, the mounting of RINGO3 is to be on a side port of the A&G unit, and this means that the telescope beam is being directed to the instrument by a 45 degree science fold mirror. Along with other issues, such as timing integrity, this science fold mirror is expected to be the source of much of the instrumental polarisation, which needs to be corrected for during data reduction. RINGO2 performed adequately with this mounting, yet the mirror may behave differently at the extended wavelength range of RINGO3. Full analysis of the instrumental polarisation analysis of both RINGO2 and RINGO3 is described in Chapter 5.

### 2.5.3 Focusing issues

The three bands of RINGO3 need to be focused independently, using the focus settings on the Nikon camera lenses which focus the collimated beam onto their respective Andor cameras. Focus runs and small adjustments are required in order to bring the three cameras to a common focus.

The focusing of the lenses is using the manual focus ring which would be used in normal photographic operation. The visual scale on the focus mechanisms of these lenses is inadequate for scientific operation. Marks were made on the lens with sharp marker pen to give a position. The small moulded grip ridges provide a uniform rotational reference which could be used to make repeatable changes to the focus. Ideally the focus ring would be set with a small bead of epoxy to prevent rotation. However to allow future modification to the position a generous amount of electrical tape was used to hold the position.

Whilst the cameras may be in focus with each other, they will not necessarily be set to focus a perfectly collimated beam. This would be corrected using the secondary mirror focus on the LT. However, an uncollimated beam could present several issues. Firstly the dichroic mirrors are sensitive in their cut-off wavebands with angle of incidence. A badly uncollimated, rotating, highly polarised beam could produce unwanted effects. Secondly in an 'undercollimated beam' scenario, vignetting issues could come into play. In RINGO2, the collimated beam was extremely short. However the insertion of dichroic mirrors vastly increases the length of the collimated beam. In the case of an undercollimated beam, the beam becomes larger with path length. This beam could be larger in diameter than the camera lenses, leading to lost flux (vignetting).

It is essential that the camera lenses are focused as close to infinity as possible to focus a collimated beam onto the CCD. The focusing of the telescope will then work backwards from this reference point to produce the collimated beam. To focus the

camera lenses to infinity, a distant terrestrial source with clear (yet narrow) lines could be observed. The narrow lines would then be analysed for each focus step and full width half maximum (FWHM) measurements of this line would inform the correct focus.

### 2.5.4 Dichroic mirror problems

As considered in Section 2.2.4, the dichroic mirror cut-off wavelengths will oscillate with the rotation of the polaroid. This could affect the measurement of polarised sources. This issue is dealt with in Chapter 3.

In order to nullify a potential effect on measurement of polarised sources, two options are available. The first is to fit some kind of 'depolariser' after the polariser. This would change the collimated beam from a 100 % linearly polarised beam rotating with polaroid angle, to an unpolarised beam. It means that the unpolarised transition curves shown in Figure 2.5 will be effective, and no oscillation of the transition wavelength of the dichroics will occur. The issue with this is a possible loss of throughput, and also a skewing of the instrumental throughput across the wavelength ranges affecting the equal signal to noise of the bands.

The second option is to fit cut-off filters to the camera lenses so that wavelengths around the transition wavelength of the dichroics are attenuated. Depending on specification, this could be expensive and again affect the throughput model. Furthermore there could be space constraints between the camera lens filters and dichroic mirrors, necessitating modification of the instrument packaging.

### 2.5.5 Camera triggering and response

The timing integrity is of prime importance in the operation of the triggered EMCCD RINGO instruments. It is defined as the ability of the deployed system to provide

consistent integration times on-sky for each of the 8 rotor positions.

The stability of the camera triggering system was untested with RINGO2. The magnetic markers had been accurately placed on the barrel of the rotation mechanism. However, they may not have provided a completely perfect 'metronomic' trigger to the cameras. This effect is one of the issues which would provide instrumental polarisation if the exposure times of each of the 8 polaroid positions were different. Nonetheless, provided that the imperfect pattern of the trigger signals is constant, measurement corrections can be made. Consequently this is not a major issue.

This raises the question of whether the temporal signature of the trigger signals is consistent. There are two conceivable effects that the rotor mechanism could contribute to timing integrity. Firstly, the drive motor is controlled by adjusting the voltage through a variable resistor. The voltage does drift with time, due to temperature or pressure changes. However, this happens slowly, on much longer time scales than a series of observations. Ideally, different rotor speeds would provide identical temporal signatures of triggers, except at differing frequencies. This remains untested. The second effect is that the instrument, and hence rotor mechanism, operates at a range of orientations as the telescope slews between targets on the sky. It is conceivable that the orientation of the rotor mechanism produces different temporal signatures.

Even if the timing integrity of the rotor mechanism is beyond doubt, the accuracy of the cameras to respond to a trigger and provide a consistent integration time is unknown. Assuming the integration time for each rotor position produces a normal distribution over a number of rotations, the final stacked data of long observations should reduce this effect.

It is likely that both the camera response time and also the triggering stability contribute to inaccuracies in measurement of the RINGO3 instrument. From an instrumental viewpoint, I believe that this is the most promising line of investigation which

could enable RINGO3 to make observations of a wider range of astrophysical objects, providing better accuracy for lower polarisation sources (e.g. Asteroids), and better time resolution for higher polarisation objects (e.g. blazars, gamma-ray bursts). An analysis of the RINGO3 current timing integrity is presented in Chapter 3. Further possibilities for investigation and improvement on this issue are outlined in Chapter 7.

### 2.5.6 On-sky calibrations

Given the Liverpool Telescope development rationale, the nature of transient astronomy and the fast moving field of GRB research, the following statement was coined by myself relating to the development of both RINGO2 and RINGO3.

> ***"In the fast moving field of transient astronomy, it is better to have an imperfect instrument on the sky, than a potentially perfect instrument in the lab."***

The analysis performed in this chapter on the RINGO3 design could have gone further to predict potential issues which we would see upon instrument commissioning. With polarimetric measurements the telescope mirrors have an effect on the polarisation state of the beam. Owing to this, it is best to view our polarimeter instrument as the full telescope and RINGO3.

With this in mind, on-sky testing of the instrument far surpasses any lab work which could be undertaken, especially if we view the instrument (telescope and RINGO3) as a 'black box' which we are confident that we can characterise and solve. By observing polarised standard stars and comparing the measurements we obtain, an empirical approach will allow characterisation of the instrument. Existing RINGO2 analysis shows is possible. In the more complex instrument of RINGO3 however, any feedback between various subsystems could lead to an empirical approach failing.

# Chapter 3

# RINGO3 commissioning

## 3.1 Instrument construction and fitting

Commissioning of RINGO3 was performed on site at the Liverpool Telescope (LT) on the Roque de las Muchachos (ORM) observatory in La Palma, during the week of November 19th-25th 2012. Owing to the reuse of sections of RINGO2, all construction of the instrument was performed on site.

Due to the nature of transient astronomy, each night during commissioning a working polarimeter was available on the LT, as RINGO2 transitioned into RINGO3. On the first night, the polariser on RINGO2 was changed to the Versalite VIS, and a night of observations taken using the existing RINGO2 setup. Image quality was unaffected and no ghosting was immediately apparent.

The next day RINGO2 was decommissioned. The rotor mechanism and camera were fitted into the RINGO3 instrument packaging without any dichroic mirrors. The lower two camera ports were made light tight in order to create a single band instrument, which covered the full wavelength range of RINGO3. Observations on the second night used the existing RINGO2 camera and control computer. The RINGO3 instrument undergoing construction is seen in Figure 3.12. Due to the larger size of

RINGO3, a different port on the A&G unit needed to be re-assigned and instruments were moved on the Telescope. The cleared port without RINGO3 can be seen in Figure 3.13.

For the third night RINGO3 was built up fully with dichroic mirrors, 3 cameras, modified triggering electronics and two new data acquisition / control computers. The three cameras were focused, as described further in Section 3.2.1. During this night, alignment of the 3 cameras was performed in order to bring the centres of the images to within 10 pixels. This was done by tilting the dichroic mirrors (vertical alignment) and by tilting the cameras (horizontal alignment). There was no visible rotation between images.

### 3.1.1 Labelling of RINGO3 bands

The Liverpool Telescope uses a naming convention for all data produced by the telescope. Each instrument is assigned a letter which is used at the beginning of the fits filename. In the acquisition system, RINGO3 is seen as three different instruments, and hence requires three letters to be assigned. These are d, e and f and were assigned to the bands based on their physical location on RINGO3, as shown in Figure 3.14. The bands are detailed in Table 3.1.

| Camera | Waveband Name | Range (nm) | Width (nm) | Optical Path with Dichroics |
|---|---|---|---|---|
| d | RED | 765 - 900 | 135 | 1 transmission |
| e | BLUE | 400 - 645 | 245 | 2 reflections |
| f | GREEN | 645 - 765 | 120 | 1 reflection, 1 transmission |

Table 3.1: Details of the RINGO3 wavebands. Whilst the bands more closely resemble a BV, R, and I bands (e,f,d respectively), the informal names of the bands are Blue, Green and Red.

## 3.2 Instrument focusing

### 3.2.1 Focusing of camera lenses

As described in Chapter 2, the focusing of the instrument is propagated from the correct focus of the camera lenses attached to the camera units. This creates an accurately collimated beam within the path of the dichroics. The issue in the lab is to create a perfectly collimated source (i.e. an object viewed at infinite distance) to focus the camera lenses.

Observations of terrestrial sources such as the Resedencia at ORM (1.8 km distant from the LT) were attempted using the cameras, to provide near infinite focus. However imaging was an issue with the seeing (atmospheric turbulence) of daytime high airmass terrestrial observations. This meant that it was difficult to gain enough contrast between building features to obtain FWHM measurements for focusing. The Isaac Newton Group (where I was on a year's placement at the time) were consulted as to whether they had any lab equipment that could readily be used to provide a collimated beam, but to no avail. In the end a system for collimation was improvised.

The improvised collimation system was created using a small amateur refractor telescope and an eyepiece with a wire reticule, shown in Figure 3.1. The wire reticule was in a relaxed focus for the human eye (as if viewing a distant object), when viewed through the eyepiece. This means that it lies close to the focal point of the eyepiece lens system. By focusing the telescope at night to the human eye, the reticule would lie close to the focal point of the primary lens of the refractor. Due to the eyepiece being of 20 mm (f1) focal length and the focal length of the refractor being $\sim$1000 mm (f2), any error in the position of the reticule wires compared to the eyepiece focal length is around 50 times reduced by the longer focal length of the primary lens of the refractor.

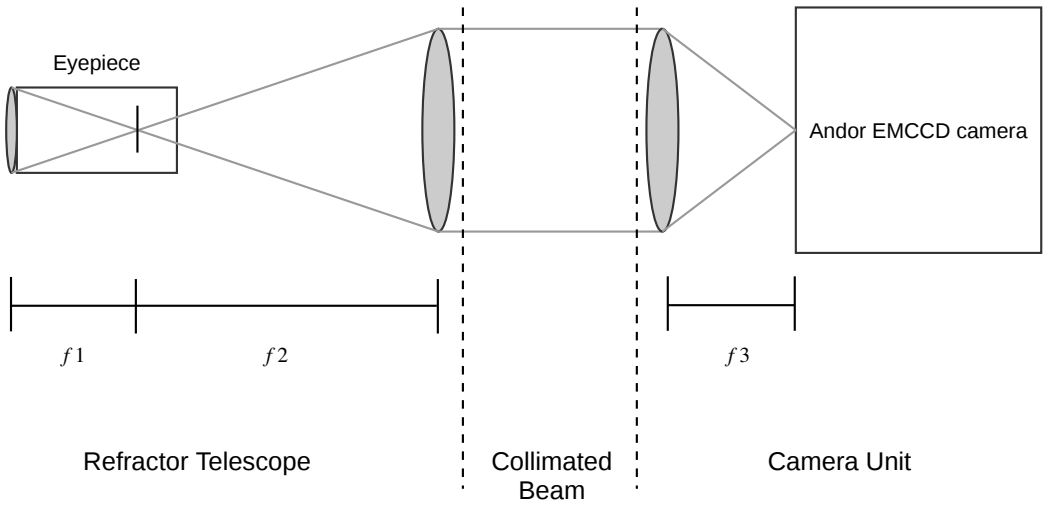


Figure 3.1: Diagram of the optical setup to focus the camera lenses on the EMCCD units for a collimated beam. A small refracting telescope was used in order to provide a collimated image of the reticule in the eyepiece.

Once focused to infinity using bright celestial objects (such as Jupiter), the refractor could be reversed to provide a collimated image of the reticule from the primary lens. By imaging with a number of focus steps on the Nikon camera lenses, and measuring the FWHM of the wire sections of the reticule image, it was possible to focus each of the camera lenses with their respective cameras.

### 3.2.2 Focus adjustments

In order to fine tune the focus of the cameras, Dr Rob Smith performed on-sky focus runs for each of the three bands of RINGO3, so that corrections could be made in order to bring all three bands within the same focus. The inital focus run was performed on 23rd November 2012 and the results are shown in Figure 3.2. A number of adjustments were required over subsequent nights to bring the 3 camera lenses into focus.

In Figure 3.2 the focus runs are expressed by changing the secondary mirror focus (SMF). As discussed in Chapter 2, the camera lenses are the reference point for focusing, and their focus is essential to obtain a collimated beam within the instrument

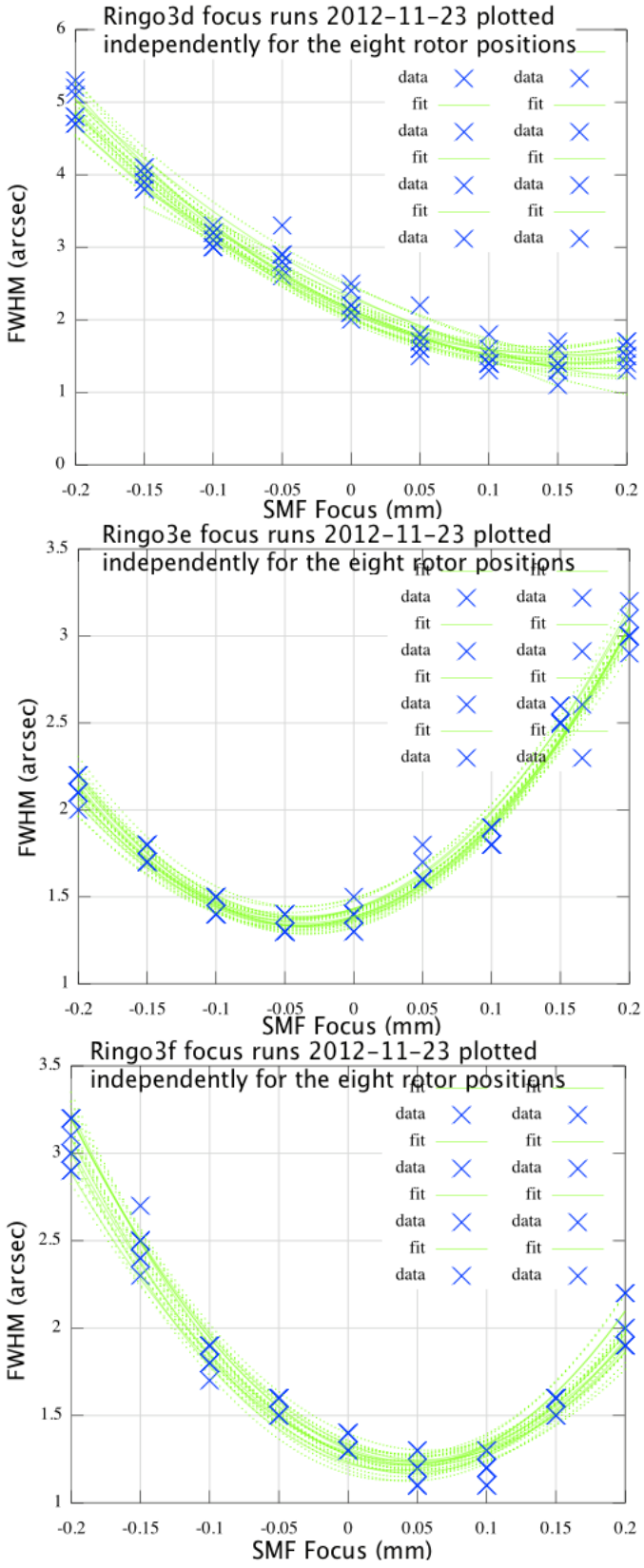


Figure 3.2: Initial on-sky focus runs of RINGO3 taken on 23rd November 2012. Analysis was done on each of the 8 images for each band. The focus scale is that of the secondary mirror focus (SMF) value. All work and plots from Dr Rob Smith.

in the section where the dichroic mirrors split the wavebands. If these are incorrectly focused, the SMF can be changed to correct for this issue, providing focused stellar images but with the issues of an under or over collimated beam. Another consideration is that the SMF value lies close to the focus values for other instruments on the Liverpool Telescope. As the primary science imager, RATcam (now decommissioned) provided the SMF zero point. With the fast response requirements of GRB science, and also the efficiency of the Liverpool Telescope scheduled observations, the SMF focus values of all instruments should be kept as close as possible. Changing the secondary mirror focus is a relatively slow process that adds overheads to the observations, especially when switching between instruments during the same pointing. For this reason the f camera with its focus being closest to other instruments, was chosen as the reference focus. The d and e cameras were then brought into focus with this reference camera.

### 3.2.3 Image quality

The initial focus run makes measurements that place upper limits on RINGO3 image quality in terms of the full width half maximum (FWHM) of the measurement. Expressed in angular form (arcseconds) it is a measure of the 2 dimensional Gaussian distribution of counts on the CCD from a point source. This deviation from a stellar point source is caused by a combination of atmospheric turbulence (seeing), telescope diffraction and inadequate focusing of the image onto the instrument detector. In the case of the Liverpool Telescope of 2 metre aperture, the diffraction limit is $\sim$0.1 arcseconds at 900nm wavelength. This is the upper operating wavelength of RINGO3, with the highest level of diffraction. We can therefore ignore the effects of diffraction as they are minimal compared to that of seeing. Hence the value of the measured FWHM of stellar sources can be attributed to a combination of the atmospheric seeing and the instrument focusing quality.

The seeing at the Liverpool Telescope site on La Palma is rarely better than 1 arcsec, and seeing of 1.5 arcseconds is considered adequate. The focus runs show that images

from all 8 rotor positions can be below 1.5 arcseconds FWHM at the best focus value. The performance of the d camera is less good with the FWHM being better than 2 arcseconds. There could be a number of factors which led to this result, including the achromatic performance of the camera and collimator lenses at wavelengths beyond the optical range. Possible tests to investigate this are described in Chapter 7.

The focus runs were performed twice more over the following week and adjustments made to bring the 3 cameras satisfactorily into focus.

## 3.3 First light

First light with RINGO3 took place on the night of 23rd November 2012. After adjusting the dichroic mirror tilt to align the fields, observations of standard polarimetric sources were undertaken. Two observable zero polarised sources were HD14069 and G191B2B which are detailed in Schmidt et al. (1992). The observational parameters are shown in Table 3.2

| Source | RA (J2000) | Dec (J2000) | Moon Distance (Degrees) | Apparent Magnitude | Spectral Type |
|---|---|---|---|---|---|
| HD14069 | 02 16 45.90 | +07 41 10.7 | 62 | 8.99 | A0 |
| G191B2B | 05 05 30.61 | +52 49 51.9 | 103 | 11.79 | DA1 |

Table 3.2: The two zero polarised standards observed during RINGO3 first light. Both standards come from Schmidt et al. (1992)

### 3.3.1 Analysis of standards

Zero polarised standards provide a celestial source which enables vital calibration for a polarimeter. They have been selected as sources providing less than 0.05 % po-

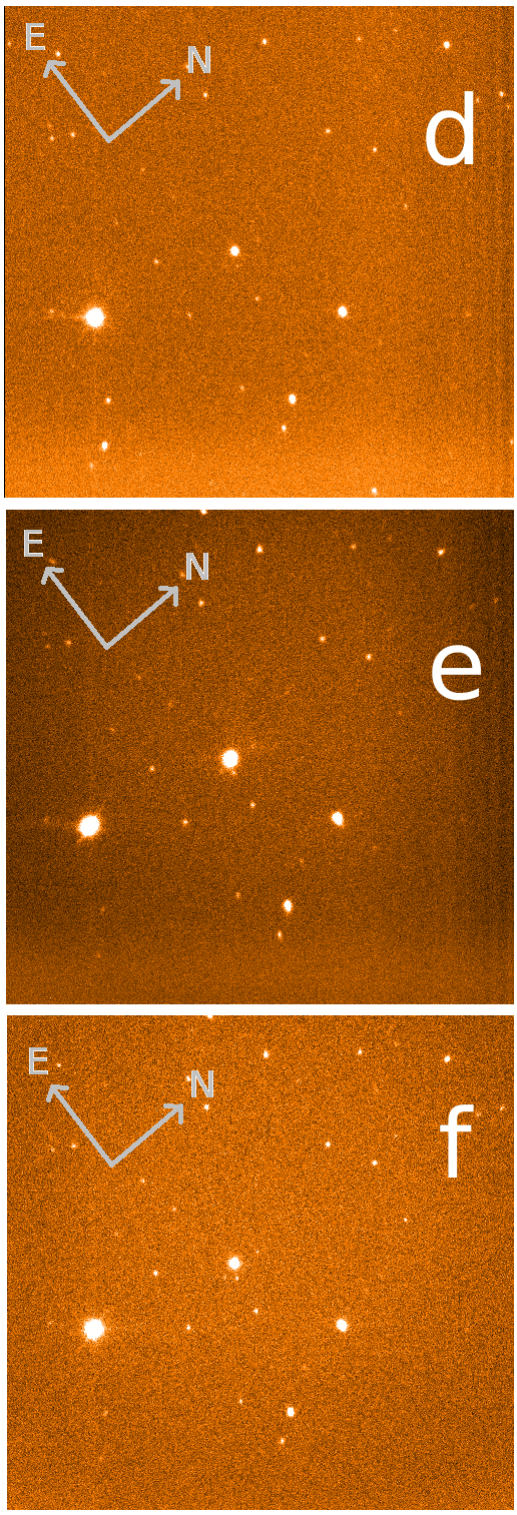


Figure 3.3: First light images of the field of G191B2B taken on the night of 20th November 2012. At this point the cameras had been aligned to within 5 pixels of each other in the x-y plane. The rotation between cameras was undetected. The images here are of a single rotor position 4, were debiased and had a single master flatfield applied. It can be seen that this single flatfield does not meet the requirements of camera e with obvious visible vignetting of the field.

larisation across the optical wavelength regime. By measurement of these sources the zeropoint of polarimetric measurements in the q-u plane is obtained. As described in Chapter 2, the full polarimetric instrument is considered to be the telescope and polarimeter, as reflections within the telescope will affect the polarimetric state of the radiation. With RINGO2 this q-u zeropoint was shown to lie at a position from the origin with vector length $\sim$0.03 corresponding to a $\sim$3 % instrumental polarisation. For RINGO3 the 3 cameras are expected to have differing zeropoints, as the telescope mirrors will change the state of the unpolarised radiation from these sources by an amount that varies with wavelength.

Five 30 second observations were taken of each standard. These were processed via the onsite pipeline, which automatically debiases, stacks and flatfields each of the 8 files for each observation. The data was reduced with the '`ripe`' pipeline which is described fully in Chapter 4.

| Camera | Average HD14069 Polarisation | Average G191B2B Polarisation | 2-sigma HD14069 Error | 2-sigma G191B2B Error | Average HD14069 Photometric Error | Average G191B2B Photometric Error |
|---|---|---|---|---|---|---|
| d | 0.068 | 0.106 | 0.009 | 0.010 | 0.0001 | 0.0061 |
| e | 0.058 | 0.052 | 0.009 | 0.004 | 0.0004 | 0.0016 |
| f | 0.008 | 0.028 | 0.009 | 0.008 | 0.0007 | 0.0034 |

Table 3.3: Measured polarisation values of the zero polarised standards HD14069 and G191B2B taken at first light.

The q-u values of each measurement are shown in the upper plot of Figure 3.4. The error bars shown are the propagated 1-sigma photometric errors, which are taken for each of the 8 photometric measurements that are required for a polarimetric measurement, and propagated through the equations which result in the normalised Stokes parameters, as described in Section 4.1.2.

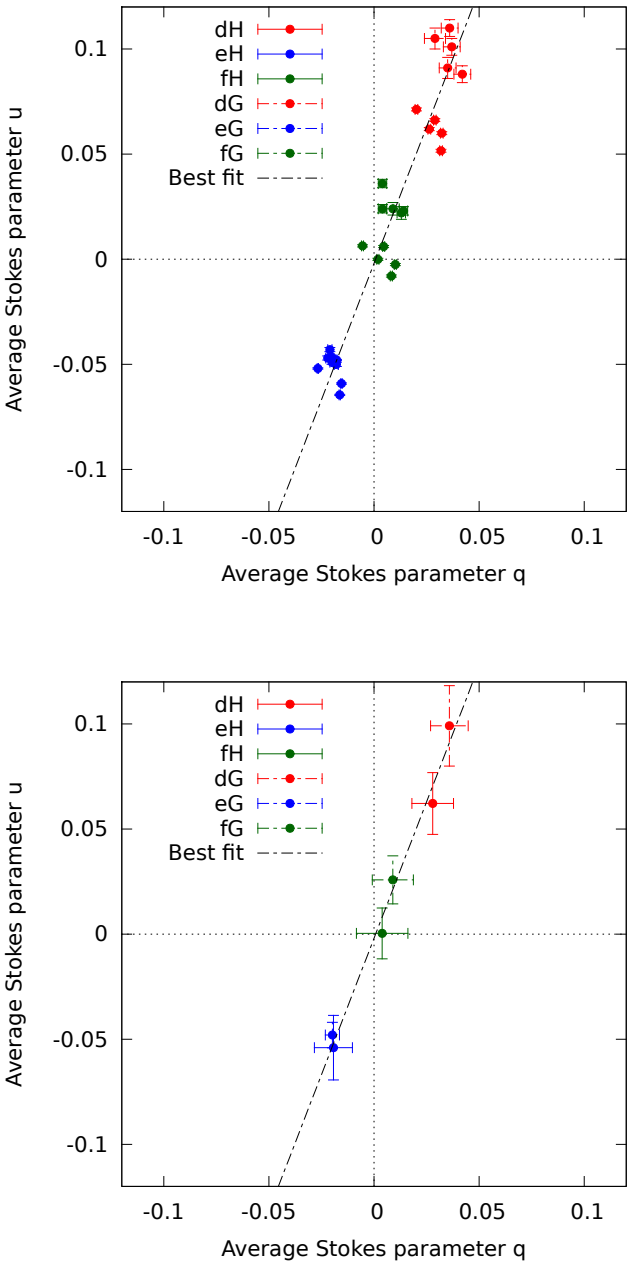


Figure 3.4: Polarisation measurements of two zero polarised sources from Schmidt et al. (1992), HD14069 and G191B2B. Five 30 second observations were taken of each source. The top plot shows the individual measurements, with error bars being the propagated photometric error on the normalised Stokes parameters, q and u. The lower plot shows the average value of the 5 measurements with 2-sigma error bars. Labelling nomenclature on the plot is CAMERA_STANDARD. For example, 'eG' is Camera e and Standard G191B2B.

In the d and f cameras it is clear that the scatter of the five measurements for both standards is greater than could be accounted for purely by photometric error. This shows that within the instrument there are other sources of error which need to be understood and accounted for. Most strikingly, the zeropoints for the d and f cameras of the two standards are distinctly different, which presents a problem. Camera e, however, shows excellent repeatable measurements of both standards. They are consistent, despite a couple of outliers.

The unexpected result was that the points of these 30 polarimetric measurements lie excellently along a line of best fit. The reason for this is unknown, and concerning as it could point to some wavelength dependent modification by the dichroic mirrors. Both standards are Spectral type A stars, with HD14069 being a hypergiant and G191B2B being a white dwarf. Despite their differences, both should give a similar thermal spectrum.

These initial results were better understood after RINGO3 gathered more data of standards over the coming weeks and months. With this data, further investigation into the validity of polarimetric measurements with RINGO3 was done and this is presented in Section 3.6

## 3.4 Vignetting issues

Immediately visible from the flatfield images taken up on commissioning was vignetting affecting the images in all 3 bands. This was an oversight in the optical extension of RINGO2 to RINGO3 and caused by the extended path length of the collimated beam within the instrument, as illustrated in Figure 3.5. Band d has the shortest path length and showed less vignetting than bands e and f which have equal and longer path lengths (see Figure 2.1)

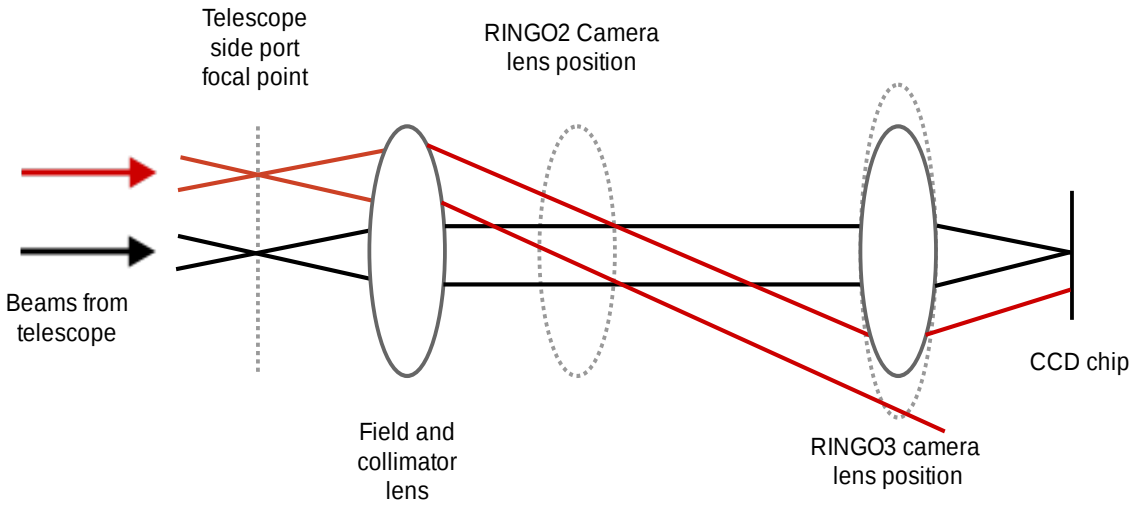


Figure 3.5: A simplified diagram showing how the extended path length of the collimated beam within RINGO3 leads to vignetting. The red beam is an off axis source which forms a collimated beam which is not parallel to the collimator and camera lens axis. It can be seen that a larger diameter camera lens is required in order to focus the full amount of flux onto the detector.

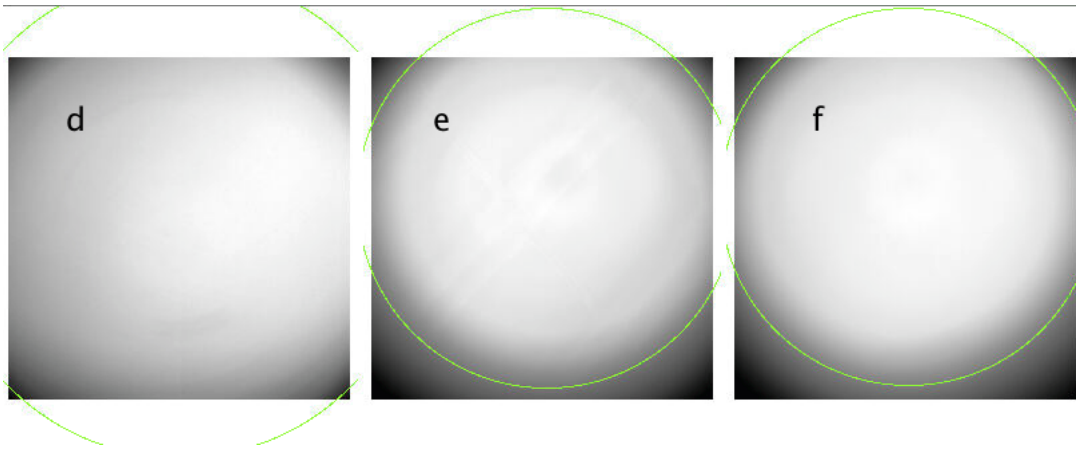


Figure 3.6: Images of final vignetting pattern of the RINGO3 bands, taken with flatfield observations. The green circles show the 50 % flux level. The patterns are circular. In bands e and f, the centre of the vignetting pattern is slighly above the centre of the frame. Analysis by Dr Rob Smith

To correct this vignetting problem and bring cameras e and f into line with the acceptable vignetting experienced in camera d, larger diameter commercial camera lenses were sourced. The 50mm f1.4 lenses (with effective diameter 36mm), were replaced with 58mm f1.2 lenses of effective diameter 48mm. These larger units had an issue with clearance inside the instrument, with risk of fouling the dichroic mirrors. Light tight spacers were produced of 10mm thickness to move the camera assembly (and attached camera lenses) back and provide room for fitting.

The different specification of the focal ratio of the camera lenses changed the pixel scale in cameras e and f. The new vignetting patterns and pixel scale were analysed by Dr Rob Smith. The addition of a depolariser (see Section 3.6) affected the vignetting patterns of the instrument. Table 3.4 and Figure 3.6 show the final vignetting patterns of RINGO3 from 6th June 2014 (fitting of depolariser) until the present.

| Camera | Pixel Scale (arcsec/pixel) | 50 % vignetted field diameter (arcmin) |
|---|---|---|
| d | 0.49 | 5.9 |
| f | 0.44 | 4.1 |
| e | 0.43 | 4.1 |
| r2 | 0.45 | >5.9 |

Table 3.4: The final pixel scale and vignetting characteristics of the RINGO3 bands after 6th June 2014, when the last major optical change was made with a movement in position of the depolariser. RINGO2 (r2) pixel scale is shown. The 50% vignetted field was unknown for RINGO2, but due to the short optical path of the collimated beam vignetting was much reduced compared to RINGO3 bands. Analysis by Dr Rob Smith

## 3.5 Timing integrity verification test

The timing integrity of the RINGO3 system is of prime importance in accurate polarimetric measurements. As discussed in section 2.5.5 of the previous chapter, any

stochastic variation in the exposure times from rotation to rotation will cause an unresolvable source of instrumental polarisation. The cause of these variations could be from two different sources. First is the mechanical polaroid rotation mechanism, and second, the camera response time to a trigger signal.

With the initial results of polarimetric measurements of zero polarised standard stars producing large spreads (Section 3.3.1), this was an area of importance for investigation into the variation of measurements which could not be explained by photometric errors alone.

In order to quantify the timing integrity, an observation of a bright, constantly polarised source is required. The best source for our requirements are dome flats, giving a repeatable and controlled observation. These are a common observational method to obtain flatfields for a telescope system during the day or during bad weather, when the telescope is closed. These flats enable a controlled environment, and most importantly, a bright source, which allows accurate measurements with very small uncertainties due to Poisson errors and read noise.

### 3.5.1 Illumination source

The illumination source for the dome flats was carefully selected. For most dome flat applications, any illumination is suitable, as a single exposure is taken (generally with an exposure time of order $\sim$ 5-10 s). This provides the flatfield pattern of the telescope and instrument. However, with the interest being in polarimetric measurements taken from a number of high cadence exposures of 125 ms, the source of illumination must be stable with very little flickering in the order of frequency of exposures ($\sim$8 Hz).

The flicker of the standard fluorescent, gas discharge, dome lamps is of concern. Their design means that the ripple amplitude on the flicker could be large. With a number of lights in the dome, it was unknown whether any flicker was in phase. With these

uncertainties, the dome lights were not deemed suitable as an illumination source. The most readily available single source at the Liverpool Telescope was an incandescent work lamp, which is run off the mains supply. We know that the frequency of flicker of this lamp is 100 Hz (twice the mains alternating voltage frequency) meaning a period of 10 ms. Also an incandescent bulb will have a lower ripple amplitude than that of a fluorescent tube. This source is also providing ripples at a frequency more than a factor of 10 greater than the sampling frequency of exposures.

### 3.5.2 Data acquisition and reduction

The data was acquired during a maintenance visit to the telescope, and only the d and e cameras were operational. The telescope was pointed at the zenith with the dome closed and mirror cover open. The light was positioned and tests were undertaken to ensure that the counts in the 125 ms frames were in the region of 2000-7000 counts, which is well within the linearity region.

A run of 250 seconds was taken, providing data for 236 rotations of the polaroid. The data was debiased and flatfielded as per the usual onsite pipeline, yet remained unstacked. This provided 236 sets of observations for each of the d and e cameras. These files were processed through the `ripe` pipeline (see Chapter 4). Instead of doing polarimetric extraction from the files, the average and standard deviation of the counts in a 20 x 20 pixel area in the centre of the field were taken using `imstat` from `cfitsio`, Pence (1999). This provided a very strong flux measurement, and after the process of flatfielding, the standard deviation of the pixel counts was used as the error value on the flux measurement.

### 3.5.3 Analysis and results

The normalised Stokes parameters of the 236 observations were calculated for both the d and e cameras, along with photometric errors. This produced four distributions,

which were separately linearly shifted to make the mean value for each equal to zero. Figure 3.7 shows these four distributions, which form an expected approximation of a normal distribution. Assuming a normal distribution, the $2\sigma$ error on the measurements was 0.0011 and 0.0016 for the d and e cameras respectively.

Clearly the spread of the distributions is narrow in the range of q and u, and even in the worst case (Camera e - q, bottom left) the spread is 0.008. When converted in quadrature (as the Stokes parameters are to calculate polarisation) this equates to a maximal spread of error in polarisation of 1.13 % or a maximal error contribution of just half that. The distributions all have a $2\sigma$ variation of less than 0.003, which is about twice the expected spread, given the photometric errors ($\sim$0.0016) on the individual measurements.

In order to analyse the results further, it can be assumed that the two cameras are receiving the trigger signals at identical times. If the variance in Stokes parameter values could be fully attributed to variations in the mechanical rotor mechanism, then the variance in the d and e camera from rotation to rotation, would be identical. To test this a differential analysis between the two cameras was performed. The first analysis was to subtract the e camera values from the d camera values for each rotation, creating a histogram of the remainder value. By randomising the order of the e values, a second analysis for comparison was done before subtracting them from the d values. Both of these analyses are shown in Figure 3.8

The remainder histograms aim to split the contributions to timing integrity errors from the electromechanical trigger and the camera response time. Both sets of histograms are almost identical with all of them having a rounded $2\sigma$ width of 0.0013. This shows that correlation between rotation number (of the 236 sets of data) and the variance in Stokes parameters between the two cameras cannot be seen. This implies that the dominant part of timing issues is from the camera response times.

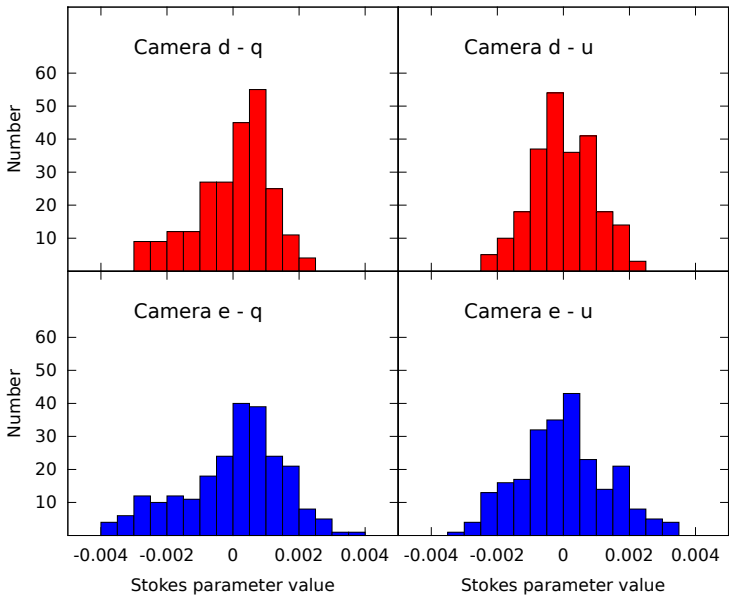


Figure 3.7: Histograms of the values of Stokes parameters for individual rotations of the polaroid on RINGO3. The distributions are shifted, so that the mean value is zero.

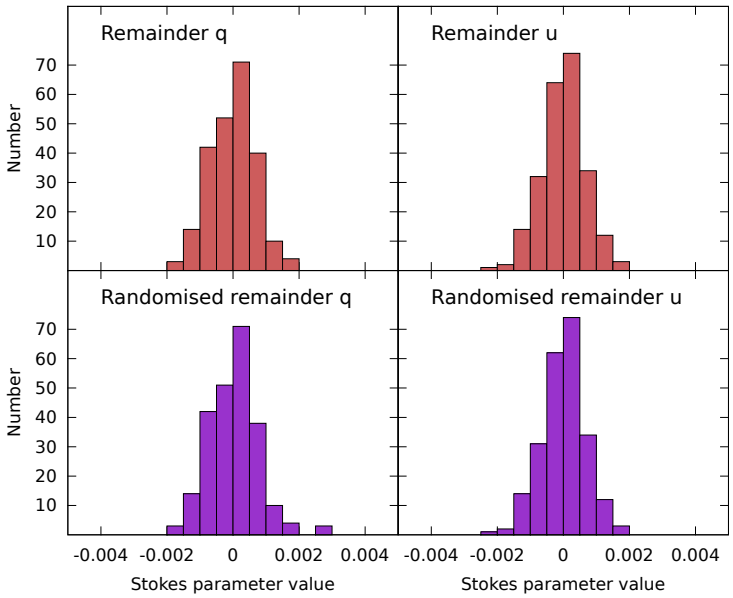


Figure 3.8: Differential histograms of the Stokes parameters between the data from cameras d and e. In the top, remainder analysis, the q and u values of the e camera were subtracted from the d camera. In the lower analysis, the values of the e camera were first randomised, then subtracted from the d camera values.

### 3.5.4 Conclusions on timing integrity

These tests show that the timing integrity of the RINGO3 system is well within tolerance for the polarimetric measurements that are required. In scientific cases, the photometric noise of faint sources will dominate over the noise introduced by the timing. We know from these tests that the $2\sigma$ error from timing issues on polarisation is less than 0.3 %. This cannot be quantified further, owing to the number of issues which could be at play (such as the 100 Hz rippling in the illumination source).

The differential analysis producing the remainder values of q and u strongly suggested that the issues of timing integrity are dominated by the camera response times. If this is the case then one possible solution to reduce the error would be to slow down the rotor[1], which would have the following effects on the RINGO3 system:

- **Minimise camera response time errors**

  By slowing the rotor the camera response error would be reduced. For example, if the rotor speed were halved (1 rotation per 2 seconds) then the exposure time of each triggered integration would be doubled, thus halving the contribution of timing error from the camera response time.

- **Reduce the time resolution of measurements**

  The maximal time resolution with RINGO3 is defined as the period of one rotation of the polaroid. In normal operation this is 1 second. However, with many scientific sources being in the range of 14th to 17th magnitude, the photometric error dictates that in order to obtain any meaningful polarisation measurements (e.g $1\sigma$ errors of 5 % or better) stacks of rotations are used which equate to greater than 10 seconds of time resolution in any case. For the majority of observations, the rotor speed could be slowed by a factor of 5 and still provide the maximal photon limit time resolution.

[1] In January 2015 the rotor frequency of RINGO3 was lowered from 1Hz to 0.4Hz, to lower the data processing overheads. This also had the benefit of improving the instrumental repeatability.

□ **Reduce the pixel saturation point of observations**

Dependent on the gain settings used in the electron multiplying (EM) gain stage of the detector, the saturation point (in photo-electrons) of the Andor cameras varies. By reducing the rotor speed the integration time of each frame is increased, moving the saturation point to lower magnitudes. At present, the brightest sources routinely observed by RINGO3 are the polarimetric standards of which HD155528 is the brightest, with a V-band magnitude of 8.7 (Schmidt et al., 1992). This source is already pushing $\sim$75 % of the saturation limit in the central pixel (dependent obviously on airmass and seeing). In the above example of slowing the rotor to 1/5th of the speed, the saturation limit of RINGO3 bands would be reduced by around 1.75 magnitudes.

□ **Reduce the data storage and processing requirements of the RINGO3 control computers**

Perhaps one of the most attractive reasons for slowing the rotor is that it would ease the processing requirements of the RINGO3 control computers. During data acquisition, this could assist in removing timing errors caused by acquisition system overload, as the bandwidth of the data passing from the cameras to the control computer would be reduced. RINGO3 data is not processed and stacked in real time, but performed as a task in the morning after the observations are taken. The smaller number of files reduces the load and the hard drive activity, which could assist in the longevity and reliability of the acquisition systems.

In the above investigation, there are two important details to be noted. Firstly, the analyses recorded the timing error produced by single rotations of the polaroid with the standard operating speed of 1 Hz. When the data are stacked, then the timing errors will be reduced by a factor of $\sqrt{N}$, where N is the number of rotations which are stacked. With the upper limit of $2\sigma$ error being 0.003 on the Stokes parameters for a single rotation, this equates to an error contribution of 0.42 %. In the case of RINGO3's best time resolution being 10 seconds, due to photometric error, then the upper limit of

timing error on the measurement would be 0.13 %. In short, the timing errors from this test are minimal for the accuracy required of RINGO3, and a change in rotor speed is not required for reasons of polarimetric accuracy.

However, this test was performed with the telescope in a singular position. It is quite possible that with the instrument under differing flexures (with varying pointings and Cassegrain rotator positions) the stability of the trigger signals is affected in a systematic way, either due to the rotor mechanism bearings, or driving motor patterns.

Finally, timing integrity of acquisition is highly unlikely as a source of error which could have created the larger than expected spread of measurements of zero polarised sources in Section 3.3.1. The repeated measurements of each standard were done with a single telescope pointing, thus mechanical rotor variation is an unlikely cause.

## 3.6 Issues with polarised beam and dichroics

RINGO3 started to build up a useful set of data via the RINGOstand programme, which operates each night to observe both polarised and unpolarised standard stars. Analysis of the zero polarised stars provided consistent results of the polarimetric zero points in the q-u plane, but with a spread larger than that of RINGO2 (which is detailed in Chapter 5).

However, the initial measurements of polarised standards were producing vastly differing values of polarisation, and even polarisation at a level above the catalogued values. RINGOstand routinely observes 6 polarised standards. As a robotic observing programme, observations are undertaken as and when possible. All observations are taken with the Cassegrain rotator set to zero, which eliminates another source of angular variation in the polarimetric setup of instrument and telescope. However, the effect of the Cassegrain rotator on polarimetric measurements is quantified in Chapter 5. On

Altitude-Azimuth telescopes, such as the Liverpool Telescope, the Cassegrain rotator is necessary to de-rotate the effect of sky rotation during tracking.

With the rotator at the same position for each observation, multiple observations of the standards give a number of different sky angles. The range of sky angles observable is dependent on the declination of the source. Given two theoretical sources at declination +85 °and declination -40 °, the former is observable all year round (from the ORM) and provides a full range of sky angles as it rotates around the North Celestial Pole. The latter would only be observable during a couple of months during the year and would provide a limited range of sky angles, transiting at a low observation altitude of 41 °, with a southern pointing.

### 3.6.1 Analysis of VICyg #12

Due to its declination of +41 °, VICyg #12 can be observed at a full range of sky angles for polarimetry (a range of 180°or more). It also has a high catalogued value of polarisation (8.95 % V-band, 7.89 % R-band). This provides the best data for analysis and investigation into the issues of the large scale of polarisation measurements.

Initial investigations by Dr Rob Smith on data from a few evenings of observations of VICyg #12, yielded erratic measurements of polarisation which ranged from ∼0 - 9 % (d band), ∼0 - 12 % (f band) and ∼0 - 16 % (e band). In polarimetric data reduction a level of instrumental depolarisation is expected, providing measured values of polarisation lower than the actual value. To have measured values above that of the catalogue value (e and f bands) was of concern.

A bulk analysis of data from 43 observations of VICyg #12 was undertaken with the `ripe` pipeline. The q-u zeropoints for each band were calculated from zero polarised sources observed over the same time frame. This yielded 40+ measurements of polarisation for each of the 3 bands after certain points were rejected. Plotting the

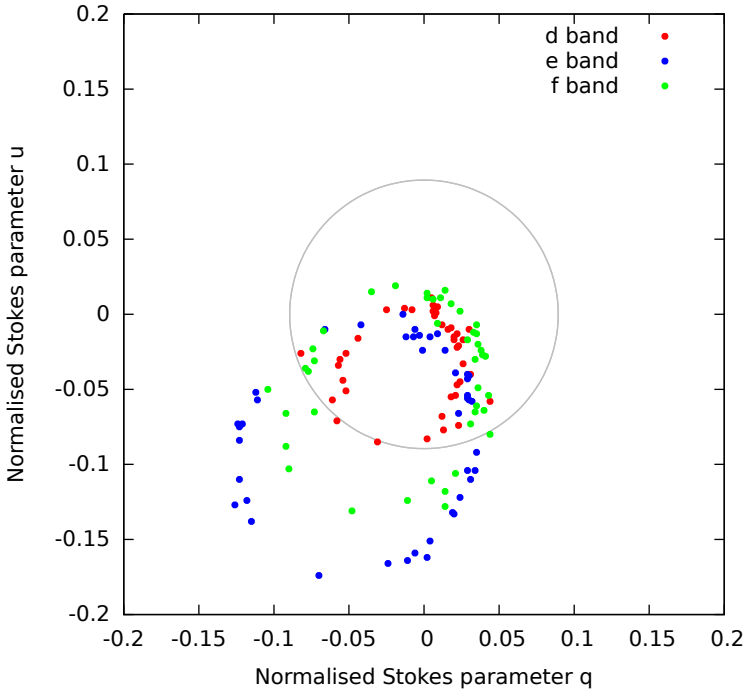


Figure 3.9: A q-u plot of polarimetric measurements of VICyg #12 from 43 observations taken before fitting of the depolariser. The grey circle shows the catalogued V band polarisation value of 8.95 % from Schmidt et al. (1992). Error bars from photometric errors are not shown as the $1\sigma$ errors are of the order of the point size due to the high signal to noise of observations of this bright stellar source.

polarisation values in the q-u plane provided an insight into the issues, as shown in Figure 3.9. The expected 'polarisation rings', an artifact of multiple observations over different sky angles, are observed. In an ideal situation, all points would lie in a circle, centred on the origin of the q-u plane and inside the grey ring showing the V-band catalogue polarisation of VICyg #12.

Using a least squares fitting method for ellipses, from Fitzgibbon et al. (1999), it was possible to find the centres and ellipticity of these polarisation rings. The results are shown in Table 3.5. It is interesting to note that in the q-u plane the semi major axis of the ellipses are aligned with the unexpected line of best fit that was found during first light with the zero polarised sources (as in Figure 3.4). The definitions and parameters of the polarisation rings are discussed fully in Chapter 5.

| Band | Centre of Ellipse (q, u) | Ellipticity $\epsilon$ | Angle of Ellipse |
|---|---|---|---|
| d | -0.015, -0.042 | 0.19 | 64.8 |
| e | -0.045, -0.090 | 0.13 | 61.4 |
| f | -0.023, -0.060 | 0.18 | 64.1 |

Table 3.5: Ellipse properties of the RINGO3 polarisation rings shown in Figure 3.9 before fitting of a depolariser. The definitions and parameters of the polarisation rings are covered in Chapter 5.

It is possible to correct the data for VICyg #12, to provide correct polarisation values, by applying a fixed Stokes zeropoint (described in Chapter 4) for each of the bands, which would be the centre of the ellipses in Table 3.5. However, with the Stokes zeropoints now being a function of source polarisation, it is impossible to measure and deduce polarisations of unknown sources, because there is a degeneracy between polarisation angle and magnitude.

With this affecting all 3 bands, it seems that there is an issue with the dichroic mirrors in both transmission and reflectance when measuring polarised sources. It can be assumed that this is due to the 100 % rotating collimated beam which is incident on the mirrors and their varying cut-off with angle.

### 3.6.2 Fitting of depolariser

A quartz wedge achromatic depolariser was sourced from Thorlabs. This optical element has a high throughput ($\gtrsim$97 %) over the operating wavelengths of RINGO3, having little effect on the instrumental throughput and efficiency. The depolariser works on the principle that it is non-homogeneous across the diameter of the optics, in that two identical parallel linearly polarised light beams with different paths through the optics will exit with different modified polarisations. When a polarised beam of a minimum diameter (6 mm) passes through the depolariser the resultant beam becomes depolarised due to the stochastic effects of the different paths. With requirements of a minimum beam diameter of 6 mm, and constraints on angle of incidence, the best

place to fit the depolariser was within the collimated beam, after the collimator lens. There was enough clearance within the RINGO3 mechanical design for this.

**Results**

With the depolariser fitted, initial commissioning observations confirmed its effectiveness. After this the observations of standards through the RINGOstand program were routinely taken at 3 Cassegrain rotator (rotmount) angles differing by 120°, every evening, producing 40 polarimetric measurements. Figure 3.10 shows the measurements in the q-u plane. The groupings of points relate to observations taken with the 3 rotmount angles. Whilst the spread of polarisations for the d camera (red points) is of concern, the data from other cameras form much tighter patterns. All points lie within the catalogued polarisation, which is expected due to instrumental depolarisation, which is fully addressed in Chapter 5.

The fitting of the depolariser also had an effect on the measurements of zero polarised standards and their zeropoints on the q-u plane. The values of the normalised Stokes parameters were analysed for all observations of zero polarised standards before and after the fitting of the depolariser. Histograms of the values are shown in Figure 3.11. It can be seen that the initially unexpected 'line of best fit' shown in Figure 3.4 has been removed and that the variance in measurements is vastly reduced by the depolariser.

## 3.7 Images of RINGO3 installation

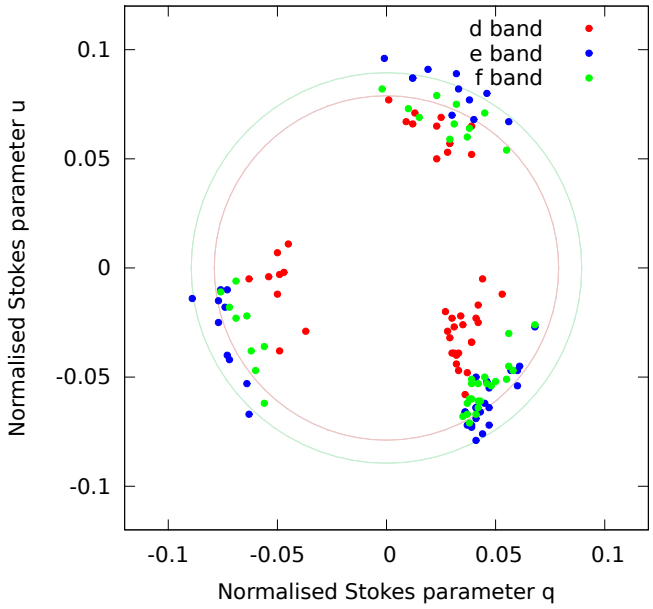


Figure 3.10: q-u plot from observations of 40 observations of VICyg #12 after the depolariser was fitted to RINGO3. The green circle shows the catalogued V band polarisation value of 8.95 % and red circle the catalogue R band polarisation of 7.89 % from Schmidt et al. (1992). As with Figure 3.9, instrumental polarisation correction was applied to the data, but no corrections relating to instrumental depolarisation were applied. The data being consistently within the catalogued rings for d and f cameras is expected as the level of measured polarisation is reduced by the telescope mirrors and optics. $1\sigma$ errors are on the order of the point size and are not shown.

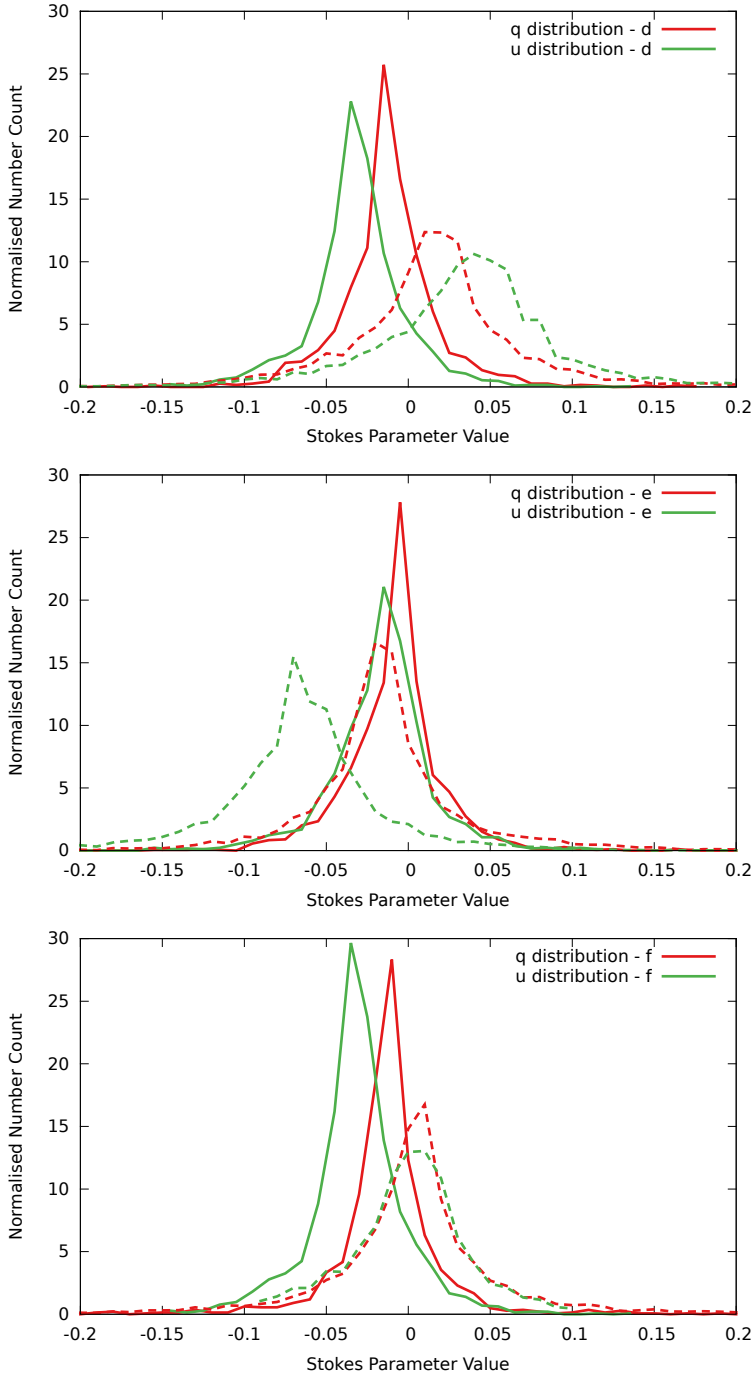


Figure 3.11: Normalised histograms of q and u values from zero polarised sources after fitting of depolariser for each of the RINGO3 bands (solid lines) and before the fitting of the depolariser (dotted lines). It can be seen that the variances in q and u for zero polarised sources are reduced by the depolariser and all have a FWHM $\sim 0.05$.

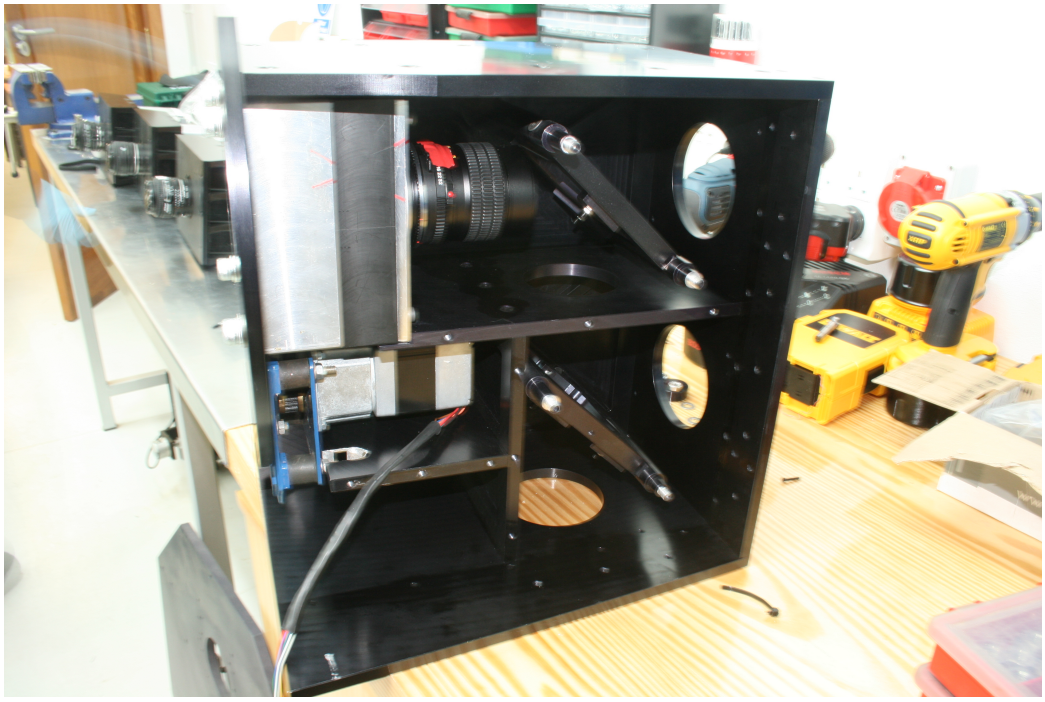

Figure 3.12: The image shows RINGO3, with the polaroid rotation mechanism, collimator lens and dichroic mirrors fitted. On the bench to the left the 3 camera units with camera lenses can be seen, ready to be mounted through the 3 obvious ports in the instrument casing.

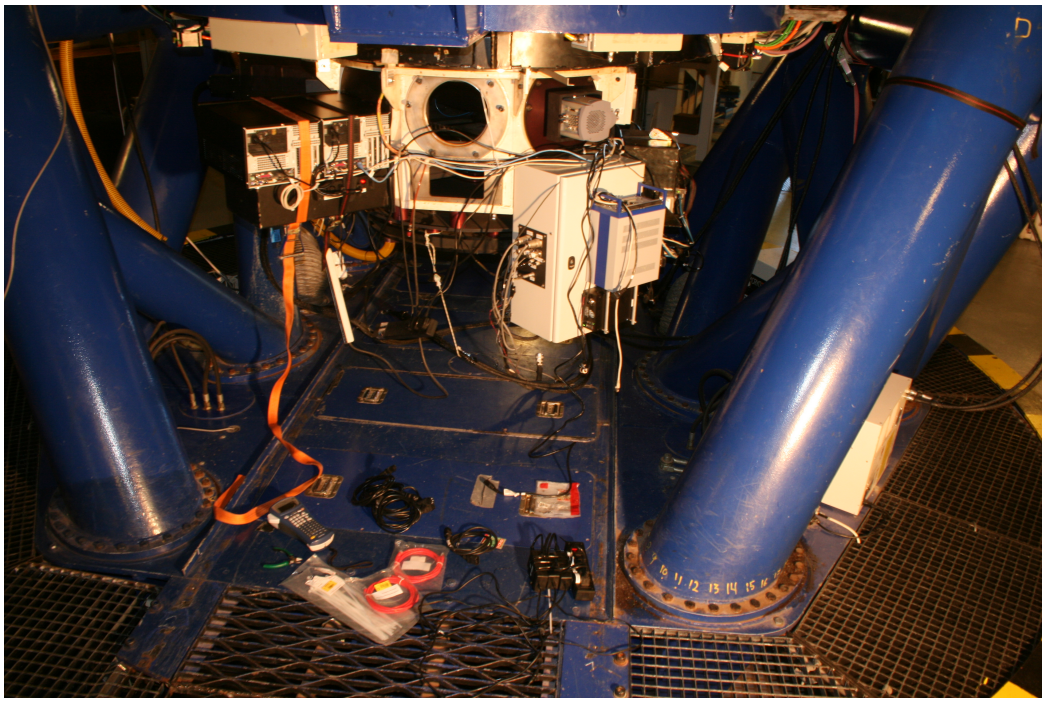

Figure 3.13: The A&G box on the Liverpool Telescope, showing the side port focus station cleared for the fitting of RINGO3. On the left of the port the two control PCs for the Andor cameras are visible and in the process of being strapped into place.

Figure 3.14: RINGO3 is shown here fitted to the telescope before cabling up of the Andor units' power supply and triggering signals.

# Chapter 4

# Data reduction

## 4.1 Polarimetric data reduction for RINGO2/3

As presented in Chapter 1, the fundamental technique for imaging polarimetry is that of differential photometry. Here we analyse elements of the photometric process that are pertinent for RINGO2+3 instruments and the subsequent data analysis, and also look at the phenomena of Instrumental Polarisation and instrumental depolarisation which need to be accounted for when making polarimetric observations.

### 4.1.1 Photometry with RINGO2+3

For the Liverpool Telescope (LT), the Airy disk is $\sim$0.1 arcsecs (2 metre aperture at 900 nm, using equation 1.8) or smaller. With a pixel scale of $\sim$ 0.5 the Airy disk would fit into a single pixel on the RINGO polarimetric instruments. It is thus that the effect of seeing at the Liverpool Telescope is the dominant effect in spreading the flux of a point stellar source across the CCD of the RINGO instruments.

Measurements undertaken at Observatory Roque de las Muchahos (ORM) over a nine month period found the mean seeing to be 0.76 arcsecs, with a median of 0.64 arcsecs (Munoz-Tunon et al., 1997). This was performed using a differential im-

age motion monitor (DIMM) on top of a 5 metre tower. Seeing varies across the ORM site and at the LT, good seeing is considered to be below 1.2 arcsecs

Seeing effects can be reduced with exposure times shorter than the frequency of turbulent movement in the atmosphere. Individual RINGO frames ($\sim$125 ms) probably do 'freeze out' the effects of seeing. However with the stacks of frames used for analysis equating to 10 seconds or more of integration time, the effect of seeing for our application is as per long exposures.

The point spread function (PSF) is the mathematical representation of the final imperfect 2D Gaussian pattern on the CCD chip, which is affected by telescope optics, focus and optical aberrations. This is telescope specific and can vary across the field. The small field of view of the RINGO instruments', PSF variation across the field is of less concern. It is reasonable to assume that the PSF is only formed by the dominant effect of seeing.

**Reduction**

Standard photometric steps are undertaken with the RINGO instruments in order to perform accurate photometry. These processes are common to all CCD based measurements of flux, to create standardised and linear measurements.

- **Debiasing**

  Before an exposure, the CCD pixels are initiated with a level of charge prior to integration. This is a requirement of CCD technology to enable correct photon counting. This bias charge can vary from pixel to pixel. A median bias charge map is obtained by taking a large number of short unexposed frames where the instrument is shutter closed and there are no sources of illumination in the telescope dome. These frames are averaged and the bias map is then subtracted from the science frames.

□ **Dark subtraction**

During an exposure, charge can be created in a pixel, via the phenomena of thermally induced charge (or dark current). This effect can be characterised and subtracted by taking dark frames which are long exposures with no illumination on the CCD. These dark frames can have structure across the CCD if there are thermal gradients across the chip. In the RINGO instruments, the CCDs are cooled to -60 °C, and the short exposures limit the dark noise. Dark frames are obtained for the cameras by a method which is described in more detail in Section 4.2.1.

□ **Flatfielding**

This is performed to correct for any pixel to pixel sensitivity variations and to correct for any telescope induced inhomogeneity of sensitivity across the field, such as vignetting. In the case of RINGO3, which displays severe vignetting at the edges of the frame, flatfielding has the effect of raising the pixel values in the vignetted areas to correctly bring them into comparison with the centre of the field. However, this also increases both the Poisson error on the photons from the source and the associated errors within the background level.

Operating with short exposures and cooling the CCD to -60 °C, the dark noise also becomes negligible compared to the Poisson noise of the source and sky. For RINGO2+3, with the electron multiplying CCD technology, the read noise is made negligible by the cameras' electron multiplying gain registers, which occurs before readout. However, due to the physics of impact ionisation in the EM gain register, the final noise value is increased by a factor of $\sqrt{2}$. We can assume that the only sources of noise for RINGO2+3 are from the errors due to counting statistics multiplied by the EM gain error factor ($\sqrt{2}$).

$$S/N = \frac{Ne^{-}_{source}}{\sqrt{2} \times \sqrt{\sigma^2_{souce} + \sigma^2_{sky}}} \tag{4.1a}$$

$$= \frac{Ne^-_{source}}{\sqrt{2} \times \sqrt{N_{pix} \times (Ne^-_{source} + Ne^-_{sky})}} \tag{4.1b}$$

As shown in Equation 1.9, the sources of noise are all proportional to the root of the number of pixels ($\sqrt{N_{pix}}$) over which the photometric measurement is made. A good metric of the accuracy of a measurement is the signal to noise (S/N) ratio. Assuming our two sources of noise are $\sigma_{source}$ and $\sigma_{sky}$, the S/N ratio can be expressed as in Equation 4.1. It can easily be shown that $S/N \propto (N_{pix}^{-0.5})$. However, as $Ne^-_{source} = f(N_{pix})$, the counts from the source will increase as aperture size increases. For accurate photometry with minimal amounts of uncertainty, the aperture size and to some degree its shape, is of prime importance. For RINGO2 this was analysed and is presented in Section 4.4.1.

### 4.1.2 Calculation of polarisation for RINGO2/3

To extract a polarimetric measurement from RINGO2/3 data a number of steps are required. First the photometry is performed on all of the frames, from which a differential analysis is undertaken, to calculate the normalised Stokes parameters. Corrections then need to be made for both instrumental depolarisation and instrumental polarisation. Figure 4.1 shows the steps involved in this process.

#### Differential photometry

The calculation of polarisation from RINGO2 and RINGO3 relies on the method of differential photometry performed on 8 measurements, which are the 8 stacked images produced by an observation.

RINGO2 and RINGO3 use the same polarimetric principles as the original RINGO instrument. The original RINGO was developed based on a concept design by Clarke & Neumayer (2002). The 8 files produced by a RINGO2/3 observation correspond to 8 sections (bins) of the rotating polaroid, each separated by 45°(See Figure 1.16 on

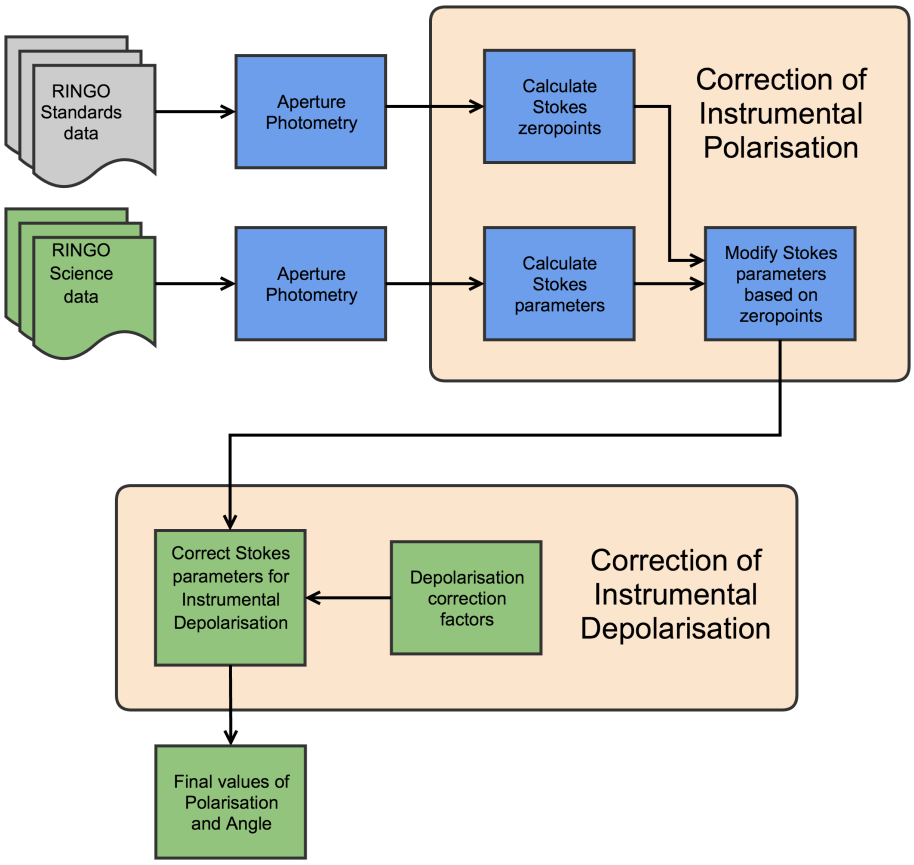


Figure 4.1: The reduction flow to obtain polarimetric measurements from RINGO2 and RINGO3 data after it has been obtained from the Liverpool Telescope data archive.

Page 45, Chapter 1). These are labelled A1, B1, C1, D1, A2, B2, C2 and D2. With the polaroid rotating through 360°, the bins of rotation separated by 180°represent an identical polaroid angle. So, for example, bin A1 is of the same orientation as bin A2.

Photometry is performed on each of the 8 files, and a value of captured counts is derived for a source (along with associated $1\sigma$ error) for each of the 8 bins. To calculate polarisation from these 8 measurements, the equations derived by Clarke & Neumayer (2002) are used. Firstly, 3 values are calculated as shown in Equation 4.2. S1 represents the integrated photometric counts of all 8 rotor positions in an observation. As a side note, this S1 value is utilised for RINGO2/3 photometric measurements from the data. S2 and S3 values are used with S1 to calculate the normalised Stokes parameters q and u, using Equation 4.3.

$$S1 = A1 + B1 + C1 + D1 + A2 + B2 + C2 + D2 \tag{4.2a}$$

$$S2 = A1 + B1 + A2 + B2 \tag{4.2b}$$

$$S3 = B1 + C1 + B2 + C2 \tag{4.2c}$$

$$q = \pi(\frac{1}{2} - \frac{S3}{S1}) \tag{4.3a}$$

$$u = \pi(\frac{S2}{S1} - \frac{1}{2}) \tag{4.3b}$$

**Effects of polarised backgrounds**

When making polarisation measurements, the background sky can show a significant degree of polarisation. The degree of background polarisation is high for observations taken close to 90°of the moon, especially during bright phases. This is due to

the background contribution from the moon being scattered into the line of sight by Rayleigh scattering in the atmosphere, and becoming polarised. This is not a problem for making polarised measurements, in that it does not require any correction above the normal data reduction methods.

In observations where a highly polarised background occurs the background level of each of the 8 observed frames will vary considerably. In normal photometric extraction of a point source, the counts obtained are background subtracted. By having a different background subtraction for each of the 8 frames the effect of a polarised background is removed from the final measurements. However, with sky noise being the dominant source of noise, the background level variation in each of the 8 frames will provide larger errors on photometry in certain rotor positions compared with their orthogonal counterparts. These variations in error between the 8 frames of an observation are then propagated through the equations and reflected in the errors of the normalised Stokes parameters. In short, observing against polarised backgrounds does not present any additional challenges for data reduction.

**Instrumental polarisation correction**

The above differential photometric calculations provide the measured Stokes parameters. However, these need to be corrected to account for the effects that the telescope mirrors and the instrument itself have on the polarimetric state of the beam within the telescope. Firstly the instrumental polarisation has to be considered.

Instrumental polarisation is caused within the telescope reflections and has the effect of polarising the beam. In RINGO2 and RINGO3, there is also the possible added effect of variation in rotator triggering, which would induce a modification to the measured polarisation. To characterise the total instrumental polarisation, known zero polarised stellar sources are observed.

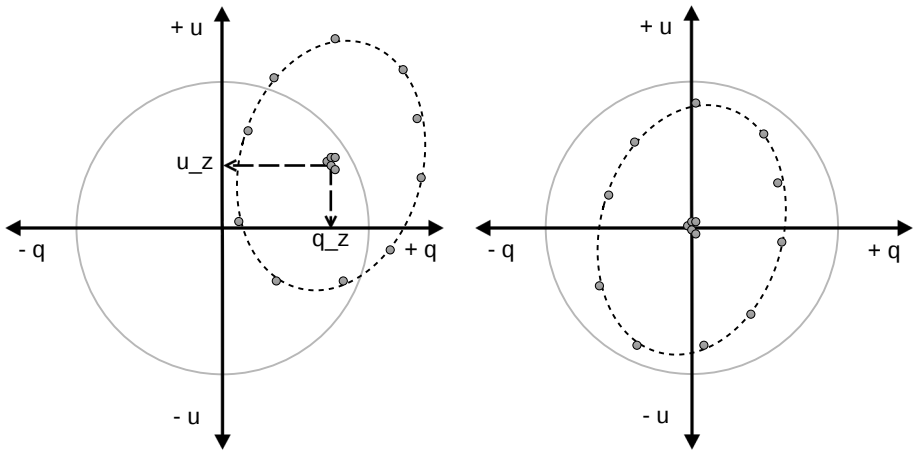


Figure 4.2: Visualisation of polarimetric data points in the q-u plane before and after correction for instrumental polarisation. The diagram on the left shows measurements of zero polarised stars (cluster of points at q_z, u_z), and a number of measurements of a polarised source at different sky angles (points on dotted ellipse). The correct q and u values for this polarised source would lie on the grey ring centred on the origin of the q-u plane. On the right the data are corrected for instrumental polarisation, but not for instrumental depolarisation, which could be a function of angle.

Figure 4.2 shows a set of simulated data points in the q-u plane from a number of measurements of an unpolarised source (cluster of points) and a polarised source taken at varying sky angles (points on dotted ellipse). The correction in the q-u plane is to define zeropoints for the normalised Stokes parameters as, $q_z$ and $u_z$. The zeropoints are then subtracted from the measured Stokes parameters, in order to correct for instrumental polarisation, producing the set of data points shown on the right of Figure 4.2.

### Instrumental depolarisation correction

Instrumental depolarisation is the effect of the optics of the telescope to scatter radiation into other orientations of oscillation. Given 100 % polarised incident radiation, a proportion of photons would have their orientation of oscillation changed by the telescope reflections. The proportion of the affected photons (and thus the depolarisation) is also a function of wavelength. Depolarisation can also be a function of the angle of polarisation of the incident polarised beam, with the telescope reflections not being

circularly symmetrical.

Depolarisation is characterised by observing known standard polarised sources at a variety of sky angles. This then allows corrections to be made. This is covered in greater detail in Chapter 5, where the modifications to the normalised Stokes parameters in order to correct for depolarisation are detailed.

**Polarisation calculation**

Values of polarisation and angle are calculated from the normalised Stokes parameters, which have already been modified for instrumental polarisation and depolarisation effects, using Equations 1.12 and 1.13 in Chapter 1.

**Errors on polarisation**

Errors on the normalised Stokes parameters are determined by propagating the errors on photometry for each bin through Equations 4.2 and 4.3. However to convert the errors on scalar values q and u to an error on the vector product p are not mathematically simple.

Figure 4.3 shows that when a polarisation distribution is created from the two normal distributions of the normalised Stokes parameters, it forms an asymmetric distribution, which can be approximated by a Rayleigh distribution. This is especially true of low value, high error polarisation measurements. To calculate the errors on the measured polarisation for Equation 1.12, we use a Monte Carlo method based on Simmons & Stewart (1985), which deals with polarisation errors in the low signal to noise regimes.

We define $p_{obs}$ as the observed polarisation calculated from $q_{obs}$ and $u_{obs}$. The error values on the normalised Stokes parameters are used to produce simulated q and u distributions ($q_{sim}$,$u_{sim}$) for all polarisations from 0 % to 50 % in steps of 0.001 %.

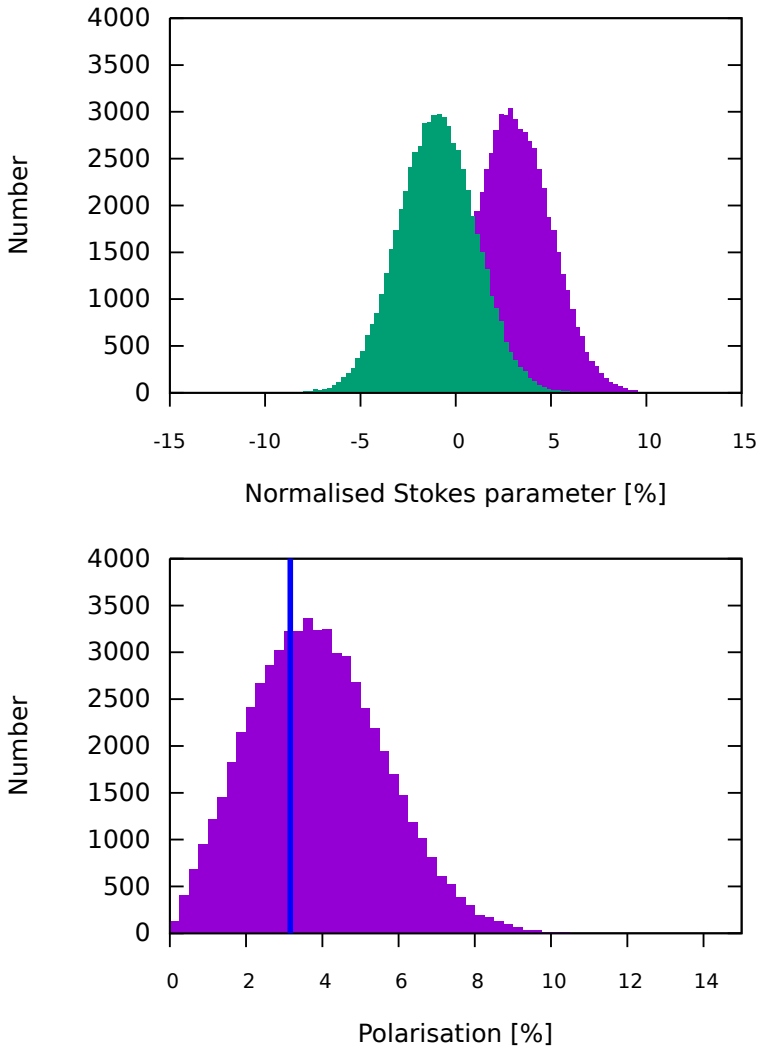


Figure 4.3: Top are the two simulated symmetric normal distributions which represent probability of the true values of q and u based on a single measurement. When these distributions are converted into polarisation, it produces the asymmetric distribution below. The peak of this distribution differs from the polarisation value calculated from the most likely q and u values (blue line). It is for this reason that polarisation measurements have asymmetric error bars. These are calculated using a Monte Carlo method. For this illustrative diagram, q and u values of 3 % and -1 % were chosen, both with $1\sigma$ error values of 2 %. The distributions each contain 60,000 points.

The polarisation distribution for each of these simulated polarisations ($p_{sim}$) is created. If the observed polarisation, $p_{obs}$ falls within the $1\sigma$ range of the simulated polarisation distribution, then $p_{sim}$ is taken as a 'valid' polarisation value. The upper and lower error values on $pobs$ are then taken as the highest and lowest values in the valid range of $p_{sim}$ values. The python code for this is provided in Listing A.3 in Appendix A.

## 4.2 Polarimetric observations with RINGO2/3

The workhorse instruments of the majority of optical telescopes are in the form of simple imagers and spectrographs. Polarimeters (or polarimetric features within the above) are infrequently used compared to workhorse instruments and can often be niche visiting instruments. The regular observing schedule for polarimeters follows that of imaging or spectroscopy, with science observations being regularly interspersed with observations of both zero polarised and polarised standards throughout the night.

The Liverpool Telescope (LT), with its robotic observing schedule and polarimeter permanently mounted, does not follow this usual method of observations. Standard stars are observed each clear night, usually performed early in the night after the telescope has finished performing flatfield observations. Users are able to schedule additional standard observations to be taken as part of their observing time, with observing constraints that force observations of the standards to be taken within the same observing block as the science observations. We believe, however, that this is an unnecessary overhead, and that use of the automatic standards is sufficient for most programmes.

The characterisation of RINGO2 and RINGO3 can be undertaken using the large datasets that are obtained by a permanently mounted polarimeter observing each clear night. These datasets allow a range of observing parameters (such as the effect of the moon) to be analysed for their effects on polarimetry, and also temporal analysis of stability of the polarimeter. A pipeline was created which was able to exploit this rich dataset for a number of scientific purposes, along with accurate calibration of the

RINGO polarimeters.

### 4.2.1 Onsite RINGO2 and RINGO3 data handling

RINGO data is analysed and pre-processed on site at the LT during the day after the observations are taken. It is then uploaded to the Liverpool telescope data archive ready for analysis.

The raw data of the previous night's observations exists on the acquisition computer in the state of individual FITS files (Flexible Image Transport System, ubiquitous in optical astronomy (Pence et al., 2010)). These files are for each exposure that the cameras take during an observation. For each observation, these frames are first de-biased and then stacked with files of the same rotor position to provide 8 FITS files. The stacking format is not a linear stack (where pixel counts in stacked frames are summed), but an average stack. At the stacking phase no shifting or aligning of the images is performed as the telescope tracking is sufficient.

The stacked images are then dark subtracted, using a catalogued dark frame. The flatfielding is then performed using a flatfield which is updated periodically (every few weeks) and after any instrument or telescope change (e.g re-aluminising of telescope mirrors, movement of instrument port, etc ...). Finally the world co-ordinate system (WCS) fitting using `WCStools` (Mink, 1999) is performed, which applies a WCS element to the FITS header.

#### Filename nomenclature

The final processed files have the following nomenclature;

[band]_e_[YYYYMMDD]_[run]_0_[rotator]_1.fits

where [band] specifies the observing band (or camera). For RINGO2, this was band p and RINGO3 uses bands d, e and f. [YYYYMMDD] is the date on the start of the night of observing and [run] is the incremental observation number for that evening. Finally [rotator] which takes the values 1→8 specifies the rotator orientation of the file in the observation, which comprises 8 FITS files.

## 4.3 ripe, an integrated photometric extractor

Should the data reduction pipeline created for the completion of this thesis require an acronym, it would be *Ringo Integrated Photometric Extractor* henceforth referred to as ripe. It was developed as a tool to provide large scale reduction and analysis of RINGO2/3 datasets and provide a framework with which to investigate polarimetric data reduction options and enable characterisation of the RINGO instruments.

### 4.3.1 Design

ripe was created on a simple premise, which is to extract all useful information from the FITS headers of the RINGO data and to perform photometry on every source in the field. It would then store this information in a format which would allow easy and quick analysis.

ripe comprises;

- cfitsio routines to extract FITS header details
- pyfits script to perform stacking of database
- pyephem script to reconstruct moon phase and position
- Source Extractor to perform photometric extraction
- A mysql database to store all extracted information
- /textttperl::DBI to interact with the mysql database

- A perl scripting language to co-ordinate all of these tasks

In addition there are various routines and scripts which provide the additional functionality. The two most notable being:

- `polcalc`
  A script which calculates the polarisation values of each source in the database. This can take many options and has various functionalities relating to configurations
- `standfind`
  This script identifies standards within the database to enable them to be pulled out for easy analysis.

**Choice of photometric extraction software**

The most important element for consideration for `ripe`, was which software to use for the photometric extraction. A number of routines exist, such as daophot (Stetson, 1987) in IRAF (Tody, 1986) or Source Extractor (`SExtractor`) developed by Bertin & Arnouts (1996). The latter was chosen, for my familiarity with the software, and thus ease of integration.

However, SExtractor's strengths are suitable for the application, namely that it is designed to identify and extract data on large numbers of sources from CCD images. Its easy configuration of output parameters is also very useful. The output files are easily parsable ASCII text files, which make it straightforward to integrate into a larger data reduction system.

**SExtractor**

`SExtractor` uses two configuration files, which in this application are `ripe.sex` and `ripe.param`. The first is the configuration file for the object iden-

tification and extraction. The important parameters for photometry in this file are: PHOT_APERTURES, which sets the circular photometric aperture size (diameter) in pixels; BACKPHOTO_TYPE, sets background measurement mode (set to LOCAL); BACKPHOTO_THICK, setting the size of the local background aperture; and GAIN, that needs to be set to obtain correct photometric errors on a measurement. An example of `ripe.sex` is provided in Listing A.6.

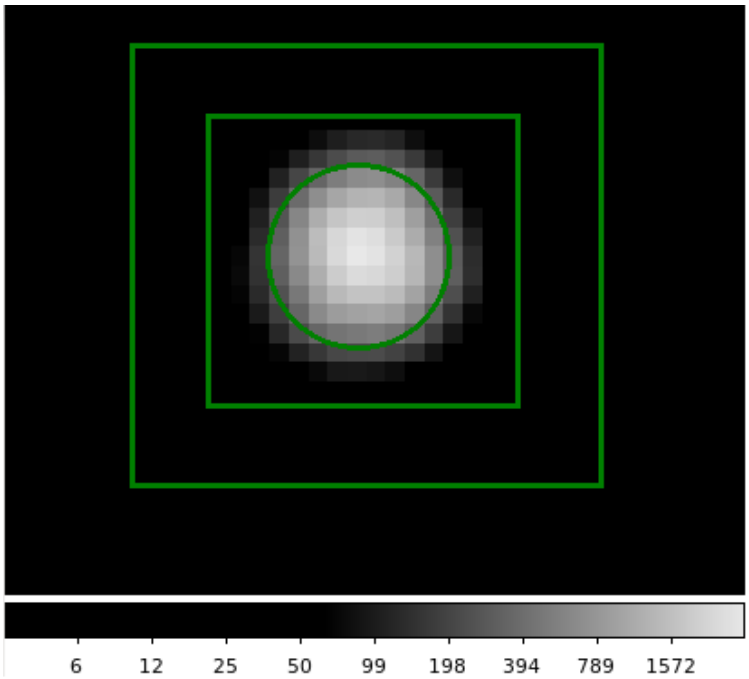


Figure 4.4: A typical stellar image from RINGO2, illustrating SExtractor apertures used for photometry. The intensity scaling of the image is logarithmic, and counts per pixel are shown underneath.

Photometry is performed using an aperture centred on the detected peak counts of a source, which can be of sub pixel accuracy due to centroiding algorithms reconstructing the peak location. Figure 4.4 shows a source from RINGO2 with an illustration of the apertures. `SExtractor` uses a circular aperture for the source photometry and then uses a square background aperture for the background. The reason for a square aperture on the background is a concession to the limits of pre-2000s comput-

ing power. Circular apertures require further statistical calculations to split counts from pixels crossed by the border of the circular annuli.

The ripe.param file specifies the output parameters of SExtractor. For our purposes the outputs are: X_IMAGE, Y_IMAGE which specify the centroid pixel of an extracted source; FLUX_APER, FLUXERR_APER the counts within the circular aperture and associated error; ALPHA_J2000, DELTA_J2000, the J2000 RA and Dec of the source in degrees; and FLAGS, which display any photometry errors.

### 4.3.2 Operation

The following quick walkthrough of ripe is intended to provide some information on the methods and considerations taken with the reduction of a large set of RINGO2/3 data. The flow diagram in Figure 4.1 illustrates the operations in ripe. The steps that are involved in each of the green sections (Initiation; Observational Data Acquisition; Photometry; and Parsing & Data Entry) in the figure are outlined below.

#### Initiation

- **Copying and parsing of configuration files**

  Upon initiation, ripe copies required configuration files into the current directory, namely ripe.param (which provides the source extractor output). It also reads the values of PHOT_APERTURES and BACKPHOTO_THICK from the ripe.sex configuration file, which are the sizes of the aperture and background subtraction region (in pixels).

- **Analysis and grouping of RINGO datasets**

  The list of files in the local directory, from where ripe was initiated, are loaded into an array and hashes are used to remove any duplicates. Using some string manipulations the list of files are grouped into datasets. Each dataset comprises 8 files, which corresponds to one observation. These are loaded into a 2D array,

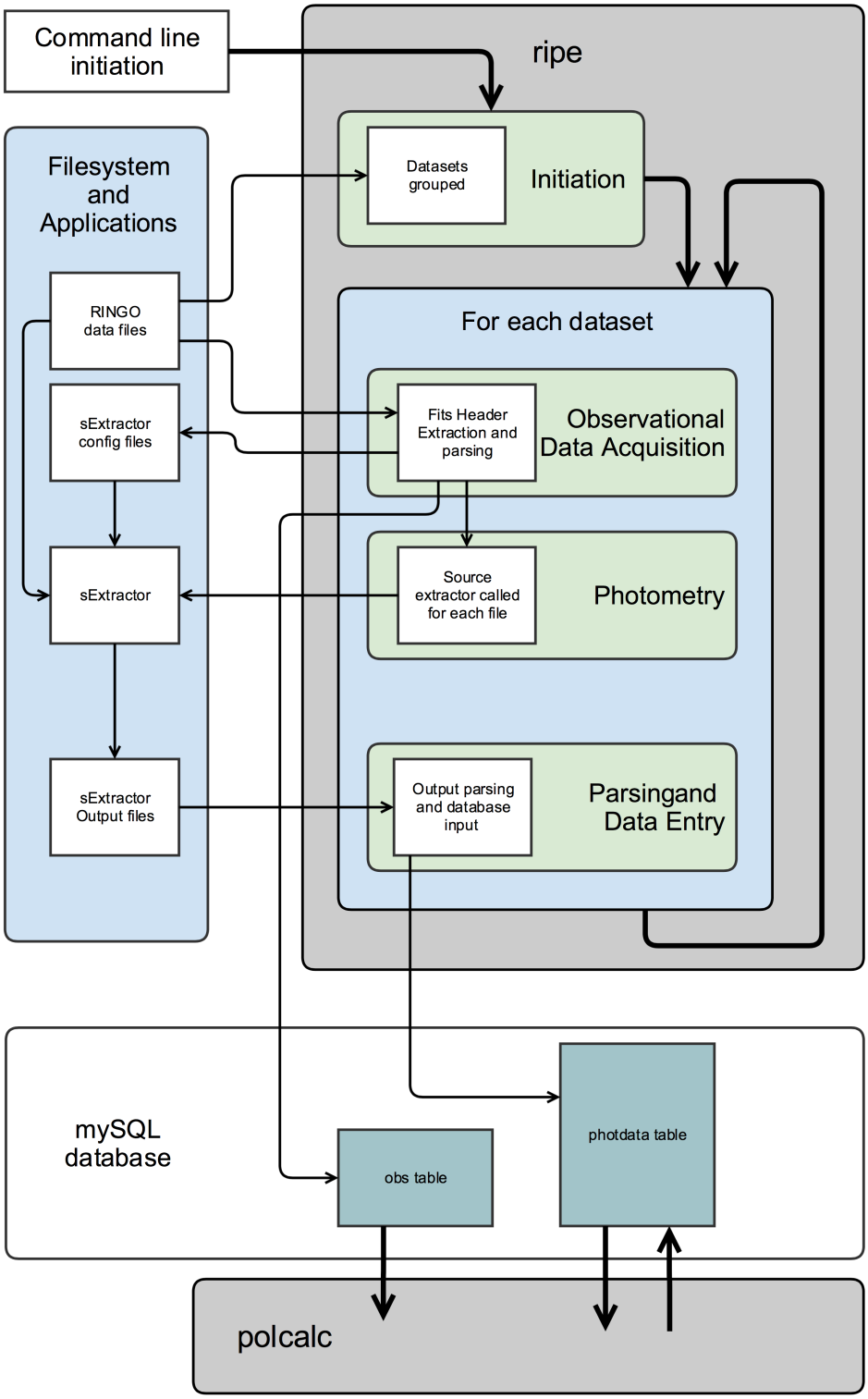


Figure 4.5: A simple flow diagram of the operation of ripe. Initial sorting and data extraction is performed by *ripe* which is a perl script incorporating a number of routines and calls to sExtractor and various python routines. See Listing A.1 on page 234. After extraction of the data has taken place by the fits files then polcalc takes information of the photometric values for each source and calculates the polarisation, applying corrections for instrumental polarisation and instrumental depolarisation. See Listing A.2 on page 241

each line having 8 elements which are the filenames of the RINGO2/3 observation. Any entries in the array which do not have 8 files are removed.

After the initiation, the following actions are performed for each dataset.

### Observational Data Acquisition

□ **FITS header extraction**

The FITS headers are crudely extracted using `modhead` and command line pipes to `sed`. An example of this is shown in the code segment below, which obtains the altitude of the observation.

```
1       $alt = `modhead $_[0] altitude | sed 's/[^0-9.]*//g'`;
        chomp $alt;
3       push (@return, $alt);
```

□ **Moon data reconstruction**

The position and phase of the moon is reconstructed using a python routine employing the `pyephem` package (Rhodes, 2011). The values of moon altitude, phase and angluar distance from the observation are taken.

□ **Observation database insertion**

The observational parameters that have been gleaned from the FITS headers, and other information are placed into the `obs` table of the mysql database. There is one entry for each observation. The table specifications are detailed in Listing A.4 and the parameters inserted are as follows;

*obs_id* - The observation name in the format [band]_e_[YYYYMMDD]_[run]

*camera* - The band name p, d, e or f

*tag* - The name of the data reduction run (multiple runs with different photometry settings can be included on the same observations)

*object* - Object name as per FITS header

*date* - [YYYMMDD] from the FITS header

*mjd* - Modified Julian Date

*wcs_ra* - RA of field centre

*wcs_dec* - Declination of field centre

*alt* - Altitude of observation

*az* - Azimuth of observation

*rotmount* - Cassegrain rotator value

*rotskypa* - Sky position angle

*ut_start* - Universal time at start of observation

*t_exp* - Exposure time of each of the 8 orientations

*t_dur* - Total duration of observation

*moon_alt* - Moon altitude

*moon_dist* - Angular moon distance from observation

*moon_frac* - Moon phase (0→1)

*numfrms* - Number of frames in stacks (i.e. number of rotations of polaroid)

*gain* - Gain value from FITS header (unused due to `setgain()`)

*apsize* - Photometric aperture size (pixels)

*backsize* - Background annulus size (pixels)

**Photometry**

□ **Creation of detection frame**

The 8 frames of the observation are stacked using python and the `pyfits` package (Barrett et al., 2012). This creates a stacked image which is used for the object detection by `SExtractor`.

□ **Setting gain value**

Due to the average stacking method of the pre-process pipeline this gain value is 0.36 multiplied by the number of frames stacked. The NUMFRMS value from the FITS headers is used and the gain is then set using the `setgain()` routine listed below, which writes the gain value into `ripe.sex` configuration file.

```
sub setgain {
  #takes a file and looks at the number of frames, then sets the gain value
 in source extractor
  $numfrms = `listhead $_[0] | grep NUMF | sed 's/[^0-9]*//g'`;
  $gain = $numfrms * 0.36;
  $shell = `cat $ripedir/config/sex/ripe.sex > $ripedir/config/sex/ripeold.
sex`;
  $shell = `cat $ripedir/config/sex/ripeold.sex | sed '/GAIN/d' > $ripedir/
config/sex/ripe.sex`;
  $shell = `echo 'GAIN              $gain' >> $ripedir/config/sex/ripe.sex`;
}

```

□ **Photometric execution**

`SExtractor` is called for each file in the dataset, with the stacked detection frame specified. It outputs the results of the photometry into 8 tab delimited text files. As the same detection frame was used for each run the output files contain the same number of sources and the same order of sources.

### Parsing and Data Entry

□ **Parsing** The data in SExtractor's 8 output files are parsed simultaneously, line by line. The xpix, ypix, ra, dec, counts and error are inserted into the `photdata` table of the mysql database. The specifications of the `photdata` table are shown in Listing A.5, where the fields that are entered are easily identifiable.

### 4.3.3 Identification of standards

With the photdata table populated, standards are identified with standfind. The database contains the standards table, which lists the RA and dec of all the standards observed with the RINGOstand programme. To identify standards each entry in the obs table is processed. If the *object* field of the observation matches that of one of the standards in the database then standard identification is performed. The *id*, *ra* and *decn* values of each source for the observation are retrieved from the photdata table. The angular difference in co-ordinates is calculated for each source. The source with the lowest angular difference (the 'nearest neighbour') is identified as the standard. The entry for this object in the photdata is then modified with the field *target* being updated to either 'P' for polarised standards, or 'U' for zero polarised standards. The angular distance between the identified standard and catalogue co-ordinates is inserted into the *target_dist* field in the units of integer arcseconds.

### 4.3.4 Polarisation calculation with polcalc

With the photdata table populated and standards identified, polarisation calculations and corrections can be applied. polcalc is a flexible routine that calculates the normalised Stokes parameters, applies polarisation corrections and calculates errors. It can be run in a number of different modes. It is supplied with the Stokes parameter zeropoints of each camera (p, d, e and f) and also elements relating to the depolarisation factor. The depolarisation factor correction is presented and described fully in Chapter 5.

#### Modes of operation

The modes of operation relate to two simple switches in the code. Firstly the choice of calculating polarisations and associated errors for all objects in the database, or just for the identified standards (which can also include GRB sources). The second switch is of more importance, dictating the three methods for instrumental polarisation

correction: Calibration = 0, applies no correction; Calibration = 1, applies user defined Stokes zeropoints; and Calibration = 2, applies Stokes zeropoints which are calculated from zero polarised standards observed within a few days of the measurement being corrected.

The Calibration = 2 mode, uses a function `get_zeropoints()` which is shown in Listing A.7 in Appendix A. This function searches the database for identified zero polarised sources, taken with the same band (p, d, e or f) measured within a specified number of days of the observation which is being corrected. If the number of identified sources is less than 3, then it will expand the search criteria by a day, until at least 3 sources are found. The average values of rotator bin counts divided by total counts (e.g. A1/S1, B1/S1, .... C2/S1, D2/S1) are obtained for these sources and Stokes zeropoints calculated from these values. The standard deviation of the 8 values are also taken and propagated to provide an error on the Stokes zeropoints.

## 4.4 Initial investigations with `ripe`

To be sure of obtaining the best polarimetric measurements from `ripe`, the parameters for photometry need to be optimal. The aperture size, as previously mentioned, will have an effect on the signal to noise ratio. The size of photometric apertures are of prime importance. With the reduction system created, a number of aperture sizes were tested.

By analysing the full dataset of RINGO2 standards with the optimal photometry settings, it was possible to perform an investigation into the accuracy of repeated polarimetric measurements made by RINGO2, which is presented later in the section. This was performed in November 2012, before RINGO3 was commissioned.

### 4.4.1 Aperture size investigation

When this investigation was undertaken, the error values from ripe were not fully understood and the setgain() function was yet to be implemented. To investigate the optimal aperture size for high S/N ratios with RINGO2 the best approach was to exploit the ripe pipeline to look at the variations in polarimetric values obtained from repeated measurements of sources in the same field. This approach also has the benefit of obtaining an optimal aperture size across a range of observing conditions.

It is assumed that sources across the field of a single observation all have the same full width half maximum (FWHM). For a common value of seeing (say 1.2 arsecs), the FWHM could be expected to be around 6 pixels with the RINGO2 pixel scale $\sim$0.5 arcsec / pixel. When performing photometry, a rule of thumb to obtain a good S/N ratio for a source is to have an aperture size twice that of the FWHM. This would suggest that an aperture of 12 pixels diameter could provide good results. However with faint sources the benefit of extra counts from the source in a larger aperture is negated by the increased noise values of said larger aperture.

#### Data and Reduction

The standard field chosen from the RINGOstand archive of standards was that of HD212311, as this is a 'busy' field offering many sources of varying magnitudes. The LT observed this field 60 times from 01 April 2011 to 19 September 2012. The data were reduced using ripe in a number of runs where the photometric aperture diameters were modified from 4 to 20 pixels in 2 pixel steps. The data was corrected for instrumental polarisation only, using the average values of the Stokes parameters for HD212311 as the zeropoints.

### Selected Sources

72 sources were extracted from the field of observation p_e_20110806_8 and ranked in order of S1 (flux counts from all orientations of the polaroid). Of these sources, 10 were chosen for the analysis, based on position in the field (sources further from the edge are likely to be detected in more observations) and to provide a range of observed magnitudes. These are shown in Table 4.1, where star 1 is HD212311.

| Source number | Number of detections | RA | Dec | S1 | Instrumental magnitude | Approximate apparent magnitude |
|---|---|---|---|---|---|---|
| 1 | 58 | 335.4943 | 56.5314 | 1373599 | -15.3 | 8.1 |
| 3 | 57 | 335.5320 | 56.5276 | 70425 | -12.1 | 11.3 |
| 9 | 53 | 335.4874 | 56.5377 | 6962 | -9.6 | 13.9 |
| 11 | 58 | 335.4619 | 56.5354 | 3922 | -9.0 | 14.5 |
| 17 | 56 | 335.4869 | 56.5469 | 2049 | -8.3 | 15.2 |
| 23 | 53 | 335.4777 | 56.5401 | 1191 | -7.7 | 15.8 |
| 33 | 49 | 335.4562 | 56.5445 | 933 | -7.4 | 16.0 |
| 48 | 42 | 335.5292 | 56.5240 | 603 | -7.0 | 16.5 |
| 65 | 28 | 335.4901 | 56.5202 | 420 | -6.6 | 16.9 |
| 71 | 12 | 335.5174 | 56.5448 | 310 | -6.2 | 17.2 |

Table 4.1: Stars selected for analysis of the effect of aperture size on photometry. RA and Dec are in the units of degrees, as per the output of SExtractor and the subsequent storage in the photdata table. All values of S1 were taken with an aperture size of 8 pixels. The Approximate Apparent Magnitude was calculated in relation to the flux obtained for HD212311 (ID 1), which has a catalogued V band magnitude of 8.12

### Analysis

It cannot be assumed that each source in the field is of low polarisation (which we define as $\lesssim$0.5 %). However with repeated measurements it is only the variance in polarisation measurements as a function of photometric aperture size that we are interested in. For each source the standard deviation of the polarisation measurement

as a function of aperture size was obtained. The results are shown in Figure 4.6.

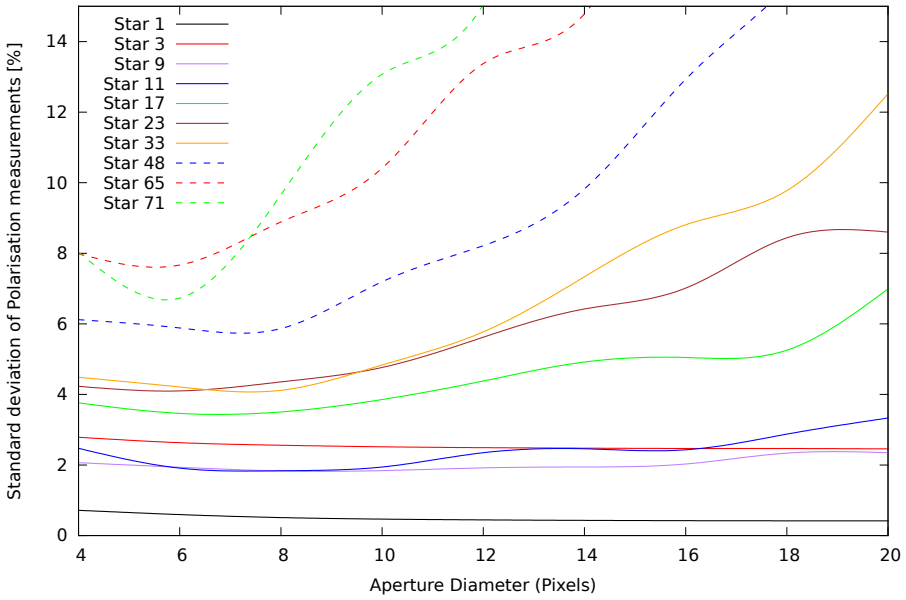


Figure 4.6: Standard deviation of polarisation values for the 10 sources selected from the field of HD212311 plotted against the photometric aperture size in pixels.

The distribution of polarisation measurements for each source is an asymmetrical distribution (similar to that illustrated in Figure 4.3) based on the true polarisation of the source, which could vary amongst the 10 sources. The standard deviation of polarisation provides an adequate if not perfect metric for the analysis. It can be clearly seen that the aperture size has a considerable effect on the measurements of sources fainter than $\sim$15th magnitude (Star 17), and that at this level of observed flux the noise floor of RINGO2 data has a considerable effect on signal to noise ratio.

The optimal pixel size for the faintest source (Star 71, $\sim$17.2 magnitude) appears to be 6 pixels. However, due to the faintness of the source it is only has a low number of detections (12) in the dataset. The oscillations in the upward curve could be due to sampling complex PSF structures, but is most likely due to stochastic counting errors on standard deviation of the small number of measurements.

For this reason, the optimal aperture size was chosen to be 8 pixels. This represents the minima of standard deviation for both Star 11 and 48. Smaller aperture sizes do have an adverse effect on the signal to noise ratio of brighter sources which is shown in Figure 4.7 with the brightest source HD212311. The aperture size of 8 pixels is not optimal for this source and a pixel size of 12 pixels would be slightly better when analysing bright standards.

However, it can be clearly seen that the curve of standard deviation approximates an exponential decay, which can be assumed not to fall below 0.4. Taking into consideration the effects of the Rayleigh distribution of polarisation measurements (i.e. the most likely measurement for a zero polarised source with near infinite signal to noise ratio, will always be non zero) a standard deviation of 0.4 % seems to relate to a limiting factor of the RINGO2 instrument's accuracy in polarimetric measurements. To investigate this further, the photometric errors need to be compared with the variations in repeated measurements.

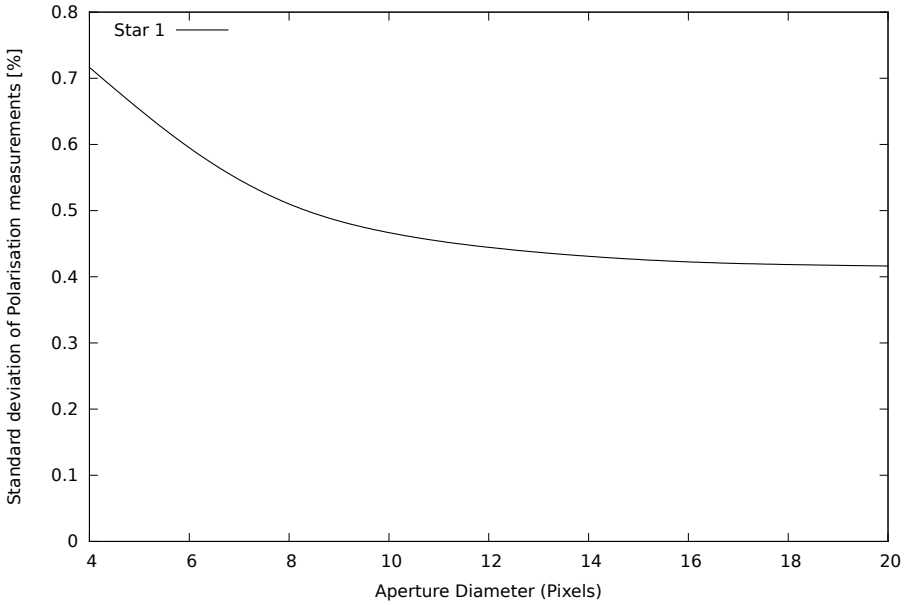


Figure 4.7: Standard deviation of polarisation values for HD212311 plotted against the photometric aperture size in pixels.

### 4.4.2 Errors and variations in repeated measurements

An investigation into the variation on repeated measurements was undertaken, comparing these variations to the photometric error on measurements. To perform this, all of the sources in the zero polarised standard fields were used, based on the reasonable assumption that the vast majority of these sources are all of low polarisation as confirmed by the measurements of 551 sources in the Galactic plane by Hall & Mikesell (1950). The metric for investigation was chosen to be Stokes parameter q, which allows a normal distribution of measurements as opposed to the Rayleigh distribution of polarisation.

#### Method

The q values and $1\sigma$ photometric errors of all the sources in the zero polarised fields were obtained and ordered by the value S1 (the total counts received). The sources were binned with a binsize of 500 sources, and a $1\sigma$ deviation of the q values was calculated as well as the average value of S1 within the bin. The $1\sigma$ deviation of the bins and the individual $1\sigma$ photometric errors were plotted against the average S1 of the bin and S1 respectively. This is shown in Figure 4.8.

#### Analysis

Looking firstly at the $1\sigma$ photometric error on q, it provides a graphic illustration of the photon counting errors and their effect on the Stokes parameters. The $1\sigma$ variation in the binned q values are at least 2.5 times above the expected values from this photometric noise floor. There are a number of possible factors which will contribute to this. Firstly, all bins except the one with highest S1 values (comprising, almost exclusively, the zero polarised sources) are affected by the possible non zero polarisations of the sources being observed. As we move to bins with fainter sources, it can be expected that the average distance to the sources increases, providing a higher likelihood of intervening Galactic dichroic dust providing higher polarisations, and standard

deviations of polarisations within the bin.

However, despite these factors, it seems that there are sources of variance in polarimetric measurements which contribute, systematically or otherwise, to a less than expected accuracy of measurements. These could be observational factors (e.g. airmass, effect of the moon), issues with the polarimetric variance across the imaging field or other yet to be identified issues.

## 4.5 Conclusions

RINGO2+3 are specialised polarimeters for high cadence polarimetric measurements of highly variable sources. Their prime science goals, design and operation vary compared to the majority of other polarimeters. With the Liverpool Telescope providing robotic observation with an extensive, permanently mounted instrument suite, polarimetric observations of standard sources can be measured each night.

The large datasets produced through these measurements are invaluable for characterisation of the RINGO2+3 instruments, and provide opportunities to perform investigations into the effect of many observational factors on polarimetry. To exploit these datasets the `ripe` pipeline was designed to reduce large sets of data and to enable easy analysis of the data using Source Extractor and a mysql database system.

The first tests of the `ripe` pipeline used RINGO2 data taken of standard fields. The data produced was used to investigate the most important photometry settings and look at the signal to noise ratio of polarimetric measurements. It was found that the variations in repeated measurements are much higher than can be accounted for by photometric error alone. Despite a contribution of this variance being due to the experimental method (viewing a large number of sources of unknown polarisation), it is evident that there are other effects which are reducing the accuracy and repeatability

of RINGO2 measurements. Further investigations should be undertaken to see if these effects are systematic and can be corrected for, or non-systematic and can be reduced.

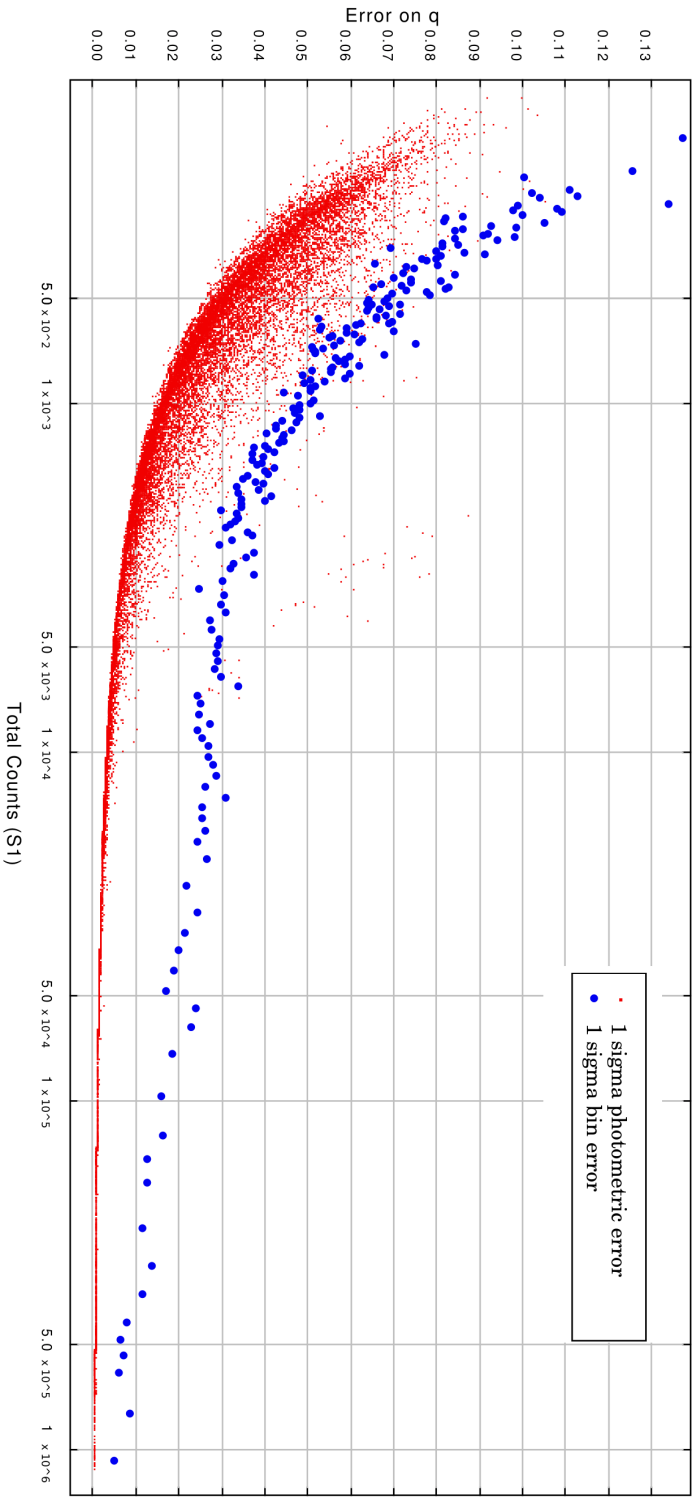


Figure 4.8: Plot of the variation in q value, in bins of 500 observations, and photometric error of q from those observations, as a function of the total counts received (S1).

# Chapter 5

# RINGO2/3 intrumental characterisation

## 5.1 Instrumental characterisation

In science the greatest challenge is not to take measurements, but to calibrate them and derive the correct statistical confidence in the results obtained. To have confidence in the measured values, a full understanding of the measurement process and any intrinsic biases it contains is essential. For Astronomy, investigation of the measurement process can be taken from a number of approaches. For example, a purely theoretical and analytical process is required at the planning stage of observations and often when investigating the performance of an instrument yet to be produced.

A specific example of a theoretical approach to polarimeter characterisation is the work performed by de Juan Ovelar et al. (2012). Here the instrumental polarisations were analysed for a potential EPOL, exoplanet polarimeter (Keller et al., 2010) on the E-ELT. Using the M&m's code (de Juan Ovelar et al., 2011), they simulate instrumental polarisations for a polarimeter mounted at the Nasmyth focus on the E-ELT. This approach was necessary to look at the viability of high contrast polarimetry measurements of proto-planetary discs with the E-ELT, a telescope that is yet to be built.

With the robotic operation of the Liverpool Telescope (LT) and its development rationale (described in Chapter 2), we take a completely different approach, which can be described as highly empirical. Mathematical models of the polarisation effects of each of the optical elements in a polarimetric system (which we define as the LT and RINGO2/3) could aid with development and troubleshooting. However, no simulation can match the accuracy, scope and usefulness of on-sky data taken by the full 'black box' polarimetric system.

For RINGO2+3, characterisation is the method of identifying, quantifying and where possible, correcting any effects that provide uncertainty in the measured values we obtain. The permanent mounting of RINGO2/3 enables observations of polarimetric standards to be performed each night (weather permitting), providing a large dataset from which an empirical approach to instrumental characterisation can be performed.

### 5.1.1 Observational data for characterisation

The data used in this Chapter for characterisation purposes comes from observations of two types of source. The zenith sky at sunset was used to provide bespoke 'polarisation flatfield' observations taken manually on site at the LT. The other type of source is the more conventional stellar form of catalogued polarimetric standard stars (both polarised and unpolarised).

#### Instrumental epochs

For clarity, it is worth defining instrumental epochs for both RINGO2 and RINGO3. These define changes that were made to the instrument or telescope that could affect the instrumental characteristics. These would include a change in the instrument port during recommissioning after an instrument suite change, or any change in the instrument optics. The changing of the polaroid orientation within the instrument is a common cause for a change in epoch. This occurs in situations where the field lens

has been changed or the rotator mechanism has undergone servicing. With the polaroid in a different orientation to the triggers, the previous Stokes zeropoints need to be re-established.

| Epoch | From | Until | Notes |
|---|---|---|---|
| R2_1 | 2010-08-02 | 2010-11-10 | Initial setup |
| R2_2 | 2010-11-10 | 2011-02-15 | New field lens fitted to reduce vignetting. Polariser angle change |
| R2_3 | 2011-03-20 | 2012-04-28 | Refitting of drive belt for rotation mechanism. Polariser angle change |
| R2_4 | 2012-04-28 | 2012-11-20 | Cassegrain mount position change |
| R3_1 | 2012-11-28 | 2013-01-23 | Initial setup |
| R3_2 | 2013-01-23 | 2013-12-12 | New field lens and polariser angle change |
| R3_3 | 2013-12-12 | 2014-06-08 | Depolariser installed after rotation mechanism and collimation lens. Polariser angle change |
| R3_4 | 2014-06-08 | 2015-06-29 | Depolariser moved to collimated beam. Polariser angle change |

Table 5.1: Instrumental epochs of RINGO2 and RINGO3. Due to the polariser being the first optical element that the telescope beam reaches, any optical changes between this and the collimator lens result in its removal and a change in angle with relation to the rotator trigger sensors.

Table 5.1 shows the instrumental epochs with details of the changes made. The polarising filter is the first optical element that the telescope beam reaches. Any changes between this and the collimator lens require its removal. Upon being replaced, the orientation of the polariser is not maintained in relation to the rotator trigger sensors. This means that the values of instrumental polarisation will change and the measured polarisation angle will be shifted in relation to the sky polarisation angle.

### Polarimetric standards

The prime requirement of standard stars is that they are temporally stable sources, enabling them to be used for calibration at any epoch of observation. For photometric standards, the stars need to be of a magnitude range suitable to provide a high signal to noise, without saturation, for large scientific telescopes (V=11.5→16.0 for example in Landolt (1992)). Also a catalogue will provide a number of different spectral types in the sample, and be of declinations which are observable from the majority of observatories (i.e. close to the celestial equator). In addition to these requirements, polarimetric standards require a stability in the magnitude and direction of their polarisation. They appear in two types: zero polarised standards and polarised standards.

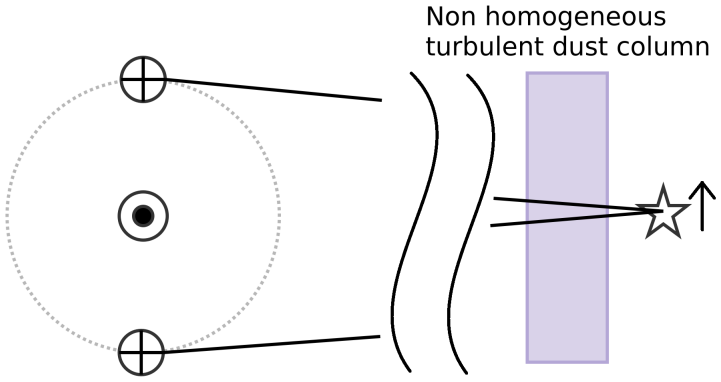


Figure 5.1: Polarimetric standards are observed through an intervening column of dichroic dust which partially linearly polarises the radiation. Standard stars are often bright, nearby stars with a measurable parallax and significant proper motion. Both these effects could play a part in standards having unwanted temporal variance.

The emission from polarised standard stars is essentially unpolarised, and polarisation of the radiation occurs due to scattering by intervening dichroic dust between the source and observer, as described in Chapter 1. Figure 5.1 shows how polarimetric stability is incompatible with the requirements of bright sources allowing high signal to noise ratios. These are often nearby stellar sources with parallax and proper mo-

tion affecting the column of dust through which they are observed. The catalogues of polarised standards for observation in the Northern Hemisphere are limited. We use standard information from Turnshek et al. (1990), Schmidt et al. (1992) and Soam et al. (2014), which provides 7 polarised sources, 5 of which have not been catalogued for over 20 years.

The zero polarised sources that are included in the catalogues have low observed polarisations ($<$0.1 % across BVRI wavebands). This is due to three features: having a symmetric non-deformed photosphere, the absence of intervening circumstellar material (which absorbs or scatters the radiation) and intervening dichroic dust. These temporally reliable sources are more than sufficient for our requirements.

**RINGOstand**

RINGOstand is a robotic observation programme on the Liverpool Telescope (LT) which until March 2015 was performed each night. It has now been modified to be performed only once every 5 nights. This change was based on the data reduction in this chapter showing adequate instrument stability. Furthermore this arbitrary gap in observations frees up telescope time for other programmes.

RINGOstand observations are generally all performed with the Cassegrain rotator set to zero. Users are also instructed to take their observations at the same angle of Cassegrain rotator, rotmount=0. This is to reduce a further variable in the telescope and instrument setup, which could affect the characterisation. With a number of measurements for RINGO3, however, RINGOstand observed rotmounts of -60 °, 0 °and +60 °, chosen to provide 3 equally spaced angles for linear polarisation.

The standards observed are listed in Tables 5.2 and 5.3. The low number (and aforementioned stability) of the polarised standards are of concern for accurate calibration of RINGO2+3. Also the polarised standards do not provide a source above 9 % linear polarisation. With the prime science goal of measuring early time GRB afterglows,

| Star | RA (J2000) | Dec (J2000) |
|---|---|---|
| HD14069 | 02:16:45.21 | +07:41:10.8 |
| G191B2B | 05:05:30.61 | +52:49:51.9 |
| HD109055 | 12:31:41.20 | +22:07:24.4 |
| BD+33°2642 | 15:51:59.86 | +32:56:54.8 |
| BD+28°4211 | 21:51:10.98 | +28:51:49.6 |
| BD+32°3739 | 20:12:02.15 | +32:47:43.7 |
| HD212311 | 22:21:58.59 | +56:31:52.7 |

Table 5.2: Zero polarised standards observed by RINGOstand for RINGO2 and RINGO3

| Star | RA (J2000) | Dec (J2000) | $P_B$ (%) | $P_V$ (%) | $P_R$ (%) | $P_I$ (%) |
|---|---|---|---|---|---|---|
| BD+64°106 | 00:57:36.70 | +64:51:26.5 | 5.51 ± .09 | 5.68 ± .04 | 5.15 ± .10 | 4.70 ± .05 |
| BD+59°389 | 02:02:42.09 | +60:15:26.4 | 6.35 ± .04 | 6.70 ± .02 | 6.43 ± .02 | 5.80 ± .02 |
| BD+25°727 | 04:44:24.90 | +25:31:42.7 | | 4.27 ± .01 | | |
| HD155528 | 17:12:19.95 | -04:24:08.8 | 4.61 ± .04 | 4.99 ± .06 | | |
| HILT 960 | 20:23:28.53 | +39:20:59.1 | 5.72 ± .06 | 5.66 ± .02 | 5.21 ± .03 | 4.46 ± .03 |
| VICyg #12 | 20:32:41.10 | +41:14:28.0 | | 8.95 ± .09 | 7.89 ± .04 | |

Table 5.3: Polarised standards observed by RINGOstand for RINGO2 and RINGO3. All data is from Schmidt et al. (1992) except for BD+25°727 which is from Turnshek et al. (1990). Full sets of polarisation values in BVRI bands are only available for sources included in the catalogue of Schmidt et al. (1992), which also lists HD155528 and VICyg #12 as 'additional commonly used polarised stars referenced to the HST system'.

which could be highly polarised (up to 70 %), this means that we have no comparable calibration sources for higher possible polarisations.

### The datasets

For the analysis of standard sources in this chapter we use data from only a few instrumental epochs. We use all epochs for RINGO2, whereas for RINGO3 only the R3_4 epoch is used. This epoch represents data taken after the issues with the dichroic mirrors were finally resolved by the fitting of the depolariser, as detailed in Chapter 3.

All data was reduced using the `ripe` pipeline, with a photometric aperture size of 12 pixels. Calculations of polarisation using `polcalc` were performed with the Calibration = 2 mode, which uses the `get_zeropoints()` function to obtain Stokes

zeropoints corrections (detailed in Chapter 4).

| Instrumental epoch | MJD range | Observations | Objects extracted |
|---|---|---|---|
| R2_2 | 55,420→55,600 | 386 | 7,247 |
| R2_3 | 55,645→56,016 | 1,365 | 28,523 |
| R2_4 | 56,077→56,119 | 108 | 3,592 |
| R3_4 | 56,809→57,082 | 11,916 | 289,639 |

Table 5.4: Details of sources extracted from RINGOstand observations

Details of the number of observations taken and the number of sources extracted are provided in Table 5.4. Sources were identified in these fields. For RINGO2 data 1659/1808 (91 %) of the standards sources listed in Tables 5.2 and 5.3 were identified, and for RINGO3 data 11347/11597 (98 %).

Failures in identification of a standard are normally due to a poor WCS fit. `standfind` will only identify a standard if the nearest neighbour method gives a source within 15 arcsecs of the most recent catalogued position taken from SIMBAD (Wenger et al., 2000).

### 5.1.2 Presentation of this chapter

With overlapping observations and techniques, it is prudent to detail the presentation of the rest of this chapter. Firstly investigations on polarimetric measurements and methods of characterisation taken with RINGO2 data are presented in Section 5.2 - RINGO2 investigations. These principles are applied and extended with RINGO3 data and observations in Section 5.3 - RINGO3 investigations. A definitive analysis of the instrumental characteristics of RINGO2+3 is provided in Section 5.4.

## 5.2 RINGO2 investigations

In Chapter 4, repeated measurements of HD212311 were analysed to find the optimal aperture size for polarimetric reduction of RINGO2. It was found that the standard deviation of the normalised Stokes parameters of these measurements would never be lower than 0.4 %. However this is four times larger than the expected error of 0.1 %, which assumes photometric noise is the dominant source of uncertainty. This implies that there are other unknown sources of noise adding variance to RINGO2 measurements. Possible factors are systematic issues relating to observational parameters or non-systematic issues relating to the instrument. Systematic errors can be corrected for, non-systematic errors cannot.

### 5.2.1 Polarisation flatfield

With polarised standard stars exhibiting observed polarisations of less than $\sim 9\,\%$, another source of higher polarisation was sought, which could test the LT and RINGO2 with the higher levels of polarisation which may be expected from a gamma-ray burst (GRB) afterglow. Harrington et al. (2011) provided information of obtaining a source which exhibits these high polarisations by observing the zenith sky during sunset. Employed as a high polarisation, high signal to noise source, the zenith sky enabled the derivation of the Mueller matrices of the Haleakala 3.7m AEOS telescope using a polarimeter at the Coudé focus.

The zenith sky at sunset will provide a source of polarisation of $\sim$85 % (at RINGO2 operating wavelengths), owing to the effect of Rayleigh scattering in the atmosphere (Coulson, 1980). However, the degree of polarisation from Rayleigh scattering is affected by the local site of observation, the turbidity of the atmospheric layers and also the quantity of aerosols in the atmosphere (Thomas & Holland, 1977), meaning that the actual value will vary with observation site and the evening of observation. The polarisation is also rapidly changing as the scattering angle at the zenith varies with

the altitude of the Sun.

However the great advantage of measurements of the zenith sky at sunset is that they provide a constant extended polarised source across the field of RINGO2. This constant source allows us to analyse the instrumental field flatness to polarisation. We can use this to characterise the effects of lack of reflectional symmetry in the telescope due to off axis sources which could cause varying polarisation measurements across the field. The RINGOstand programme always centres the sources on the centre of the field with good pointing accuracy, so analysis of polarimetric standard data could not provide cross field coverage for comparison.

**Observations and Reduction**

Observations of the zenith sky were taken with RINGO2 on 19th September 2012 as the Sun was setting. The telescope was in its parked position, pointing directly at the zenith. The zenith sky is a constantly changing source and was observed for about half an hour either side of sunset. It was found that with the primary mirror cover closed on the LT, observations yielded $\sim$1/8th of the counts of observations taken with the mirror cover open. This is due to reflected light entering the acquisition and guidance (A&G) unit through the exposed baffle which protrudes from the primary mirror cover. The sources of scattered light are as follows: from the telescope struts illuminated by near daytime brightness levels; radiation from a large portion of sky; and reflected light from the black mirror cover being reflected by the secondary mirror.

With the mirror cover open for a focused observation of $4 \times 4'$ area of the sky, the above reflections (bar the reflections from the secondary mirror cover) will affect the polarisation measurements. We therefore took a series of exposures as the Sun was setting, alternating between mirror cover open and closed. This enabled a subtraction of the unwanted illumination in the mirror cover open observations.

The data was subject to the usual bias / dark subtraction and flatfielding undertaken by the onsite pipeline. To reduce the data, the exposures either side of the science exposure (mirror cover open) were averaged. The resultant frame was then subtracted from the science observation of the zenith sky. The corrected science frame was then analysed using `ripe`, with `imstat` in the place of `sExtractor`.

A 6 pixel region around the science frame was ignored, to provide a $500 \times 500$ pixel field. `imstat` was then called for each $10 \times 10$ pixel region in the field, providing a $40 \times 40$ grid of polarisation bins representing the zenith sky. The size of pixels was chosen to represent a comparable size to the photometric aperture size of 12 pixels diameter used in measurements of standards. It is worth noting that the high level of counts and uniform nature of this source mean that photometric errors (i.e. the standard deviation) in the $10 \times 10$ pixel bins are negligible and therefore ignored. The results of the highest polarisation observation are shown in Figure 5.2.

**Analysis**

These flatfield polarisation measurements show that the field varies by less than 1.5 % in a $\sim$85 % linearly polarised source. It is in the form of an approximate linear gradient from the bottom right to the top left. This check of the full field shows that variations in measurements of polarisation across the field for sources with up to 30 % polarisation will be less than 0.6 %

These measurements show that the polarimetric variation across the field of RINGO2 is well within the required tolerance and cannot account for the variation in measurements seen in Chapter 4. It would be possible to correct for the variance in polarisation. However maps would need to be created for all polarisation angles and it was felt that this was an unnecessary line of further investigation.

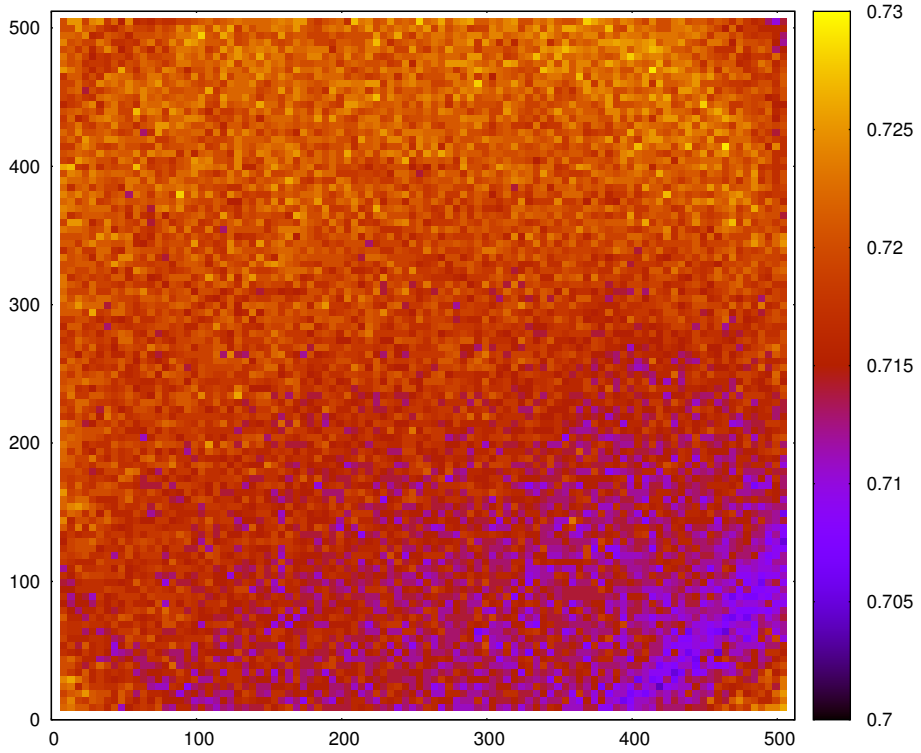


Figure 5.2: The measured polarisation across the field of RINGO2 when looking at the zenith sky during sunset, uncorrected for instrumental polarisation or depolarisation. Rayleigh scattering in the atmosphere provides an extended full field source with around ∼85 % polarisation, which is detected here at around the ∼72 % level, due to instrumental depolarisation. Each $10 \times 10$ pixel bin was calculated using `imstat` to measure the counts in each of the 8 frames.

### 5.2.2 Instrumental polarisation

Instrumental polarisation is defined as the polarisation which RINGO2 would measure, without any corrections, when unpolarised radiation enters the telescope. There are two processes which will contribute to this value of instrumental polarisation which is represented by the Stokes zeropoints. The dominant source of this instrumental polarisation is due to polarisation state of the incoming radiation being modified within the telescope before it reaches the instrument. The incident radiation to the telescope is focused to a beam at the RINGO2 instrument by reflections of the primary, secondary and sciencefold mirror (M1, M2 and M3 respectively). M1 and M2 can provide varying modification to the polarisation state of the radiation based primarily on the glow discharge process used in re-aluminising. This process can align and create a crystalline structure on the mirror (Gehrels, 1960). The instrumental polarisation could be

significant or non existent for M1 and M2 at any wavelength based on the prevalence and scale size of this crystalline structure. Interestingly, Gehrels finds that thickness of coating and dust on the mirrors have little effect on instrumental polarisation. CnewAddition Being radially symmetrical to the incoming beam it is believed that M1 and M2 have little effect on changing the polarisation state of the reflected radiation.

It is thus expected that M3 will dominate instrumental polarisation with its 45 °angle of incidence (Cox, 1976). A plane mirror which deflects the beam by 90 °such as M3, could have up to 5 % effect on the instrumental polarisation (Gehrels, 1960).

Measurements of the unpolarised standards sources provide the Stokes zeropoints which are both the measure and correction factors of instrumental polarisation.

**Characterisation**

To determine and correct for the levels of instrumental polarisation, observations of known zero polarised standards (i.e. as presented in Table 5.2) are observed with the polarimeter. The measured normalised Stokes parameters of these sources are the level of instrumental polarisation. We refer to these as Stokes zeropoints, as they define the zero polarisation point on the Stokes q-u plane. For characterisation, the data taken on the zero polarised fields was analysed across the instrumental epochs for RINGO2.

The average Stokes zeropoints from the observations at the different instrumental epochs are detailed in Table 5.5. A small number of outliers (less than 1 % of points) severely affected the values and standard deviations, so these were omitted if more than an arbitrary 5 % from the average values of q and u. The reason for these outliers is not fully understood. When dealing with large datasets these stray observations are expected and can be removed without fully understanding the causes for their erroneous results.

| Instrumental epoch | $\mu_q$ (%) | $\mu_u$ (%) | $\sigma_q$ (%) | $\sigma_u$ (%) | $\mu_p$ (%) | $\mu_\beta$ (°) | $\sigma_p$ (%) | $\sigma_\beta$ (°) |
|---|---|---|---|---|---|---|---|---|
| R2_1 | 0.30 | -2.50 | 0.31 | 0.41 | 2.54 | 48.5 | 0.41 | 3.7 |
| R2_2 | -2.61 | -0.74 | 0.47 | 0.31 | 2.73 | 7.9 | 0.48 | 3.2 |
| R2_3 | -0.30 | 2.97 | 0.25 | 0.36 | 2.99 | 137.7 | 0.35 | 2.6 |
| R2_4 | -0.31 | 2.64 | 0.17 | 0.41 | 2.66 | 138.3 | 0.41 | 2.0 |

Table 5.5: The mean ($\mu$) and standard deviation ($\sigma$) of the values of Stokes zeropoints (q, u), magnitude and angle of instrumental polarisation (p, $\beta$) for RINGO2 across different instrumental epochs.

The mean magnitude of instrumental polarisation for RINGO2 is between 2.5 % and 3.0 % across the instrumental epochs, which is within the $\lesssim$5 % levels expected from Cox (1976). When analysed across all instrumental epochs the mean value instrumental polarisation is 2.89 % with a standard deviation of 0.41 %. This shows that variations in the magnitude of instrumental polarisation are within the expected uncertainty and can be assumed to be constant with different instrument epochs.

The difference of angles of the instrumental polarisation for epochs R2_3 and R2_4 are 0.6 °. Given the magnitude of the errors, this can be considered to equate to no change in angle. Between these epochs the A&G unit (which manages the Cassegrain rotation) was repositioned on the telescope. As a consequence the angle of `rotmount=0` (at which RINGOstand observations are taken) was rotated by 16 °. The lack of a corresponding angle change in the instrumental polarisation clearly shows that, over the wavelength band of RINGO2, it is the science fold mirror (M3) that is causing the instrumental polarisation and any contribution from mirrors M1 and M2 is insignificant.

In order to visualise the instrumental depolarisation a density plot of a large number of sources from zero polarised fields was created (Figure 5.3. This contains 25,000+ sources which were identified in the zero polarised fields. It cannot be assumed that all sources are unpolarised. However, due to the large number of datapoints and sky angles of observation, it is assumed that the average Stokes parameters measured for these sources will be at the Stokes zeropoints for instrumental polarisation. It can be

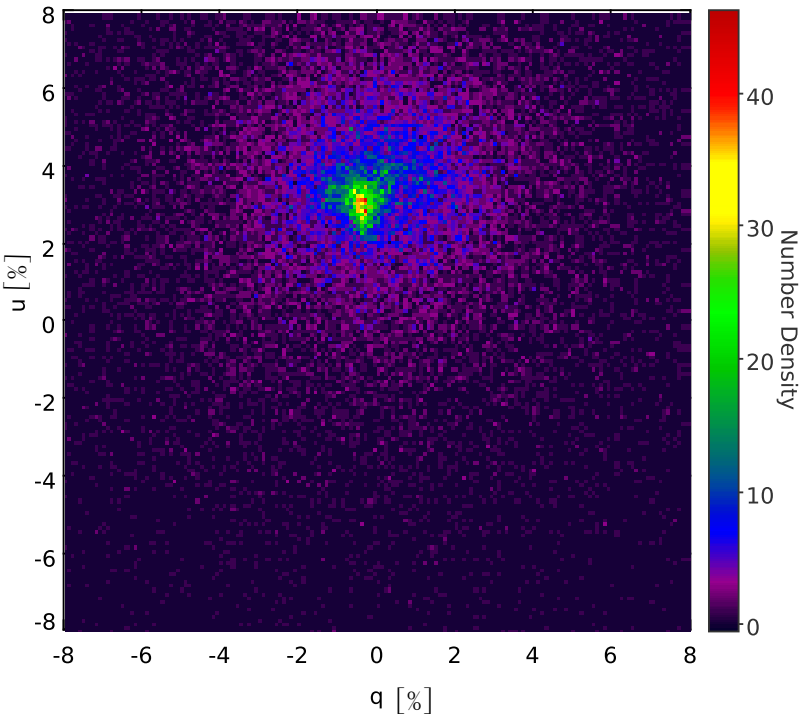


Figure 5.3: A plot of q and u values of all sources contained in zero polarised fields during epoch R2_3 and R2_4, with total counts S1 $>$ 2000 ($\sim$16th magnitude).

seen that the peak of the density plot (at $\sim$[-0.3, 3.2]) is comparable with the average zeropoints obtained for the bright zero polarised sources. However the distribution of points is non rotationally symmetric about this peak (the blue area of number density 5-10).

This asymmetry could arise from two sources: temporal stability and rotor bias. The latter would occur when the signal to noise ratio of measurements drops, revealing any polarisation bias due to variations in the noise at different rotor positions. For example, a polarised background sky with greater error in certain rotations of the polaroid, would be a candidate. This bias due to noise, however, will be correctly accounted for in the error propagation of the 8 photometric measurements to the normalised Stokes parameters.

The other source of asymmetry is due to the temporal stability of the RINGO2 instrument zeropoints during the 20 months which this plot covers. Any drift in the zeropoints will not produce the expected symmetric 2D Gaussian.

### Temporal stability

The temporal stability of the Stokes zeropoints across the instrumental epochs was analysed using the output values of the `get_zeropoints()` function in `ripe`. This function is called for each observation with a range of 2 days either side of the observation (i.e. a 5 night window). If this function finds fewer than 3 observations of zero polarised sources to derive average Stokes zeropoints, it expands the window by one night each side. Thus the output of the averaged Stokes zeropoints is a running (or smoothed) average, with a minimum bin size of at least 3 objects.

Figure 5.4 shows the output of `get_zeropoints()` for the modified Julian date for which it was called. Points with a standard deviation in the bin of greater than 1 % were omitted ($\lesssim 0.05$ % of points). The changing of polaroid angles can easily be seen for R2_2 and R2_3. Data for instrumental epochs R2_3 and R2_4, which we now treat as one epoch, provides a 20 month log of instrumental stability. A purely visual analysis of the data sees no consistent drift in the values or obvious periodic fluctuation which would require any further investigation. It can clearly be seen that the variance in q is smaller than in u. A numerical analysis confirms this with standard deviations of 0.11 % and 0.20 % respectively. It is unknown what creates this larger variation in the Stokes zeropoint for u, and again could be due to error bias in a certain polaroid rotation.

### Error Biases

There is the possibility of an error bias in RINGO2 measurements. This would be created when one or more polaroid rotations have an unnaturally high error. This effect could explain the non rotationally symmetric distribution in the density plot

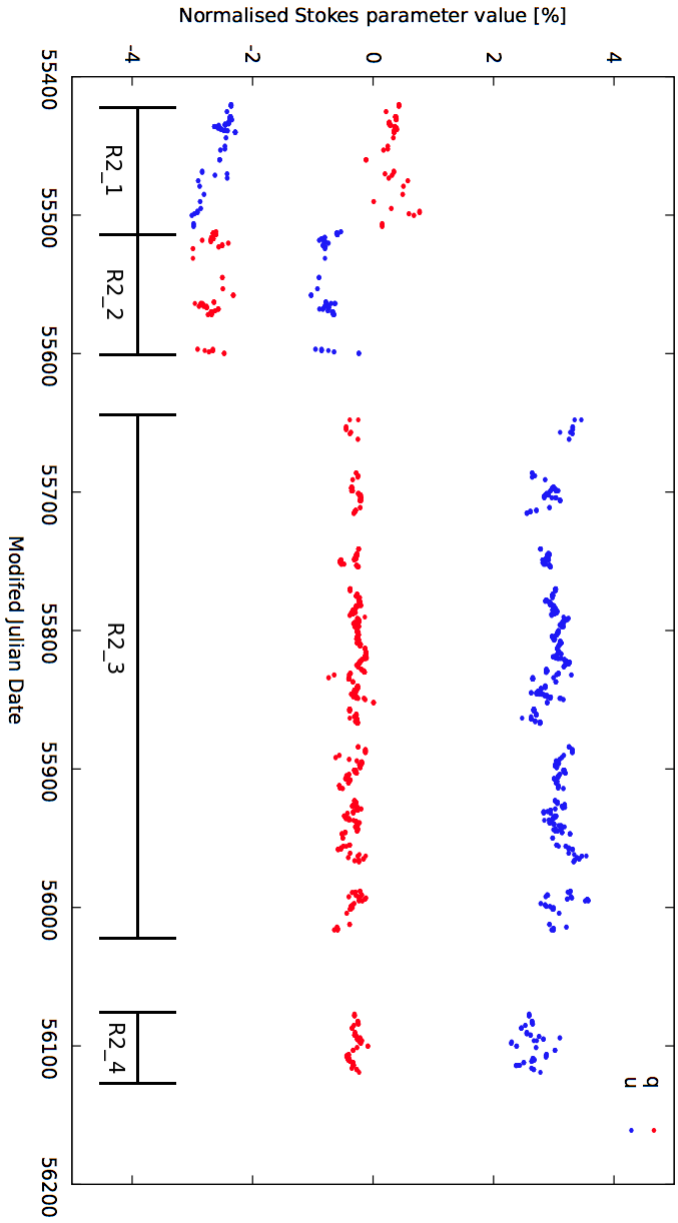


Figure 5.4: The Stokes zeropoint values from the function `get_zeropoints()` plotted against the modified Julian date. The different instrumental epochs are marked and are clearly visible by the changes in zeropoints.

(Figure 5.3) and also the near doubling in variance in Stokes zeropoint u compared to q (Figure 5.4) during epochs R2_3 and R2_4.

To look into this requires a simple query of the photdata table in the database. The query below selects the average values of photometric error as a proportion of the signal for unpolarised standards observed during epoch R2_3. This is done for each combined polaroid orientation (i.e. A1 is combined with A2), to create an analysis for combined A, B, C and D orientations.

```
select avg(a1_err/a1) + avg(a2_err/a2), avg(b1_err/b1) + avg(b2_err/b2), avg(
c1_err/c1) + avg(c2_err/c2), avg(d1_err/d1) + avg(d2_err/d2) from photdata where
target='U' and tag_link='R2_3'
```

The results of this query are as follows, A - $5.55 \times 10^{-3}$, B - $5.46 \times 10^{-3}$, C - $5.12 \times 10^{-3}$, D - $5.68 \times 10^{-3}$. These results show a slightly lower error proportion in the combined C orientation, but the variance in values is not enough to have any impact on increasing the error on one Stokes parameter over another. This is confirmed by looking at the average *q_err* and *u_err* values in the photdata table of the database for the same observations, which come out as 0.24 % and 0.23 % respectively. This conclusively shows that there is no error bias which is providing vastly different errors on the Stokes zeropoints.

### Conclusions of instrumental polarisation and corrections

With no observed rotation in the instrumental polarisation between epochs R2_3 and R2_4 (where the A&G unit was rotated by 16 °) we can conclusively state that the science fold mirror within the A&G box provides the majority of the ∼2.9 % instrumental polarisation seen across all instrumental epochs. Furthermore it shows that the primary and secondary mirror do not cause any measurable instrumental polarisation

in the wavelength band of RINGO2 ($\sim 450 \rightarrow 800nm$). The glow ionisation process which is undertaken during re-aluminising at the Isaac Newton Group could produce aligned crystalline structures on the mirror surface, which could cause instrumental polarisation from the primary mirror at lower wavelengths. The lower operating wavelength of RINGO3 is only 50 nm lower than that of RINGO2; therefore it is not a concern for RINGO3.

The stability of the instrumental polarisation is good with standard deviations of less than 0.5 % on the Stokes zeropoints. The variation of the zeropoints in instrumental epochs R2_1 and R2_2 seem somewhat erratic, but are much more stable in epochs R2_3 and R2_4. In these latter epochs the outputs of the zeropoints used for corrections in the `ripe` pipeline show almost double the variance on the u value as opposed to the q value. This cannot be explained through the average errors on each of the polaroid rotations and any associated error bias.

This analysis has shown that there are extreme outliers in the frequent measurements of unpolarised standard sources. With such good instrumental stability in the averages, these outliers are better explained by erroneous phenomena (e.g. cosmic rays, very poor seeing, photometric measurement failures) rather than a large shift in the instrumental polarisation. When users apply a correction to their data to account for instrumental polarisation it should be taken from a large number of observations with outliers of more than 3 standard deviations rejected. Alternatively the values in Table 5.5 can be used.

Hereafter we only employ data from epochs R2_3 and R2_4 for RINGO2 characterisation.

### 5.2.3 Instrumental depolarisation

When polarised light is reflected by a mirror, the polarisation state is not maintained for a small proportion of the radiation. This produces instrumental depolarisation, whereby the measured polarisation at the detector is lower than that of the true polarisation state of radiation entering the telescope. Again, this is a wavelength dependent term, based on reflections from mirrors M1, M2 and M3 and may also have an angular dependence. To characterise this depolarisation, observations of polarised standards are used.

For ease of labelling in the numerous plots, the six polarised standards observed by RINGOstand are given a designator. These are listed in Table 5.6. Henceforth, all data are corrected for instrumental polarisation.

| Standard | Designator |
|---|---|
| BD+59°389 | *a* |
| BD+64°106 | *b* |
| HD155528 | *c* |
| Hiltner 960 | *d* |
| BD+25°727 | *e* |
| VI Cyg #12 | *f* |

Table 5.6: Designators of polarised standard stars used in plots.

#### Polarisation rings

'Polarisation rings' (or segments thereof) are produced in the q-u plane, by repeated measurements of the polarised standards taken at differing sky angles. This is a natural artifact of the RINGOstand programme observing standards with the Cassegrain rotator at a fixed angle (rotmount=0) and the Liverpool Telescope being an altitude azimuth telescope. Dependent on the declination of the source, we are able to ob-

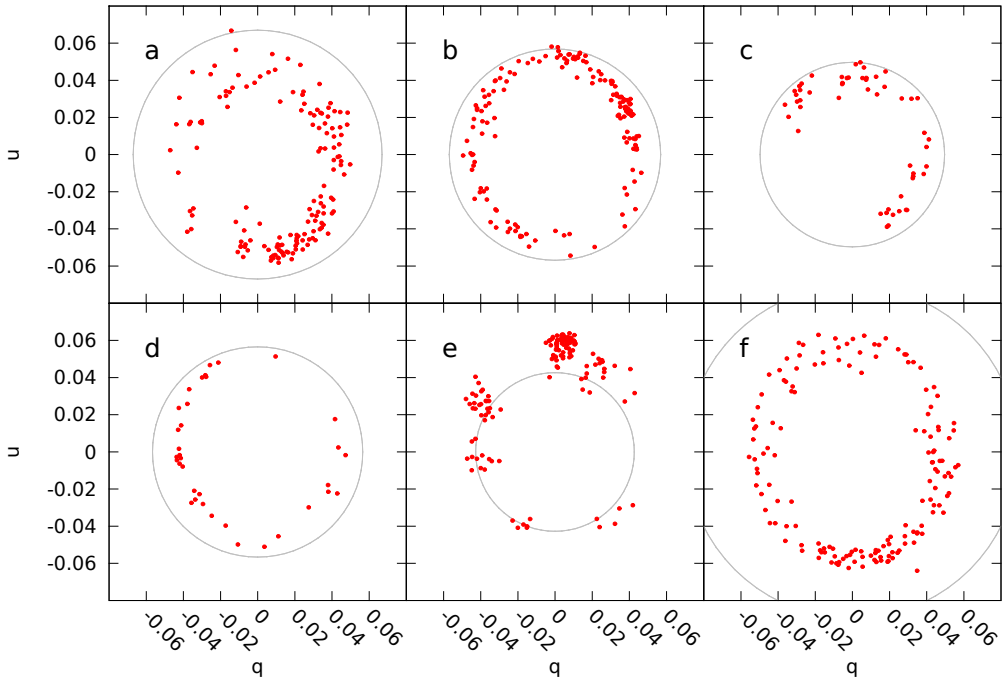


Figure 5.5: q-u plots of polarised standards observed during R2_3 and R2_4. The grey rings indicate the catalogue V-band polarisation of these standards taken from Schmidt et al. (1992) and Turnshek et al. (1990).

tain observations which measure the full range of polarisation input angles into the telescope.

Plotting the measured polarisation of polarised standards in the q-u plane provides a good illustration of the depolarisation characteristics of RINGO2. Figure 5.5 shows the measurements of polarised standards during epochs R2_3 and R2_4. It can be seen that good coverage of polarisation angles is provided by standards BD+59°389, BD+64°106 and VI Cyg #12 (a, b and f)

All of the rings produced, apart from ring e, show points which fall within the grey catalogue polarisation circles, where the measurements should lie. This shows the effect of instrumental depolarisation. Ring e (BD+25°727), provides points which are in excess of this value. This is most likely due to a shift in the polarisation of the source since it was measured and catalogued in Turnshek et al. (1990) over 20 years before the RINGO2 observations.

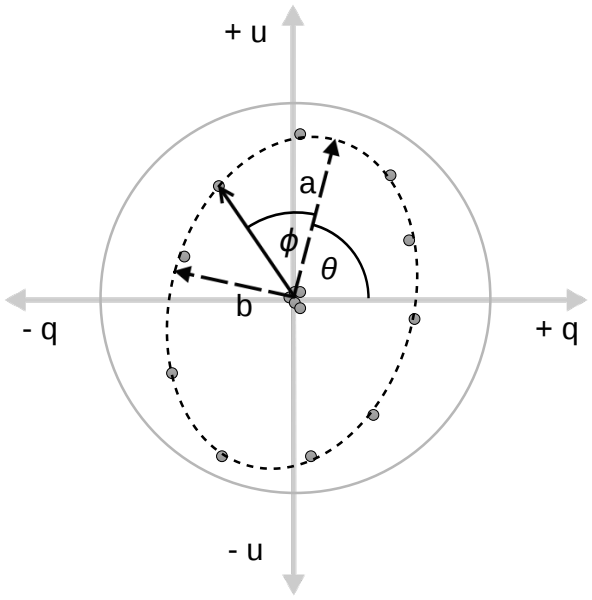


Figure 5.6: Simulated polarimetric data points in the q-u plane for a polarised source viewed at a number of sky angles. The ellipse is defined as follows: a - semi-major axis; b - semi-minor axis; $\theta$ - angle of ellipse; and $\phi$ - angular location of datapoint on the ellipse.

The rings also show a level of ellipticity, which is most prominent in rings *b*, *d* and *f*, with the major axis of the ellipse aligned close to the u-axis. This ellipticity is a mark of the angular dependence of depolarisation.

### Characteristic Ellipse

We define the characteristic ellipse as the ellipticity in these q-u polarisation rings, and use this information to correct for ellipticity before correcting for a single depolarisation factor. Ellipses are defined based on two parameters which are shown in Figure 5.6. These are the angle of the ellipse, $\theta$, and the ellipticity, $\epsilon$. The angle of the ellipse is the angle between positive q axis and the major axis of the ellipse counter clockwise. The ellipticity is defined by Equation 5.1, where a and b are the lengths of the semi-major and semi-minor axes respectively. An ellipticity of 0 specifies a circle and 1 specifies a straight line.

$$\epsilon = \frac{a - b}{a} \tag{5.1}$$

To measure the characteristic ellipse of RINGO2, we employed a least square fitting method which is developed by Fitzgibbon et al. (1999). This fitting was applied to all polarisation rings in Figure 5.5 and the results are detailed in table 5.7. Polarisation rings *a*, *b* and *f* were identified to provide the fullest coverage of angles. However it can be seen that ring *a* has a high amount of variance at certain angles. The other rings, *c*, *d* and *e* have either poor or incomplete sampling of a full ellipse and this makes the method of ellipse fitting more prone to error.

| Designator | Polarimetric Standard | Number of Observations | Ellipticity ($\epsilon$) | Angle of Ellipticity ($\theta$) |
|---|---|---|---|---|
| *a* | BD+59°389 | 134 | 0.18 | 98 |
| *b* | BD+64°106 | 119 | 0.14 | 89 |
| *c* | HD155528 | 51 | 0.14 | 118 |
| *d* | Hiltner 960 | 30 | 0.12 | 97 |
| *e* | BD+25°727 | 121 | 0.18 | 100 |
| *f* | VI Cyg #12 | 148 | 0.14 | 95 |
| CE | Characteristic Ellipse | n/a | 0.14 | 92 |
| | RINGO3 Sky rotation | n/a | 0.15 | 66 |

Table 5.7: List of polarised standards observed with the Liverpool Telescope and the RINGO2 instrument showing ellipticity of best fits and angle of ellipse

The ellipticity of rings *b* and *f* (BD+64°106 and VI Cyg #12 respectively) are taken to be the true values. We define the characteristic ellipse for RINGO2, epochs R2_3 and R2_4 to be $\epsilon = 0.14$ and $\theta = 92$. It is interesting to note that the poorer sampled rings do provide least squares fits that approximate this ellipticity and angle. The ellipse created in the single RINGO3 sky observation also provides an insight into the validity of the ellipse model at much higher polarisations (up to 80 %) and the ellipticity, $\epsilon$, of 0.15 (in d band camera) marries well with the values obtained for RINGO2. The change of angle compared to RINGO2 is an expected consequence of a differing polaroid angle

within the instrument.

### Correction of Ellipticity

The correction of ellipticity is required to bring all points in the polarisation rings into line with a constant magnitude of the polarisation vector. Once this is complete a single depolarisation factor can be derived for all angles of linear polarisation. We define the angle $\phi$ as the angular distance between the major axis of the ellipse and a datapoint which requires correction (see Figure 5.6).

There are 3 corrections which can be applied to create a circular set of datapoints from points on an ellipse. Firstly the datapoints could be moved only in the vector of the semi-major axis, which would result is a change of angle on the ellipse ($\phi$) and polarisation angle ($\beta$). Secondly the datapoints could be extended along their vector, maintaining both $\phi$ and $\beta$. In the third instance, a mixture of both of the above could be employed.

To deduce the appropriate type of correction, an observation of the zenith sky taken with RINGO3 provides a serendipitous answer. The observation ran as the telescope rotated in azimuth during maximal polarisation and the frames of the RINGO3 camera were unstacked and analysed individually. These observations provided a very high signal to noise ratio observation, taking an area of 40x40 pixels in the centre of the frame to obtain the polarisation measurement. A q-u plot of the polarisation values obtained during this observation are shown in Figure 5.7. It is known that the rotation rate in azimuth is extremely stable (2 $^{\circ}$per second) and the camera triggering also ($\sim$1 Hz). This provides a sample of high signal to noise points with the polarisation angle of the source at equal spacing. Analysis of the points enables us to deduce whether points on the ellipse created by an angular dependence on instrumental depolarisation are subject to an angle change or not. This enables us to exclude one of the 3 types of corrections previously mentioned.

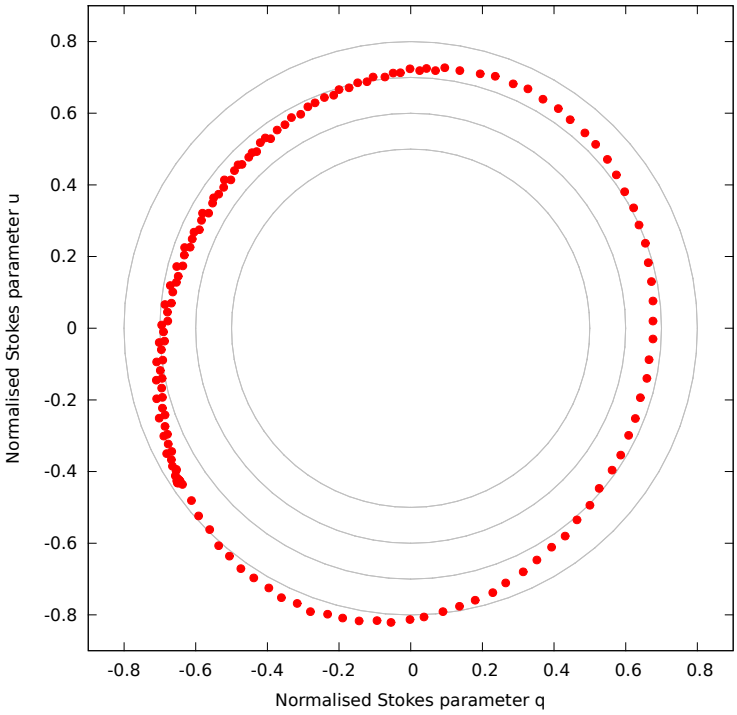


Figure 5.7: An observation of the zenith sky at sunset with RINGO3 camera d. The data were not stacked, and the polarisation was sampled for every rotation of the polaroid (∼1 Hz sampling). During this time the azimuth axis of the telescope was rotated by over 180 degrees, varying the angle of polarisation. The data form an ellipse similar to those seen with standard star data from RINGO2, but at a much higher level of polarisation (∼80 %) and at a different angle of rotation of the ellipse.

Figure 5.8 shows the angular separation between consecutive points in Figure 5.7 as a function of angle (red). The oscillation in the angular step change between points is obvious. Given that the rotation of the telescope is stable, and also the triggering of the RINGO3 camera, this conclusively shows that an angle change does occur due to depolarisation in the telescope and instrument. To confirm that ellipse correction is achieved solely by a modification of a point along the semi-major axis (b) vector, a set of simulated points was created (blue). This was done by creating a set of datapoints that formed a circle, then modifying them by movement in the semi-major axis vector only. This creates an ellipse of equal ellipticity and angle to the observations of the zenith sky in Figure 5.7. The excellent fit of these simulated data to the angular step change confirms that the correct ellipse correction method is to extend a datapoint along the semi-major axis of the characteristic ellipse.

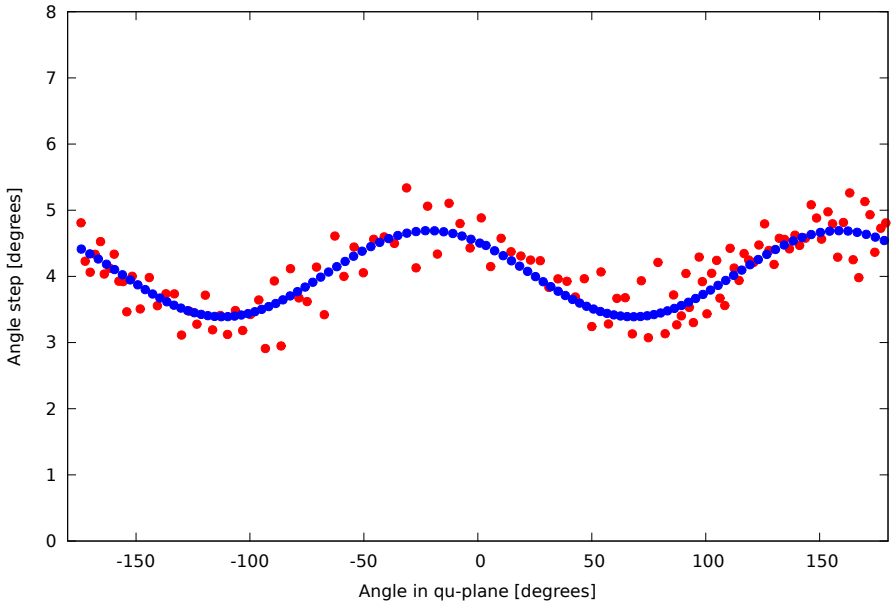


Figure 5.8: Plot showing the angular step change between points in Figure 5.7 (Red). A simulated set of datapoints (Blue) show the angular step change if equally spaced points around a circle are modified into an ellipse, of equal ellipticity and angle to the RINGO3 sky ellipse, by movement in the semi-major axis vector only.

### Ellipticity correction equations

The characteristic ellipse of RINGO2 for epochs R2_3 and R2_4 is defined in Section 5.2.3. Given the specifications of this ellipse, we are able to correct a datapoint for ellipticity using Equations 5.2. We define $q_i$ and $u_i$ as the initial normalised Stokes parameters which have been corrected for instrumental depolarisation using the Stokes zeropoints. $q_c$ and $u_c$ are the normalised Stokes parameters after being corrected for ellipticity.

$$\phi = tan^{-1}\left(\frac{u_i}{q_i}\right) - \theta \tag{5.2a}$$

$$a = \sqrt{\frac{q_i^2 + u_i^2}{\cos^2(\phi) + (1 - 2\epsilon + \epsilon^2)\sin^2(\phi)}} \tag{5.2b}$$

$$\Delta b = a\epsilon \times \sin(\phi) \tag{5.2c}$$

$$\Delta q = -\Delta b \times \sin(\theta) \tag{5.2d}$$

$$\Delta u = \Delta b \times \cos(\theta) \tag{5.2e}$$

$$q_c = q_i + \Delta q \tag{5.2f}$$

$$u_c = u_i + \Delta u \tag{5.2g}$$

| Designator | Standard | Observations | Uncorrected | | Corrected | |
|---|---|---|---|---|---|---|
| | | | $\mu_p$ | $\sigma_p$ | $\mu_p$ | $\sigma_p$ |
| *a* | BD+59°389 | 112 | 4.79 | 0.72 | 5.09 | 0.67 |
| *b* | BD+64°106 | 96 | 4.81 | 0.44 | 5.18 | 0.37 |
| *c* | HD155528 | 50 | 4.03 | 0.54 | 4.27 | 0.56 |
| *d* | Hiltner 960 | 33 | 4.51 | 0.40 | 4.94 | 0.36 |
| *e* | BD+25°727 | 109 | 5.40 | 0.73 | 5.58 | 0.63 |
| *f* | VI Cyg #12 | 121 | 5.57 | 0.60 | 5.91 | 0.55 |

Table 5.8: Details of the mean ($\mu_p$) and standard deviation ($\sigma_p$) of polarisation values from polarised standards before and after ellipse correction. This information is displayed graphically in Figure 5.10.

The `polcalc` routine was modified to perform the ellipticity correction and the polarisations were recalculated using the characteristic ellipse of RINGO2 ($\epsilon$ = 0.14, $\theta$ = 92). Table 5.8 shows the average and standard deviation of the polarisation measurements before and after ellipse correction. It can be seen that standard deviations of polarisation are reduced for all standards, apart from *c* (HD155528). In all cases the average polarisation rises. This is expected as the datapoints on a polarisation ring are only moved to higher polarisations. The ellipticity corrected polarisation rings were checked visually and the ellipse fitting method called for the data. In all cases visual ellipticity was eliminated and the ellipticity of all rings was less than $\epsilon$ = 0.05. The corrected q-u plots of the polarised standards from Figure 5.5 are shown in Figure 5.9.

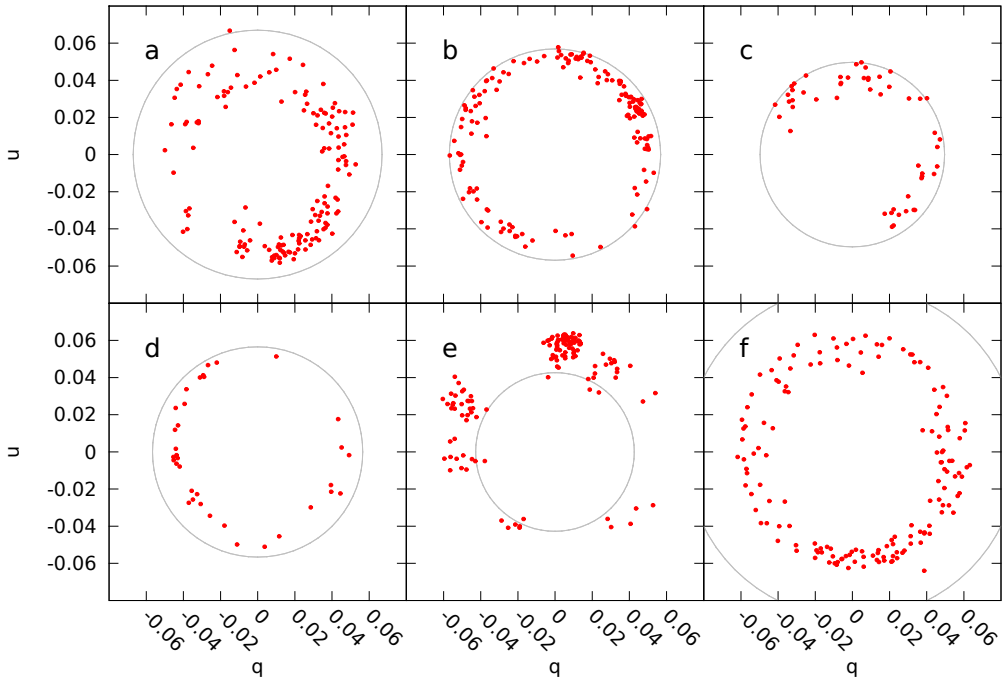


Figure 5.9: Ellipse corrected q-u plots of the data of the polarisation rings from Figure 5.5. It can be seen that for all standards, apart from standard *d*, that ellipticity in the rings is no longer visually noticeable.

Full derivations of Equations 5.2 are presented in Appendix B

### Depolarisation Factor and Correction

With the ellipticity correction taking care of any angular dependence in the depolarisation correction, a single depolarisation factor can be determined and applied for any measurement. The depolarisation factor, $D$, is shown in Equation 5.3 and is applied to the vector product of the corrected Stokes parameters ($q_c$ and $u_c$, corrected for instrumental polarisation and ellipticity) to obtain the true polarisation value, $p$.

$$p = D \times \sqrt{q_c^2 + u_c^2} \tag{5.3}$$

To measure the depolarisation factor with RINGO2, the average values of measured polarisation from the R2_2 dataset were taken and plotted against the catalogue values

as shown in Figure 5.10. A crude line of best fit for each of the 6 points (i.e. unweighted for sample size and standard deviation) was used to provide an initial value. This was forced through the origin and we were able to deduce the depolarisation factor, $D$, as the inverse of the gradient. For a gradient of 0.82 a depolarisation factor was determined of, $D = 1.22$

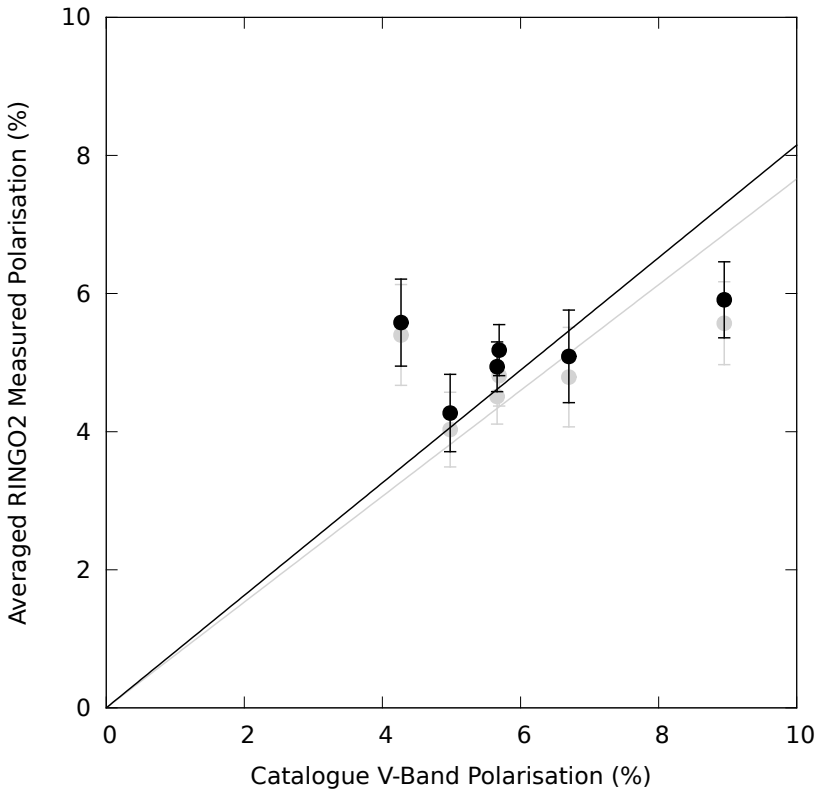


Figure 5.10: Plot of polarised standards' catalogue values versus measured values before (grey) and after (black) ellipse correction with information from Table 5.8. Error bars are the standard deviation of the measurements. For the catalogued values, the standard deviation of measurements from Schmidt et al. (1992) and Turnshek et al. (1990) are on the order of the point size thus omitted. The lines of best fit, forced through the origin, have gradients of 0.77 (grey) and 0.82 (black).

This quick analysis provides an insight into the likely depolarisation factor. However, it is obvious that the fit is poor. This is confirmed by negative regression factors

and also the fact that the unconstrained line of best fit with the point for VI Cyg#12 removed gives a negative gradient. The expected cause for the poor fit is due to lack of stability of the polarised standards; their polarisations having changed since the catalogue measurements were taken over 25 years ago.

It is difficult to find new catalogue measurements of polarised standards in the literature for the Northern Hemisphere standards which we are observing. However, one set of data by Soam et al. (2014) gives the necessary data for correct determination of the depolarisation factor, $D$, and, therefore confidence in this result.

**Contemporaneous measurements of BD+59°389**

The team of Soam, Maheswar and Eswaraiah used the AIMPOL polarimeter (Rautela et al., 2004) mounted on the 1.04m Sampurnanand telescope (Sagar et al., 2012) at ARIES, Nainital, India. They measured the fields of the Northern Hemispheric polarised standards from Schmidt et al. (1992) in VRI bands. Using the $\sim$8 arcmin diameter field of view they measured a number of neighbouring fainter sources in order to find stable polarised sources for large diameter ($>$2m) telescopes. These measurements included the field of BD+59°389 and provided contemporary measurements to those taken by RINGO2 during the R2_3 instrumental epoch, in the R band.

By modifying the `standfind` routine in `ripe`, the sources measured in Soam et al. (2014) were identified in the ripe database. These are shown in Figure 5.11. The measurements in the database were selected with an upper threshold of 1 % imposed on the polarisation error to yield the dataset for analysis. This arbitrary threshold was used to remove erroneous and low signal to noise measurements. Creating polarisation rings with the q and u values of each measurement (Appendix, Figure C.1) provided visual confirmation of the conclusion by Soam et al. (2014) that Star 3 provides a highly stable, yet low polarisation standard.

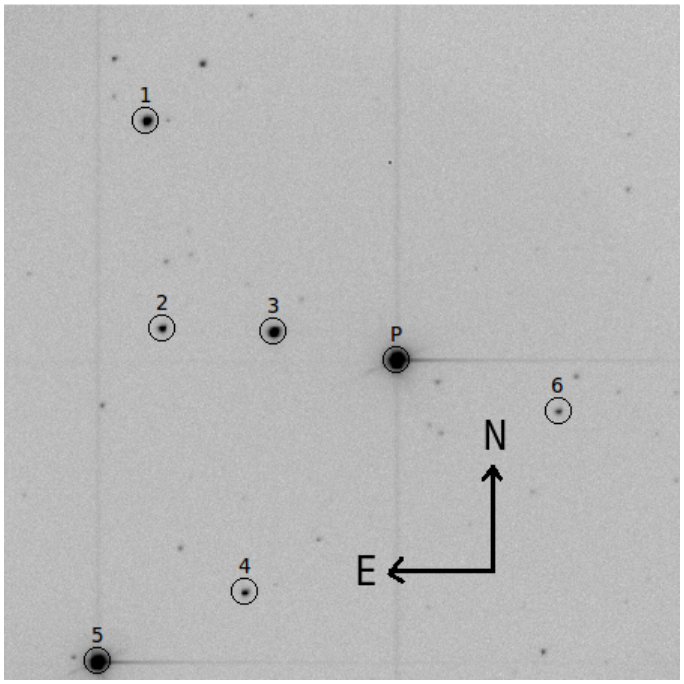


Figure 5.11: RINGO2 image of the field of BD+59°389, which is identified by 'P'. The numbering of other stellar sources in the field matches the identifiers given by Soam et al. (2014)

A temporal analysis of the measurements was then performed for BD+59°389 and Star 3 superimposing the data from AIMPOL and RINGO2 using a depolarisation factor of $D = 1.22$ (Figure 5.12 and Appendix, Figures C.2 and C.3). The plots provide interesting insight into the two instruments and their strengths. AIMPOL provides datapoints with good polarimetric accuracy, but the number and cadence of observations cannot sample accurately any possible variation in the shift of the standards. Being close stellar sources with a high parallax and scope for large proper motions, there is a chance of periodic and linear shifts in polarisation value.

Conversely, RINGO2 data are well sampled temporally (due to the RINGOstand programme) yet have high error, making any subtle changes in polarisation of the standards stars indistinguishable. Interestingly there is a feature in the RINGO2 data of both BD+59°389 and Star 3 which occurs at MJD ∼55790. For a handful of nights either side of this date in both sources there is a drop in polarisation and a rise. This is the only obvious visually correlated feature in the data and would need further investigation to deduce if it was an instrumental shift, observational issue (e.g. Moon

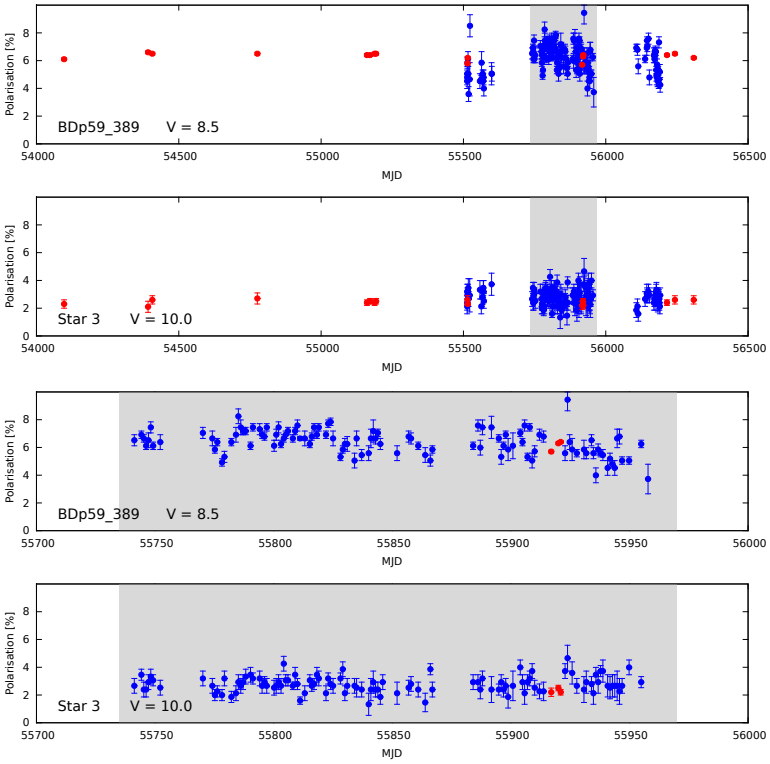


Figure 5.12: Comparison of contemporaneous polarimetric measurements of BD+59°389 and 'Star 3' with AIMPOL (R band) and RINGO2. AIMPOL datapoints are in red, RINGO2 datapoints in blue. The data for RINGO2 are corrected for instrumental polarisation and ellipticity. The depolarisation factor applied is $D = 1.22$.

position or phase) or an astrophysical change.

In any case the comparisons of the measurements of AIMPOL and RINGO2 are visually consistent when a depolarisation factor of 1.22 is applied. When the comparative data of AIMPOL and RINGO2 are plotted into Figure 5.10 the two new values of average polarisation are consistent with the previously matched depolarisation of $D = 1.22$ (Figure 5.13). Star 3 provides a lower value of polarisation than any of the other sources from Schmidt et al. and Turnshek et al., providing extra confidence in the obtained depolarisation value.

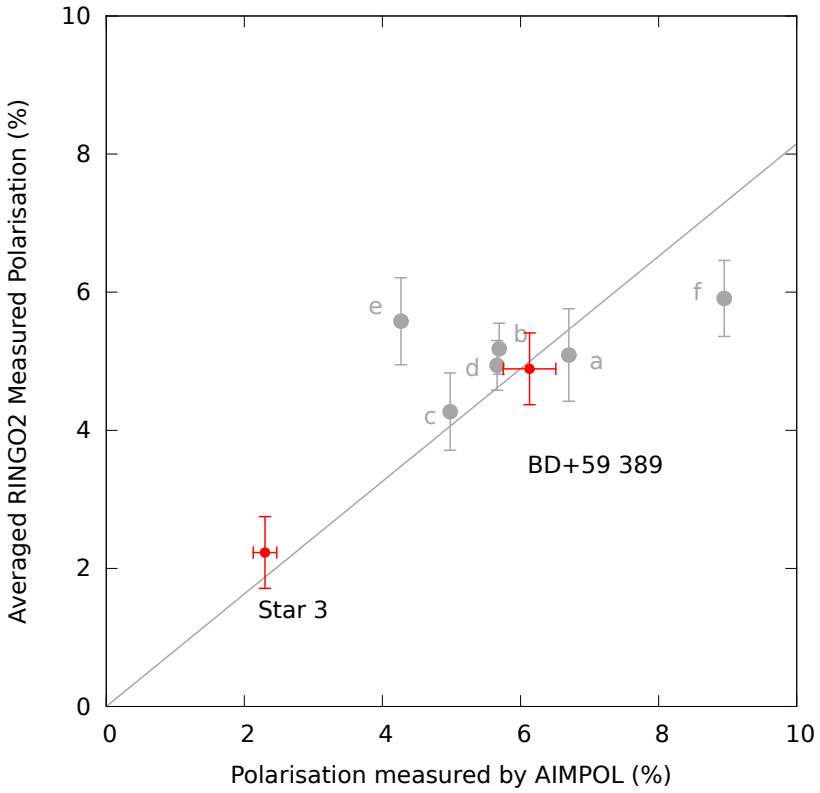


Figure 5.13: The comparison of the average values of contemporaneous AIMPOL (R-band) and RINGO2 observations of BD+59°389 and field star 'Star 3', superimposed on data of Figure 5.10. The points are the average of 114 measurements from RINGO2 and 3 observations from AIMPOL from the period denoted by grey shading in Figure 5.12

### Conclusion on instrumental depolarisation

It has been shown in this section that the instrumental depolarisation of RINGO2 is an angle dependent effect. In order to correct for depolarisation there is a two part process. By defining the variation of depolarisation with angle in the form of an ellipse, we determine an ellipticity correction that removes any angle dependency from the data. Once this dependency is removed a singular depolarisation factor, $D$, is applied to the data.

There is a large, unquantified uncertainty in the value of the true depolarisation factor, with archaic catalogue data and lack of recent observations. Linked to this is the wider operating band of RINGO2 (a composite V+R band) throughout which there

may be different polarimetric characteristics of the telescope optics and instrument. This leads to questions about whether a single set of ellipse corrections and depolarisation factor is compatible for sources with vastly varying spectral classifications. This is discussed further in Chapter 7.

For gamma-ray burst science, uncertainties in the depolarisation are less important than it might first seem. Firstly the depolarisation corrections are systematic. Whilst true values of measured polarisation may be a few percent away from where an inaccurate depolarisation factor places them, the aim of RINGO2 and RINGO3 are to measure temporal polarimetric variation. Secondly, with GRB measurements being 6-8 magnitudes fainter than those of the standard sources observed for this chapter, the photometric uncertainty for the GRBs becomes a dominant effect of uncertainty in any polarimetric measurement. RINGO2 satisfies its intended prime purpose of high cadence, high polarisation measurements. With the rich dataset provided by the RINGOstand observation program, it is unfortunate that RINGO2 cannot provide a more accurate insight into the stability and variation of polarimetric standards.

### 5.2.4 Polarisation angle calibration

The last part of creating a publishable polarimetric measurement from RINGO2 or RINGO3 is to convert the angle of polarisation from the normalised Stokes parameters to an on-sky angle. Whilst not involving any complicated mathematics or analysis, this contains a number of tricky elements. The instrument has a certain angle on the sky which is provided by the parameter *rotskypa* in the FITS headers of the observations. This is used with the measured polarisation angle, $\beta$, to measure the on-sky angle.

For the sky polarisation angle $\theta_{sky}$, there needed to be an analysis of the 'direction' of the measured polarisation angle. This direction can be viewed simplistically as which way the polaroid is spinning in relation to the sky image, which may be flipped due to telescope optics. This was deduced to give Equation5.4 to convert measured

polarisation angle, $\beta$, to sky polarisation angle, $\theta_{sky}$.

$$\theta_{sky} = (\beta + (rotskypa + 360) - \theta_c) \,\%\, 180 \tag{5.4}$$

In the $\beta \rightarrow \theta_{sky}$ conversion equation, $\%$ is the modulo operator which finds the remainder after division by the subsequent number. Using the operator in the $\%$ 180 term at the end converts the angle into the linear polarisation range of $0^\circ \rightarrow 180^\circ$. In the equation $rotskypa$ is incremented by 360 (a full rotation) as the values from the fits headers of RINGO2 and RINGO3 run in the range $-360^\circ \rightarrow 360^\circ$, and a negative angle value is not compatible with the equation. The correction angle, $\theta_c$ is a value which is affected by the polaroid angle in relation to the triggers of the exposures. As described in Section 5.1.1, this is affected each time the polaroid unit is removed and replaced.

Figure 5.14 shows histograms of the correction angle required to match catalogue angles for the polarimetric standard stars. We see that standards a, b, c and f are consistent with $\theta_c$ of 48°, with standard e showing a correction angle of 41°. The stable polarimetric standard, Star 3, from the BD+59°389 has a very wide distribution. This is owing to the the low levels of polarisation ($\sim 2.3\,\%$) and the errors on q and u have a larger effect on the polarisation angle at lower polarisations.

From these data we deduce a correction angle for RINGO2 epoch R3_3 of 48°and believe that the angle of polarised source BD+25°727 has decreased by $\sim 6^\circ$from the time of the measurements presented in Turnshek et al. (1990)

### 5.2.5 Attempted correlation with observing parameters

The rich dataset of standards data provided from the RINGOstand program was investigated to try and deduce if there were any observational factors which will affect polarisation measurements. The `ripe` database provided values of various parameters.

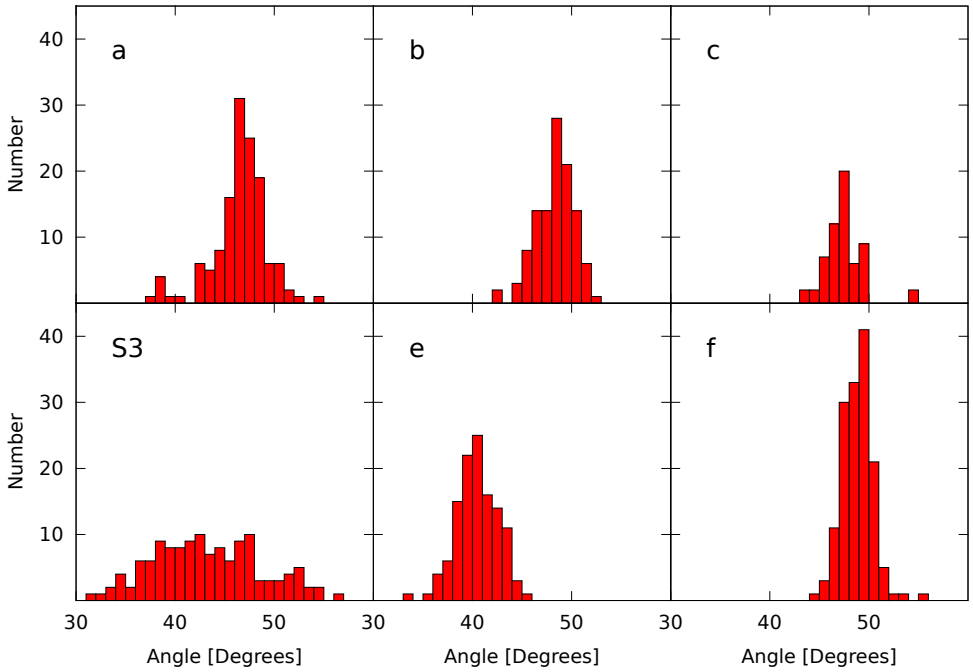


Figure 5.14: Histogram of the polarisation correction angle, $\theta_c$, required to make the measured polarisation angle match the catalogue polarisation angle. The data is of each RINGO2 observation of standards during instrumental epoch R2_3, filtered to remove any observations with the arbitrary polarisation error upper limit of 1 %. NOTE: The small number of datapoints for Hiltner 960 (d) have been replaced with data for Star 3 from BD+59°389 (S3)

Obvious parameters that we looked at were airmass, and the moon's effect (phase and distance from target) on measurements.

No obvious trends or patterns could be observed within the data, partly due to the unfortunately large errors on RINGO2 measurements. They do, however, provide some interesting asides to the observational sampling of RINGO2 RINGOstand observations and hence plots of the effects of altitude, moon phase and moon distance are included in Appendix D.

## 5.3 RINGO3 investigations

On commissioning, RINGO3 had debilitating issues regarding polarisation, which were associated with the 100 % polarised rotating beam within the instrument (Chapter 3,

Section 3.6). The subsequent addition of depolarising optics solved this problem. The RINGOstand dataset here is for the R3_4 instrumental epoch (Table 5.1) and covers a period of $\sim 270$ nights. However, due to the issues with polarimetry, the RINGOstand programme was performed quite aggressively after the fix and included observations at 3 different Cassegrain rotator angles, which were not covered for RINGO2.

The dataset used in this section was cleaned of erroneous results, using the same arbitrary upper limit of 1 % on polarisation error. Table 5.9 details the number of observations of each polarised standard at different rotmount angles.

| Standard | Designator | Rotmount (°) | Obs |
|---|---|---|---|
| BD+59°389 | *a* | -60 | 27 |
| | | 0 | 206 |
| | | 60 | 27 |
| BD+64°106 | *b* | 0 | 320 |
| HD155528 | *c* | -60 | 138 |
| | | 0 | 141 |
| | | 60 | 136 |
| Hiltner 960 | *d* | -60 | 332 |
| | | 0 | 328 |
| | | 60 | 325 |
| BD+25°727 | *e* | -60 | 276 |
| | | 0 | 264 |
| | | 60 | 272 |
| VI Cyg #12 | *f* | -60 | 291 |
| | | 0 | 290 |
| | | 60 | 289 |

Table 5.9: Details of R3_4 dataset observations of polarised standards.

### 5.3.1 Cassegrain rotator angle

These data provide an excellent opportunity to investigate the effect of Cassegrain rotator (Rotmount) angle on polarimetric measurements. Measurements were taken of zero polarised and polarised stars for every 10 °of rotation with RINGO2. However, with single measurements, no significant variation (i.e. above the $1\sigma$ polarimetric

errors) was detectable. With the full polarimetric instrument considered to be both the telescope and RINGO3, rotations of the instrument in relation to the rest of the telescope could easily be expected to change the characteristics.

With the much richer dataset, small variations should be detectable, as the standard error on the mean will be much reduced. Here we analyse both zero polarised and polarised sources. All zero polarised sources are included, however we only consider data from two polarised standards. These two were chosen due to their large numbers of observations and obvious visual stability when the normalised Stokes parameters were plotted (Figure 5.15). Hiltner 960 (standard *d*) provides well sampled polarisation rings due to the number of observations that are taken with different sky angles. Conversely BD+25°727 provides 3 'clumps' of points. With a declination of +25 °, this source transits at $\sim 87°$and, as such, presents a much smaller range of polarisation angles to the alt-azimuth Liverpool Telescope.

### Instrumental Polarisation and Rotmount

The Stokes zeropoints for the dataset were analysed for each rotmount angle for which data was taken, using the `ripe` database with the mySQL query in Listing 5.3.1. This produced the values in Table 5.10.

```
1   SELECT distinct camera, round(rotmount,-1), count(p), round(avg(q*100),2),
    round(avg(u*100),2), round(stddev(q*100),2), round(stddev(u*100),2) FROM obs,
    photdata where obs_id = obs_id_link and target='U' and p_err_minus<0.01 group by
    camera, round(rotmount,-1) order by camera, rotmount
```

As previously observed with RINGO2, the data provides strong confirmation that angle of instrumental polarisation is invariant with rotmount angle. This provides the conclusion that the instrumental polarisation contributions from the M1 and M2 (primary and secondary mirrors) are minimal compared to that of M3 (45 °science fold

| Band | Rotmount(°) | Obs | $\mu_q$ (%) | $\mu_u$ (%) | $\sigma_q$ (%) | $\sigma_u$ (%) |
|---|---|---|---|---|---|---|
| d | -60 | 363 | -2.20 | 3.31 | 0.21 | 0.24 |
| | -20 | 104 | -2.29 | 3.03 | 0.33 | 0.31 |
| | 0 | 533 | -2.19 | 3.26 | 0.25 | 0.31 |
| | 20 | 106 | -2.34 | 3.09 | 0.33 | 0.30 |
| | 40 | 105 | -2.21 | 3.10 | 0.32 | 0.31 |
| | 60 | 370 | -2.21 | 3.32 | 0.21 | 0.26 |
| e | -60 | 557 | -1.14 | 1.99 | 0.21 | 0.30 |
| | -20 | 109 | -1.22 | 2.18 | 0.20 | 0.20 |
| | 0 | 854 | -1.15 | 2.12 | 0.23 | 0.31 |
| | 20 | 112 | -1.15 | 2.25 | 0.20 | 0.22 |
| | 40 | 110 | -1.08 | 2.19 | 0.23 | 0.27 |
| | 60 | 588 | -1.05 | 2.04 | 0.20 | 0.33 |
| f | -60 | 486 | -2.15 | 3.33 | 0.22 | 0.25 |
| | -20 | 105 | -2.19 | 3.35 | 0.24 | 0.23 |
| | 0 | 676 | -2.19 | 3.38 | 0.24 | 0.27 |
| | 20 | 109 | -2.18 | 3.43 | 0.25 | 0.22 |
| | 40 | 109 | -2.16 | 3.44 | 0.25 | 0.25 |
| | 60 | 504 | -2.11 | 3.36 | 0.23 | 0.29 |

Table 5.10: Data on Cassegrain rotator effects on Stokes zeropoints.

mirror) and nuances relating to RINGO3 in timing and optics.

**Depolarisation angular dependence**

For polarised standards, observations were taken at 3 rotmount angles, -60 °, 0 °and +60 °. With the Stokes zeropoints valid to correct for instrumental polarisation at rotmount angles, corrections were made to the dataset using the `getzeropoints()` function (Appendix A, Listing A.7). With the polarised standards plotted in the q-u plane, for all rotmount angles of observation (-60 °, 0 °, +60 °), the polarisation rings were produced as shown in Figure 5.15.

Hiltner 960 (standard *d*) produces the most well sampled polarisation rings, and a visual analysis shows an obvious ellipticity for the f and e bands. The fact that there are not 3 superimposed ellipses of different angles shows that the data is consistent with a well sampled singular population polarisation ring across the 3 rotmount angles for which the data was taken.

The data for bands d and f of Hiltner 960, were split into datasets for each of the rotmount angles of observation. The ellipticity, $\epsilon$, and angle of ellipse, $\theta_\epsilon$ were deduced for the datasets and results are tabulated in Table 5.11.

| Band | Rotmount(°) | $\epsilon$ | $\theta_\epsilon$ (°) |
|---|---|---|---|
| d | -60 | 0.04 | 103 |
| | 0 | 0.10 | 110 |
| | 60 | 0.09 | 132 |
| f | -60 | 0.11 | 119 |
| | 0 | 0.12 | 117 |
| | 60 | 0.10 | 120 |

Table 5.11: Analysis of the ellipticity, $\epsilon$, of polarisation rings for Hiltner 960, plotted using data from different rotmount angles. The data had been corrected for instrumental polarisation, but not instrumental depolarisation. Each measurement was taken on a sample of $\sim 100$ datapoints.

The data for the d band shows variance in the polarisation rings. However, with a lower ellipticity than the other bands (see Table 5.15) there would be an expected higher variation in angle. Variation in ellipticity for the -60 °datapoints is unexplained and no quantitative analysis into the likelihood of this result being consistent with the number and position of data points has been undertaken.

The conclusion of this investigation is that with the f camera there is no effect on the angular dependence of depolarisation with rotmount angle. In the absence of further data and analysis, we tentatively extend this conclusion to all bands of RINGO3.

### Depolarisation factor

Once the data was corrected for ellipticity, analysis of the average polarisations and standard deviations of the magnitude of polarisation were undertaken for both Hiltner 960 and BD+25°727. The data is presented in Table 5.12

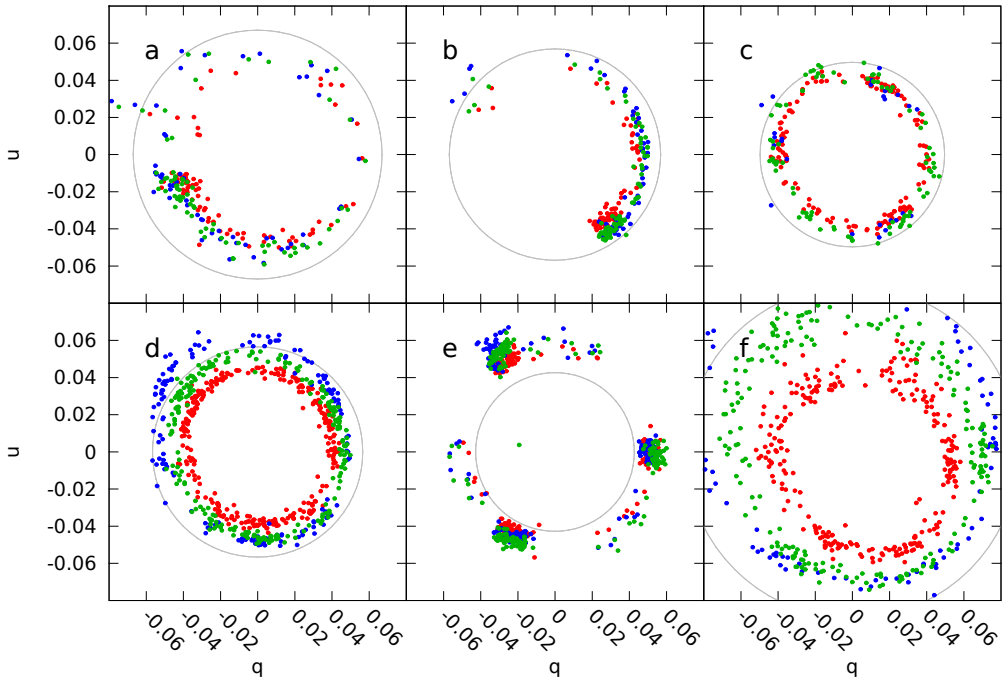


Figure 5.15: Polarisation rings plotted with data for all 3 RINGO bands (d-red, e-blue, f-green) at all rotmount angles. The clear ellipses for standards *d* and *f* show that the rotmount angle has no visible effect on the angle dependency of depolarisation. The threshold for data to be included was 1 %, explaining the lower number of points for standard *c* in the RINGO3 e band

With the depolarisation factor, there is a variation between the average polarisation between different angles for all cameras that are beyond the standard error on the mean (defined as $\sigma_p/\sqrt{N}$). This shows that the means of the distributions are definitely not consistent. This implies that there could be a noticeable difference between rotmount angles in the level of depolarisation of the telescope optics.

However, with no correlation between the two standards, or between the cameras, it is assumed that the variance is not a systematic effect and remains unexplained. It can be seen with Hiltner 960, that the standard deviation of measurements is the greatest with band e, but this is not the same with observations of BD+25°727.

| Standard | Band | Rotmount(°) | Obs | $\mu_p$ | $\sigma_p$ | $SE_\mu$ |
|---|---|---|---|---|---|---|
| BD+25°727 | d | -60 | 63 | 5.53 | 0.31 | 0.04 |
| | | 0 | 62 | 5.46 | 0.27 | 0.03 |
| | | 60 | 65 | 5.12 | 0.27 | 0.03 |
| | e | -60 | 59 | 6.26 | 0.53 | 0.07 |
| | | 0 | 57 | 5.74 | 0.37 | 0.05 |
| | | 60 | 58 | 5.58 | 0.32 | 0.04 |
| | f | -60 | 68 | 5.98 | 0.58 | 0.07 |
| | | 0 | 68 | 6.01 | 0.28 | 0.03 |
| | | 60 | 68 | 5.93 | 0.27 | 0.03 |
| Hiltner 960 | d | -60 | 92 | 4.17 | 0.34 | 0.04 |
| | | 0 | 91 | 4.35 | 0.28 | 0.03 |
| | | 60 | 91 | 4.34 | 0.31 | 0.03 |
| | e | -60 | 52 | 5.75 | 0.76 | 0.11 |
| | | 0 | 53 | 5.89 | 0.59 | 0.08 |
| | | 60 | 49 | 5.66 | 0.54 | 0.08 |
| | f | -60 | 79 | 5.03 | 0.30 | 0.03 |
| | | 0 | 77 | 5.23 | 0.28 | 0.03 |
| | | 60 | 77 | 5.14 | 0.24 | 0.03 |

Table 5.12: Average polarisations of observations of HILT 960 and BD+25°727 taken at 3 different rotmount angles. The averages, $\mu_p$, are of data which has been corrected for instrumental polarisation and ellipticity, but not by the depolarisation factor. The standard deviation, $\sigma p$ and standard error on the mean, $SE_\mu$ are also included.

### Conclusion on effect of rotmount

With instrumental polarisation and the angular dependence of depolarisation, there is no discernible effect from differing rotmount angles on the data. With the rich dataset, we conclude that rotmount is not of concern when making polarimetric measurements, with any variation undetectable, being smaller in magnitude than the normal variation of RINGO3 measurements.

However, with depolarisation factor the data are not so clear. The variances here remain unexplained and uninvestigated. We label them to be not of concern, as when observing science sources the lower signal to noise dominates the uncertainty in measurements. Furthermore, science measurements are taken at a single rotmount angle, and can be expected to be consistent with each other in the levels of depolarisation.

### 5.3.2 Field flatness to polarisation

As with RINGO2, the RINGO3 field flatness to polarisation was performed using observations of the zenith sky on the night of 22nd September 2013. The observing and reduction methods used were identical to those specified in Section 5.2.1. A series of observations with mirror closed and open were performed on the evening of 22nd September 2013 over the period of half an hour of sunset. One observation which is presented in Figure 5.16 was obtained at 19:14:01 UT, which corresponded to the sun having an altitude of -1 °.

Whilst the polarisation flatfield for RINGO2 (Figure 5.2) showed little discernible structure, the flatfields for RINGO3 show a ringed pattern which mirrors the vignetting patterns described in 3.6. The measured polarisation increases towards the edges. This is expected as the light which is vignetted will be from reflections on one side (edge) of the mirror, leading to non rotational symmetry in the reflections for the rest of the beam.

Considering only the unvignetted region, the polarisation flatfields confirm similar performance to RINGO2 for band d and band f, with a variation of $\sim$2 % on the polarisation measurement within the non heavily vignetted field, the boundary of which is defined at the point at which the flux is 50 % of that in the field centre.

However the e camera (2 dichroic reflections), has a slightly worse performance with a variance of $\sim$4 % on the measurement. Also there is a pattern of two streaks of a lower polarisation level within this area, which coincide with features visible on the standard photometric flatfield for which the data were corrected before doing this analysis.

The conclusion is that cameras d and f have no issues (above and beyond RINGO2) with polarisation across the non heavily vignetted field. However, the e band perfor-

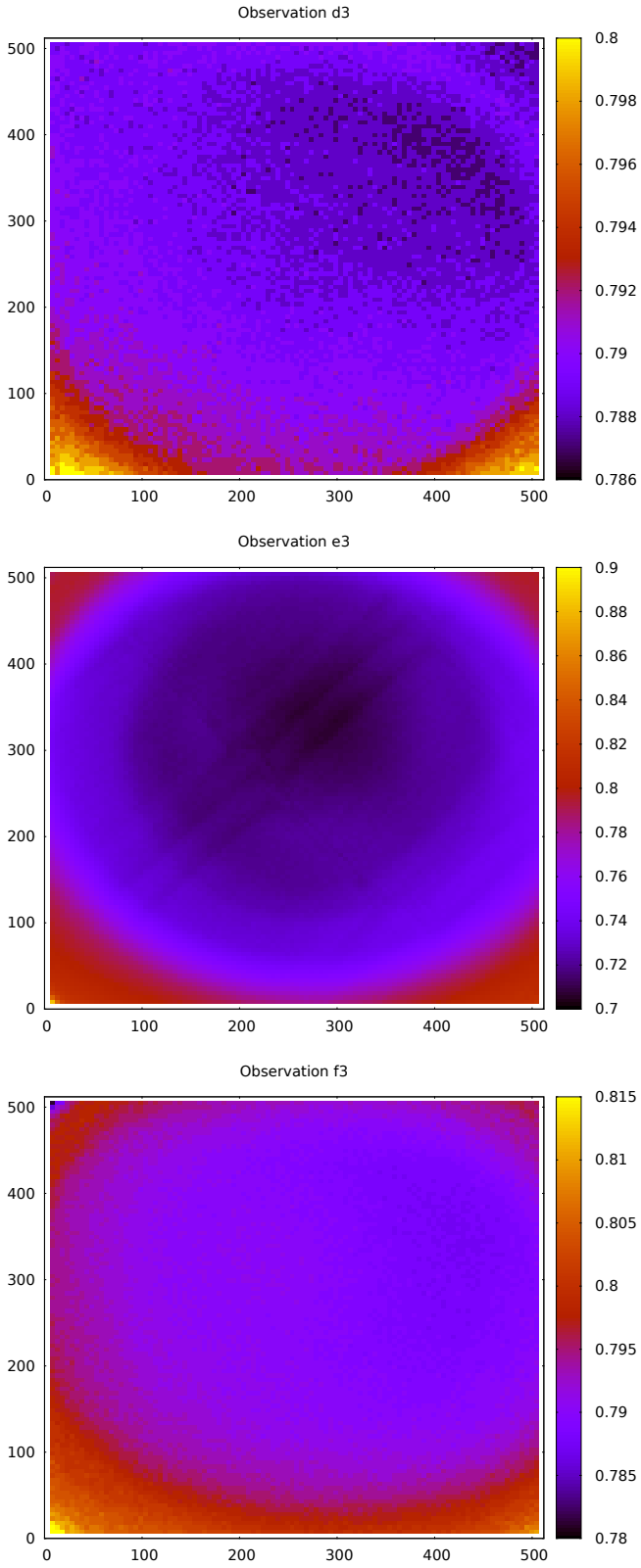


Figure 5.16: Polarisation flatfields of the d (top), e (middle) and f (bottom) bands of RINGO3 from a single observation of the zenith sky at sunset (19:14:01 UT) on 22/09/13. Polarisations on the heat legend for each plot are shown in decimal rather than percentage form.

mance regarding repeatability is markedly poorer, with up to a $\sim$6 % variance in the field. As described previously, to make corrections for these features would require observations and analysed correction maps for all angles of polarisation, which have not been performed due to the complexities of the required investigations.

### 5.3.3 Instrumental depolarisation

As with RINGO2, the characterisation of depolarisation for RINGO3 involved using the definition of a characteristic ellipse to allow depolarisation angle dependency to be corrected. After this a single depolarisation factor, $D$, can be deduced for all data. The calculation of this depolarisation factor is considered in a different fashion to the RINGO2 analysis which used contemporaneous measurements of BD+59°389, to confirm a less than convincing 'line of best fit approach'.

For this further analysis we consider the spectral dependence of polarisation in the standards and devise a best fit method with the data and resources available.

#### Characteristic ellipses

The large dataset was analysed for any angular dependence using the same method as RINGO2, namely finding characteristic ellipses from plots of polarisation rings. The polarisation rings prior to ellipse correction have already been presented in Figure 5.15.

Analyses of the polarisation rings, which comprise data from multiple rotmount angles, were performed using the same least squares fitting method as for RINGO2, namely Fitzgibbon et al. (1999). The data for all polarisation rings is presented in Table 5.13.

Using human discretion (based on the visual quality of the data in Figure 5.15) and a method looking for the mode of the data, we define the characteristic ellipses for each camera. The data is presented in Table 5.15.

### Measured polarisation values

After correcting all data for ellipticity using the characteristic ellipse values, the average measurements of the standards were taken to deduce the depolarisation factor for each of the RINGO3 bands. The values are included in Table 5.13. It is the trend for all standards (bar HD155528, standard *c*), that the measured polarisation is lowest in the higher wavelength bands. Whilst this could be an instrumental effect (differing depolarisation factors for each band), this trend is expected to be observed. With the standards being polarised sources due to intervening dichroic dust scattering, we know that shorter wavelengths have a higher chance of being scattered, leading to higher polarisations.

Confirmation of the visual data of the polarisation rings is also provided. Namely that observations of standards *a* & *f* are unstable and almost twice as variable compared to the other sources. Secondly, the e band seems to suffer the greatest variation in polarisation measurements, with standard deviations $\sim 1.5 \rightarrow 1.8$ times larger than the other two bands.

### Deducing Hiltner 960 polarisations for RINGO3 bands

In contrast to the RINGO2 analysis of depolarisation factor, a single shot approach was attempted based on the assumption that the catalogue values of Hiltner 960 provided in Schmidt et al. (1992) are correct and still valid. Whilst the analysis done for RINGO2 (Figure 5.13) showed that the standards are not reliable, the analysis showed that the polarisation of Hiltner 960 was consistent with the catalogue value.

| Standard | Designator | Band | $\epsilon$ | $\theta_\epsilon$ (°) | $\mu_p$ (%) | $\sigma_p$ (%) |
|---|---|---|---|---|---|---|
| BD+59°389 | *a* | d | 0.07 | 168 | 4.82 | 0.65 |
| | | e | 0.19 | 140 | 5.77 | 0.72 |
| | | f | 0.16 | 136 | 5.60 | 0.59 |
| BD+64°106 | *b* | d | 0.16 | 124 | 4.54 | 0.30 |
| | | e | 0.20 | 128 | 5.37 | 0.41 |
| | | f | 0.16 | 124 | 5.17 | 0.27 |
| HD155528 | *c* | d | 0.09 | 123 | 4.19 | 0.25 |
| | | e | 0.11 | 118 | 4.48 | 0.45 |
| | | f | 0.14 | 124 | 4.64 | 0.25 |
| Hiltner 960 | *d* | d | 0.08 | 120 | 4.29 | 0.32 |
| | | e | 0.14 | 122 | 5.77 | 0.64 |
| | | f | 0.12 | 120 | 5.13 | 0.28 |
| BD+25°727 | *e* | d | 0.09 | 107 | 5.37 | 0.34 |
| | | e | 0.15 | 114 | 5.86 | 0.51 |
| | | f | 0.11 | 112 | 5.97 | 0.40 |
| VI Cyg #12 | *f* | d | 0.10 | 113 | 5.16 | 0.74 |
| | | e | 0.14 | 118 | 9.04 | 1.15 |
| | | f | 0.13 | 123 | 7.38 | 0.49 |

Table 5.13: Ellipticity, $\epsilon$ and angle, $\theta_\epsilon$, of polarisation rings for RINGO3 shown in Figure 5.15. The values were calculated as per RINGO2 using the least squares method defined by Fitzgibbon et al. (1999). The average values of polarisation, $\mu_p$ and the standard deviation, $\sigma_p$ are the measured values **after** ellipse correction, but not corrected by depolarisation factor, $D$.

This assumption allows us to use the best observed standard which provides the least variation in the RINGO3 polarimetric measurements. Hiltner 960 also has catalogue values for UBVRI bands.

With polarisation being a function of wavelength, the catalogue values in Johnson and Cousins bands (Bessell, 1979; Johnson & Morgan, 1953) will need to be converted to RINGO3 bands. Figure 5.17 shows the coverage of these bands versus the 3 bands of RINGO3. For RINGO3 we calculated a mid flux wavelength for each band to match to the standard data.

The mid flux wavelength is defined as the wavelength which splits the band into two equal flux regions for a colourless (flat spectrum) source. This takes into account the overall instrument throughput devised in Chapter 2, which comprises lens throughput and CCD quantum efficiency. The data for the response of the Johnson and Cousins bands were obtained from the Lausanne Photometric Database (Mermilliod

et al., 1996), and the mid flux wavelengths of each band were similarly calculated.

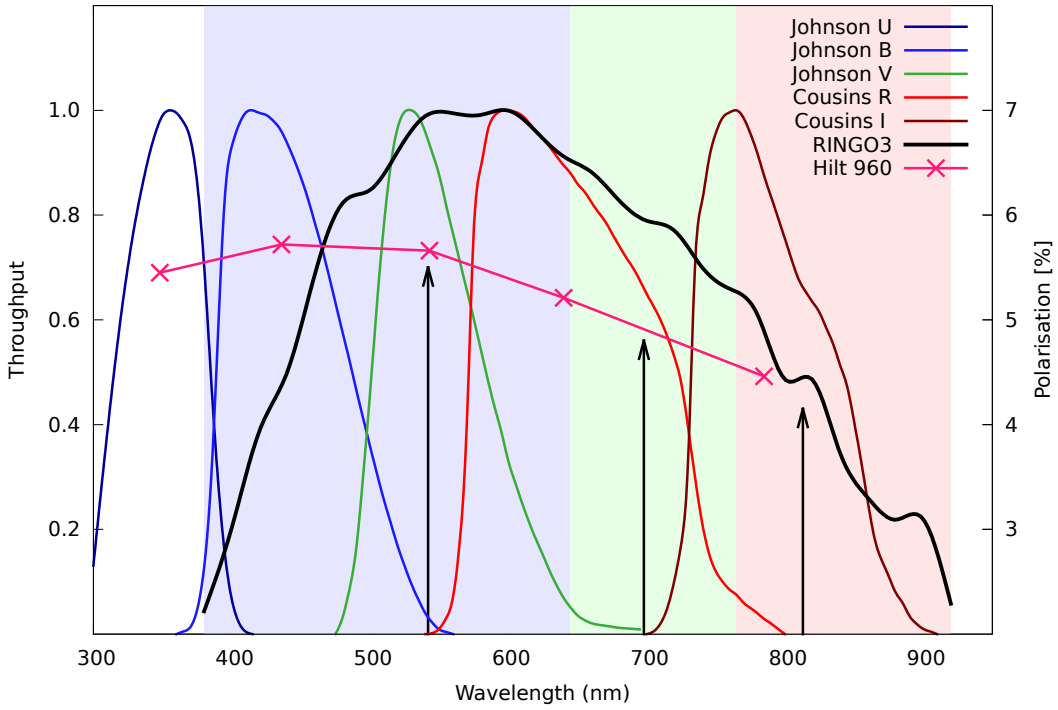


Figure 5.17: Comparison of RINGO3 bands and overall instrument throughput against the response of the photometric bands used for measurements of polarisation in Table 5.3 from Schmidt et al. (1992). Data of response curves for Johnson Cousins bands was obtained from the Lausanne Photometric Database Mermilliod et al. (1996). The measured polarisations of Hiltner 960 for UBVRI bands is shown. The vertical arrows show the mid flux wavelength of the RINGO3 bands, when a colourless source (flat spectrum) is observed.

The assumption is made that the variation on polarisation between the mid flux observations in UBVRI are linear. We take the true polarisation which the RINGO3 bands should measure as the intersection of the RINGO3 mid flux wavelength with this line. We deduce the expected, measured and depolarisation factor of each band as shown in Table 5.14

The results produce depolarisation factors where $D \leq 1$ for all bands. The physical meaning of these values would be an inverse depolarisation effect in the telescope and

| Band | Measured Polarisation | Expected Polarisation | Depolarisation Factor |
|---|---|---|---|
| d | 4.29 | 4.31 | 1.00 |
| e | 5.77 | 5.66 | 0.98 |
| f | 5.13 | 4.91 | 0.95 |

Table 5.14: Depolarisation factors ($D$) of RINGO3 from analysis of Hiltner 960. These are calculated from the measured ($M_p$) and expected values ($E_p$), where $D = E_p/M_p$. The measured polarisation is the ellipse corrected average value of data from all rotmount angles. The expected values were obtained from the intersection of the RINGO3 mid flux wavelengths for each band with the curve of Hiltner 960 polarisation (Figure 5.17).

instrument. It is strongly believed that this result is false and could be due to a mixture of three effects. Firstly, in the process of ellipse correction the value of polarisation for a datapoint can only ever increase, thus amplifying the measured polarisations. Secondly, the polarisation of Hiltner 960 could well have changed since its measurement nearly 25 years before the RINGO3 observations in Schmidt et al. (1992).

The final possible reason for this is related to the differing spectra of sources. Figure 5.17 shows perfectly how the polarisation of a source varies throughout the wavelength range of the instrument. Narrow band observations of polarisation are more immune to effects of differing spectral profiles of sources. However with wider bands, such as band e ($\sim$265 nm), the spectral profile of sources will have an effect on the measured polarisation. This is discussed further in Section 5.4.

**Depolarisation factor with available standard data**

To deduce the depolarisation factor more accurately, the analysis is reverted to that performed for RINGO2. This analysis involved the plotting of measured versus catalogue polarisation with the depolarisation factor being the inverse of the gradient of the line of best fit. To obtain expected polarisation values, the same analysis performed for Hiltner 960 is extended to that of the other 5 polarimetric standards.

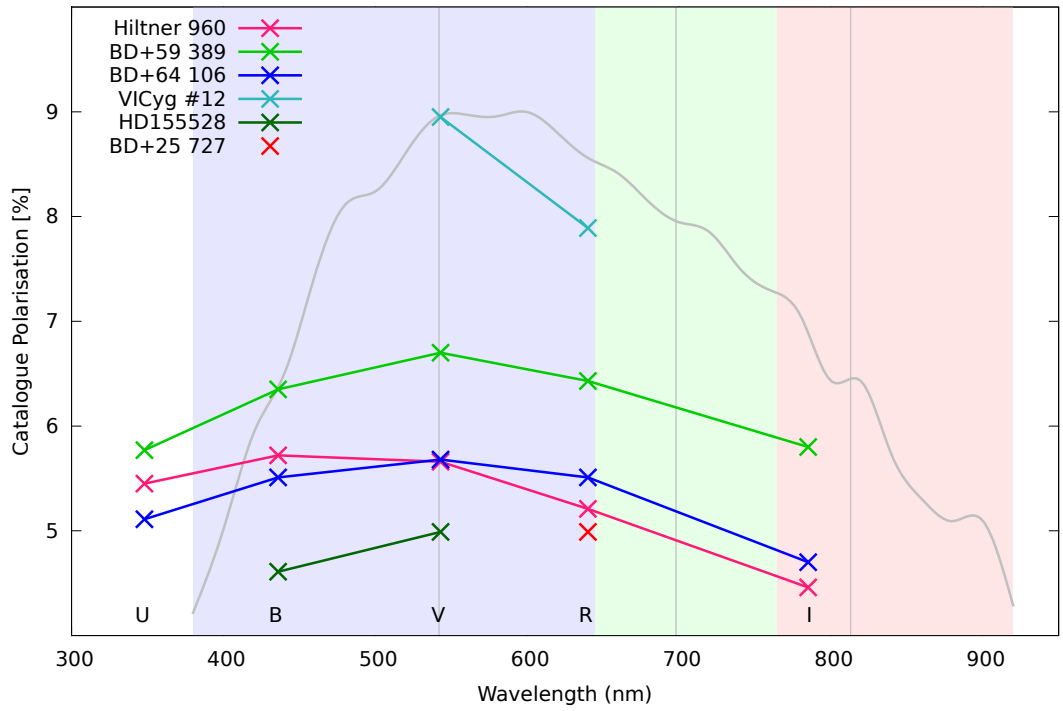


Figure 5.18: Comparison of measurements of polarimetric standards and RINGO3 wavebands. In grey are the response curve of RINGO3, and the mid flux wavelengths for each band (calculated for a colourless source).

Figure 5.18 shows the polarisation data available for the 6 polarimetric standards, with values as in Table 5.3. The expected polarisation for the e camera is as per the catalogue V-band values. For band f, the point of intersection of the mid flux wavelength with the 3 available curves provides the expected value. For band d, the gradient of the line crossing the f band is extended and the intersection found.

The plots of the measured (Table 5.13) versus expected polarisation values are presented in Figures 5.19. The lines of best fit were calculated using the linear regression function in `gnuplot`. The resultant gradients were 0.93, 0.99 & 0.97 for the d, e & f bands respectively. This yields depolarisation factors of $D_d = 1.07$, $D_e = 1.01$ & $D_f = 1.03$.

As with RINGO2, the dearth of polarimetric standards, and recent measurements thereof, is a major hindrance in the accurate calibration of polarimeters such as RINGO2/3

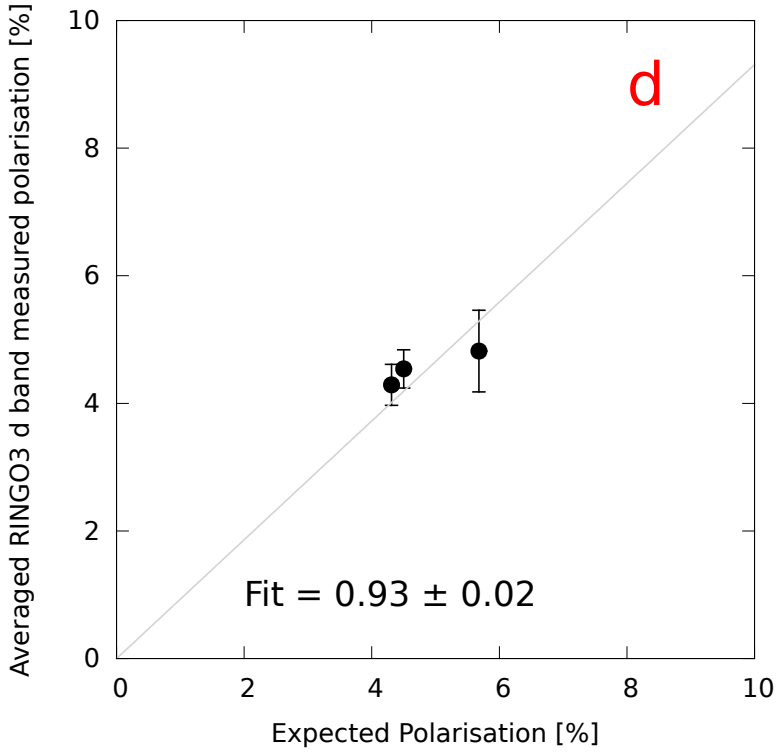


Figure 5.19: Plot of measured versus expected polarisation for standards in RINGO3 d band with the gradient of the least squares fit and the asymptotic standard error. The inverse of the gradient is the calculated depolarisation factor.

which have wide operating bands. However, the analysis here provides reasonable depolarisation factors.

### 5.3.4 Polarisation angle calibration

The same procedure as performed for calculating the polarisation angle correction for RINGO2, was used for the 3 bands of RINGO3. By comparing measured versus catalogue values of polarisation angle for the six standards, a distribution of correction angles were produced for each source in each band. Figure 5.22 contains the histograms of the correction angle required for each observation in the analysed dataset. As with RINGO2, the conclusion that the polarisation angle of BD+25°727 (standard *e*) is $\sim 10\,^{\circ}$ lower than listed in Turnshek et al. (1990).

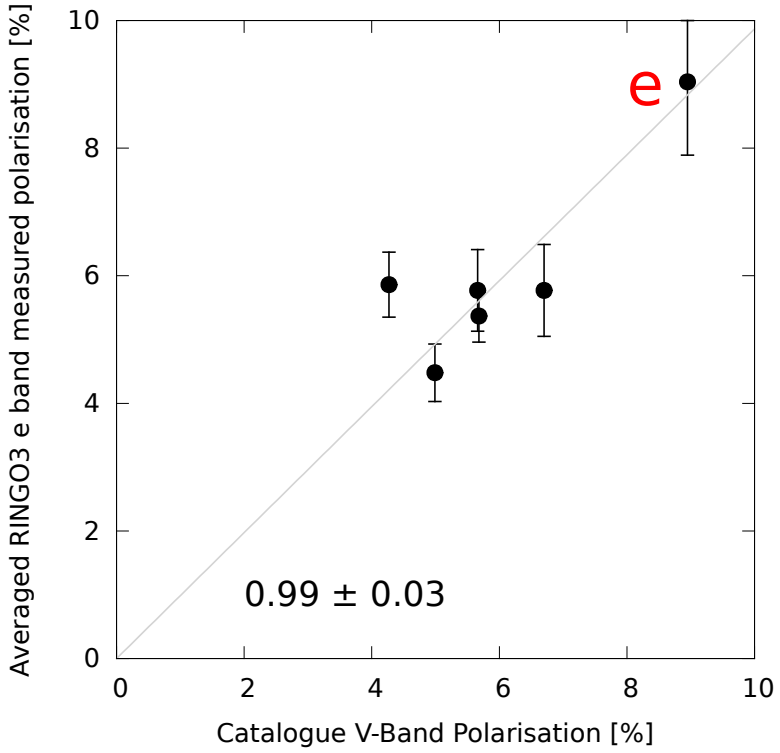


Figure 5.20: Plots of measured versus expected polarisation for standards in RINGO3 e band with the gradient of the least squares fit and the asymptotic standard error. The inverse of the gradient is the calculated depolarisation factor.

With the single polaroid for the 3 bands of RINGO3, the correction angle should be identical across them. By analysing the histograms we find the correction angle, $\theta_c$=154°.

Histograms for the individual bands are provided in Appendix E. It is interesting to note that the histograms of the f band of RINGO3 are much tighter than that of the other two bands, especially for VICyg #12 (standard *f*).

## 5.4 RINGO2+3 characteristics

Presented in this section is a short summary of the investigations performed on RINGO2 and RINGO3 for characterisation purposes. It covers the field flatness of

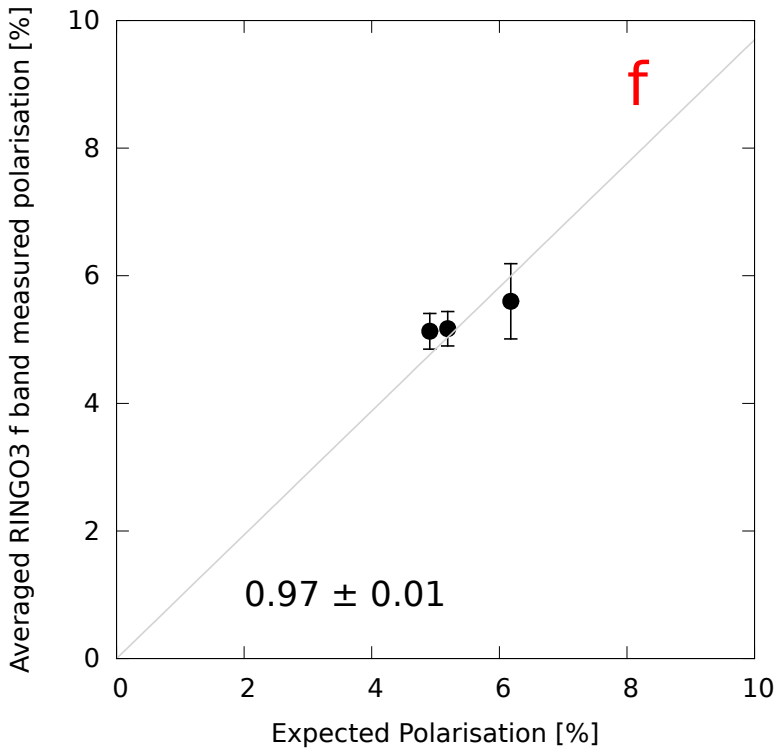


Figure 5.21: Plots of measured versus expected polarisation for standards in RINGO3 f band with the gradient of the least squares fit and the asymptotic standard error. The inverse of the gradient is the calculated depolarisation factor.

the instruments, the effect of rotmount on observing, the instrumental polarisation and depolarisation and finally review the performance of the polarimeters for their intended science goal.

### Field flatness to polarisation

Observations of the zenith sky at sunset provided a high polarisation source, which was uniform in polarisation magnitude across the field. Whilst the environmental brightness during this time provided scattered radiation within the telescope optics, observations with the mirror cover open and closed enabled a subtraction to be made on the data to remove the scattered light.

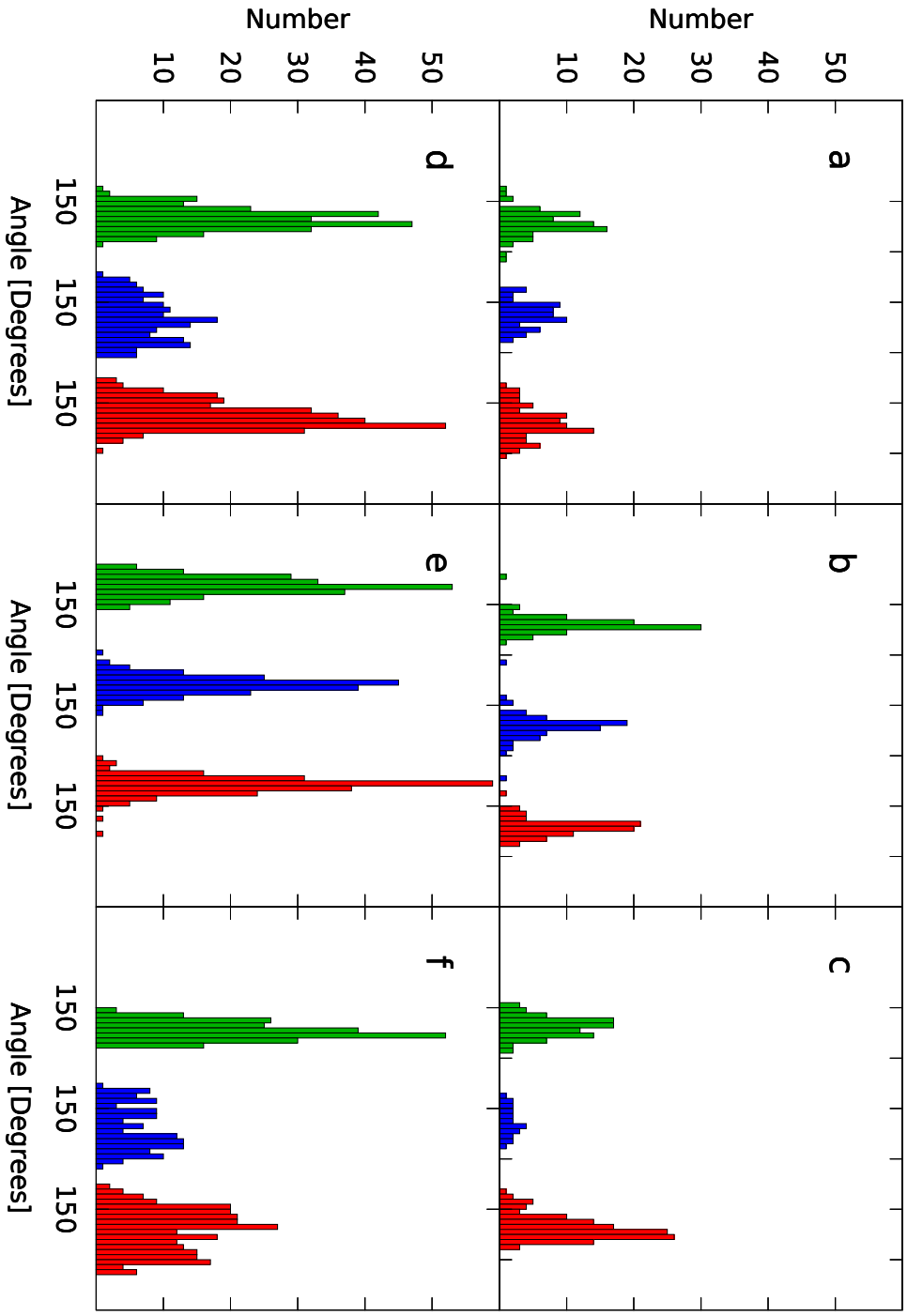


Figure 5.22: Histograms of the correction angles, $\theta_c$, for the 3 RINGO3 bands to enable each measurement to match its catalogue angle from Schmidt et al. (1992) and Turnshek et al. (1990). Each band is separated by 20°in the plot, and the histograms are presented individually in Appendix E. See Equation 5.4. Standard *f*, BD+25°727, has a correction angle of $\sim 10°$ less in all bands, as with RINGO2 (Figure 5.14). This is a strong suggestion that the polarisation angle stated in Turnshek et al. (1990) has changed by $\sim -10°$. We take the correction angle to be identical for all 3 bands, at $\theta_c = 154°$.

The polarisation flatfields for RINGO2 provided confirmation that measurements made across the $4 \times 4$ arcminute field had variations of less than 3 % on the measured polarisation value. The flatfields for RINGO3, however, instantly showed ring features in the measured polarisation which matched the vignetting pattern seen in the instrument due to the longer path length of the collimated beam within the instrument. With RINGO3, the area in the region of less than 50 % vignetting showed a variance of 4 % on the measurement across the field for bands d and f, with 6 % variance for band e. The higher variance in band e is due to two 'streak' features which are also apparent in the e band flatfield.

Corrections for the variance were not investigated, as this would have required flatfield maps of the field to be created for every possible incoming polarisation angle. This would be a possible future line of investigation. However attempts at gaining data for this by observing the zenith sky, whilst rotating the telescope in azimuth, proved less than successful.

**Effect of Cassegrain rotation**

There were issues seen with RINGO3 due to an interaction between the dichroic mirrors and the rotating 100 % linearly polarised collimated beam. After this flaw in the instrument was resolved by placing the depolarising element into the collimated beam directly after the collimator lens , data of the standards was taken intensively at a number of Cassegrain rotator (rotmount) angles, providing a rich dataset for analysis.

As with a previous investigation with RINGO2, no evidence was found that the rotmount angle had any effect on instrumental polarisation or depolarisation. This is an especially important result when following up GRBs. For the fastest follow-up, the LT-TRAP pipeline does not move the Cassegrain rotator from the position that the last overridden observation was using.

The other important conclusion from this result is that the angular dependence of depolarisation is most likely due to the reflection of the 45°science fold mirror in the A&G unit of the Liverpool Telescope. A side mounting port is less than ideal for a polarimeter and a mount at the Cassegrain focus would provide the best observing performance in this respect. Due to the varied instrument suite on the Liverpool Telescope and the weighting of scientific importance, the Cassegrain focus is reserved for the main imaging instrument (formerly RATCam, now IO-O).

**Instrumental polarisation**

Analysis of observations of zero polarised standards shows adequate instrumental stability in the temporal realm. However, there is a concerning, and uncorrelated variation from measurement to measurement. For most accurate values of instrumental polarisation it is recommended to take an average of the Stokes zeropoints from a large number of measurements taken by the RINGOstand programme in the nights preceding and after the science observations.

**Instrumental depolarisation**

The correction for instrumental depolarisation has been the most difficult element to investigate and quantify. RINGOstand routinely takes observations at a limited number of set rotmount angles, with only one angle being used for RINGO2. An artifact of observing with a fixed rotmount on the altitude-azimuth Liverpool Telescope is the production of polarisation rings in the q-u plane. These provide an excellent visualisation of the polarimetric measurements.

Within these polarisation rings the angular dependence of depolarisation was evident in the slight ellipticity of the polarisation rings. This ellipticity was investigated and equations provided to define the ellipse and thus make corrections to the datapoints. A process of ellipse correction was defined to correct datapoints to remove any angular variance in depolarisation, allowing a single depolarisation factor to be applied.

The depolarisation factor was obtained for both RINGO2 and RINGO3 by comparing the average measured polarisation against the catalogue polarisation. However with a limited number of polarimetric standards and the possibility of a change in polarisation since their cataloguing over 20 years ago, this is a less than precise analysis.

Provided in Table 5.15 are the necessary characteristic ellipse parameters and depolarisation factors to correct data for instrumental depolarisation taken with the instruments during the periods shown. Also included are the correction angles required to transform a polarisation angle from RINGO2/3 into a sky angle, using equation 5.4.

| Instrument | Date Range (yyyy/mm) | $\epsilon$ | $\theta_\epsilon(^\circ)$ | D | $\theta_c(^\circ)$ |
|---|---|---|---|---|---|
| RINGO2 | 2011/03 $\rightarrow$ 2012/09 | 0.14 | 92 | 1.22 | 48 |
| RINGO3_d | | 0.09 | 120 | $1.07 \pm 0.02$ | 154 |
| RINGO3_e | 2014/06 $\rightarrow$ 2015/03 | 0.14 | 118 | $1.01 \pm 0.03$ | 154 |
| RINGO3_f | | 0.13 | 123 | $1.03 \pm 0.01$ | 154 |

Table 5.15: The final deduced characteristics of depolarisation and correction angles for RINGO2 and RINGO3. The errors quoted on the values of the depolarisation factor D are from the asymptotic standard error of the least squares fits from Figures 5.19, 5.20 and 5.21. These are errors of the fit only. Due to the small number of standards and the lack of confidence in the true values of polarisation the true error on these values is unquantifiable

The depolarisation factors for the bands of RINGO3 are consistently lower (between 12 % $\rightarrow$ 17 %) than for RINGO2. If one studies the extinction ratio of the two different models of polarising filter used between the instruments (Chapter 2 Figure 2.2) the results can be expected. Within the RINGO2 band, above 700nm, the contrast ratio of the polaroid drops significantly. This is viewed as an increase in depolarisation. Similarly with the RINGO3 bands, the higher depolarisation factor for the d band (compared to e & f bands) can be explained by the lower contrast ratio of the polarising filter at the higher wavelengths. This gives confidence in the validity of the method for deducing the depolarisation factor.

### 5.4.1 RINGO polarimeters in context

RINGO2 and RINGO3 are very specific polarimeters, optimised for high cadence observations of highly transient events. The unique design required to enable this high cadence operation is not without drawbacks, and provides an unidentified variance above what would be expected by the photometric error, when observing bright standards.

However, the RINGOstand observations of polarimetric standards has provided an extensive dataset to perform many investigations into the stability and characteristics of the instruments. There is an unquantifiable uncertainty in the accuracy of the depolarisation factor. However as the prime science goal of the instruments is to observe depolarisation evolution in faint sources, this is not of major concern.

# Chapter 6

# Gamma-ray burst follow-up with RINGO2

As part of LT-TRAP (Liverpool Telescope Transient Rapid Acquisition Pipeline) (Guidorzi & et al, 2006), RINGO2 provided the polarimetric capabilities of the Liverpool Telescope's follow-up capabilities from 1st August until decommissioning on 26th October 2012. The policy upon a GRB coordinates network (GCN) trigger was to perform a first response observation with RINGO2, before switching to RATcam for a series of wider field (4.6 x 4.6 arcmin) observations to allow detection of a transient. Over time, the first response polarimetric observation of RINGO2 was extended to 600 seconds.

Subsequent identification (or non-identification) of an optical counterpart to the gamma-ray burst (GRB) then informed the next steps. With a member of the team alerted, a second polarimetric observation to the first response could be manually scheduled. Decisions were made based on the magnitude and decay rate of any identified transient. The time frame for these secondary observations was between 20 - 60 minutes post trigger. The trigger time is labelled as $T_0$. Observation time post trigger is referred to in terms of $t - T_0$.

For each observation the onsite reduction pipeline stacked the raw data of each polaroid rotation, producing 8 files for initial analysis. After this, the raw data could be arranged into smaller temporal stacks, called sub observations. From the raw data there is the possibility of producing any number of polarimetric and photometric datapoints during the epoch of observation, albeit with a reduced signal to noise ratio. This flexibility has enabled RINGO2 and RINGO3 to be successful high cadence photometers as well as polarimeters.

This chapter focuses exclusively on GRBs observed by RINGO2 and includes much material that resulted from work performed by astrophysicists within the Liverpool Telescope GRB collaboration. Onsite data reduction (flatfielding, debiasing, etc.) and stacking of sub observations was performed by Dr Rob Smith.[1] Further to this Dr Rob Smith also performed analysis on the photometric band equivalence of RINGO2 to the Sloan photometric system (Fukugita et al., 1996). Photometric analysis of RINGO2 data, linking with observations from other observatories and lightcurve fitting was performed by Dr Drejc Kopač.[1,2] Polarimetric analysis was undertaken by myself with guidance from Professor Iain Steele.[1]. Analysis and interpretation was achieved with assistance from other members of the team, namely Professor Andreja Gamboc,[2,3] Professor Shiho Kobayashi,[1] Dr Francisco Virgili,[1] Dr Richard Harrison,[1,4] Dr Christiano Guidorzi,[5] Dr Andrea Melandri[6] and Jure Japelj.[2] The collaboration was led and coordinated by Professor Carole Mundell.[1,7]

[1]Astrophysics Research Institute, Liverpool John Moores University, IC2, Liverpool Science Park, L3 5RF, UK
[2]Department of Physics, Faculty of Mathematics and Physics, University of Ljubljana, Jadranska 19, 1000 Ljubljana, Slovenia
[3]University of Nova Gorica, Vipavska 13, 5000 Nova Gorica, Slovenia
[4]Department of Astrophysics, School of Physics and Astronomy, Tel Aviv University 69978 Tel Aviv, Israel
[5]Physics Department, University of Ferrara, Via Saragat, 1, 44122 Ferrara, Italy
[6]INAF/Brera Astronomical Observatory, via Bianchi 46, 23807, Merate (LC), Italy
[7]University of Bath, Claverton Down, Bath, BA2 7AY, UK

## 6.1 Observations of gamma-ray bursts with RINGO2

During the observational lifetime of the instrument, 19 GRB triggers were followed up with RINGO2. Of these, 9 GRBs were bright enough during the time of observation ($\lesssim$19th magnitude) to enable a photometric measurement to be made. Polarimetric analysis of these observations was undertaken in their fully stacked forms (i.e. 8 files for the observation period).

Details of the GRB observations are listed in Table 6.1. Of these observations, a preliminary analysis of polarisation was performed on the data for GRB 110205A and presented in Cucchiara et al. (2011).

| GRB | Redshift | RA | Dec | $t - T_0$ (s) | Magnitude (R band) |
|---|---|---|---|---|---|
| 100805A | | 19:59:30.47 | +52:37:39.90 | 140 – 320 | 17.29±0.13 |
| | | | | 1020 – 1198 | 18.76±0.57 |
| 101112A | | 19:28:54.87 | +39:21:11.10 | 176 – 355 | 15.77±0.03 |
| | | | | 715 – 893 | 16.61±0.05 |
| 110205A | 2.22 | 10:58:31.05 | +67:31:30.20 | 422 – 722 | 16.92±0.68 |
| | | | | 3026 – 3506 | 16.37±0.07 |
| 110726A | 1.04 $\rightarrow$ 2.7 | 19:06:52.16 | +56:04:16.00 | 191 – 783 | 17.99±0.11 |
| 120119A | 1.73 | 08:00:06.91 | -09:04:54.30 | 194 – 793 | 17.65±0.04 |
| 120308A | 3.2 $\rightarrow$ 4.0 | 14:36:20.09 | +79:41:12.30 | 240 – 838 | 16.51±0.03 |
| 120311A | | 18:12:22.11 | +14:17:46.40 | 181 – 779 | 18.41±0.18 |
| 120326A | 1.798 | 18:15:37.12 | +69:15:35.50 | 216 – 872 | 18.88±0.14 |
| 120327A | 2.813 | 16:27:27.50 | -29:24:54.10 | 1664 – 2263 | 16.66±0.03 |
| | | | | 2605 – 2784 | 17.11±0.05 |

Table 6.1: GRB observations made with RINGO2, which provided a photometric detection of the optical transient (OT). All bursts were triggered from a SWIFT satellite detection, apart from GRB 101112A, which was detected by INTEGRAL. Redshift constraints were determined for various bursts by other observatories, either by spectroscopic methods (GRB 110205A, GRB 120119A, GRB 120326A, GRB 120327A) or via photometric redshift related to the Alpha-Lyman dropout (GRB 110726A, GRB 120308A). Photometric data for each observation was calculated by Dr Drejc Kopač.

### 6.1.1 Photometry

Photometry was performed for analysis of the RINGO2 GRB sample with observations from RINGO2 and also RATcam. These two instruments provided data that was converted into Sloan $r'$, $g'$, $i'$ and $z'$ magnitudes to create multi-colour lightcurves. To enable better lightcurve sampling, RINGO2 observations were sliced into a number of shorter temporal stacks from the raw data. The depth of these stacks was optimised to provide the best balance between temporal sampling and photometric error. To enable photometric analysis, the 8 data files produced by RINGO2 were stacked together to give a single full flux FITS file. Photometry was performed using an aperture photometry method (detailed in Chapter 4) with an 8px – 10px aperture and an annulus of double the aperture value. The variance of aperture was to provide the most accurate photometry over observations with varying seeing conditions. Instrumental magnitudes were calculated using the standard formula $-2.5\log_{10}(counts)$.

#### Photometric calibration

To convert an instrumental magnitude into an observed magnitude required two standard steps. Firstly the photometric zeropoint of each instrument and band was found using observations of standard photometric fields taken on each night. The observed magnitude then had to be converted into the Sloan band system. These photometric transformations between band systems are common, and depend on the colour (spectral profile) of the source being observed.

For RINGO2, analysis was performed by Dr Rob Smith to determine any required transformations between the observed magnitude of the composite V+R band of the instrument and the Sloan photometric system. A single observation of the field of BD+32°3739 with IO:O was compared with 54 observations with RINGO2. It was found that RINGO2's band equates extremely well with Sloan $r'$ band across a wide colour range. This result means that no photometric transformation is required. The results are shown in Figure 6.1

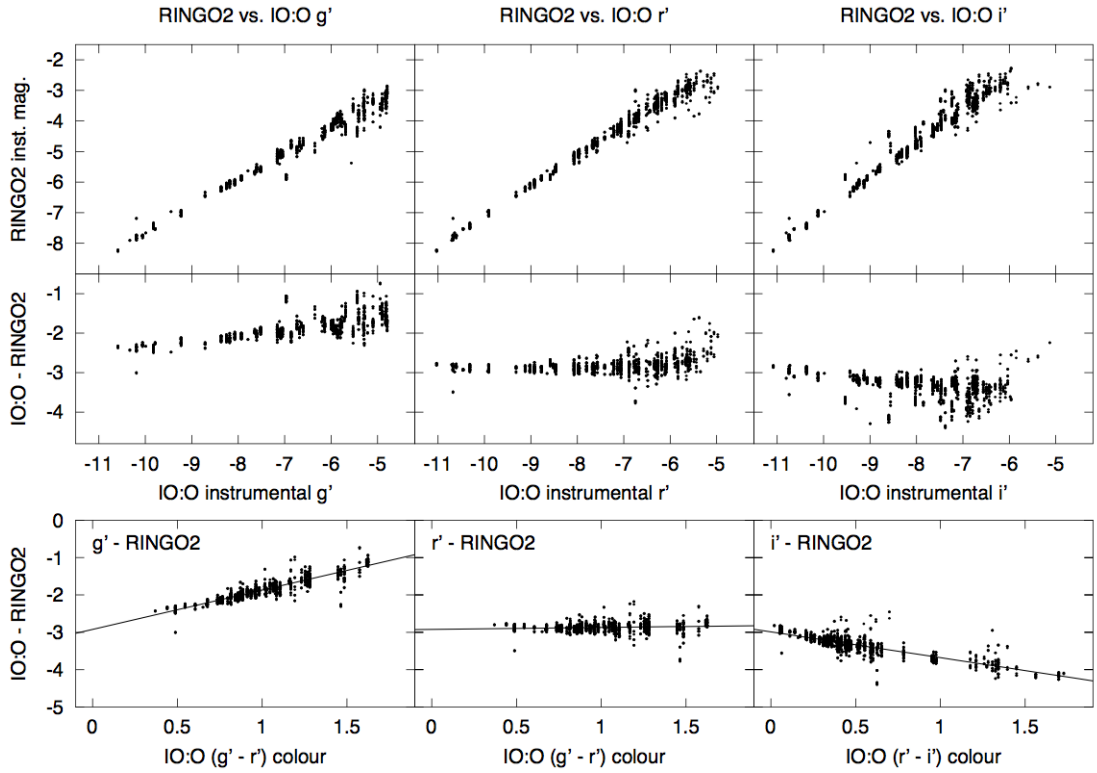


Figure 6.1: Aperture photometry of all stars in the field surrounding star BD+32°3739 (HD 331891). RINGO2 data are observations of this standard star on all photometric nights between 3 June 2012 and 26 October 2012. The comparison IO:O data are a single epoch, obtained on the night of 4 September 2013. The left panels compare RINGO2 to IO:O+$g'$ filter, the central column is RINGO2 and IO:O+$r'$ and the right panels show IO:O+$i'$. The top row directly compares the instrumental magnitudes from the two instruments. The middle row plots the magnitude difference between RINGO2 and various IO:O filters, effectively the zeropoint difference between the instruments, which is shown to be independent of magnitude for filter $r$. The bottom row derives zeropoint colour transformations between the RINGO2 filter and the various SDSS-type filters. Again $r$ is seen to be a good match to the RINGO2 band without applying any colour corrections. All work performed by Dr Robert Smith.

With GRBs being extragalactic sources, Galactic absorption of radiation needs to be accounted for to define lightcurves of the emitted, rather than observed, radiation. This is especially important with a source undergoing spectral evolution during the observations. The absorption (or reddening) caused by Galactic dust has been characterised in a number of studies. Reddening maps give the absorption in magnitudes for different band systems. Schlafly & Finkbeiner (2011) was used to provide reddening values for all bursts apart from GRB 120308A, which used data from Schlegel et al. (1998).

**Lightcurve fitting**

With the necessary photometric corrections being made to all datapoints for observations with RINGO2 and RATcam ($g', r', i', z'$) the data were combined with X-ray data from the Swift x-ray telescope (XRT) (Burrows et al., 2003). To better sample the lightcurves, available data for GRB 110205A was obtained from observations with Swift's ultra-violet/optical telescope (UVOT) (Nousek et al., 1999). For GRB 120119A data from observations with the Panchromatic Robotic Optical Monitoring and Polarimetry Telescopes (PROMPT) (Reichart et al., 2005) in R and I bands provided additional data.

Fitting of lightcurves was performed with either simple power law fitting ($F \propto t^{-\alpha}$) or using the Beuermann function (Beuermann et al., 1999). The 9 lightcurves are presented in Figure 6.2, and individually in Appendix F. GRBs 100805A, 120311A, 120326A and 120327A exhibit lightcurves that are a single power law decay, showing emission which can be accounted for solely by the forward shock. GRBs 101112A, 110205A, 110726A, 120119A and 120308A indicate the presence of significant reverse emission components, either from steep rises in the lightcurve (GRBs 101112A & 110205A) or from brightening 'bumps' in the decay curve.

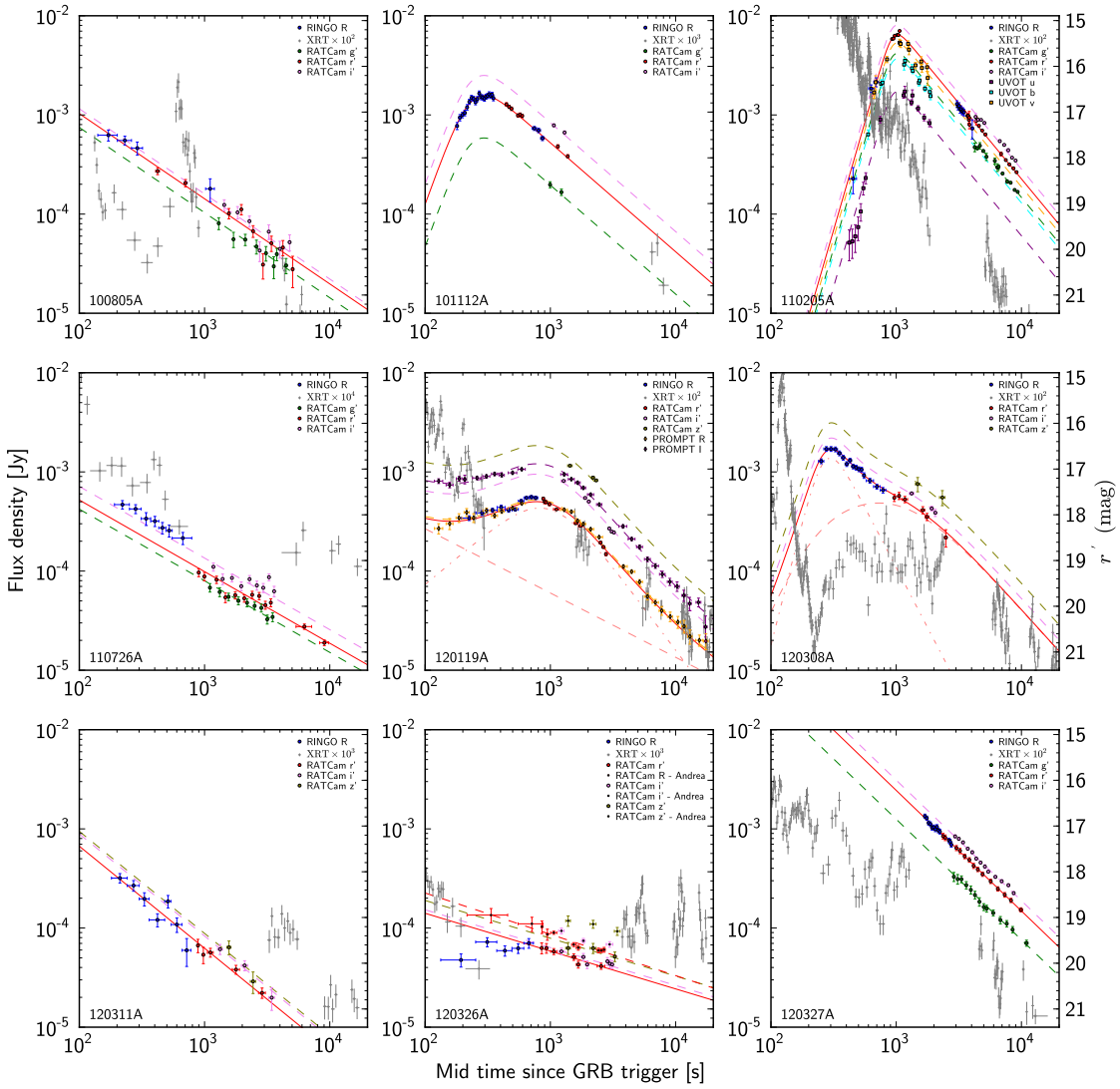


Figure 6.2: Lightcurves showing RINGO2 and RATcam observations with XRT data. Additional optical fitting points from UVOT (GRB 110205A) and PROMPT (GRB 120119A). Larger versions of each lightcurve are in Appendix F. All work performed by Dr Drejc Kopač.

### 6.1.2 Initial polarimetric analysis

Polarimetric analysis was initially performed on the RINGO2 sample before all investigations into the instrumental polarisation and depolarisation of RINGO2 were established (see Chapter 5) and whilst routine error values on polarimetric measurements were not implemented by the `ripe` pipeline. At this stage a quick check to see if the polarisation signal was significant was performed for each observation with RINGO2. To do this plots of Polarisation versus Instrumental magnitude were produced for each burst. The `ripe` pipeline was employed to provide polarimetric analysis of all sources in the field of each full RINGO2 observation. In this quick analysis instrumental polarisation values were basic, and depolarisation was corrected for just using a depolarisation factor of 1.33 (no ellipse correction applied and depolarisation factor without ellipse correction).

Galactic sources can be assumed to have true observed polarisations of less than 1 % (Hall & Mikesell, 1950). However when the photon counting noise affects the precision of photometry on the 8 measurements taken to gain a polarimetric value, then understandably the measured polarisation can be high. The Polarisation versus Instrumental magnitude plots (Figure 6.3) show how fainter Galactic stellar sources in the field give measured polarisations due to the increasing Poisson noise on photometry. All GRBs, bar one, provided polarimetric values which were consistent with the values of stellar sources of similar brightness, indicating no significant polarisation measurement. For these bursts however, the RINGO2 polarimetric observations would be able to provide upper limits on polarisation.

GRB 120308A indicated a polarisation of $\sim$21 %, which was greater than 4 times the measured polarisation of $\sim$4 – 5 % of sources of comparable brightness in the field. This initial analysis showed a highly significant polarisation which could not be explained by photometric noise. In investigating the polarisation signal from 120308A, we developed analysis and techniques which were later applied to the full sample of RINGO2 GRB observations.

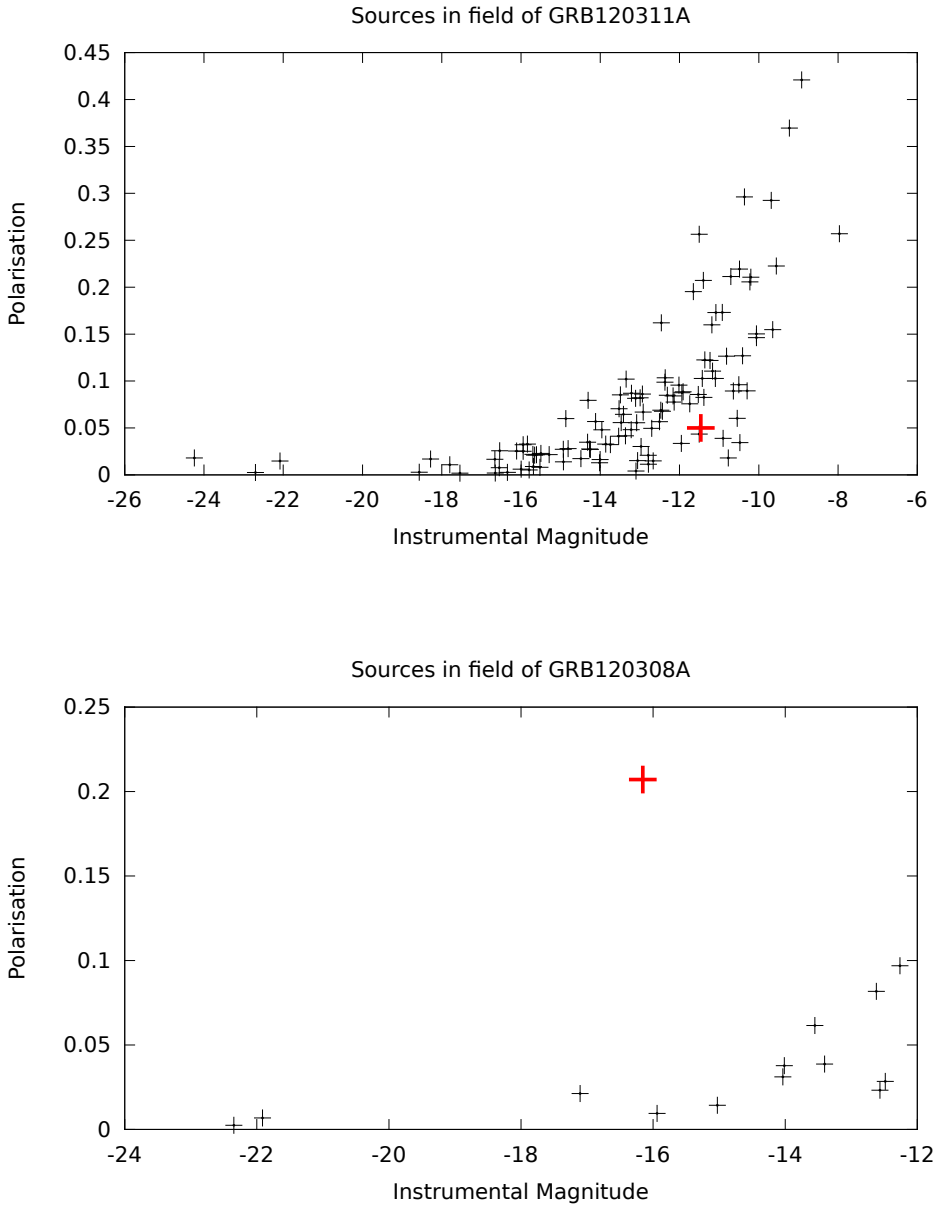


Figure 6.3: Polarisation vs Instrumental Magnitude plots for every source in the field of observations of GRB 120311A and GRB 120308A. Polarisation is expressed in decimal rather than percentage form. Sources with higher instrumental magnitude exhibit higher measured polarisations as the signal to noise ratio of the observation deteriorates. Assuming that all stellar sources in the field are of low polarisation ($\lesssim$1 %), the effect of photometric error on measured polarisation can be observed. The measured polarisation and instrumental magnitude of the GRBs are plotted in red. For GRB 120311A, the measured polarisation can be assumed to be related to photometric noise, as stellar sources of a similar magnitude also exhibit comparable measured polarisations. In the case of GRB 120308A there is strong indication that the measured polarisation of $\sim$21 % is a real signal, for which photometric noise could not account.

## 6.2 Polarimetric analysis of GRB 120308A

All work presented for GRB 120308A is as per the published information in Mundell et al. (2013). This paper was published before a full understanding of the angular dependence of polarisation with RINGO2 was analysed. As such, all reduction was performed without ellipse correction and using a depolarisation factor, $D$ of 1.33. The effect of this is discussed in Section 6.2.5.

### 6.2.1 Observations and reduction

GRB 120308A was discovered by the SWIFT satellite at 06:13:38 UT on 12th March 2012 (Baumgartner et al., 2012). The prompt emission was analysed to have a $T_{90}$ (15-350 keV) of $60.6 \pm 17.1$ s, (Sakamoto et al., 2012) placing the burst firmly in the population of long GRBs (see Figure 1.8). The Liverpool Telescope responded and began a first response polarimetric observation of 598 s with RINGO2 at 06:17:38 UT, 240 s post burst.

The moon was full (99.7 % illumination), at a declination of +0°and an altitude of +10°from the Observatorio Roque de las Muchachos, La Palma. With the high declination of GRB 120308A (+80°) the moon angle was 84°. Whilst there was no correlation between the moon state and polarimetric observations with RINGO2, it is worth noting that this scenario is close to a situation producing a highly polarised background (full moon, 90°angle between moon and telescope pointing).

With the initial polarimetric analysis of GRB 120308A showing a significant average polarisation of greater than 20 % over the 598s of observation, the raw data was re-stacked into 7 sub observations of roughly 85s each to provide the opportunity of temporal analysis of this polarisation signature. The last 3 observations of the set were analysed and with the fading source, did not provide enough signal to noise to give useful polarimetric constraints. Therefore these observations were stacked, thus giving 4

observations of 85s and one of 225s.

Reduction of these data were performed using the `ripe` pipeline with sExtractor (Bertin & Arnouts, 1996) employed for photometric extraction. As per investigations in Chapter 4, the optimal aperture size of 9 pixels was used. Instrumental polarisation was corrected for using Stokes zeropoints of $q_z$ = 0.10 %, $u_z$ = 3.63 % which were the average of observations of all sources brighter than $\sim$16th magnitude in fields of zero polarised standards during instrumental epochs R2_3 and R2_4 (See Figure 5.3, Chapter 5). A depolarisation factor of 1.33 was applied to the data, no ellipse correction was made.

Errors on the measurements were made by taking the $1\sigma$ errors on photometry and propagating them through the equations for the calculations of normalised Stokes parameters q & u. These values of q & u and their associated errors were analysed using the Monte Carlo method described in Chapter 4 (see Section 4.1.2).

This analysis of the data yielded the measurements in Table 6.2. From these values there is strong evidence of polarisation evolution during the observations from a high level of linear polarisation ($28^{+4}_{-4}$) which falls over time. The polarisation angle shows no sign of significant rotation during this period. From the 5 observations, the average polarisation angle is 44.8°. Of these observations, 3 are consistent with this average polarisation angle, within their $1\sigma$ error bars. From a sample of measurements of a fixed value, it would be expected that 68 % of measurements would be consistent with this value, within their $1\sigma$ error bars.

For a small sample of 5 measurements, this would equate to 1.6 measurements not showing consistency. The Poisson noise on this count is 1.3. Hence if there was no rotation in the polarisation angle, we would expect 0.3 to 1.9 measurements to not be consistent. Whilst non integer numbers of observations is a nonsense, these values show that there is no detection of any polarisation angle evolution. Further we can

constrain that any evolution in angle would have been less than 34°with a $1\sigma$ certainty.

| Observation | Start time (UT) | End Time (UT) | P (%) | PA (deg) |
|---|---|---|---|---|
| 1 | 06:17:38 | 06:19:01 | $28^{+4}_{-4}$ | $34 \pm 4$ |
| 2 | 06:19:01 | 06:20:25 | $23^{+4}_{-4}$ | $44 \pm 6$ |
| 3 | 06:20:25 | 06:21:49 | $17^{+5}_{-4}$ | $51 \pm 9$ |
| 4 | 06:21:49 | 06:23:13 | $16^{+7}_{-4}$ | $40 \pm 10$ |
| 5 | 06:23:13 | 06:27:25 | $16^{+5}_{-4}$ | $55 \pm 9$ |

Table 6.2: Polarimetric values obtained for the 5 sub observations of GRB 120308A

### 6.2.2 Confirmation analyses

#### Field comparison analysis

To confirm the validity of the measurements and the observed polarisation evolution, a number of analyses were performed to ensure that the result could not be an artifact of observational issues (e.g. polarised background, due to perpendicular full moon) or instrumental instability. To confirm beyond doubt that the polarisation signature was real, the full observation of 598 s was first analysed. All sources in the field were calibrated from instrumental magnitudes to observed magnitudes, and a Polarisation vs Magnitude plot produced with $1\sigma$ error bars (Figure 6.4). This analysis conforms that GRB 120308A is the only source in the field with a measured polarisation which is significant.

#### Rank analysis

In order to provide a more quantitative analysis on the confidence of the polarisation detection, a rank analysis was used. This technique had been developed and performed for GRB 090102A, detailed in Steele et al. (2009). This analysis tests the probability

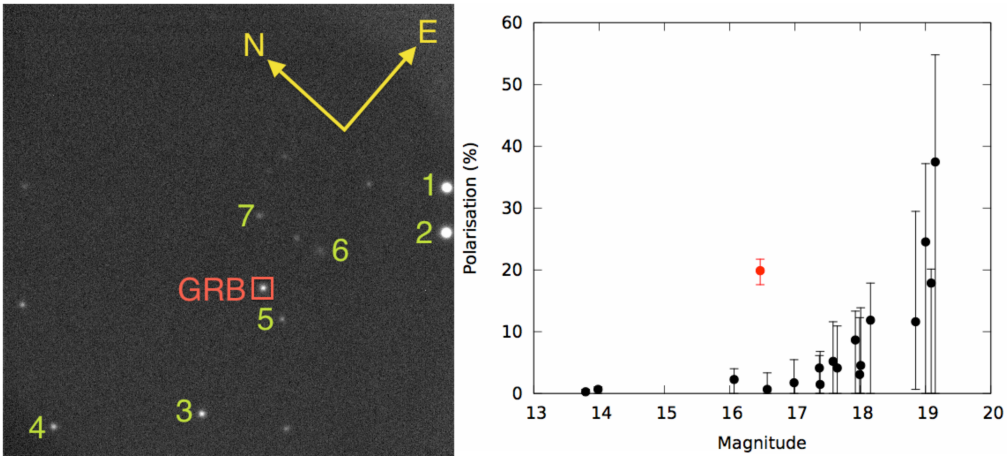


Figure 6.4: The field of GRB 120308A, showing the GRB and 7 stellar sources used for confirmation analysis. Right is the plot of Polarisation vs Magnitude for all sources in the field. With $1\sigma$ error bars, all sources in the field are consistent with being completely unpolarised. GRB 120308A is the only source which has a measured polarisation which is significant. From Mundell et al. (2013).

that the measured polarisation could have been caused by stochastic noise on the measurements, whilst avoiding complications of analysing photometric noise. For the original RINGO instrument, the polarisation ring was split into 36 bins (10°each), instead of the usual 8 used for the polarimetric measurement. Using a Monte Carlo method, these bins were randomly assorted 10,000 times and the resulting polarisations of these 'jumbled' rings measured. The distribution of the polarisations were then compared against the measured polarisation (Figure 6.5), providing a likelihood rank. For GRB 090102A it was found to a confidence level of 99.9 % that the measured polarisation was not due to stochastic noise.

For RINGO2 and RINGO3, there is no possibility to further sub divide the 8 measurements as with the ringed images of RINGO. Whilst the 32 bins of the RINGO ring provided $\sim 2.6 \times 10^{35}$ permutations, requiring a Monte Carlo approach, reordering of 8 bins of RINGO2 yields only $40,320$ permutations. When considering that permutations in reverse order, or shifted permutations (identical order, but starting with a different bin) provide identical polarisation values, the permutations are reduced to $2520$.

Before the reordering of the 8 flux bins, each was corrected for instrumental polarisation. To do this, each of the flux values was divided by the a correction factor to depolarise the flux bin. The correction factor was the average of all sources in zero polarised fields taken with RINGOstand, above an arbitrary S1 value of 500 counts, 2 days either side of the observation. The MySQL query for obtaining the 8 correction factors is shown below.

```
SELECT count(p), AVG (a1 / (S1 /8)), AVG (b1 / (S1 /8)), AVG (c1 / (S1 /8)), AVG (
  d1 / (S1 /8)), AVG (a2 / (S1 /8)), AVG (b2 / (S1 /8)), AVG (c2 / (S1 /8)), AVG (
  d2 / (S1 /8)) from photdata,obs  where obs_id=obs_id_link and object like '%zpol%
  ' and S1 > 500 and abs (date - 20120308) < 3
```

With only 40320 bin reordering permutations, polarisations for all of these permutations were calculated. The standard instrumental depolarisation factor of 1.33 was applied to each of obtained values of polarisation from bin reordering. Figure 6.5 shows the resulting rank plot with that of GRB 090102A for comparison. Whilst the limits of RINGO2 yields a poorer analysis than for RINGO, the rank score gives a confidence level of 99.4 % in the measured polarisation of GRB 120308A.

### Polarisation evolution field analysis

To verify the polarisation evolution obtained from the 5 sub observations, the measured polarisations of field stars were compared with that of the GRB. Figure 6.4 shows the 7 stellar sources in the field used for comparison and their details are listed in Table 6.3.

Plots were initially conducted by comparing the measured polarisation evolution of GRB 120308A against the 4 brightest field stars. This showed that there was no matching measured polarisation evolution between observations for the field stars. However,

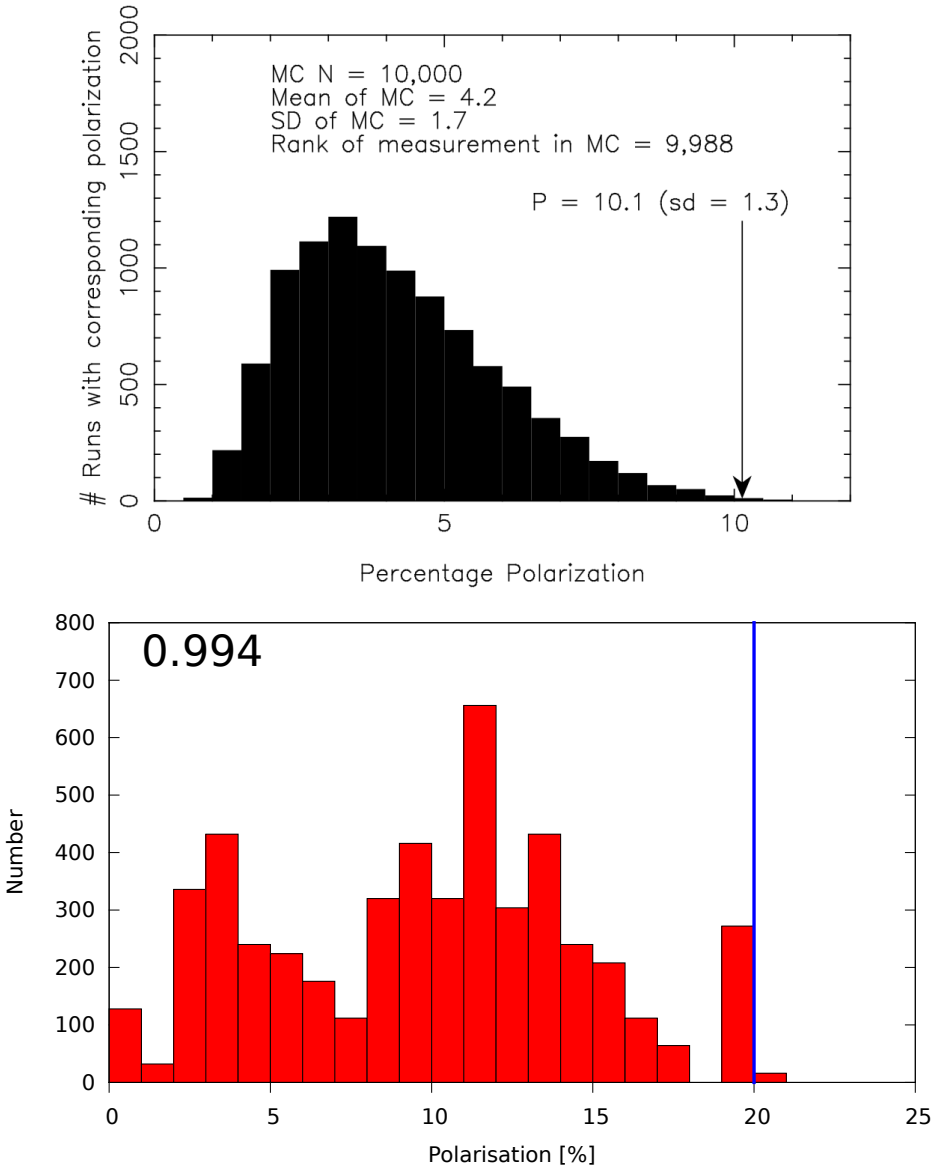


Figure 6.5: Rank analysis of GRB 090102A (top, Steele et al. (2009)) and GRB 120308A (bottom). GRB 090102A was observed with RINGO, permitting 32 bins for reordering and a Monte Carlo analysis to produce the distribution of possible polarisations from reordering the bins. With GRB 120308A, the number of bins for reordering is only 8 due to instrument design. This is the reason for the visibly jagged profile of the distribution, due to there only being 2520 possible polarisation values from the permutations. However the analysis is still able to provide a confidence level value of 99.4 %, albeit with less certainty.

Star 1, being at the edge of the field, did show 2 measured polarisations not consistent with zero. See Figure 6.6.

With these 4 bright sources all being close to the edge of the field, there was a concern that the evolution of GRB 120308A could be a field dependent artifact of the instrument. In order to test this hypothesis, stellar sources local to the field position of the GRB were analysed. These sources (Stars 5, 6 & 7) however, were too faint to provide an adequate constraint on measured polarisation. Hence the flux of these sources from each of the 8 observation bins were co-added (along with errors in quadrature) before a polarisation measurement was taken on this *co-added local source*. Again the measured polarisation of this co-added source was consistent with zero for 4 out of the 5 observations, and no evolution that correlated with that observed on GRB 120308A was observed.

**Conclusions on verification analyses**

The analysis of the full 598 s observation of GRB 120308A with RINGO2 using the Polarisation versus Magnitude plot and the quantitative analysis of the rank plot provide strong evidence that the measured polarisation of GRB 120308A is a real observed signal. The high level of polarisation would not be expected to be produced by any intervening mechanisms such as dichroic dust which produces the observed polarisations for the polarised standard stars.

| Object | RA (J2000.0) | DEC (J2000.0) | $r'$ magnitude |
|---|---|---|---|
| 1 | 14:37:01.0 | +79:40:32 | 14.0 |
| 2 | 14:36:54.0 | +79:40:16 | 13.8 |
| 3 | 14:35:52.3 | +79:40:50 | 16.1 |
| 4 | 14:35:29.9 | +79:41:46 | 16.6 |
| 5 | 14:36:18.1 | +79:40:52 | 17.4 |
| 6 | 14:36:33.6 | +79:41:02 | 17.9 |
| 7 | 14:36:30.8 | +79:41:41 | 17.6 |
| GRB | 14:36:20.3 | +79:41:12 | 16.5 |

Table 6.3: Positions and $r'$ magnitudes of stellar sources in field of GRB 120308A. The labels refer to the field as shown in Figure 6.4.

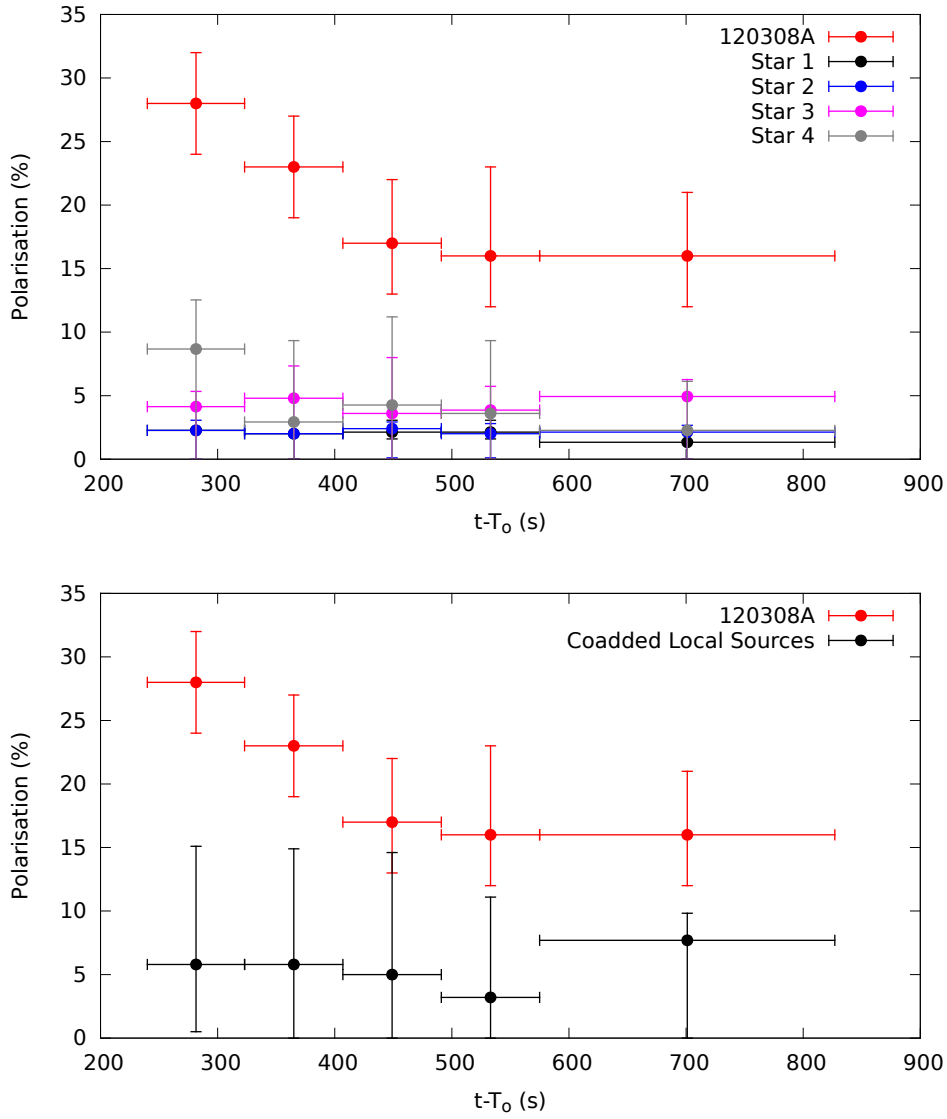


Figure 6.6: Measured polarisations of field sources and GRB 120803A over the 5 sub observations. Top are the 4 brightest sources in the field and below the co-added source of Stars 5, 6 and 7 in the field local to the GRB.

Confidence in the polarisation evolution of the burst is strong evidence that there is a changing polarisation produced in the GRB, and not due to any intervening effects. It was shown by comparing the 5 sub observations with the field sources that the measured evolution in polarisation is not due to any unwanted observing artifacts which would also affect the field sources. However within the $1\sigma$ error bars, one could assume a constant polarisation (say the average of 21 % across the 598 s observation). The data is consistent with this assumption, with only the first point not agreeing.

Again, with the $1\sigma$ error bars, it would be expected that 32 % of the measured values would not be consistent with the true value.

Whilst there is no compelling evidence for polarisation evolution in the data, there are two pieces of complementary evidence which support the view that polarisation evolution is occurring in the source. Firstly, the measured values are falling and flattening off. Secondly, the lightcurve of the GRB afterglow can be interpreted to show forward and reverse shock components changing in dominance at this time. Although it has to be acknowledged that this is somewhat cyclical reasoning, the two observations support each other and strengthen a view of polarisation evolution.

### 6.2.3 Lightcurve and polarisation

The lightcurve was fitted by Dr Drejč Kopac, using RINGO2 and RATcam observations converted into the Sloan $r'$ band. The RINGO2 data were split into 16 sub observations for photometric analysis and sampling of the lightcurve. The lightcurve along with polarimetric measurements is shown in Figure 6.7. Due to the fast response of the Liverpool Telescope, observations started as the optical afterglow was still brightening, although there is only the first datapoint to confirm the rise of the GRB.

The blue line of the lightcurve is the expected best fit to the data if the emission followed a forward shock only scenario. The grey line of best fit matches the data better and is a compound lightcurve fit which matches a type II burst (See Chapter 1, Figure 1.12). The dotted lightcurves show the theoretical forward and reverse shock components which contribute to this compound lightcurve best fit.

Compared to a forward shock only emission, the steeper rise (constrained only by one RINGO2 photometric sub observation), steeper fall and subsequent flattening of lightcurve (RATcam observations) confirm that there was a strong reverse shock com-

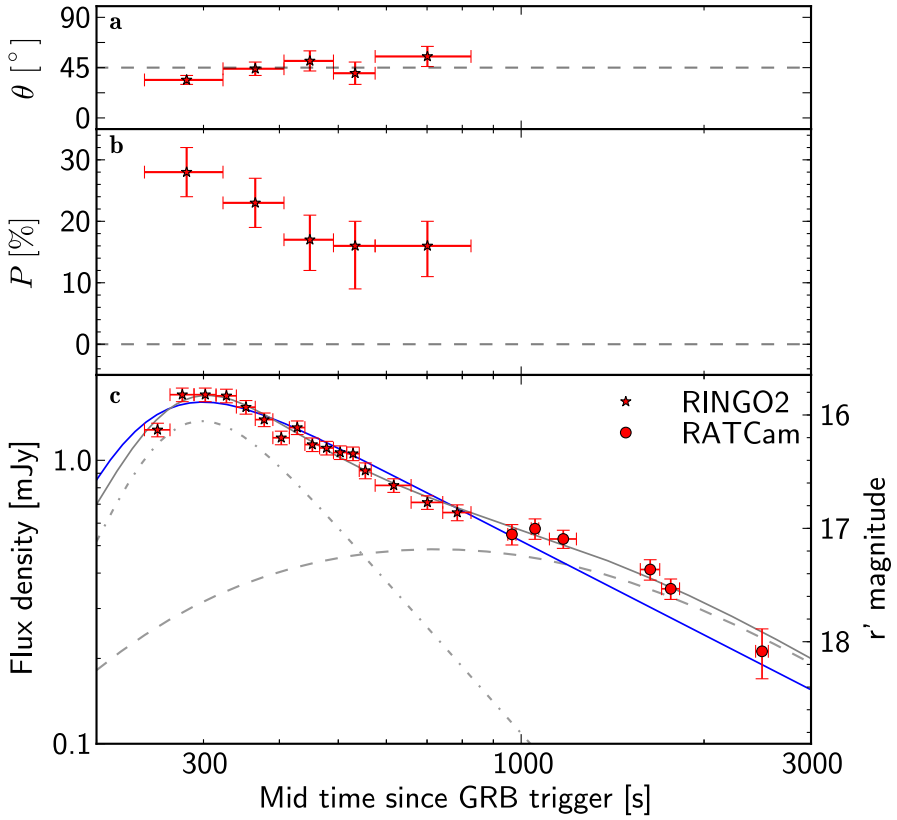


Figure 6.7: Lightcurve and polarisation data of GRB 120308A. The photometric data from RINGO2 and RATcam observations best fit a 2 component lightcurve (grey line), which would be explained by an early-time strong reverse shock component being dominant before a forward shock component takes over at later times (dashed grey lines). The datapoints show significant deviation from a forward shock only model (blue line), with a steeper rise and decay before a flattening of the lightcurve as the later peaking forward shock becomes dominant.

ponent at early times. A further data point taken by the 1.5 m Russian Turkish Telescope (Aslan et al., 2001), approximately 18 hours after the burst provides a late time agreement to the 2 component model of this burst. The burst was observed at this time to have a magnitude of Rc = $21.14 \pm 0.08$ (Bikmaev et al., 2012).

### 6.2.4 Interpretation

The high polarisation of the optical afterglow of GRB 120308A, with no evidence of rotation of the angle rules out the fact that the polarisation could be due to plasma or magnetohydrodynamical instabilities within the jet. The compound lightcurve with a

dominant reverse shock component at early times has a peak which coincides with the highest measured value of polarisation. Whilst the error bars on the polarisation are $1\sigma$, making a confident statement of polarisation evolution difficult, the cyclical reasoning between theory and observations gives evidence to the polarisation evolution.

As the measured polarisation falls, the emission switches from being dominated by the fading reverse shock to the rising forward shock. The emission region of the forward shock front is modelled to contain only locally produced, tangled magnetic fields. This has been confirmed by late time polarisation measurements of GRBs yielding low polarisations (Greiner et al., 2003; Wiersema et al., 2012).

From these observations a constraint is placed on the fireball magnetisation (the ratio of magnetic to kinetic energy within the jet) of $>$500 (Mundell et al., 2013)

### 6.2.5 Conclusions

These polarimetric measurements of GRB 120308A are the first observations to detect a high polarisation in the optical afterglow. The lack of rotation in the angle shows that stable ordered magnetic fields can exist in GRB jets long after the release of the prompt emission.

As mentioned, the analysis presented in this section relates to data reduction that did not correct the angle dependence on depolarisation of RINGO2 (ellipticity). Compared to the angle of the characteristic ellipse of 92.7°, the angle of polarisation, $\beta$ is near perpendicular (179.5°) and hence lies on the semi major axis of the characteristic ellipse. Whilst this angle requires the greatest factor of ellipse correction, with very little rotation in the polarisation angle between the sub observations, a linear offset of the polarisation magnitude will apply to all observations. Any small variations in offset are due to angle being non significant compared to the errors on measurement. In short there is no effect which could affect our conclusions regarding polarisation evolution.

An analysis of the full 598 s observation shows that there is a factor difference of 1.06 (i.e. 6 % of the measured value) between ellipse corrected and non ellipse corrected reduction (Table 6.4).

| | q | u | P(%) | $\beta(^\circ)$ |
|---|---|---|---|---|
| Non corrected | -0.147 | -0.028 | 19.9 | 179.52 |
| Ellipse corrected | -0.171 | -0.029 | 21.2 | 179.51 |

Table 6.4: Comparison of GRB 120308A polarisations of the full 598 s observation with RINGO2, with and without ellipse correction. Due to the timing of investigations, ellipse correction was not applied to the data for publication of the findings in Mundell et al. (2013). For the non ellipse corrected data the depolarisation factor of $D$=1.33 was applied. For the ellipse corrected data the depolarisation factor $D$=1.22 was applied. Whilst the polarisation angle $\beta$ is close to the Factor of 1.06

## 6.3 RINGO2 GRB Sample

The analysis of GRB 120308A showed the possibility of significant, angle stable polarisations during a time when a reverse shock element was dominant in producing the observed emission. This single burst provided evidence to a high confidence level that there were large scale, ordered magnetic fields within the jet, providing the first direct observational confirmation of a highly magnetised jet where the energy was predominantly contained and released through Poynting flux rather than through the kinetic energy of baryons.

The RINGO2 sample of bursts and their polarisations provide further confirmation of this result.

### 6.3.1 Reduction and results

The polarisations of the remaining GRB afterglow observations were analysed as per the 120308A burst using the *ripe* pipeline with sExtractor. Stokes zeropoints for each burst were taken using observations of zero polarised standards on the 3 nights either side of the burst inclusive (7 nights in total). A depolarisation factor of $D$=1.33 and no ellipse correction. The characteristic ellipse values of the instrument were only obtained for instrumental epochs R2_3 and R2_4, which do not cover the epochs of observation og GRBs 100805A, 101112A and 110205A. Ellipse correction was omitted in order to process all bursts identically. The lower signal to noise and non-significant polarisations of the rest of the sample, together with the minimal differences between ellipse and non-ellipse corrected values in GRB 120308A, give us confidence with this approach.

The $1\sigma$ errors on the polarisations were calculated using the Monte Carlo method described in Chapter 4 (See also `ringoerror.py`, Appendix A).

The analyses performed for GRB 120308A were automated to obtain data from the `ripe` database and output Polarisation vs Magnitude plots and rank analysis for each burst. For completeness, these are included in graphical form in Appendix G

Table 6.5 on Page 224 summarises the polarisation findings of the RINGO2 GRB sample (Kopač, Steele, et al. *submitted*). For the majority of observations, only upper limits of polarisation were obtained. In this case, where the measurement is consistent with zero polarisation to $1\sigma$ confidence, a constraint on polarisation angle is not possible.

In addition to GRB 120308A, GRBs 101112A and 110205A provide significant polarisations, with strong evidence of reverse shock scenarios in both GRBs. The two observations of 101112A provide also a stable polarisation between the measurements

with no evidence of any rotation of angle, and a $1\sigma$ confidence that any rotation would be less than $30^{\circ}$.

### 6.3.2 Analysis of results

Observations started on GRBs 101112A, 110205A and 120308A before the peak of the lightcurve occurred, enabling the rise of the lightcurve to be observed. The rise in flux was $\alpha_{rise} \sim 5$ where $F(\nu) \propto t^{\alpha}$. The steepness of these rises are consistent with strong reverse shock signatures from both a theoretical perspective (Kobayashi, 2000; Zhang et al., 2003) and observationally (Japelj et al., 2014).

However these two bursts (101112A, 110205A) do not exhibit a bump in the lightcurve decay as for GRB 120308A, and the decay indexes of $\alpha \approx 1.1$ and $\alpha \approx 1.5$ (where $F(\nu) \propto t^{-\alpha}$) agree with both reverse and forward shock components peaking at similar times, whereas there was a distinct temporal peaking of reverse and forward shock emission in GRB 120308A.

These two bursts with reverse shocks showing a significant polarisation signal give strong support to the existence of ordered magnetic field structures within GRB jets. Firstly they confirm that GRB 120308A was not a unique event, whose polarimetric measurements were due to orientation effects of the observing angle of the jet. Secondly, the lower levels of measured polarisation during the peak are expected in these bursts with near simultaneous peaks in both forward and reverse shock. In 120308A, the highly polarised reverse shock was dominant, explaining its higher value of observed polarisation.

A further analysis by Dr Drejc Kopač compared the $\alpha_{decay}$ values of the bursts in the sample against the obtained values of polarisation and upper limits (Figure 6.8). The value of $\alpha_{decay}$ is an indication of the ratio of the reverse to forward shock emission. It can be seen that a near linear relationship is achieved for the significant measurements

of polarisation, with all upper limits (bar GRB 120327A, $\alpha_{decay}$=1.22, P$\lesssim$4 %) being consistent with this trend.

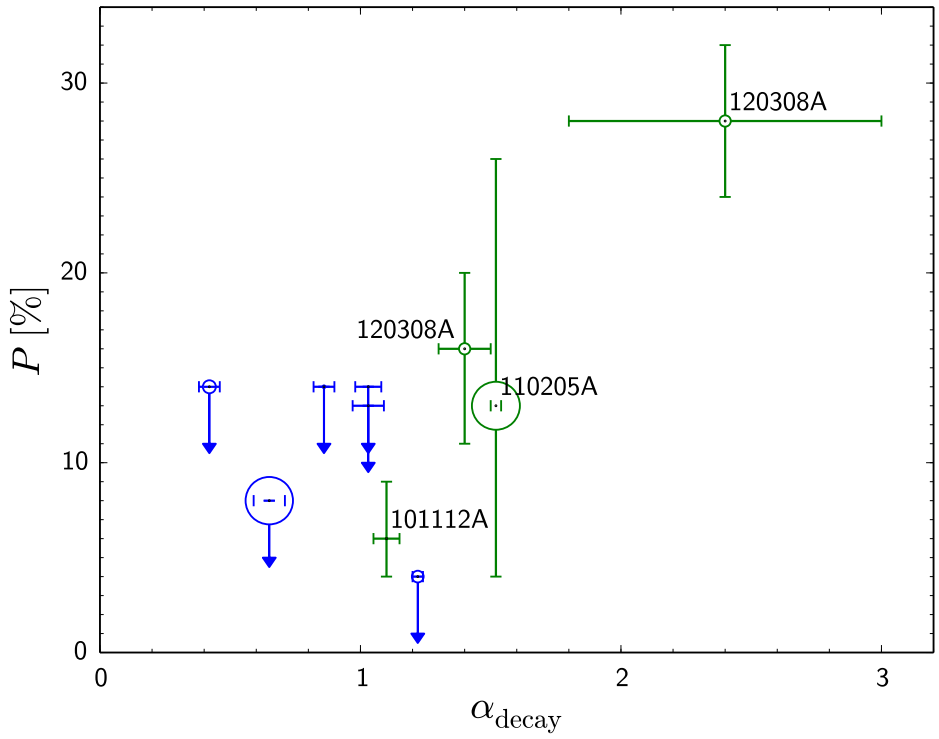


Figure 6.8: Polarisation vs $\alpha_{decay}$ of the RINGO2 sample of GRBs. The value of $\alpha_{decay}$ is an indication of the ratio of reverse to forward shock emission. The linear fit of significant polarisation detections provides strong evidence of highly polarised reverse shock emission from stable, ordered magnetic fields within the jet, that are 'diluted' by the low polarisation forward shock emission. Plot by Dr Drejc Kopač.

As additional evidence that the polarised emission is from a reverse shock, the temporal parameter space of polarisation measurements can be probed. With reverse shocks only theorised and observed to occur at early times, analysis of polarisation vs the rest-frame time since the prompt emission can be undertaken. For bursts with known redshift constraints it is possible to calculate the rest-frame time of the polarimetric measurements of the GRB, $(t - t_0)/(z + 1)$. These were combined with data of the RINGO bursts 060418A and 090102A, with a further optical polarimetric point on 091208B measured by Uehara et al. (2012). Figure 6.9 provides a visual analysis

of the possible polarisation region against time in the rest-frame of the burst. Ignoring 110205A Observation 3, the trend is that high polarisations (>10 %) can only be expected in the first 300 s → 400 s from the prompt emission. These constraints show that the polarised emission is linked to times when a reverse shock will be providing the greatest contribution to the emission.

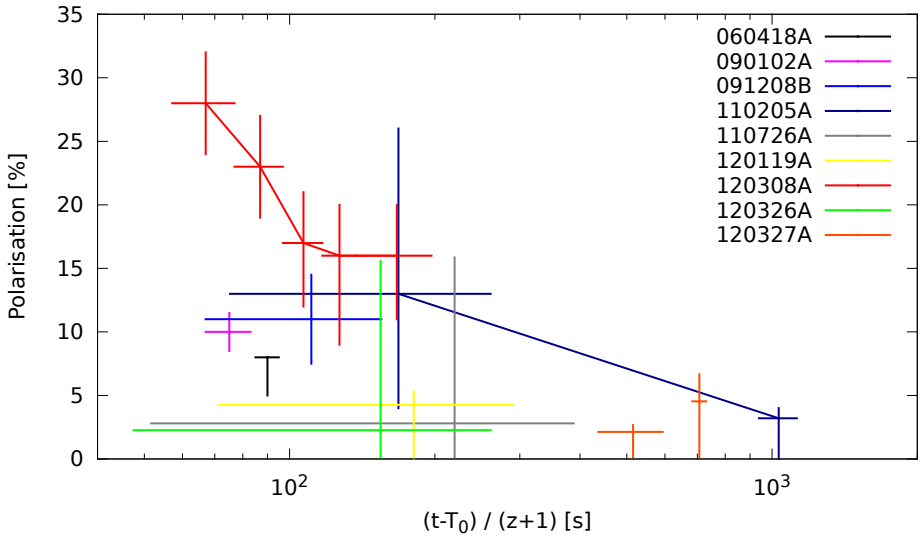


Figure 6.9: Plot of polarisation vs rest-frame time for bursts with redshift constraints. It can be seen that the values obtained and upper limits show a trend of a possible region of polarised optical emission at early times, when a reverse shock's contribution to the overall observed emission is greatest.

## 6.4 Conclusions

The aim of the RINGO series of instruments was to probe the early time polarisation evolution and hence magnetic field structure within GRB jets. Competing models of the mechanism by which the central engine launches jets and their composition of energy (baryonic or magnetic) and subsequent conversion to the observed radiation can be tested by deducing the magnetisation of the jet.

RINGO2 proved to be not only a successful polarimeter, but also photometer, which allowed flexible sampling of photometric datapoints for lightcurve fitting. With well constrained lightcurves from both RINGO2 and RATcam observations the rate of rise and decay in the lightcurves ($\alpha_{rise}$,$\alpha_{decay}$) and also any bumps in decay (120308A) enabled the presence and properties of the reverse shocks to be deduced.

For GRBs 101112A and 120308A, the absence of evidence for any rotation in the polarisation angle supports the theories of highly ordered, stable magnetic fields which are required in the Poynting flux model of jets developed by Lyutikov & Blandford (2003). Furthermore the relative strengths of forward and reverse shocks in the 3 observed GRBs with significant polarisation measurements support the evidence that the polarised emission is originating from within the jet. Although the sample size is small, 3 GRBs (101112A, 110205A, 120308A) show polarisation properties which are consistent with models of magnetised ejecta and a Poynting flux mechanism for energy release (Lyutikov, 2009; Lyutikov & Blandford, 2003; Zhang & Kobayashi, 2005).

| GRB | $t - t_0$ (s) | $P$ (%) | EVPA (deg) | Rank | Afterglow onset $t_{\rm peak}$ (s) | LC morphology | z |
|---|---|---|---|---|---|---|---|
| 100805A | $140 - 320$ | $< 14$ | / | 0.377 | $< 140.4$ | PL | $\approx 1.3$ |
| 101112A | $176 - 355$ | $6^{+3}_{-2}$ | $71 \pm 10$ | 0.978 | $299.0 \pm 6.0$ | FS (+ RS possibility) | $\lesssim 3.5$ |
| | $715 - 893$ | $6^{+4}_{-3}$ | $76 \pm 15$ | 0.934 | | | |
| 110205A | $240 - 840$ | $13^{+13}_{-9}$ | $126 \pm 26$ | 0.967 | $1027.0 \pm 8.0$ | FS + RS | 2.22 |
| | $3047 - 3645$ | $< 5$ | / | 0.883 | | | |
| | $3960 - 4140$ | $< 23$ | / | 0.486 | | | |
| 110726A | $191 - 783$ | $< 14$ | / | 0.331 | $< 191.2$ | PL (+ RB possibility) | $1.04 < z < 2.7$ |
| 120119A | $194 - 793$ | $< 8$ | / | 0.713 | $< 194.4$ | PL + RB | 1.728 |
| 120308A | 240 - 323 | $28 \pm 4$ | $34 \pm 4$ | $> 0.99$ | $298.0 \pm 16.0$ | RS + FS | $2.22^{+0.25}_{-0.27}$ |
| | 323 - 407 | $23 \pm 4$ | $44 \pm 6$ | $> 0.99$ | | | |
| | 407 - 491 | $17^{+4}_{-5}$ | $51 \pm 9$ | $> 0.99$ | | | |
| | 491 - 575 | $16^{+4}_{-7}$ | $40 \pm 10$ | $> 0.99$ | | | |
| | 575 - 827 | $16^{+4}_{-5}$ | $55 \pm 9$ | $> 0.99$ | | | |
| 120311A | $181 - 779$ | $< 13$ | / | 0.008 | $< 180.6$ | PL | $\lesssim 3$ |
| 120326A | $216 - 872$ | $< 14$ | / | 0.139 | $< 216.0$ | PL (shallow decay) | 1.798 |
| 120327A | $1664 - 2263$ | $< 4$ | / | 0.505 | $< 1663.8$ | PL | 2.81 |
| | $2605 - 2784$ | $< 7$ | / | 0.823 | | | |

Table 6.5: Analysis of polarimetric observations of the RINGO2 GRB sample. The lightcurve (LC) morphology codes are, PL = simple power law decay likely due to forward shock, FS = forward shock peak, RS = reverse shock peak, RB = late time re-brightening. From Kopač, Steele, et al. (in prep)

# Chapter 7

# Summary and Conclusions

## 7.1 Summary

In Chapter 2 the design of RINGO3, and its opto-mechanical components were presented. Over the operating wavelength range of 380 nm $\rightarrow$ 900 nm, the goal was to obtain 3 bands which would provide equal signal to noise ratios when observing gamma-ray burst (GRB) afterglows. With the signal received being dependent on the throughput of the instrument across the operating wavelength, lab tests were performed using a monochromator to deduce the throughput of each optical component for which data was not available (camera and collimator lenses). Combining these measurements with data of polariser throughput and CCD quantum efficiency an overall instrument throughput model was obtained. The spectrum of synchrotron emission (theorised and observed) was used for the model signal and observations of the dominant source of noise, the sky background, were obtained for the La Palma observatory site from Benn & Ellison (1998).

The findings of this signal to noise analysis provided the wavelengths of the band boundaries which would be served by specific polarisation tolerant dichroic mirrors. This gave the instrument 3 bands of 400-645 nm, 645-765 nm and 765-900 nm which approximate to Sloan g'/r', r'/i' and i'/z bands respectively. The lower wavelength

band is twice the width of the other two, due to the synchrotron spectra.

Chapter 3 described the commissioning of RINGO3 during 19th - 25th November 2012. With an increased path length of the collimated beam within the instrument compared to RINGO2, it was important to ensure the accuracy of the collimation. Tests on far away terrestrial targets (approximating infinity for the small camera lenses) with the Andor camera units and camera lenses were attempted, but proved unsuitable. A bench rig was set up with a small refractor telescope which had been focused to produce a collimated beam image. With this the 3 camera lenses were focused.

First light of RINGO3 produced images which showed significant vignetting due to the increased collimated beam path length. The effect of this vignetting was reduced by exchanging the camera lenses for ones of wider effective aperture, (from 36 mm to 48 mm) within the instrument. A concern of the instrument was the temporal stability of the polaroid rotation and triggering mechanism, which could provide variations in the polarisation signal. Using a series of dome flat observations any issues with timing integrity were tested and the variation of polarisation values between rotations formed a distribution with a FWHM variation of 0.04 %. As observations are created from a large number of rotations, any effect due to the timing of the rotator and triggers could be considered to be negligible.

The first light measurements of unpolarised and polarised standard stars catalogued in Schmidt et al. (1992) showed repeatability of measurements to be a factor of 2 worse than RINGO2. As time went on and more data of these standard fields was taken, the polarimetric performance of the instrument was found to be very poor, and there was an observed degeneracy between polarisation and polarisation angle, which voided all polarimetric observations. The issue was traced to the variation in the cut-off wavelength of the dichroics as a function of polarisation angle. Having a rotating 100 % linearly polarised beam meant that the cut-off wavelengths of the dichroics were oscillating by 12 - 15 nm. To solve this issue a depolariser was fitted within the collimated

beam to ensure no variation in cut-off wavelength of the dichroics.

Chapter 4 looked at the photometric principles required to obtain a polarimetric measurement from RINGO2 and RINGO3. It detailed the development of a pipeline to analyse RINGO2 and RINGO3 data 'en masse' which could be used for instrumental characterisation. Using sExtractor (Bertin & Arnouts, 1996) for photometry, the `ripe` pipeline utilised the Perl programming language to automate photometric extraction and enter the data of each source in each observation into a database. Further routines automated the calculation of polarisation and the necessary corrections required. Also included in the database were information from the FITS headers relating to the parameters of the observation (e.g. altitude, azimuth, moon state, etc.)

The first investigation using the `ripe` pipeline was to determine the optimal photometry settings and aperture for photometric measurements. During this analysis it was found that repeated measurements of sources over a number of different nights varied by a factor $\sim$2 greater than would be expected by the photometric error, and that repeated measurements of the brightest sources (HD212311, 8.1 magnitude) had a standard deviation of 0.5 % in polarisation, suggesting a variation 'floor' in measurements due to non-systematic effects.

Further investigation into a possible cause for this variation floor for RINGO2 was undertaken in Chapter 5. Analysis of the temporal stability of the zeropoints showed standard deviations of 0.11 % and 0.20 %. These variations accounted for half of the observed variation floor. This gave evidence to inform that to accurately set zeropoints for science observations, the average zeropoint values from a number of evenings around the science observation should be used in reduction.

The stability of the polarisation measurements across the $4 \times 4$ arcmin field of RINGO2 was performed using the zenith sky at sunset to provide a high signal to noise polarimetric flatfield. The most extreme variations in the field were found to be less than

0.8 % on the value of measured polarisation.

The instrumental depolarisation of RINGO2 was analysed and was seen to have an angle dependence. A method was developed to correct this angular dependence, by defining characteristic ellipses in the q-u plane for measurements of a constant polarisation at differing angles. After ellipse correction a single depolarisation factor was then applied to all data. However with only six observable Northern Hemisphere polarised standards, which were of dubious stability, confidence in the defined polarisation factor was not high. Contemporaneous measurements of the field of BD+59°389 by Soam et al. (2014) provided confidence in the established depolarisation factor of $D$=1.22 for ellipse corrected data and $D$=1.33 for non ellipse corrected data.

For RINGO3, there was a rich dataset of polarimetric standard sources which had been taken at a number of Cassegrain rotator angles. By analysing the mean and standard deviation of the zeropoints and the values of polarised sources for a number of Cassegrain rotation angles, there was no variation in the instrumental polarisation or depolarisation that could be distinguished from the data. This result is important as the characterisation of RINGO2 used data taken with a single Cassegrain rotator angle. However, due to considerations of fast follow-up, GRB afterglows can be observed at any Cassegrain rotator angle, as the mount is not rotated from its position when the observational override trigger was received.

RINGO3 showed a similar temporal stability in the Stokes zeropoints to RINGO2. The angular dependence on polarisation was also characterised by defining the characteristic ellipse of the instrument in each of the 3 bands. The depolarisation factors of the 3 bands were smaller than that of RINGO2, a result which could be due to the better performance (contrast ratio) of the polariser over the full wavelength range. In comparison the RINGO2 polariser's contrast ratio dropped off severely at the higher end of the composite V+R band of the instrument.

The application of RINGO2 in its prime science goal of GRB afterglow polarisation was presented in Chapter 6. During its operational lifetime, RINGO2 observed 9 bursts of sufficient magnitude on which to perform accurate photometry. This producing a sample in which lightcurves and polarimetry could be linked an analysed. Of these 9 bursts, 3 provided polarimetric observations which gave a significant non zero polarisation signal with high ($> 2\sigma$) confidence. Of these bursts, GRB 120308A gave a breakthrough observation of polarisation evolution ($28\pm4\,\% \rightarrow 16^{+5}_{-4}\,\%$) over the 598 s of observation, with no evidence of any polarisation angle rotation above 34°with a $1\sigma$ confidence.

With evidence of reverse shocks in the 3 bursts which exhibited polarisation, and the polarisation of each matching the timing and relative strengths of forward and reverse shock peaks, we can conclude that the polarised emission is from the reverse shock emission region. This provided the first direct evidence of large scale ordered magnetic fields within GRB jets and confirmed high levels of fireball magnetisation, supporting the Poynting flux model of GRB energy emission developed by Lyutikov & Blandford (2003).

## 7.2 Conclusions

The polarimeters within the RINGO series were designed specifically to probe the early-time polarisation properties of gamma-ray burst (GRB) afterglows. From the first detection of higher than 10 % polarisation over a 60 s observation of GRB 090102A with RINGO, to the photometric and polarimetric measurements of 9 bursts with RINGO2, these novel polarimeters have delivered conclusive firsts in their measurements.

RINGO3 was a natural extension to the polarimetric capabilities of the Liverpool Telescope GRB team, and although plagued with issues early on, it has evolved into a capable, stable instrument which will allow further observations to constrain the

magnetohydrodynamical properties of GRB jets.

Since the installation of RINGO3 there has been a dearth of GRB triggers coming from the SWIFT satellite. Therefore fewer have been followed up by the Liverpool Telescope. There is no evidence that the triggering procedures or observing schedules have been modified on the SWIFT satellite. However it is the suspicion of the team that modifications to the triggering or observing algorithm have taken place. One GRB was observed with RINGO3, GRB 140430A, which was bright enough for polarimetric analysis. Presented in Kopač et al. (2015), RINGO3 proved to give well sampled multicolour lightcurves starting 124 s post trigger. The main polarimetric finding was that although the lightcurve proved to be complex, there was no evidence of Polarisation above 12% (to 1 $\sigma$) limits.

### 7.2.1 RINGO2

The characterisation of RINGO2 investigated the stability of this instrument and checked numerous aspects (such as field flatness to polarisation, repeatability of measurements, observational effects, etc) that could affect the performance of the instrument. It was hoped that by characterising variations in measurement and correlating them with observational parameters, the performance of the instrument could be enhanced. Whilst investigations were not successful in finding the causes of variation, the analyses performed gave constrained instrumental stability to acceptable levels which would not be significant in the photon counting noise dominant observations of 16th magnitude and fainter GRB afterglows.

### 7.2.2 RINGO3

RINGO3 has become a stable instrument, which when characterised is shown to provide near equal performance to RINGO2 in the d and f bands. The challenge for such an instrument is to use an empirical approach of observing stellar standards with

black body spectra, and to calibrate wide wavelength bands, which will be used to observe objects exhibiting synchrotron spectra. The vast colour difference between these two types of spectra means that for wide bands, there can be no certainty in the validity of calibrations derived from one, and applied to the other.

To minimise this effect, shorter wavelength bands would be an ideal solution. However this is not possible where the measurements are so heavily limited by the achievable signal to noise ratio. For RINGO3 further analysis of the wavebands and instrumental throughput, linked with the colours of calibration and science sources, is required.

### 7.2.3 GRB jet magnetisation

The observations of RINGO2 GRBs provided convincing evidence that GRB jets can be highly magnetised. These observations have provided the first direct observational evidence which can help distinguish between two competing models of jet dynamics. These observations show that the energy in the jets of the observed GRBs exists primarily in the form of advected magnetic fields from the central engine and not through the kinetic energy of relativistic baryons.

With jets being observed at a multitude of scales, those of GRBs are valuable probes into the poorly understood mechanisms involved in the removal of energy from the black hole central engine, to the observed relativistic jets.

## 7.3 After RINGO3

The Liverool telescope team have ambitious plans for a new joint telescope development with the Instituto de Astrofisica de Canarias (IAC). The project aims to produce a new 4 metre class robotic telescope, with a segmented mirror design (Copperwheat

et al., 2014). With new projects coming online, such as the Square Kilometre Array, Large Synoptic Survey Telescope, Gaia and gravitational wave detection, there are strong requirements for a large fast followup telescope with spectroscopic capabilities.

The Liverpool Telescope 2 will aim to slew with double the speed of the current LT, to be able to respond to triggers on the order of tens of seconds.

A polarimetric replacement for RINGO3 is in the proposal and design stage. MOPTOP (Multicolour OPTimised Optical Polarimeter) plans to use a Wollaston prism design along with a continuously rotating half wave plate. Using this setup, with 2 different cameras, no flux is lost as per the setup with a linear polaroid of the RINGO instruments. Plans are under way to split the two beams after the Wollaston prism (ordinary and extraordinary rays) into red and blue bands to create a 2 band polarimeter (Jermak et al., 2016). This will require four high speed imaging cameras similar to those found on RINGO3.

## 7.4 Future work

Presented here are ideas for future investigations, which would help improve the high cadence polarimetric capabilities of the Liverpool Telescope.

### 7.4.1 Accuracy of collimated beam within RINGO3

The crude method for calibrating the collimated beam for RINGO3 could have been performed more accurately. There is a fear that the mixed angles of incidence in an under or over collimated beam could be affecting the polarimetric stability. A simple set up of parallel lasers could be used to provide accurate collimation. These parallel lasers would be fired at the camera lens and camera units in a lab environment and the focus adjusted until they form a single spot on the CCD frame.

### 7.4.2 Achromatic performance of the RINGO3 d band camera

With RINGO3 using standard commercial camera lenses there were uncertainties about the achromatic performance of the lens for the d band camera which extends beyond the normal operating range for photographic cameras. To test this a field with standard sources of extreme colour should be selected, and the full width half maximum of the sources compared over a number of observations under good seeing conditions. Alternatively a focus run could be performed on this field and the optimal focus points for different coloured standards noted.

# Appendix A

# Details of `ripe` pipeline

Executable perl script for `ripe`, which reviews and sorts datasets in current working directory. For each dataset it runs SExtractor and then parses the text file output before insertion into the `ripe` mysql database.

```
#!/usr/bin/perl


# Main Perl script for processing RINGO2 fits files and populating grb database
# Doug Arnold May 2012


# PERL MODULES WE WILL BE USING
use DBI;
use DBD::mysql;
use File::Copy;
use lib '/home/disrail/ripe/lib';
use ripe;


#settings
$rotcheck = 0;

# Debug options
$DEBUG = 0;

# Check for TAG
if (!$ARGV[0]) {
```

```
  print "\nplease add a tag (id / memorable info etc) to label this set added to the
    db\n";
  die;
}

$tag = $ARGV[0];

############################
# Obtain list of fits files #
############################


# Set to local directory
$basepath=`pwd`;
chomp $basepath;
$ripedir = "/home/disrail/ripe";
# Open the directory.
opendir (DIR, $basepath)
or die "Unable to open $basepath: $!";


# First remove any full stacked files from previous runs
unlink glob "*F_1.fits";

# Read in the fits files and sort them lexically
my @files =  sort grep {/fits/} readdir (DIR);

# Close the directory.
closedir (DIR);



# check that we have a multiple of 8 files
$no_files = @files;
if ($DEBUG) {
  print "No of files in Dir: $no_files\n";
  for (@files) {print "$_\n";}
}

#if ($no_files%8 != 0){
#   print "WARNING: Incomplete data set: Number of fits files not multiple of 8\n";
#  die;
#}



############################
```

```
# Group files into data sets #
##############################

# Create array of only date and obs ID info in file, then remove duplicates using
    hashes
for (@files) {
  push(@data,  substr($_, 0, -8));
}

my %hash = map { $_ => 1 } @data;
my @datasets = keys %hash;
$no_datasets = @datasets;
if ($DEBUG) { print "No of Datasets: $no_datasets\n"; for (@datasets) {print "$_\n"
    ;}}


# Create 2d array of datasets and filenames

for $dat (@datasets) {
  @tmp = grep (/^$dat/ , @files);
  $no_file = @tmp;

  if ($no_file != 8) {
    print "Error: Only $no_file files for dataset $dat. Ignoring this dataset!\n"
  }

  else {
    push @file_array, [ @tmp ];
  }
}

######################
# Open db connection #
######################



# PERL DBI CONNECT and Check tables exist
ripe::db_connect();



# Grab the sextractor default files and pop in local directory
copy("$ripedir/config/sex/ripe.param", "$basepath/ripe.param") or die "Copy of params
     failed: $!";

# Grab the aperture photometry settings
```

```
$apsize = `cat $ripedir/config/sex/ripe.sex | grep PHOT_APERTURES | sed 's/[^0-9:.]*//g'` ;
$backsize = `cat $ripedir/config/sex/ripe.sex | grep BACKPHOTO_THICK | sed 's/[^0-9:.]*//g'` ;

################################################
# Loop through each data set: AKA THE BUSINESS! #
################################################


# go through each dataset
for $ds (0 .. ($no_datasets-1)) {
  if ($DEBUG) {print "\n\nDataset no $ds\n";}


  $obs_id = substr($file_array[$ds][0], 0 , -8);
  $camera = substr($file_array[$ds][0], 0 , 1);
  print "Procesing [$ds/$no_datasets]\t\t$obs_id\r";

  $fullfile = "${obs_id}F_1.fits";

  # Create a stack of all 8 orientation files
  $stack = `imarith.py $file_array[$ds][0] $file_array[$ds][1] $file_array[$ds][2]
    $file_array[$ds][3] $file_array[$ds][4] $file_array[$ds][5] $file_array[$ds][6]
    $file_array[$ds][7] $fullfile `;

  # Grab fits info from 1st file in dataset
  undef @fits_headers;
  @fits_headers = ripe::fitsdat($file_array[$ds][0]);


  # Set the gain value in Source Extractor from the Number of frames
  # Then get the gain  and numfrms to record in the Database
  ripe::setgain($file_array[$ds][0]);
  $gain = ripe::getgain();
  $numfrms = ripe::numfrms($file_array[$ds][0]);



  # Populate dataset info into db if not duplicate then perform photometry
  $insert = $ripe::DB_grb->prepare_cached('INSERT INTO obs VALUES
    (?,?,?,?,?,?,?,?,?,?,?,?,?,?,?,?,?,?,?,?,?)');
  if ($insert->execute($obs_id, $camera, $tag, @fits_headers, $numfrms, $gain,
    $apsize, $backsize)) {
    # Populate photomertry database
    phot_tbl();
  }
```

```
155 }

157 # Restore folder to original untouched state
    print "\n";
159 ripe::cleanup();

161 ########################################
    ##########   END OF CODE ###############
163 ########################################


165


167 ######################################
    ############## SUBS ##################
169 ######################################

171 sub phot_tbl {
    # sextract all sources and populate photometry table
173
      # for each orientation
175   for $o (0 .. 7) {
        # Run Sextractor 2>/dev/null
177
        # Following line for NORMAL operation
179     $sex=`sex -c $ripedir/config/sex/ripe.sex $fullfile $file_array[$ds][$o] -
        CATALOG_NAME $o.sex`;

181     # Following line for SKY measurement in 100 x 100 bins of 5x5 pixels
        # $sex=`ripe-fieldstat $file_array[$ds][$o] > $o.sex`;
183
        # Following line for 50 x 50 pixel measurement in centre of field pixel by pixel
185     # $sex=`ripe-centrestat $file_array[$ds][$o] > $o.sex`;

187     # Following line for a single 50 x 50 pixel measurement in centre of field
        # $sex=`ripe-singlestat $file_array[$ds][$o] > $o.sex`;
189


191     if ($rotcheck) {
      #Check that the header of the file shows correct orientation. Error Checking
193   $rotnumber = `modhead $file_array[$ds][$o] RROTPOS | sed 's/[^1-8]*//g' | sed 's
        /18//g'`;
      chomp $rotnumber;
195   if ($rotnumber != $o+1) {
        print "Failed on file $file_array[$ds][$o]\n";
197     print "Rotator in fits is: $rotnumber\n";
        $o+=1;
199     print "But in the file array should be: $o\n";
```

```
    die;

  }
}
}



# Open Sextractor file
open sex0, "0.sex" or die $!;
open sex1, "1.sex" or die $!;
open sex2, "2.sex" or die $!;
open sex3, "3.sex" or die $!;
open sex4, "4.sex" or die $!;
open sex5, "5.sex" or die $!;
open sex6, "6.sex" or die $!;
open sex7, "7.sex" or die $!;



# Go through files and pull info of all orientations, and enter them into database
$objcount=0;
while ($s0 = <sex0>) {

  $s1 = <sex1>;
  $s2 = <sex2>;
  $s3 = <sex3>;
  $s4 = <sex4>;
  $s5 = <sex5>;
  $s6 = <sex6>;
  $s7 = <sex7>;

  # if no hash is found as the first character of the first line
  if (!($s0 =~ /^\s*#/)){
    $objcount+=1;
    ($xpix0, $ypix0, $counts0, $counts_err0, $ra0, $dec0, $flag0) = split(" ",$s0);
    ($xpix1, $ypix1, $counts1, $counts_err1, $ra1, $dec1, $flag1) = split(" ",$s1);
    ($xpix2, $ypix2, $counts2, $counts_err2, $ra2, $dec2, $flag2) = split(" ",$s2);
    ($xpix3, $ypix3, $counts3, $counts_err3, $ra3, $dec3, $flag3) = split(" ",$s3);
    ($xpix4, $ypix4, $counts4, $counts_err4, $ra4, $dec4, $flag4) = split(" ",$s4);
    ($xpix5, $ypix5, $counts5, $counts_err5, $ra5, $dec5, $flag5) = split(" ",$s5);
    ($xpix6, $ypix6, $counts6, $counts_err6, $ra6, $dec6, $flag6) = split(" ",$s6);
    ($xpix7, $ypix7, $counts7, $counts_err7, $ra7, $dec7, $flag7) = split(" ",$s7);

    chomp $flag0;
    chomp $flag1;
    chomp $flag2;
```

```
        chomp $flag3;
        chomp $flag4;
        chomp $flag5;
        chomp $flag6;
        chomp $flag7;

        $flag_all = $flag0 + $flag1 + $flag2 + $flag3 + $flag4 + $flag5 + $flag6 +
      $flag7;

        #perform some checking to make sure the lines sync
        if ($xpix0 != $xpix1 || $xpix0 != $xpix2 || $xpix0 != $xpix3 || $xpix0 !=
      $xpix4 || $xpix0 != $xpix5 || $xpix0 != $xpix6 || $xpix0 != $xpix7) {
   die "Sextracter output file sync issue at line for Object $objcount in obeservation
       $obs_id\n;"
        }

        # put info into database
        $insert = $ripe::DB_grb->prepare_cached('INSERT INTO photdata VALUES
      (?,?,?,?,?,?,?,?,?,?,?,?,?,?,?,?,?,?,?,?,?,?,?,?,?,?,?,?,?,?,?,?,?,?,?,?,?,?,?)')
      ;
        $insert->execute(null, $obs_id, $tag, null, null, null, $xpix0, $ypix0, $ra0,
      $dec0, $counts0, $counts1, $counts2, $counts3, $counts4, $counts5, $counts6,
      $counts7, $counts_err0, $counts_err1, $counts_err2, $counts_err3, $counts_err4,
      $counts_err5, $counts_err6, $counts_err7, $flag_all, null, null, null, null, null
      , null, null, null, null, null, null, null);
      }

      }

}
```

Listing A.1: `ripe` which performs photometric extraction and database entry for large numbers of datasets. Data is extracted of each observation into the `obs` table of the database. For each observation, each object is analysed for each of the 8 rotor positon files and the photometric data inputted into the `photdata` table.

Below is the polcalc routine, which after extraction of data to the ripe database, performs polarimetric calibrations. It has a number of switches and options for calculating polarimetric zeropoints from single Stokes values, from 8 rotation correction values or by automatically searching the database for zero polarised observation using `get_zeropoints()` function, described in Listing A.7.

```
#!/usr/bin/perl


# Script to go through Phot data and perform calculations on data


# PERL MODULES WE WILL BE USING
use DBI;
use DBD::mysql;
use File::Copy;
use lib '/home/disrail/ripe/lib';
use ripe;
use Math::Trig;
use Math::Complex;
$pi = 3.14159265;
$counter =0;
$DEBUG=1;

if ($DEBUG) {
  open DEBUG, ">debug.log";
}




# Calibration Switches
# Calibrate = 0 --> No calibration
# Calibrate = 1 --> Stokes q, u offest calibration
# Calibrate = 2 --> A1, B1 ..... C2, D2 calibration
# Calibrate = 3 --> Grab q and u stokes offsets from nearby the date
$calibrate = 3;


# Mode switches
# Mode = 1 --> Calibrate all sources
# Mode = 2 --> Calibrate identified standard sources only
```

```
$mode = 2;

# Ellipse Correction = 1 --> Apply a stokes scaling parameter. It is found that q * 1.14 provides better polrings
# Ellipse Correction = 2 --> Modify values to correct for ellipse of ellipticity E (0 -> 1) and ellipse angle theta
$ellipse_correction = 0;



$q_scaling_factor = 1.145;
$u_scaling_factor = 1.0;



$dE = 0.09; #Ellipticity
$dtheta_deg = 120; #Degrees
$dtheta = $dtheta_deg / 180 * $pi;

$eE = 0.14; #Ellipticity
$etheta_deg = 118; #Degrees
$etheta = $etheta_deg / 180 * $pi;

$fE = 0.13; #Ellipticity
$ftheta_deg = 123; #Degrees
$ftheta = $ftheta_deg / 180 * $pi;

$q_zeropoint = -0.0031631; #2011/12 average zeropint
$u_zeropoint = 0.0290815; #2011/12 average zeropoint
$q_zeropoint_error = 0.0000;
$u_zeropoint_error = 0.0000;









$A1_correction = 0.9786;
$B1_correction = 1.0245;
$C1_correction = 1.0258;
$D1_correction = 0.9753;
$A2_correction = 0.9723;
$B2_correction = 1.0115;
$C2_correction = 1.0224;
$D2_correction = 0.9895;

  if ($calibrate){
      print "Running with Calibration options\n\n";
    }
```

```
83
85
87
89 # Open connection
   ripe::db_connect();
91
   #Prepare input quiery
93 $input = $ripe::DB_grb->prepare('UPDATE photdata SET S1 = ?, S2 = ?, S3 = ?, q = ?, u
       = ?, q_err = ?, u_err = ?, p = ?, p_err_minus = ?, p_err_plus = ?, beta = ?,
       beta_err = ? WHERE id = ?');
95 #Grab data
   if ($mode == 1) { # Calculate everything
97   $grab=$ripe::DB_grb->prepare("Select id, a1, b1, c1, d1, a2, b2, c2, d2, a1_err,
       b1_err, c1_err, d1_err, a2_err, b2_err, c2_err, d2_err, p, target, mjd, camera,
       xpix, ypix from photdata, obs where obs_id_link=obs_id and tag_link=tag");
   }
99
   if ($mode == 2) { # Calculate targets only
101  $grab=$ripe::DB_grb->prepare("Select id, a1, b1, c1, d1, a2, b2, c2, d2, a1_err,
       b1_err, c1_err, d1_err, a2_err, b2_err, c2_err, d2_err, p, target, mjd, camera,
       xpix, ypix from photdata, obs where obs_id_link=obs_id and tag_link=tag and
       target is not null");
   }
103
   $grab->execute();
105
107
   #go through each row
109 while (@data = $grab->fetchrow_array()){

111  $id = $data[0];
     $a1 = $data[1];
113  $b1 = $data[2];
     $c1 = $data[3];
115  $d1 = $data[4];
     $a2 = $data[5];
117  $b2 = $data[6];
     $c2 = $data[7];
119  $d2 = $data[8];
     $a1_err = $data[9];
121  $b1_err = $data[10];
     $c1_err = $data[11];
```

```
$d1_err = $data[12];
$a2_err = $data[13];
$b2_err = $data[14];
$c2_err = $data[15];
$d2_err = $data[16];
$pol = $data[17];
$target = $data[18];
$mjd = $data[19];
$camera = $data[20];
$xpix = $data[21];
$ypix = $data[22];

if ($calibrate == 2) {
  $a1 /= $A1_correction;
  $b1 /= $B1_correction;
  $c1 /= $C1_correction;
  $d1 /= $D1_correction;
  $a2 /= $A2_correction;
  $b2 /= $B2_correction;
  $c2 /= $C2_correction;
  $d2 /= $D2_correction;
}


$s1 = $a1 + $a2 + $b1 + $b2 + $c1 + $c2 + $d1 + $d2;
$s2 = $a1 + $a2 + $b1 + $b2;
$s3 = $b1 + $b2 + $c1 + $c2;

$s1_err = sqrt(($a1_err**2)+($a2_err**2)+($b1_err**2)+($b2_err**2)+($c1_err**2)+(
  $c2_err**2)+($d1_err**2)+($d2_err**2));
$s2_err = sqrt(($a1_err**2)+($a2_err**2)+($b1_err**2)+($b2_err**2));
$s3_err = sqrt(($b1_err**2)+($b2_err**2)+($c1_err**2)+($c2_err**2));

print "Running on ID: $id\n";
# calculate q and u
$q = $pi * (0.5 - ($s3/$s1));
$u = $pi * (($s2/$s1) - 0.5);

$q_err = $pi * sqrt( (($s3_err / $s1)**2) + (($s1_err * $s3 / ($s1**2))**2));
$u_err = $pi * sqrt( (($s2_err / $s1)**2) + (($s1_err * $s2 / ($s1**2))**2));

# Apply calibration options for q and u
if ($calibrate == 1){ #calibration from zero polarised spreads.

  $q += -$q_zeropoint;
  $u += -$u_zeropoint;
```

```
169     $q_err_prev = $q_err;
        $u_err_prev = $u_err;
171
        $q_err = sqrt (($q_err_prev ** 2) + ($q_zeropoint_error ** 2));
173     $u_err = sqrt (($u_err_prev ** 2) + ($u_zeropoint_error ** 2));

175   }

177   if ($calibrate == 3){ # Calibration of q and u taken from an n day spread around
        observation

179
        ($q_zeropoint, $u_zeropoint, $q_zeropoint_error, $u_zeropoint_error) = ripe::
        get_zeropoints($mjd, $camera, 2);
181
        $q += -$q_zeropoint;
183     $u += -$u_zeropoint;

185     $q_err_prev = $q_err;
        $u_err_prev = $u_err;
187
        $q_err = sqrt (($q_err_prev ** 2) + ($q_zeropoint_error ** 2));
189     $u_err = sqrt (($u_err_prev ** 2) + ($u_zeropoint_error ** 2));

191   }

193


195   if ($ellipse_correction == 1) {
        print "SCALING\n";
197
        $q *= $q_scaling_factor;
199     $u *= $u_scaling_factor;

201     $q_err *= $q_scaling_factor;
        $u_err *= $u_scaling_factor;
203   }

205
      if ($ellipse_correction == 2) {
207     # All this is in a RINGO polarimetric data reduction document D.Arnold Jan 2015

209     if ($camera eq d){
          $E = $dE;
211       $theta = $dtheta;
          print "$camera --> NOT\n\n";
213     }
```

```
215     if  ($camera eq e){
          $E = $eE;
217       $theta = $etheta;
          print "$camera --> THERE\n\n";
219     }

221     if  ($camera eq f){
          $E = $fE;
223       $theta = $ftheta;
          print "$camera --> HERE!!!!!\n\n";
225     }

227

229

        $phi = atan2($u, $q) - $theta;
231     $r_squared = $q**2+$u**2;
        $a = sqrt($r_squared / ((cos($phi)**2) + ((1-(2*$E)+($E**2)) * (sin($phi)**2))));
233     $delta_b = $a * $E * sin($phi);
        if ($DEBUG) {
235       print DEBUG "Camera = $camera, E = $E, theta = $theta\t$q\t$u\t$phi\t$a\t$r\n";
        }
237     $q -= $delta_b * sin($theta);
        $u += $delta_b * cos($theta);
239   }

241

    # Calculate polarisation and angle
243 $pol = sqrt(($q**2)+($u**2));

245

    print DEBUG "TARGET: $target\n";
247 if ($target) {
      $pol_err_minus = $pol * 0.5 * ((sqrt( ((2 * $q_err * $q)**2) + ((2 * $u_err * $u)
      **2))) / (($q*$q)+($u*$u)));
249   $pol_err_plus = $pol_err_minus;
    }
251

    else
253 { # Do monte carlo analysis
      print "Target detected. Doing Monte Carlo Errors\n";
255   ($pol, $pol_err_minus, $pol_err_plus) = ripe::mcerror($q, $u, $q_err, $u_err);
    }
257

    if ($q != 0 && $u != 0) { # Stops division by zero.
259   $beta = (atan2 $u,$q) / 2; # See atan2 and why the normal atan function does not
```

```
    work here.
    $uOVERq_err = sqrt ((($u_err / $u)**2) + (($q_err / $q)**2)) * ($u / $q);
    $beta_err = $uOVERq_err / (1 + (($u / $q)**2)) / (2 * $pi) * 360;
    $beta_deg = (($beta / (2 * $pi)) * 360) + 90;
  }


  # Grab and apply pol correcttion on field
  $polcor = 0;

  if ($polcor) {
    $pol_correction = ripe::field_correct($xpix, $ypix);
    $pol -= $pol_correction;
  }

  # print "$id\n";
  $input->execute($s1, $s2, $s3, $q, $u, $q_err, $u_err, $pol, $pol_err_minus,
    $pol_err_plus, $beta_deg, $beta_err, $id);
  $counter++;
  print "Processed:\t$counter\n\n";

}
```

Listing A.2: `polcalc` which performs the polarisation and error calculations on each detected source in the databse. Numerous switches exist in the code for methods of instrumental polarisation correction, with either defined Stokes zeropoints, or a dynamic calculation using the `get_zeropoints()` routine listed in Listing A.7.

```
#!/usr/bin/python
from pylab import *
import sys
import math

def ringo_pol_error(q_obs, u_obs, q_err, u_err):
    c = u_obs/q_obs
    p_obs = sqrt(q_obs*q_obs+u_obs*u_obs)
    good_pols = [] # empty list
    for pol in arange(0.001,50.0,0.001):
        q_val = sqrt(pol*pol/(1+c*c))
        u_val = sqrt(pol*pol/(1+1/(c*c)))
        q=q_val+q_err*randn(1000)
        u=u_val+u_err*randn(1000)
        p = sqrt(u*u+q*q)
        lower=percentile(p,16)
        middle=percentile(p,50)
        upper=percentile(p,84)
        if p_obs>lower and p_obs<upper:
            good_pols.append(pol)
    raw_pol = p_obs
    corrected_pol=0.0
    upper_pol=0.0
    lower_pol=0.0
    if (len(good_pols)!=0):
        corrected_pol = mean(good_pols)
        lower_pol = min(good_pols)
        upper_pol = max(good_pols)
    return([raw_pol, corrected_pol, lower_pol, upper_pol])
(raw_pol, corrected_pol, lower_pol, upper_pol) = ringo_pol_error(float(sys.argv[1]),
    float(sys.argv[2]), float(sys.argv[3]), float(sys.argv[4]))
print raw_pol, corrected_pol, lower_pol, upper_pol
```

Listing A.3: ringoerror.py, which uses a Monte Carlo method to calculate the asymmetric errors on polarisation.

```
| Field      | Type                    | Null | Key | Default | Extra |
+------------+-------------------------+------+-----+---------+-------+
| obs_id     | varchar(30)             | NO   | PRI |         |       |
| camera     | enum('p','d','e','f')   | YES  |     | NULL    |       |
| tag        | varchar(16)             | NO   | PRI |         |       |
| object     | varchar(40)             | YES  |     | NULL    |       |
| date       | varchar(8)              | YES  |     | NULL    |       |
| mjd        | float(10,3)             | YES  |     | NULL    |       |
| wcs_ra     | float(8,4)              | YES  |     | NULL    |       |
| wcs_dec    | float(8,4)              | YES  |     | NULL    |       |
| alt        | float(8,4)              | YES  |     | NULL    |       |
| az         | float(8,4)              | YES  |     | NULL    |       |
| rotmount   | float(5,3)              | YES  |     | NULL    |       |
| rotskypa   | float(6,3)              | YES  |     | NULL    |       |
| ut_start   | varchar(14)             | YES  |     | NULL    |       |
| t_exp      | float(10,4)             | YES  |     | NULL    |       |
| t_dur      | float(10,4)             | YES  |     | NULL    |       |
| moon_alt   | int(16)                 | YES  |     | NULL    |       |
| moon_dist  | int(16)                 | YES  |     | NULL    |       |
| moon_frac  | float(4,2)              | YES  |     | NULL    |       |
| numfrms    | int(16)                 | YES  |     | NULL    |       |
| gain       | float(10,5)             | YES  |     | NULL    |       |
| apsize     | int(16)                 | YES  |     | NULL    |       |
| backsize   | int(16)                 | YES  |     | NULL    |       |
```

Listing A.4: specifications of the obs table for the ripe mysql database. This contains details of each observation.

```
| Field          | Type         | Null | Key | Default | Extra          |
+----------------+--------------+------+-----+---------+----------------+
| id             | int(16)      | NO   | PRI | NULL    | auto_increment |
| obs_id_link    | varchar(22)  | YES  |     | NULL    |                |
| tag_link       | varchar(16)  | YES  |     | NULL    |                |
| target         | char(1)      | YES  |     | NULL    |                |
| target_dist    | int(11)      | YES  |     | NULL    |                |
| target_score   | int(11)      | YES  |     | NULL    |                |
| xpix           | float(6,3)   | YES  |     | NULL    |                |
| ypix           | float(6,3)   | YES  |     | NULL    |                |
| ra             | float(8,5)   | YES  |     | NULL    |                |
| decn           | float(8,5)   | YES  |     | NULL    |                |
| A1             | float(12,3)  | YES  |     | NULL    |                |
| B1             | float(12,3)  | YES  |     | NULL    |                |
| C1             | float(12,3)  | YES  |     | NULL    |                |
| D1             | float(12,3)  | YES  |     | NULL    |                |
| A2             | float(12,3)  | YES  |     | NULL    |                |
| B2             | float(12,3)  | YES  |     | NULL    |                |
| C2             | float(12,3)  | YES  |     | NULL    |                |
| D2             | float(12,3)  | YES  |     | NULL    |                |
| A1_err         | float(12,3)  | YES  |     | NULL    |                |
| B1_err         | float(12,3)  | YES  |     | NULL    |                |
| C1_err         | float(12,3)  | YES  |     | NULL    |                |
| D1_err         | float(12,3)  | YES  |     | NULL    |                |
| A2_err         | float(12,3)  | YES  |     | NULL    |                |
| B2_err         | float(12,3)  | YES  |     | NULL    |                |
| C2_err         | float(12,3)  | YES  |     | NULL    |                |
| D2_err         | float(12,3)  | YES  |     | NULL    |                |
| flag           | int(8)       | YES  |     | NULL    |                |
| S1             | float(13,3)  | YES  |     | NULL    |                |
| S2             | float(13,3)  | YES  |     | NULL    |                |
| S3             | float(13,3)  | YES  |     | NULL    |                |
| q              | float(7,6)   | YES  |     | NULL    |                |
| u              | float(7,6)   | YES  |     | NULL    |                |
| q_err          | float(7,6)   | YES  |     | NULL    |                |
| u_err          | float(7,6)   | YES  |     | NULL    |                |
| p              | float(4,3)   | YES  |     | NULL    |                |
| p_err_minus    | float(4,3)   | YES  |     | NULL    |                |
| p_err_plus     | float(4,3)   | YES  |     | NULL    |                |
| beta           | int(16)      | YES  |     | NULL    |                |
| beta_err       | int(16)      | YES  |     | NULL    |                |
```

Listing A.5: specifications of the photdata table for the ripe mysql database. This contains the data and polarisation values for each source extracted by ripe

```
# GAIA SExtractor configuration parameters file.
CATALOG_NAME       GaiaCatalog0.ASC
PARAMETERS_NAME      ripe.paramTotnes
CATALOG_TYPE       ASCII_HEAD
DETECT_MINAREA     3
THRESH_TYPE        RELATIVE
DETECT_THRESH      3
ANALYSIS_THRESH    1.0
FILTER             Y
FILTER_NAME        /usr/local/starlink/star-hikianalia/bin/extractor/config/default.
    conv
DEBLEND_NTHRESH    32
DEBLEND_MINCONT    0.005
CLEAN              Y
CLEAN_PARAM        1.0
MAG_ZEROPOINT      0.0
PHOT_APERTURES     9
PHOT_AUTOPARAMS       2.5,3.5
PHOT_PETROPARAMS   2.0,3.5
PHOT_FLUXFRAC      0.5
MASK_TYPE          CORRECT
DETECT_TYPE        CCD
PIXEL_SCALE        1.0
SATUR_LEVEL        60000.0
MAG_GAMMA          4.0
SEEING_FWHM        1.2
STARNNW_NAME       /star/bin/extractor/config/default.nnw
BACK_SIZE          64
BACK_FILTERSIZE    4
BACK_TYPE          AUTO
BACK_VALUE         0.0
BACKPHOTO_TYPE     LOCAL
BACKPHOTO_THICK    18
CHECKIMAGE_TYPE    NONE
CHECKIMAGE_NAME    check.fits
MEMORY_OBJSTACK    2000
MEMORY_PIXSTACK    300000
MEMORY_BUFSIZE     1024
VERBOSE_TYPE       QUIET
GAIN               16.56
```

Listing A.6: ripe.sex configuration file for sExtractor extraction in the ripe pipeline

```
sub get_zeropoints {
        # range is number of days either side of observation for which to take the
    zpol value
        (my $mjd, my $camera, my $range) = ($_[0], $_[1], $_[2]);
        $averages = $DB_grb->prepare("SELECT count(p), avg(A1/S1), avg(B1/S1), avg(C1
    /S1), avg(D1/S1), avg(A2/S1), avg(B2/S1), avg(C2/S1), avg(D2/S1), stddev(A1/S1),
    stddev(B1/S1), stddev(C1/S1), stddev(D1/S1), stddev(A2/S1), stddev(B2/S1), stddev
    (C2/S1), stddev(D2/S1), max(mjd) - min(mjd) from photdata, obs where obs_id_link=
    obs_id and object like '%zpol%' and abs(mjd-?) < ? and camera=? and target='U'")
    ;
        $averages->execute($mjd, $range, $camera);
        ($num, $A1, $B1, $C1, $D1, $A2, $B2, $C2, $D2, $A1_err, $B1_err, $C1_err,
    $D1_err, $A2_err, $B2_err, $C2_err, $D2_err, $mjd_range) = $averages->
    fetchrow_array();
        if ($num < 2) {
                $range += 1;
                if ($DEBUG) {print "DBG --> get_zeropoints: Number of sources is $num
    , recalling with range $range\n";}
                ($q_zeropoint, $u_zeropoint, $q_zeropoint_err, $u_zeropint_error) =
    get_zeropoints($mjd, $camera, $range);
        }
        else {
        ($q_zeropoint, $u_zeropoint, $q_zeropoint_err, $u_zeropint_error) =
    stokes_calc($A1, $B1, $C1, $D1, $A2, $B2, $C2, $D2, $A1_err, $B1_err, $C1_err,
    $D1_err, $A2_err, $B2_err, $C2_err, $D2_err);
        }
        if ($DEBUG) {print "$num, $q_zeropoint, $u_zeropoint, $q_zeropoint_err,
    $u_zeropint_error, $mjd_range\n";}
        return($q_zeropoint, $u_zeropoint, $q_zeropoint_err, $u_zeropint_error);
}
```

Listing A.7: sub routine getzeropoints(), from ripe.pm, which obtains the Stokes zeropoints for an observation by analysing the database for unpolarised standards at a similar epoch.

```
|-- bin
|   |-- fitellipse.py
|   |-- grabdat
|   |-- imarith.py
|   |-- imstat
|   |-- imstat-cust
|   |-- invariance_test
|   |-- jumble
|   |-- make_ellipse
|   |-- make_ellipse_visual
|   |-- mc.py
|   |-- modhead
|   |-- monte_jumble
|   |-- moonephem
|   |-- moonstate
|   |-- polcalc
|   |-- ripe
|   |-- ripe-centrestat
|   |-- ripe-fieldstat
|   |-- ripe-imstat
|   |-- ripe-imstat-50
|   |-- src
|   |   |-- imarith.c
|   |   |-- imstat.c
|   |   |-- imstat-cust.c
|   |   |-- modhead.c
|   |   |-- README
|   |   |-- ripe-centrestat.c
|   |   |-- ripe-fieldstat.c
|   |   `-- ripe-singlestat.c
|   |-- standfind
|-- config
|   |-- sex
|   |   |-- ripeold.sex
|   |   |-- ripe.param
|   |   `-- ripe.sex
|   |-- standards
|   |   |-- standards.lst
|   |   `-- stands
`-- lib
    |-- ripe.pm
```

Listing A.8: ripe directory structure and files

# Appendix B

# Ellipticity equations

Presented here are the full workings of Equations 5.2 in Chapter 5. For clarity Diagram 5.6 is repeated to detail the geometric quantities in the q-u plane.

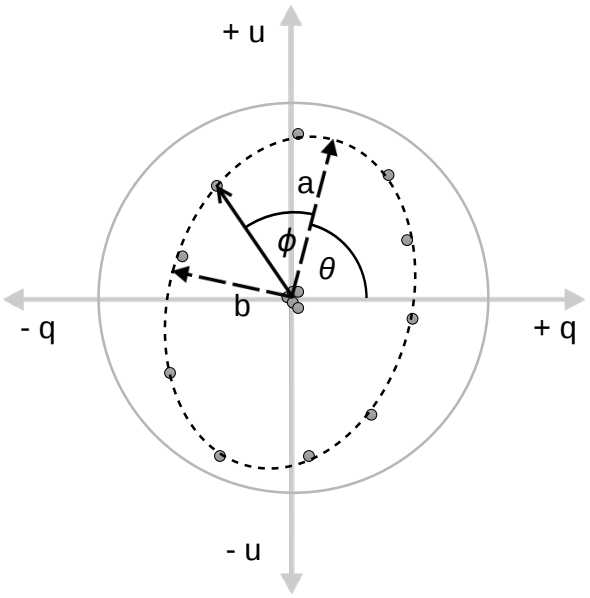


Figure B.1: Simulated polarimetric data points in the q-u plane for a polarised source viewed at a number of sky angles. The ellipse is defined as follows: a - semi-major axis; b - semi-minor axis; $\theta$ - angle of ellipse; and $\phi$ - angular location of datapoint on the ellipse.

$$\phi = tan^{-1}\left(\frac{u}{q}\right) - \theta \tag{B.1a}$$

$$r = \sqrt{(q^2 + u^2)} \tag{B.1b}$$

$$r = \sqrt{a^2\cos^2(\phi) + b^2\sin^2(\phi)} \tag{B.1c}$$

$$\epsilon = \frac{a-b}{a} \tag{B.1d}$$

$$b = a - \epsilon a \tag{B.1e}$$

$$r^2 = a^2\cos^2(\phi) + (a - \epsilon a)(a - \epsilon a)\sin^2(\phi) \tag{B.1f}$$

$$r^2 = a^2\cos^2(\phi) + (a^2 - 2\epsilon a^2 + \epsilon^2 a^2)\sin^2(\phi) \tag{B.1g}$$

$$\frac{r^2}{a^2} = \cos^2(\phi) + (1 - 2\epsilon + \epsilon^2)\sin^2(\phi) \tag{B.1h}$$

$$a = \sqrt{\frac{q^2 + u^2}{\cos^2(\phi) + (1 - 2\epsilon + \epsilon^2)\sin^2(\phi)}} \tag{B.1i}$$

$$\Delta b = (a - b)sin(\phi) \tag{B.1j}$$

$$\Delta b = a\epsilon \times \sin(\phi) \tag{B.1k}$$

$$\Delta q = -\Delta b \times \sin(\theta) \tag{B.1l}$$

$$\Delta u = \Delta b \times \cos(\theta) \tag{B.1m}$$

# Appendix C

# Plots of polarimetric of the field of BD+59°389

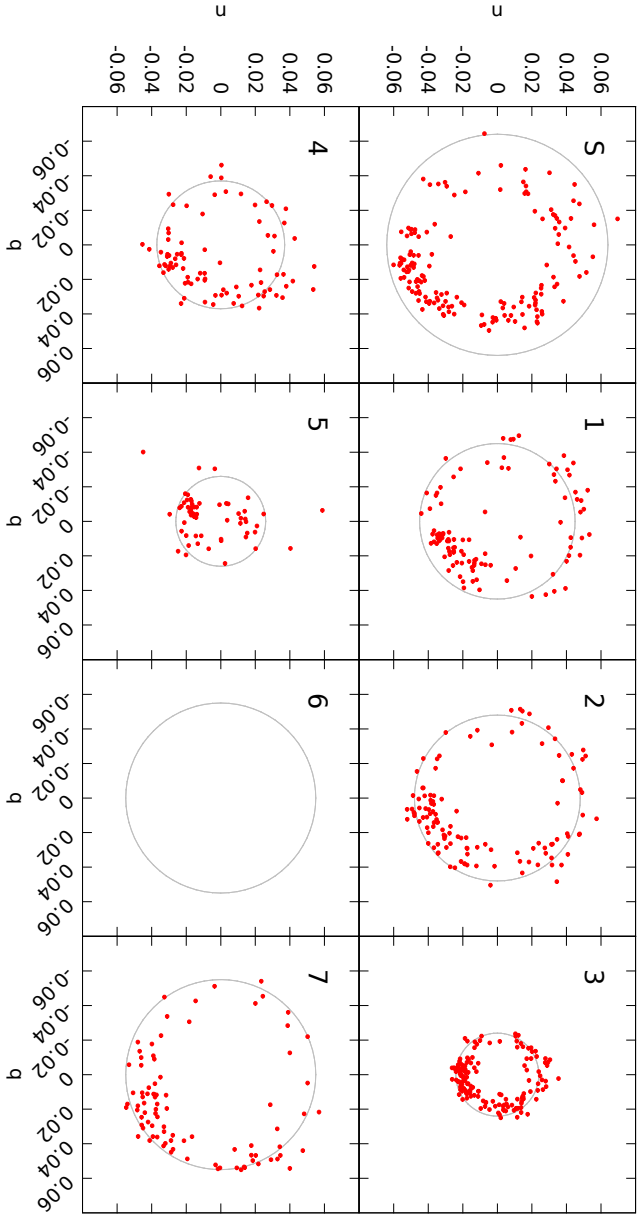


Figure C.1: Polarisation rings for RINGO2 observations of sources in the field of BD+59°389, with ellipticity correction but not depolarisation correction. There is no data for Star 6 as no measurements met the upper threshold of a 1% error on polarisation for inclusion in the analysis. The grey rings are the values of polarisation measured in the V band by the AIMPOL polarimeter from Soam et al. (2014).

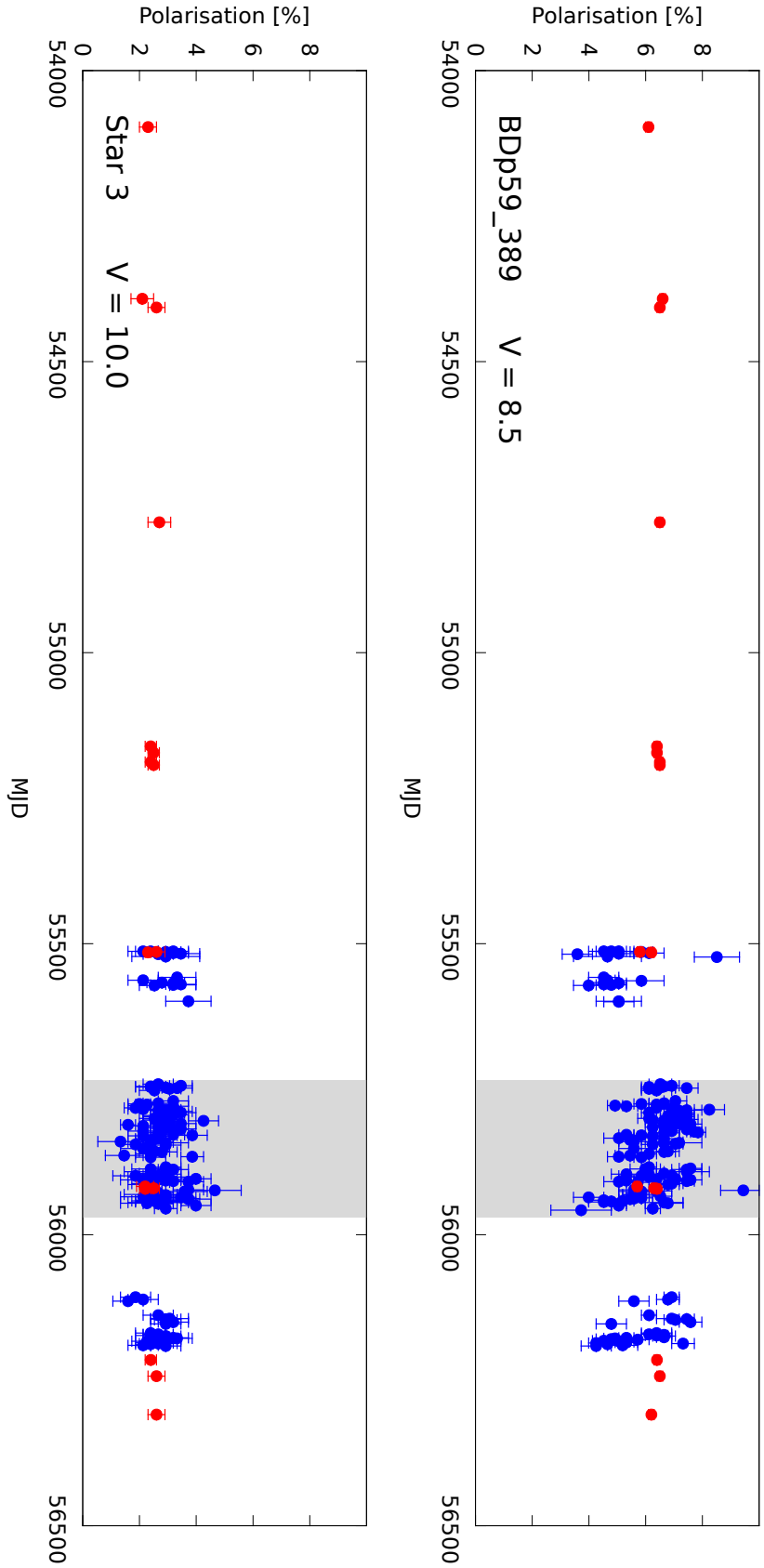


Figure C.2: Temporal visualisation of contemporaneous polarisation measurements of BD+59°389 and Star 3. The data are from Soam et al. with AIMPOL in V-band (Red points) and RINGO2 (Blue points). AIMPOL data from Soam et al. (2014)

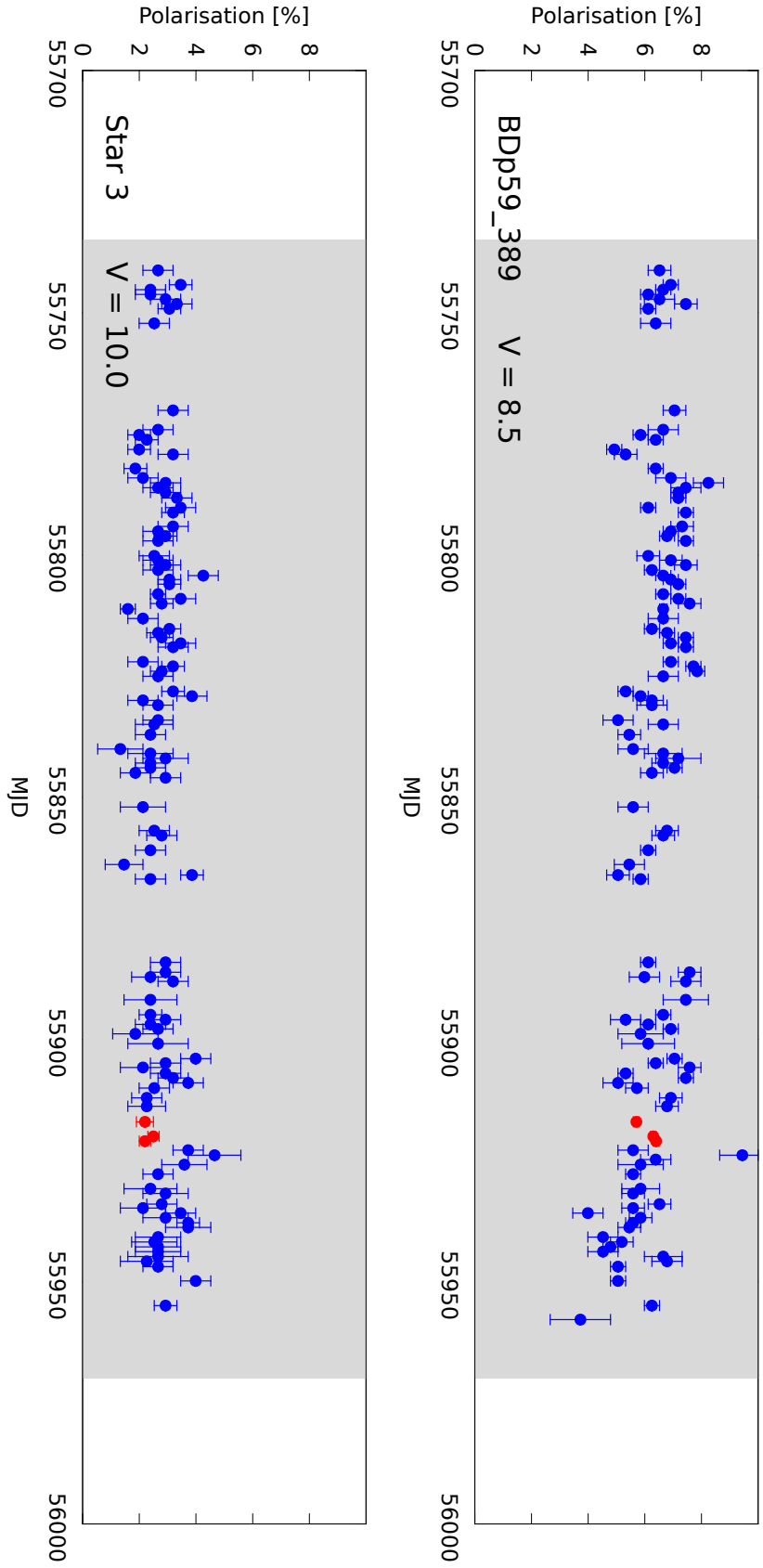


Figure C.3: Zoom of Figure C.2 to show the period in grey, in which AIMPOL and RINGO2 observations have the most temporal overlap.

# Appendix D

# Attempted correlations of RINGO2 polarisations with observing parameters

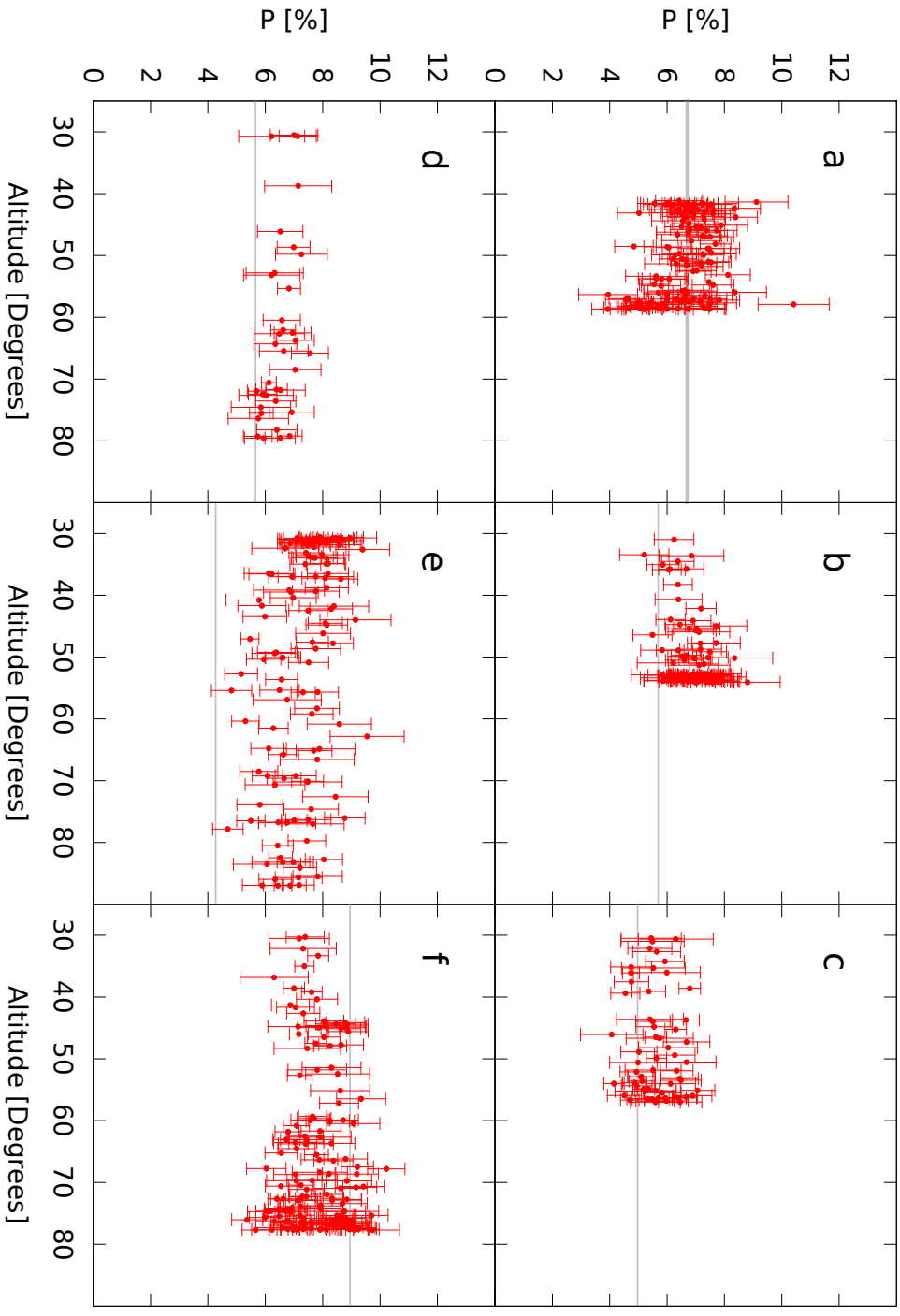


Figure D.1: Polarisation vs observing altitude for polarimetric standards for RINGO2. Grey lines are the catalogue polarisations from Schmidt et al. (1992) and Turnshek et al. (1990).

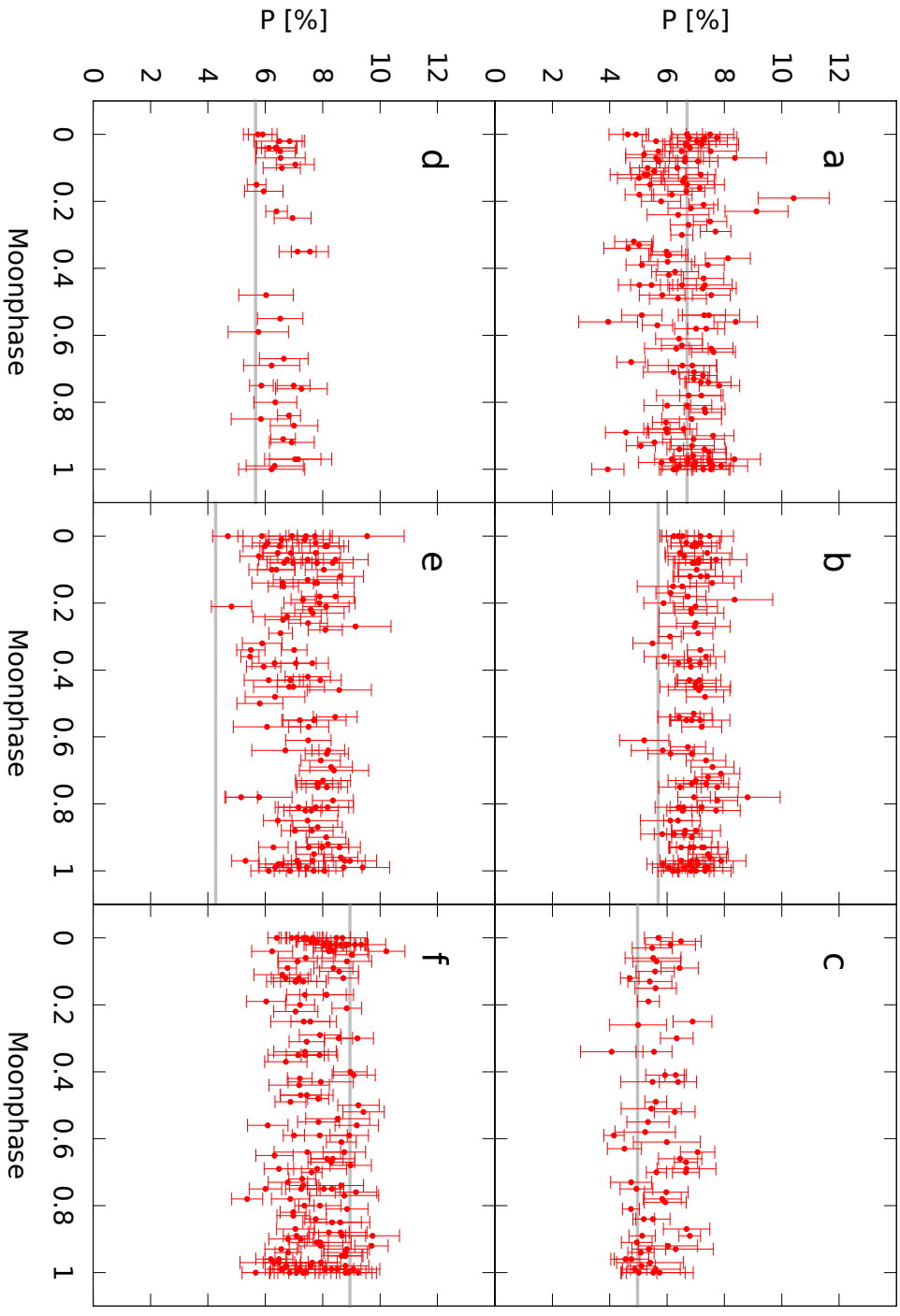


Figure D.2: Polarisation vs Moon phase for polarimetric standards RINGO2. Grey lines are the catalogue polarisations from Schmidt et al. (1992) and Turnshek et al. (1990).

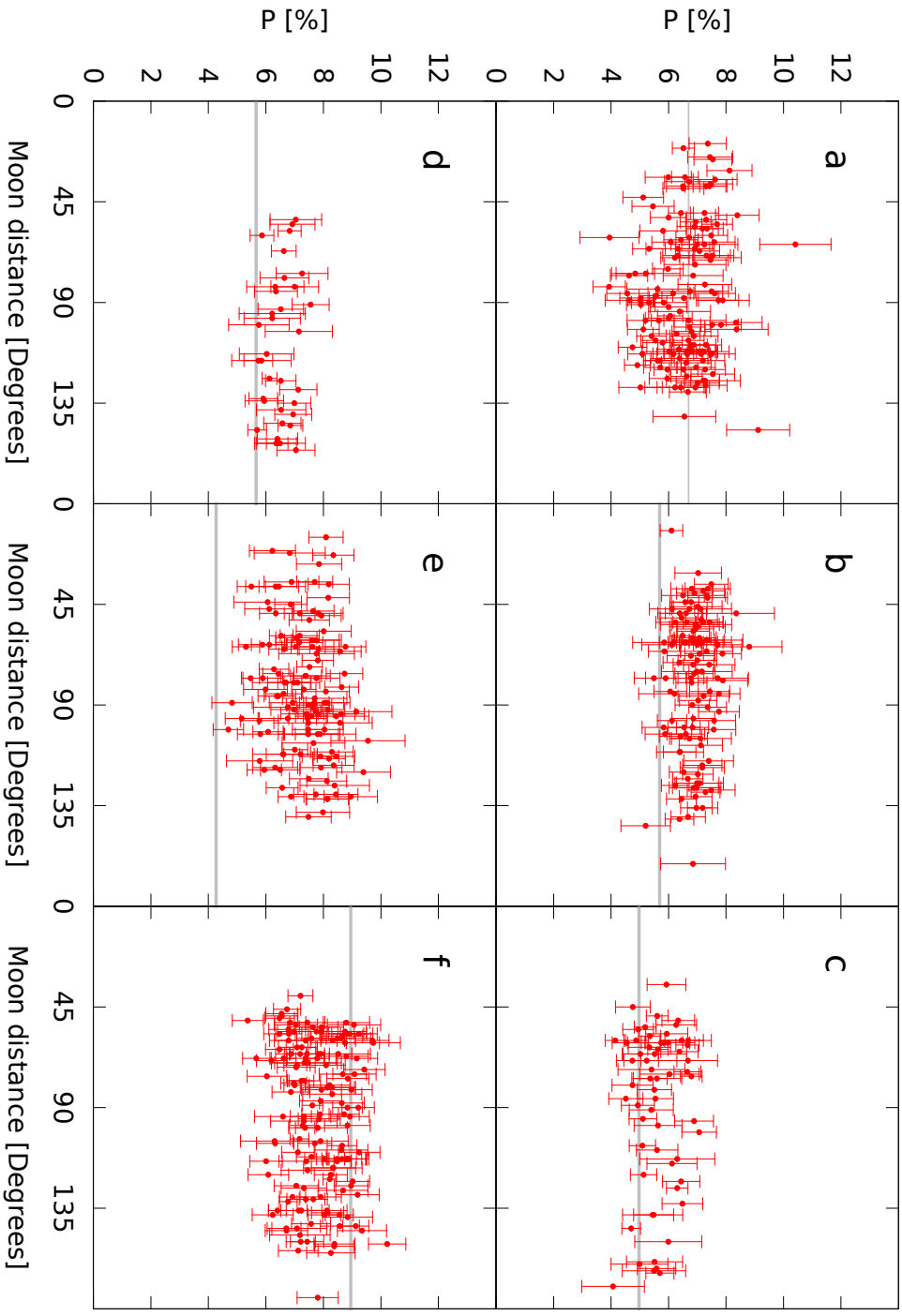


Figure D.3: Polarisation vs angular Moon distance for polarimetric standards RINGO2. Grey lines are the catalogue polarisations from Schmidt et al. (1992) and Turnshek et al. (1990).

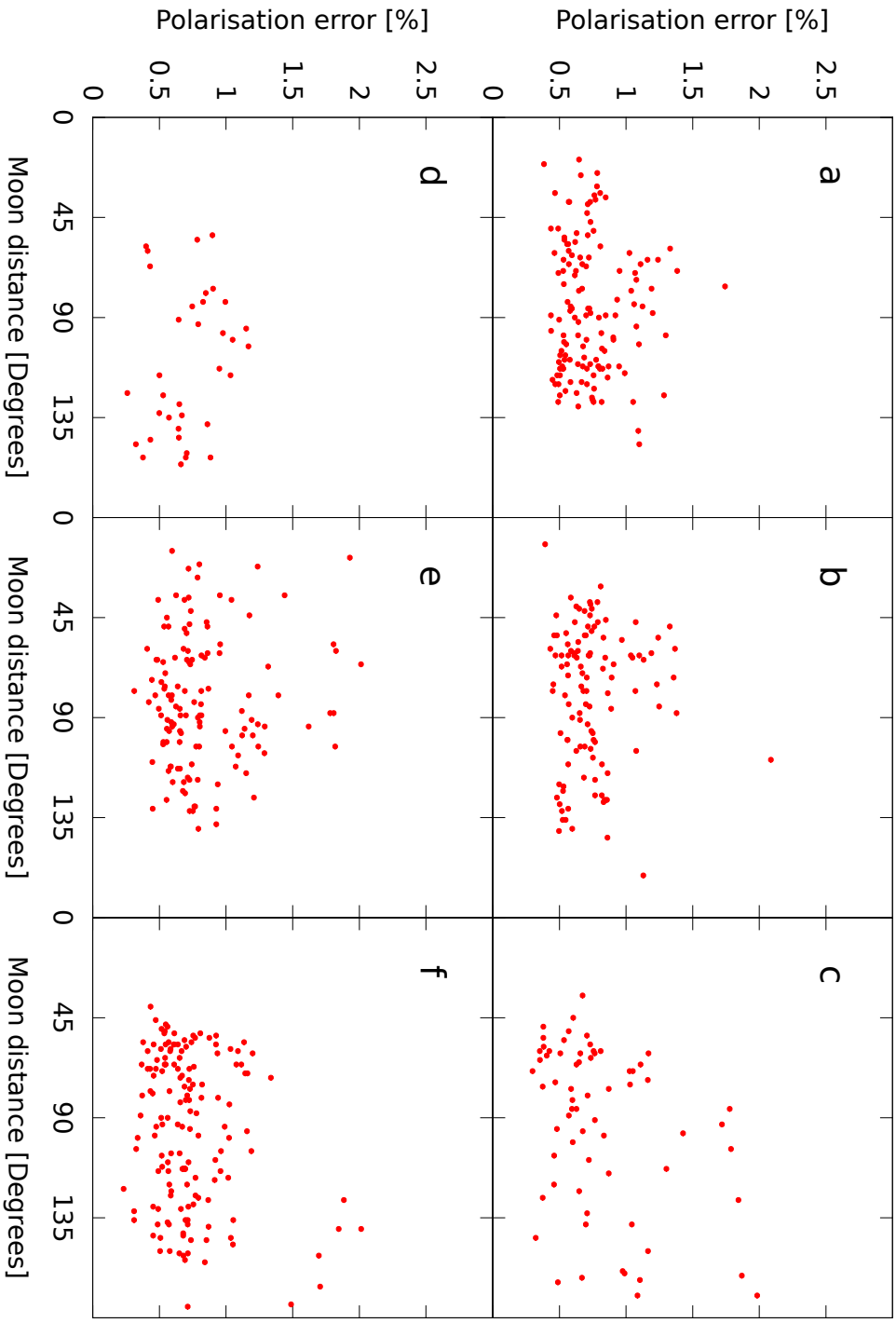


Figure D.4: Polarisation error vs angular Moon distance for polarimetric standards RINGO2.

# Appendix E

# Histograms of RINGO3 correction angle

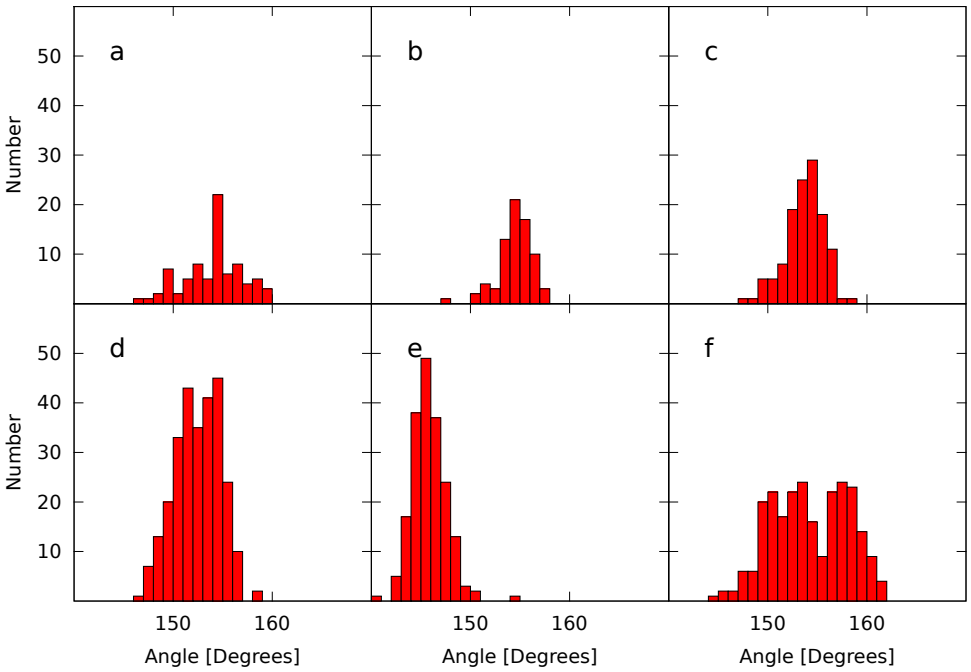


Figure E.1:

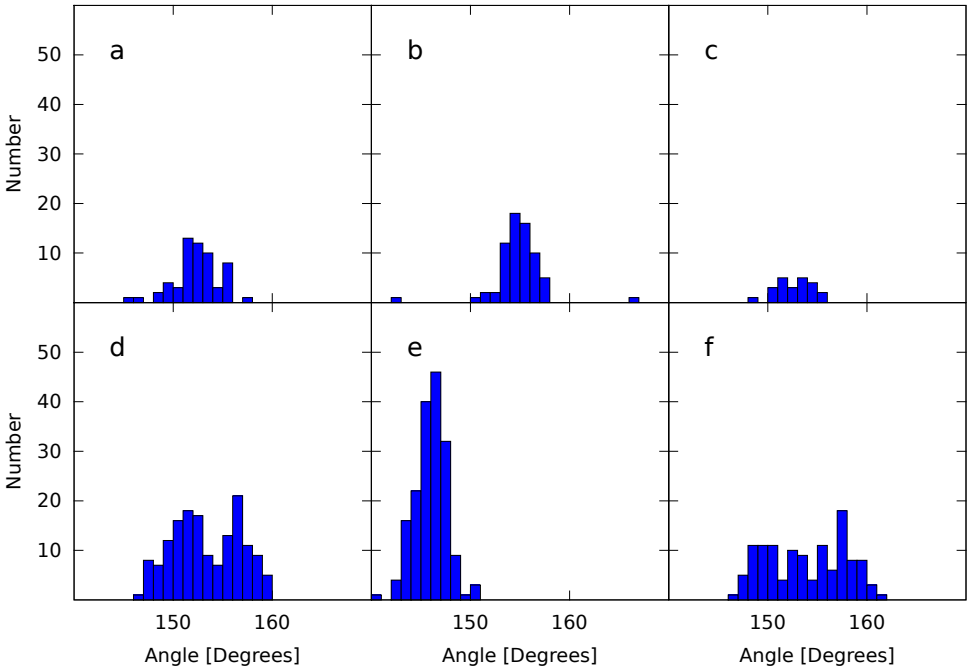


Figure E.2:

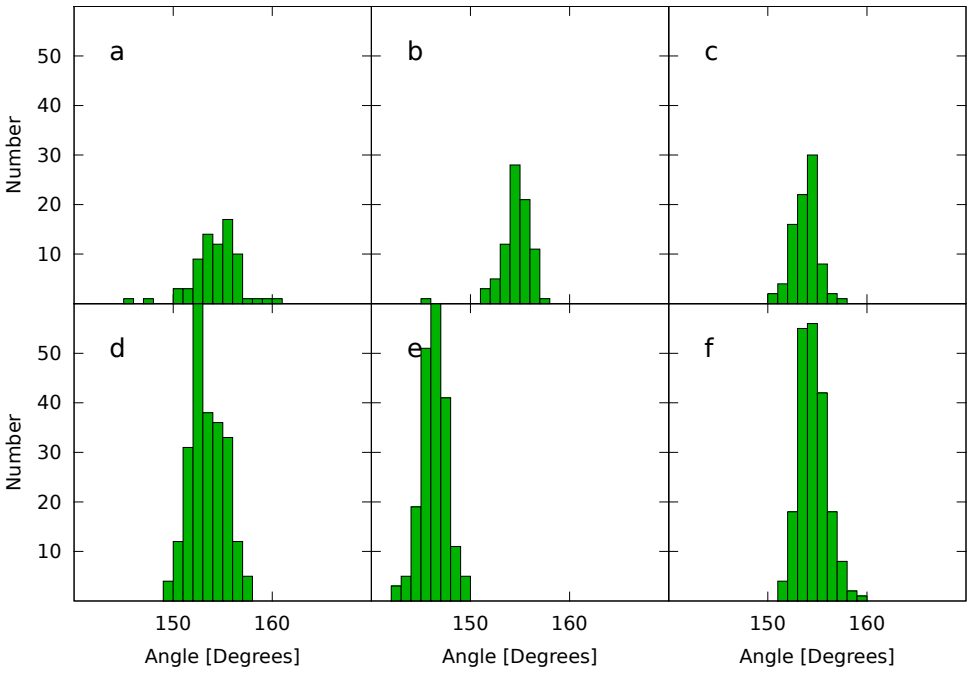
a
b
c
d
e
f
Number
Number
50
40
30
20
10
150
160
Angle [Degrees]
Angle [Degrees]
Angle [Degrees]

Figure E.3:

# Appendix F

# Multi-band photometric lightcurves of RINGO2 GRB sample

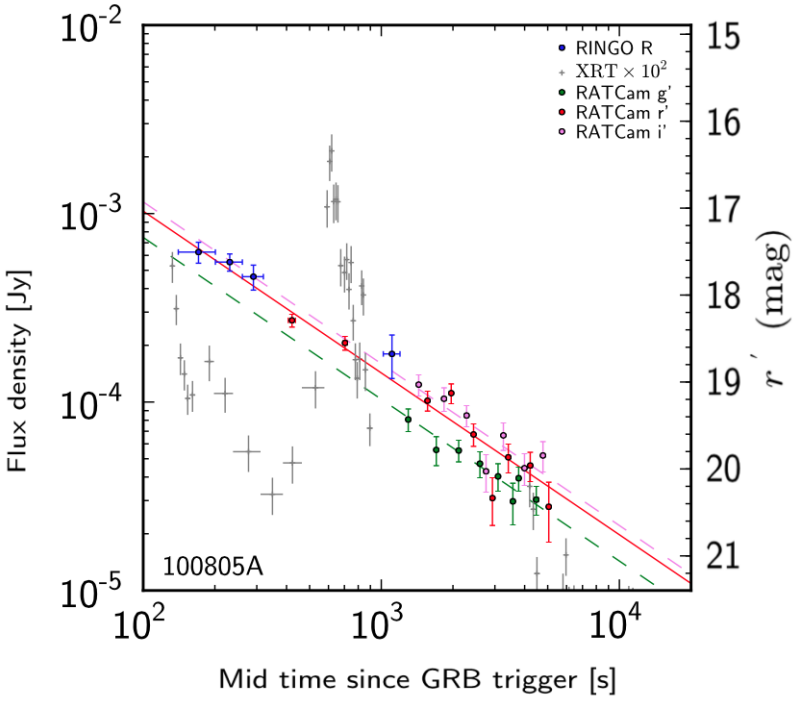


Figure F.1: GRB 100805A lightcurve

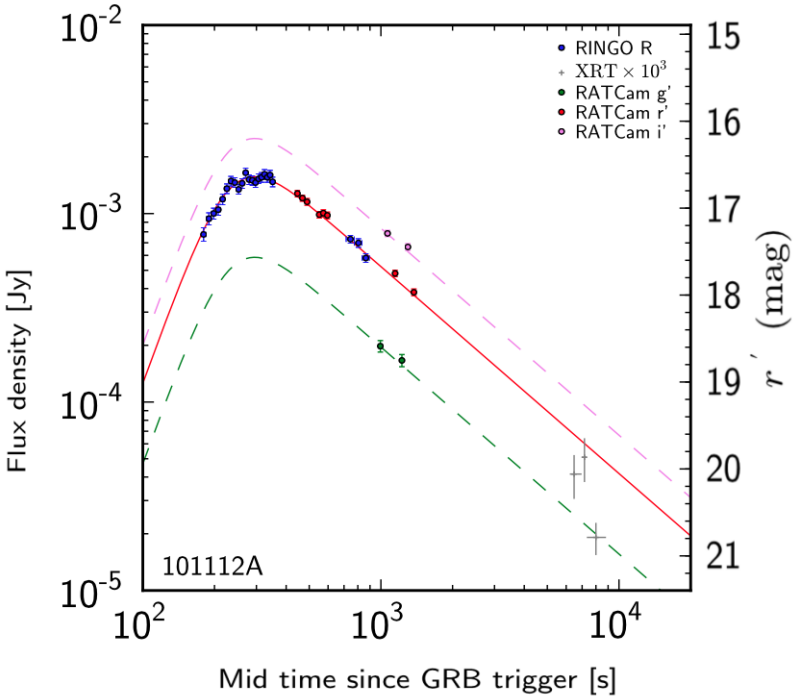


Figure F.2: GRB 101112A lightcurve

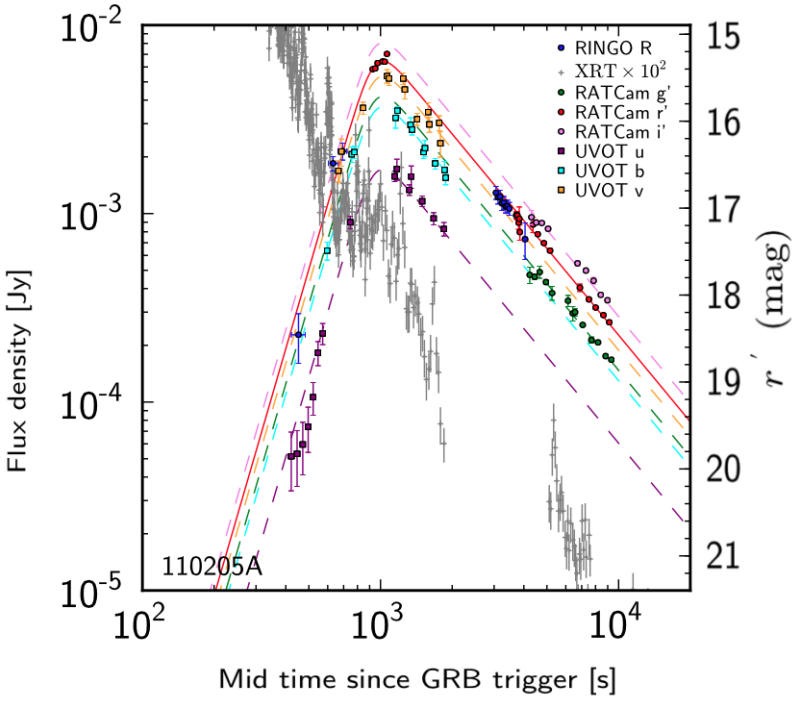


Figure F.3: GRB 110205A lightcurve

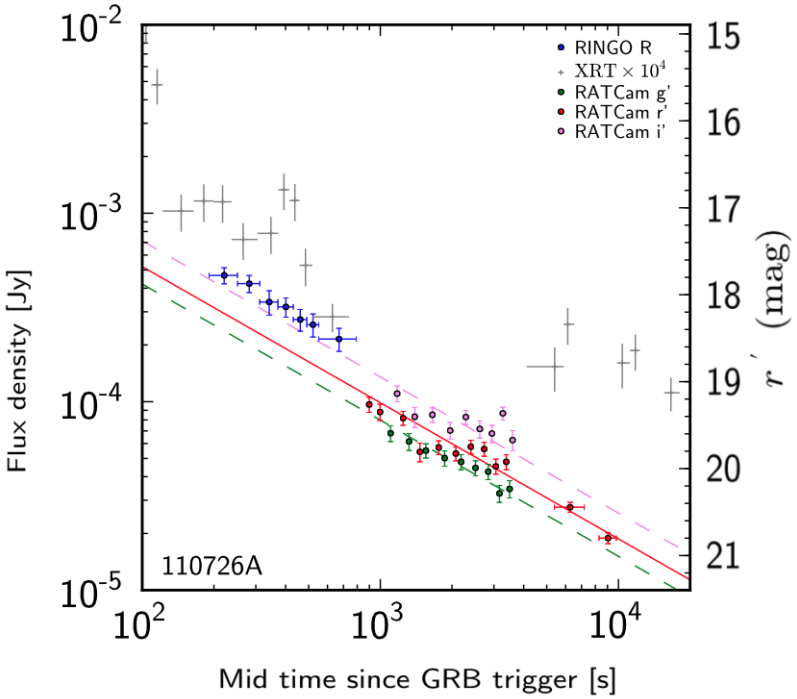


Figure F.4: GRB 110726A lightcurve

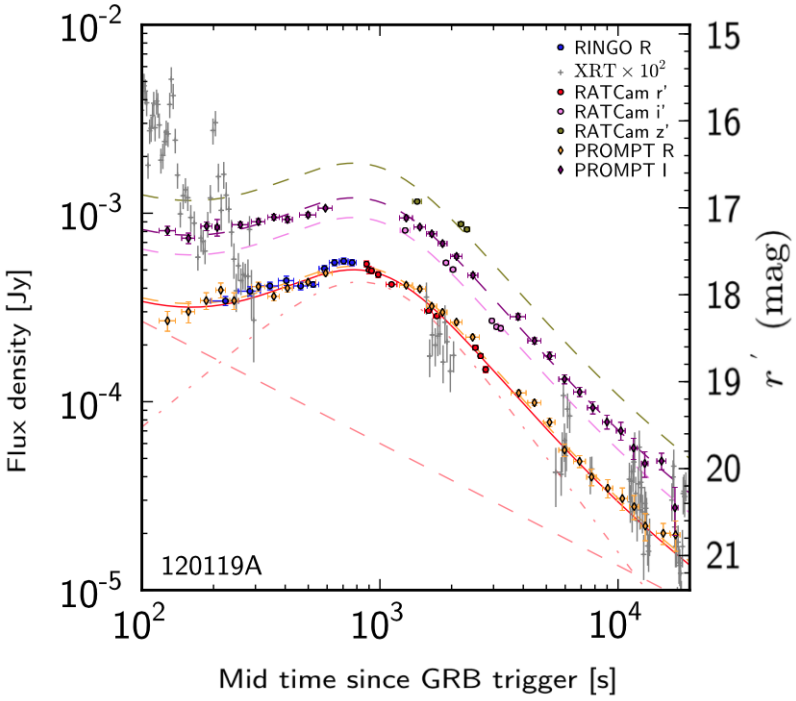


Figure F.5: GRB 120119A lightcurve

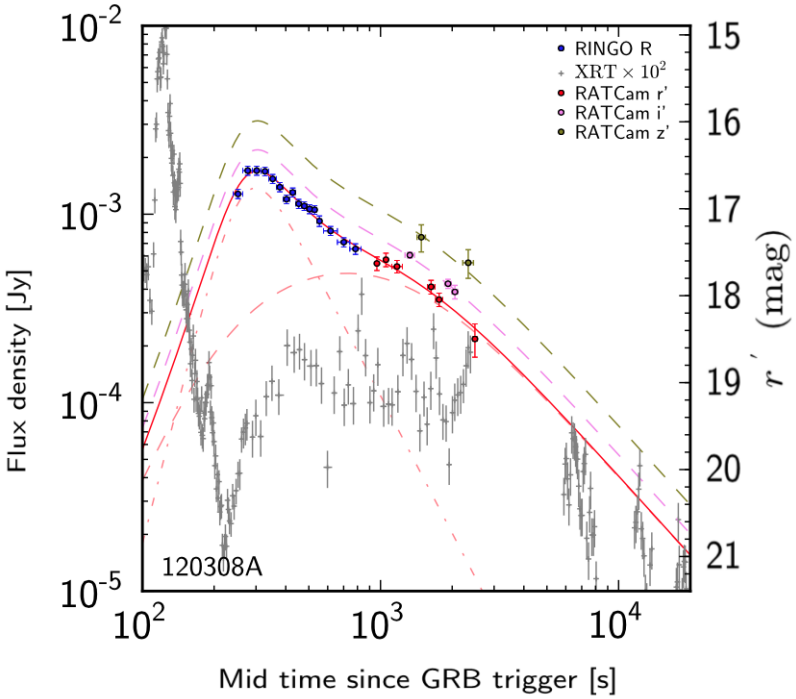


Figure F.6: GRB 120308A lightcurve

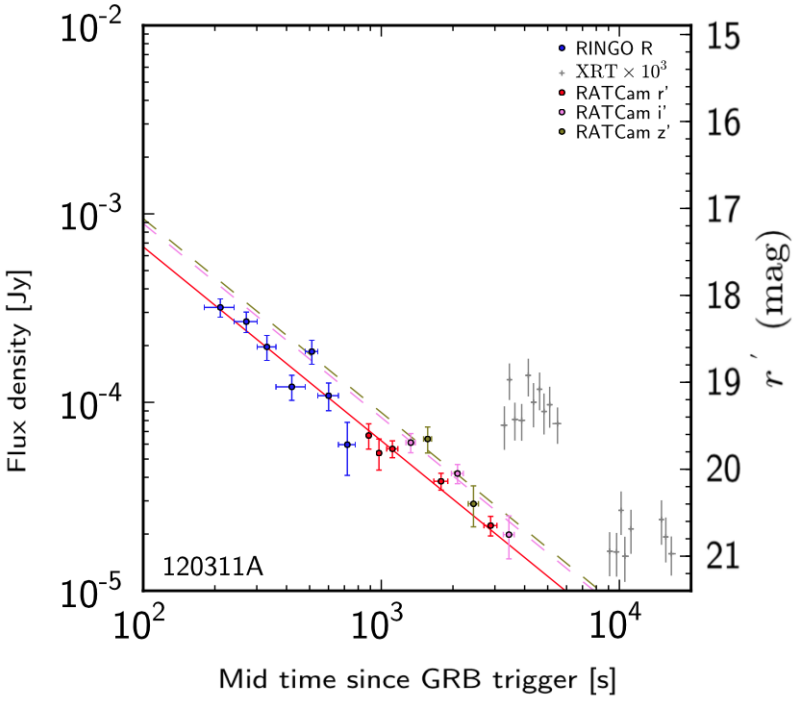


Figure F.7: GRB 120311A lightcurve

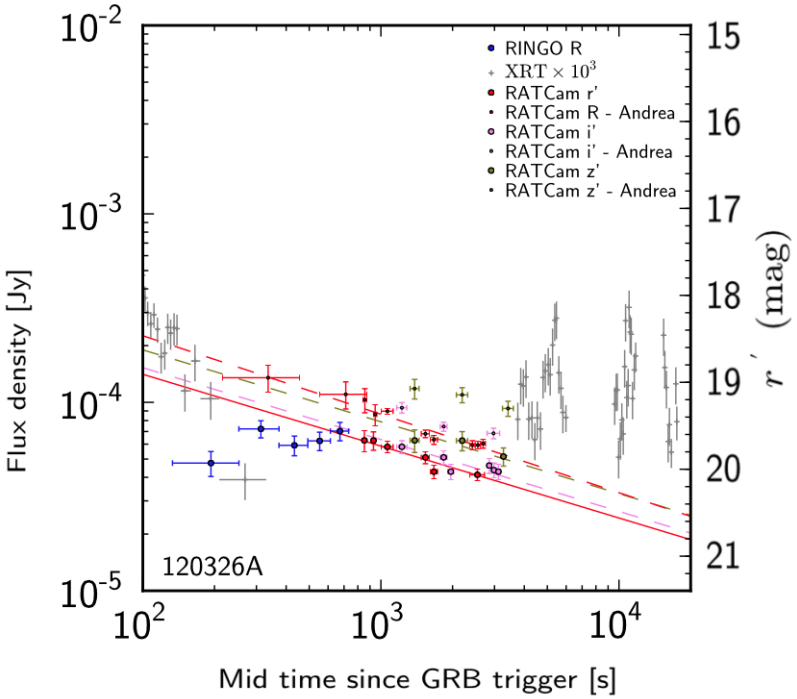


Figure F.8: GRB 120327A lightcurve

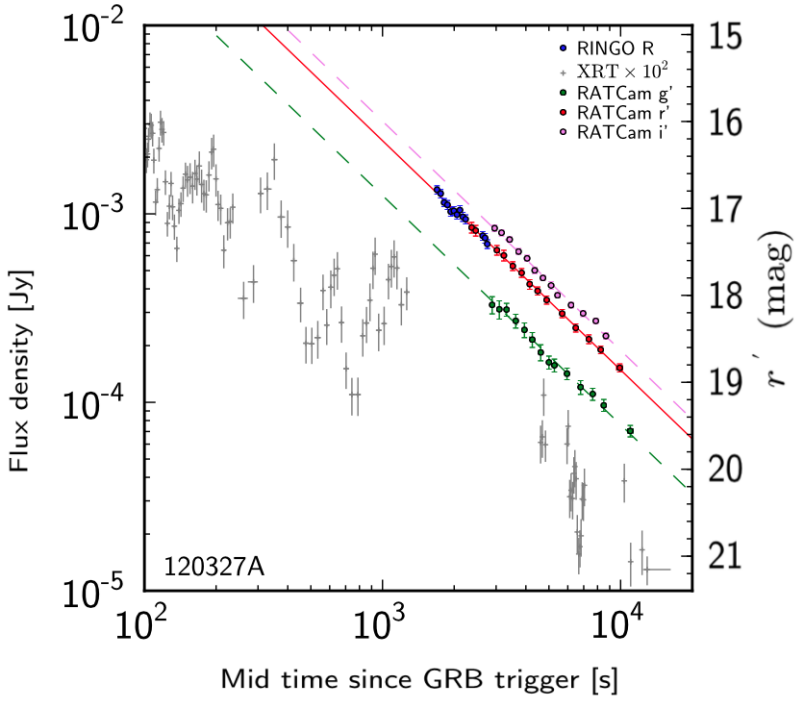


Figure F.9: GRB 120327A lightcurve

# Appendix G

# Polarisation verification plots of RINGO2 GRB sample

Contained in this Appendix are plots of the polarimetry parameters for all sources in the fields of the RINGO2 gamma-ray burst observations, bar GRB 120308A, which is covered by more detailed analysis in Chapter 6. Each figure relates to one observation and contains four plots. In all plots the GRB point is marked in red. Points relating to other sources in the field are marked black.

The order of plots in each figure is;

- The q-u space plot of GRB with all other sources in field included as points with no errors.
- The normalised Stokes parameters versus magnitude
- The Rank plot
- The Polarisation versus magnitude

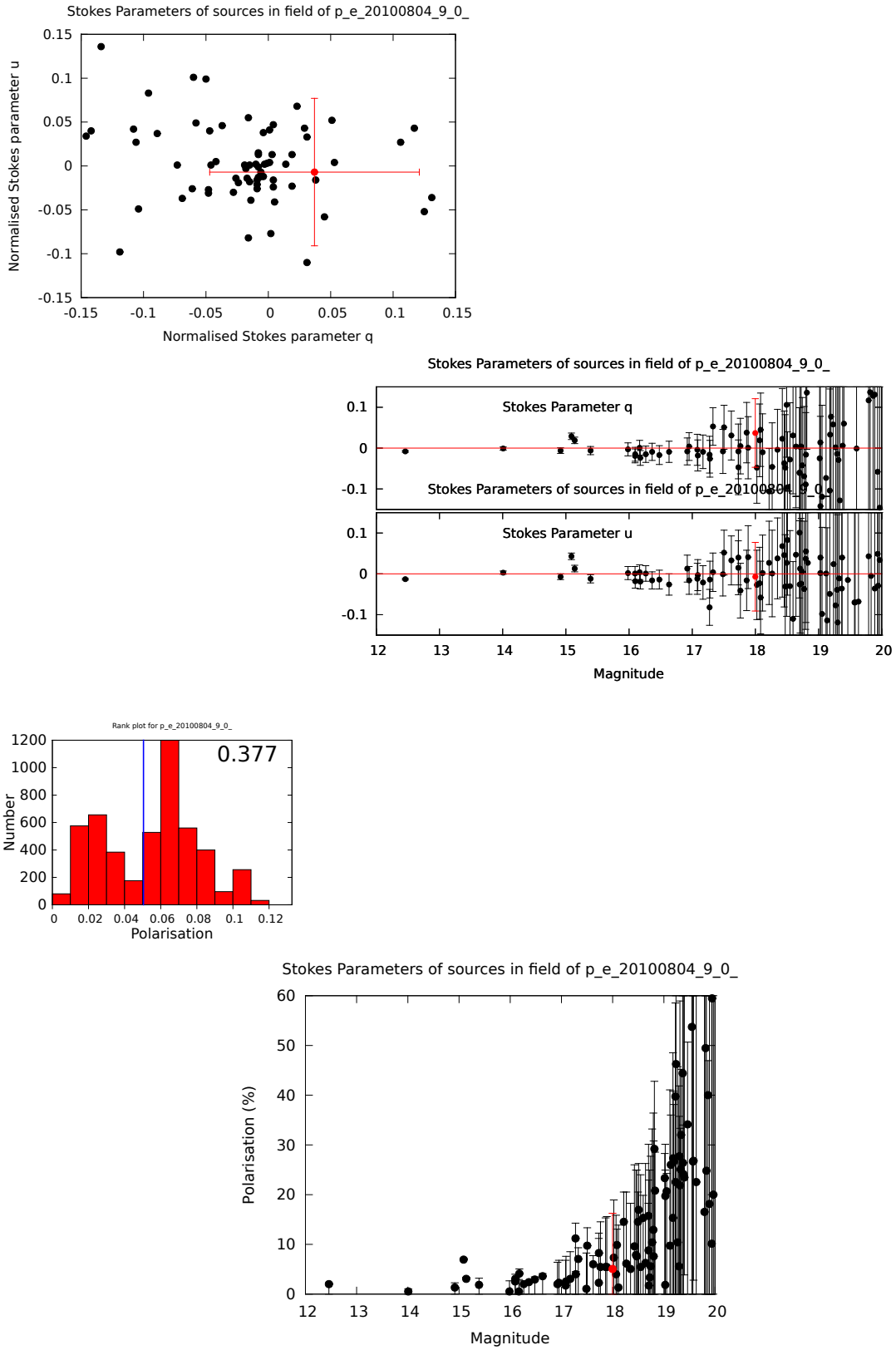


Figure G.1: GRB 100805A polarisation verification plots.

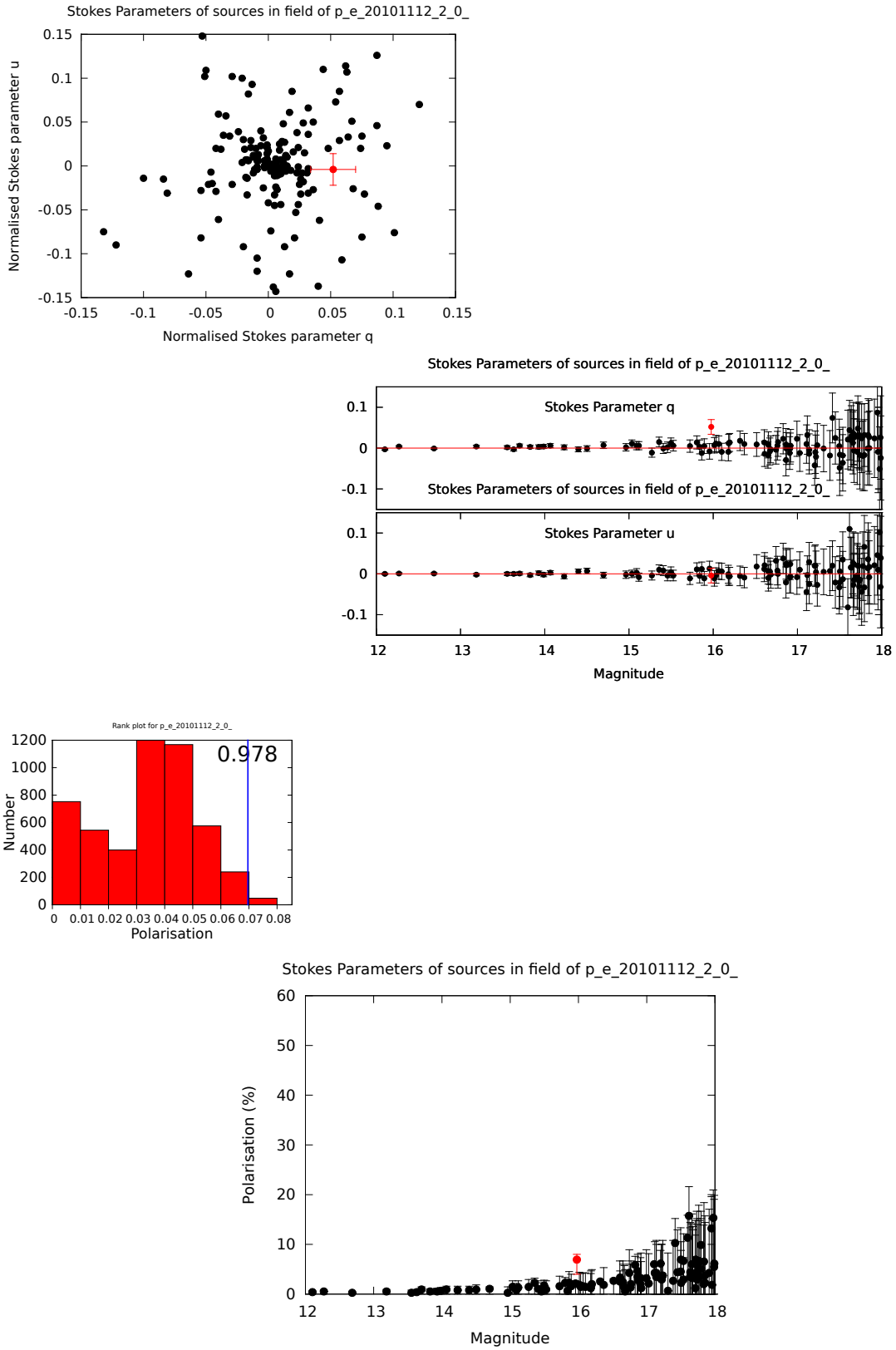


Figure G.2: GRB 101112A polarisation verification plots (Obs 1).

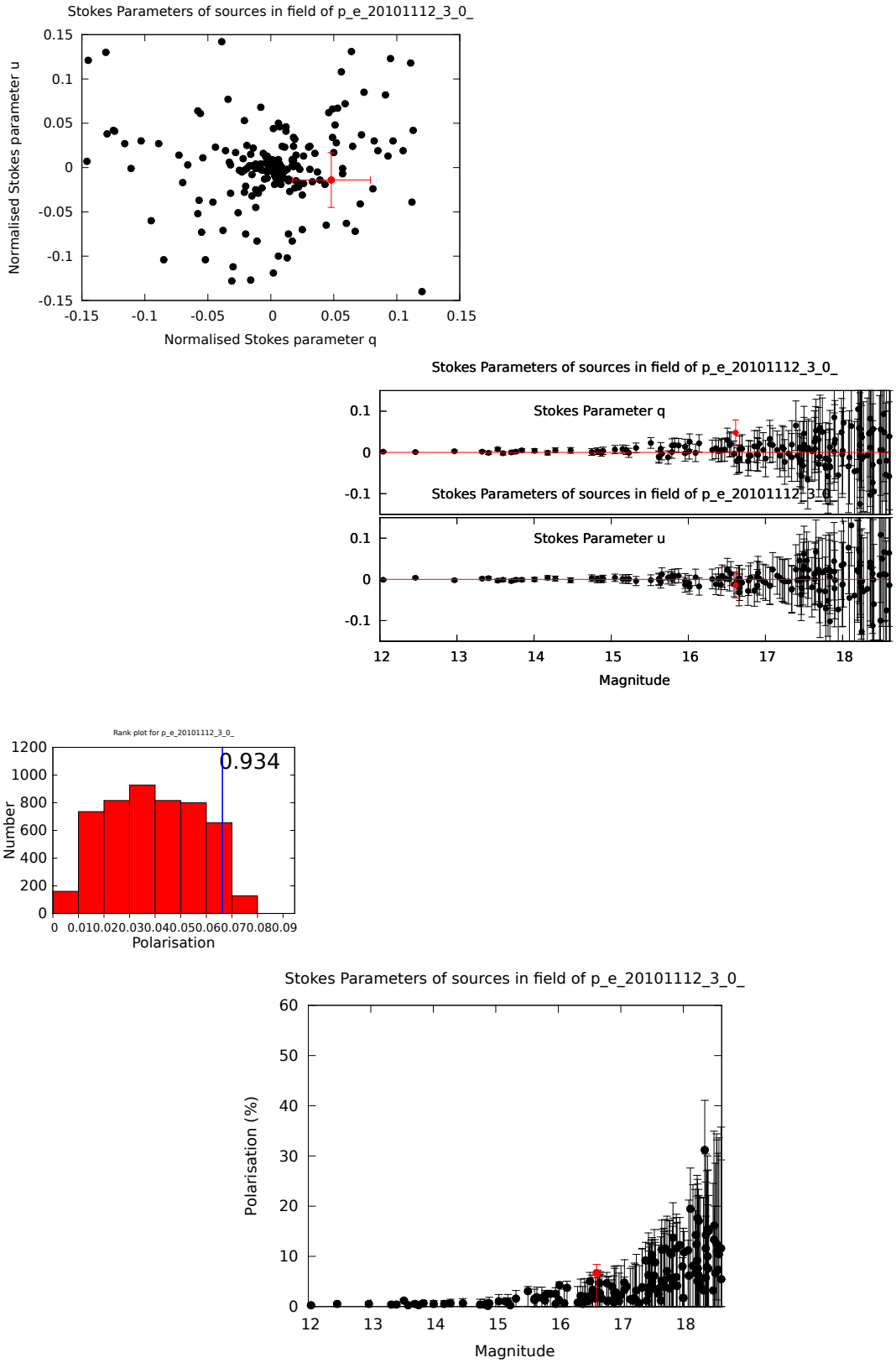


Figure G.3: GRB 101112A polarisation verification plots (Obs 2).

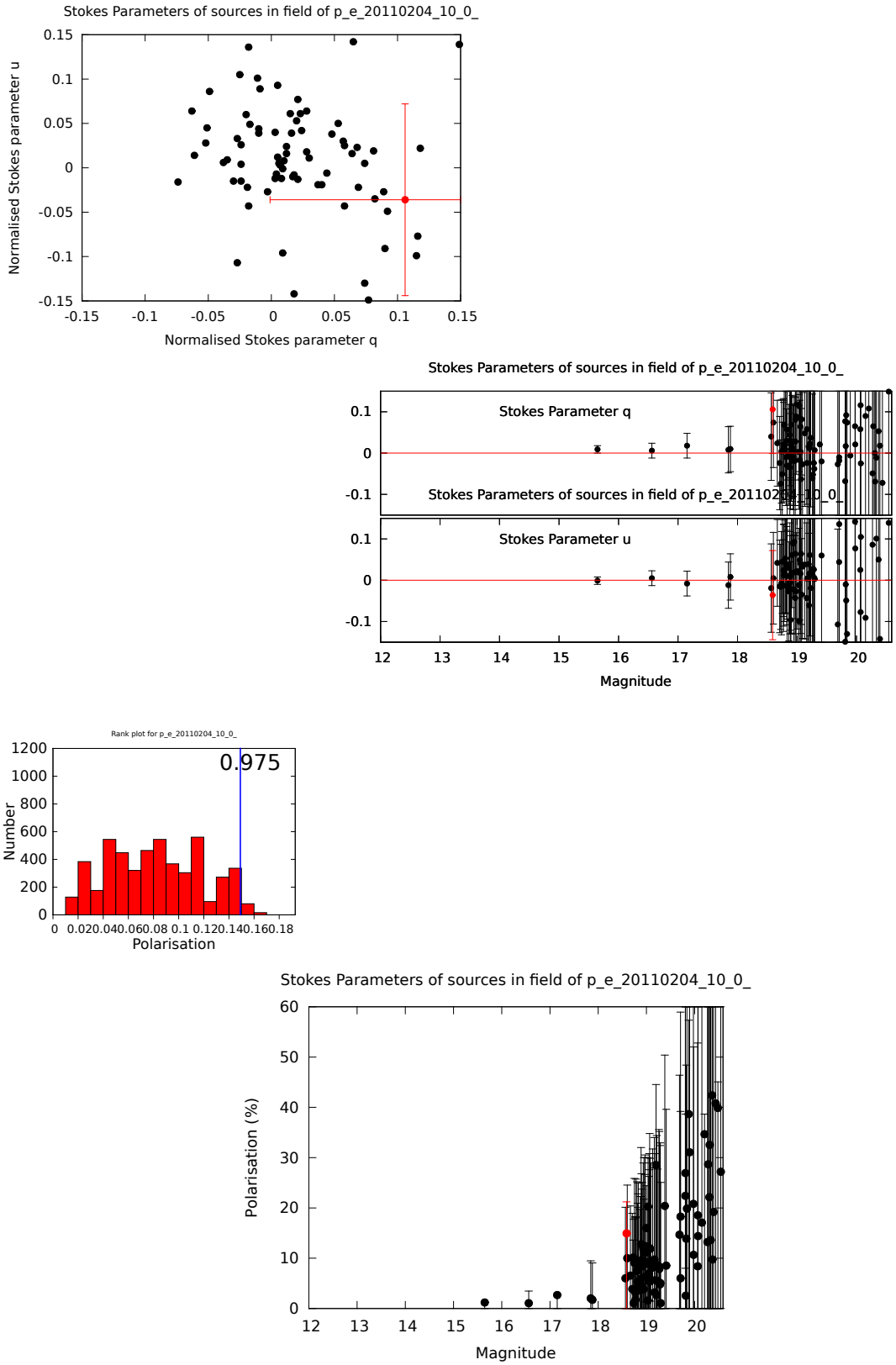


Figure G.4: GRB 110205A polarisation verification plots (Obs 1).

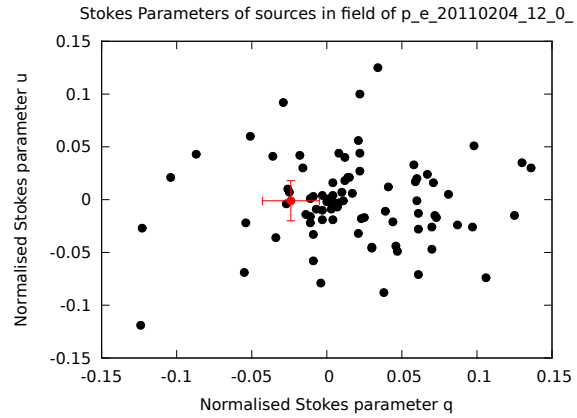


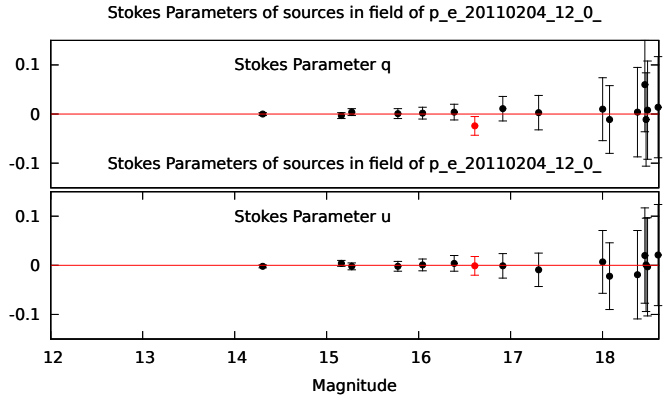


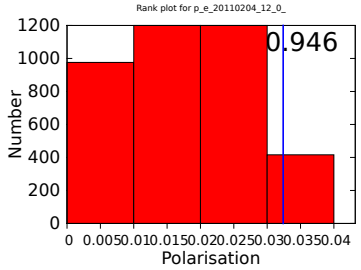


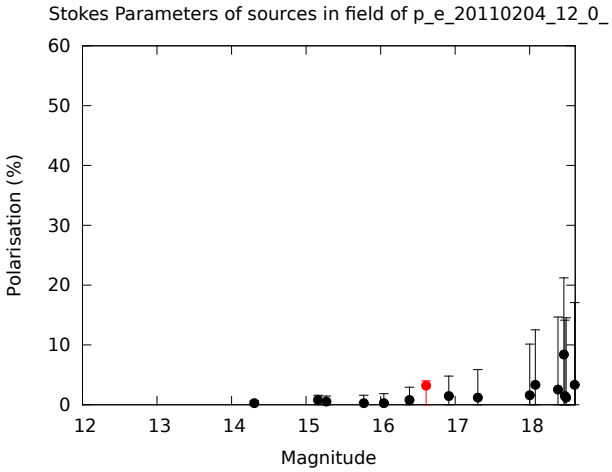


Figure G.5: GRB 110205A polarisation verification plots (Obs 2).

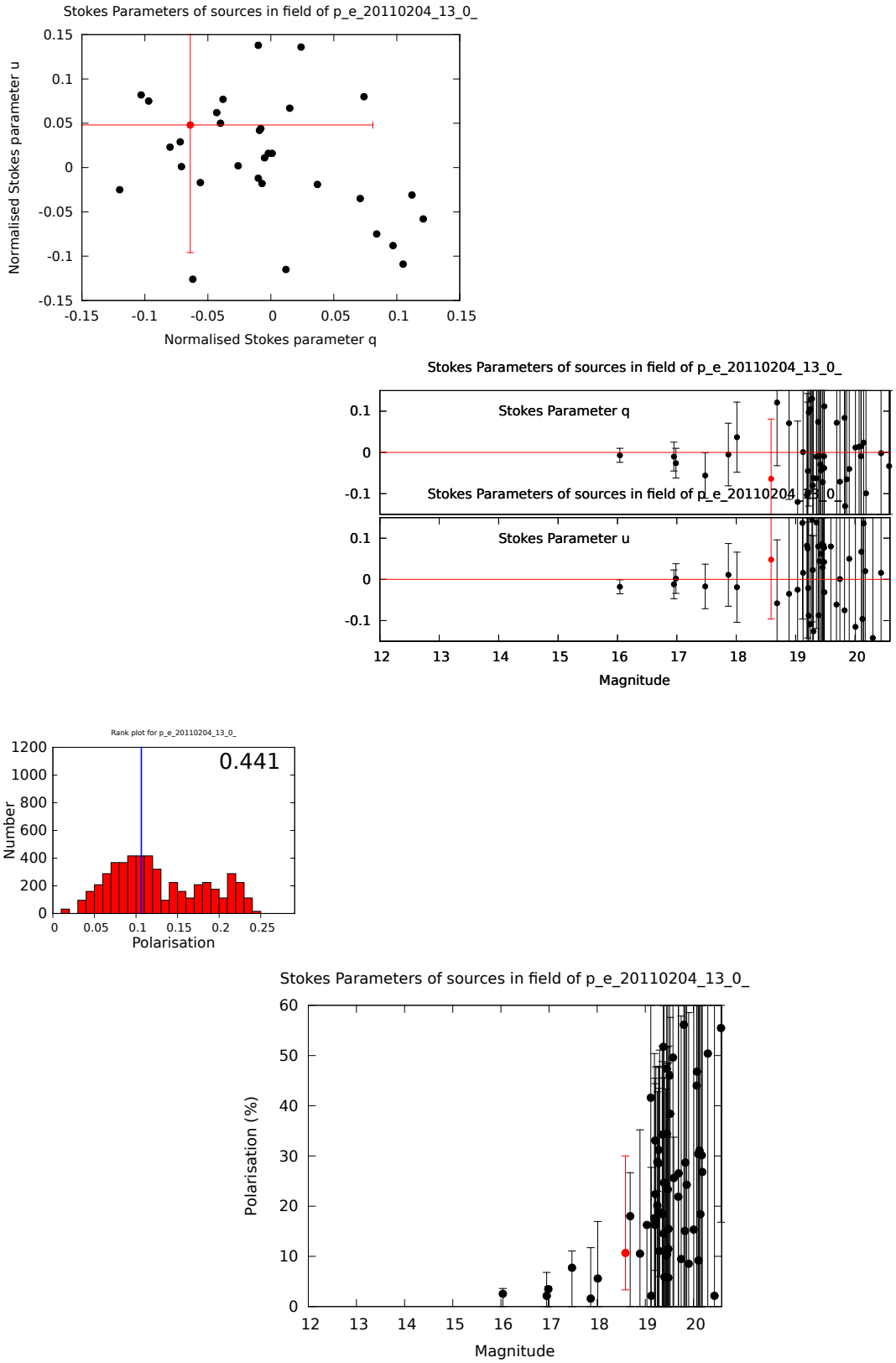


Figure G.6: GRB 110205A polarisation verification plots (Obs 3).

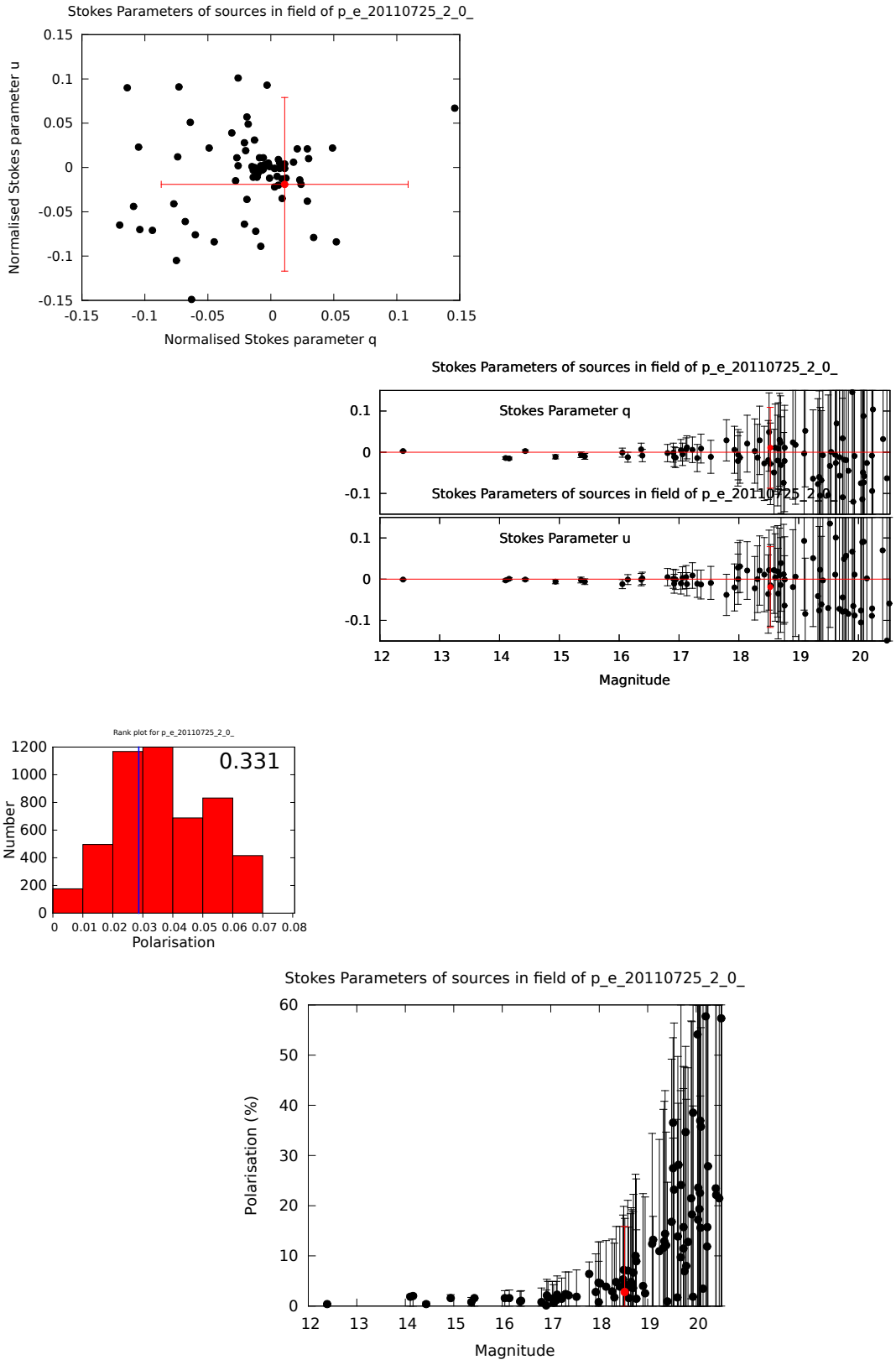


Figure G.7: GRB 110726A polarisation verification plots.

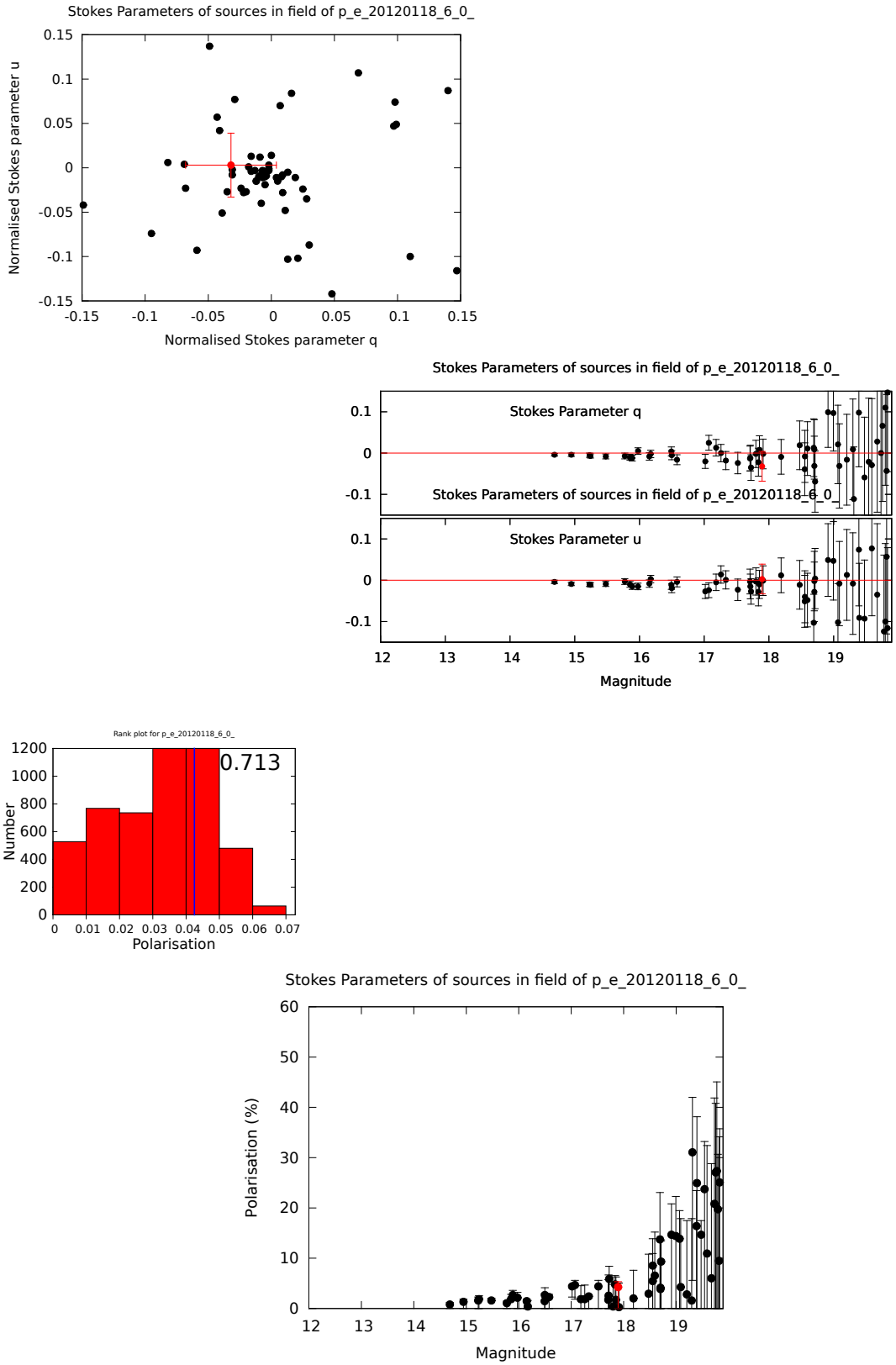


Figure G.8: GRB 120119A polarisation verification plots.

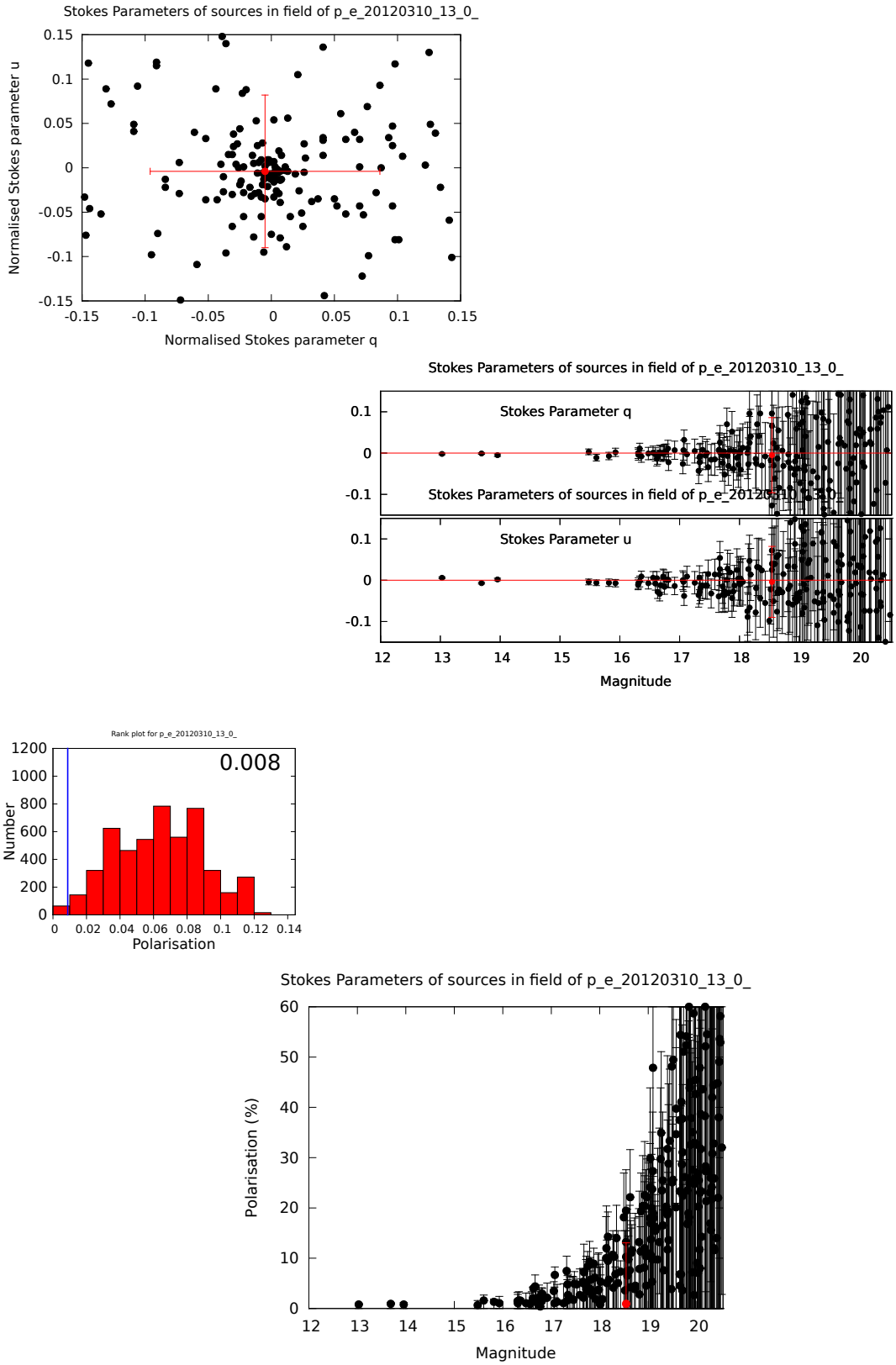


Figure G.9: GRB 120311A polarisation verification plots.

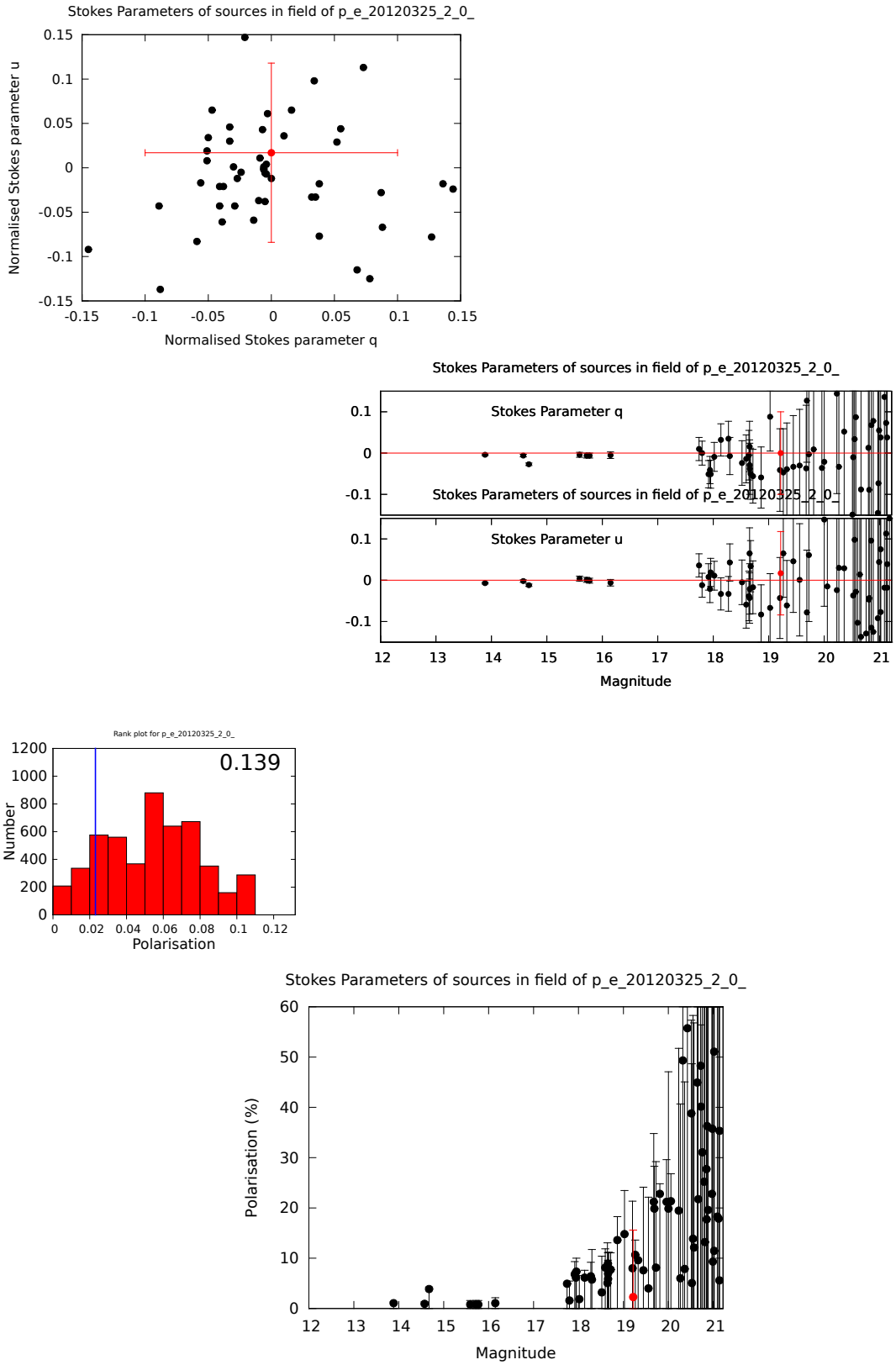


Figure G.10: GRB 120326A polarisation verification plots.

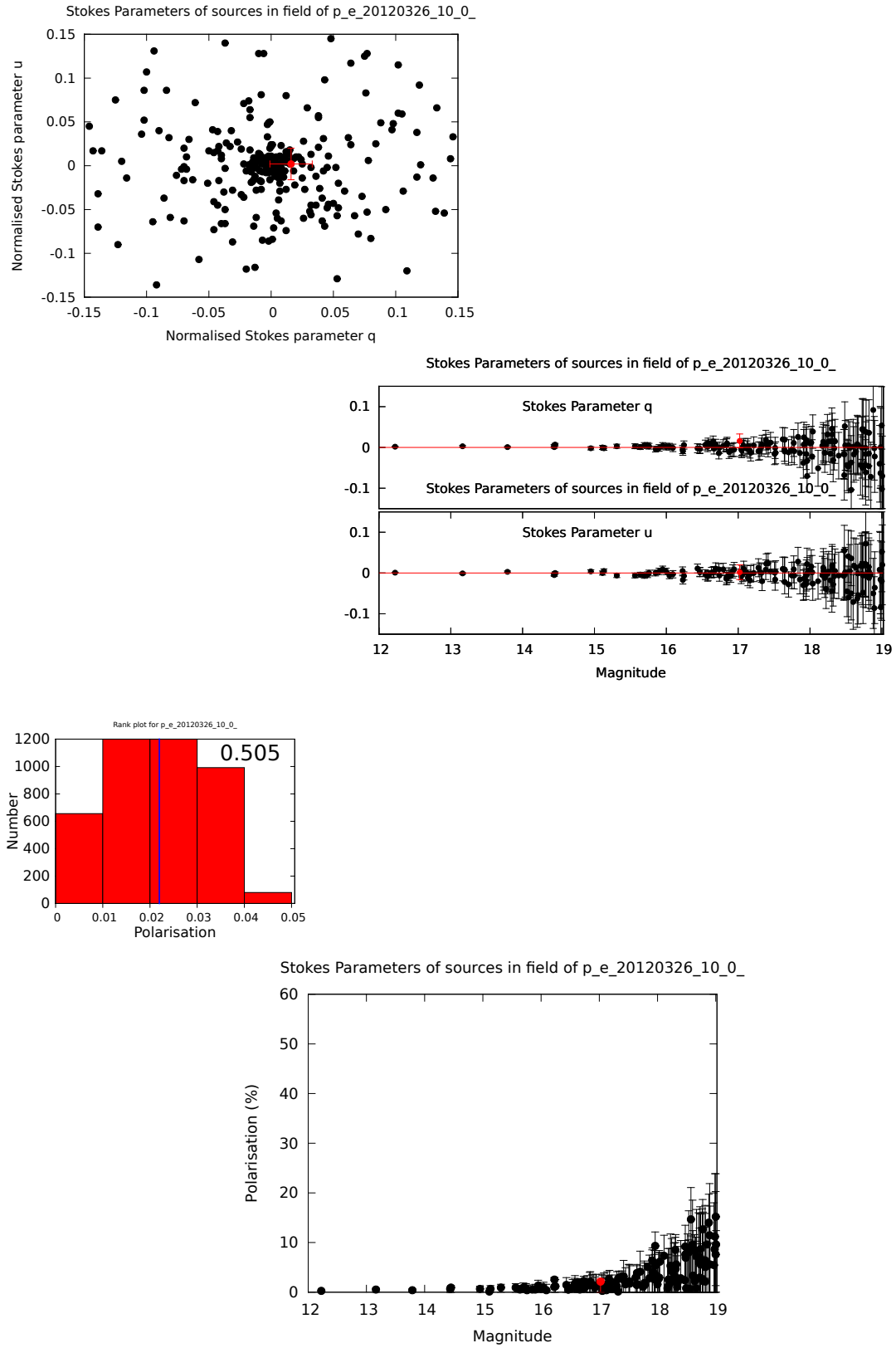


Figure G.11: GRB 120327A polarisation verification plots (Obs 1).

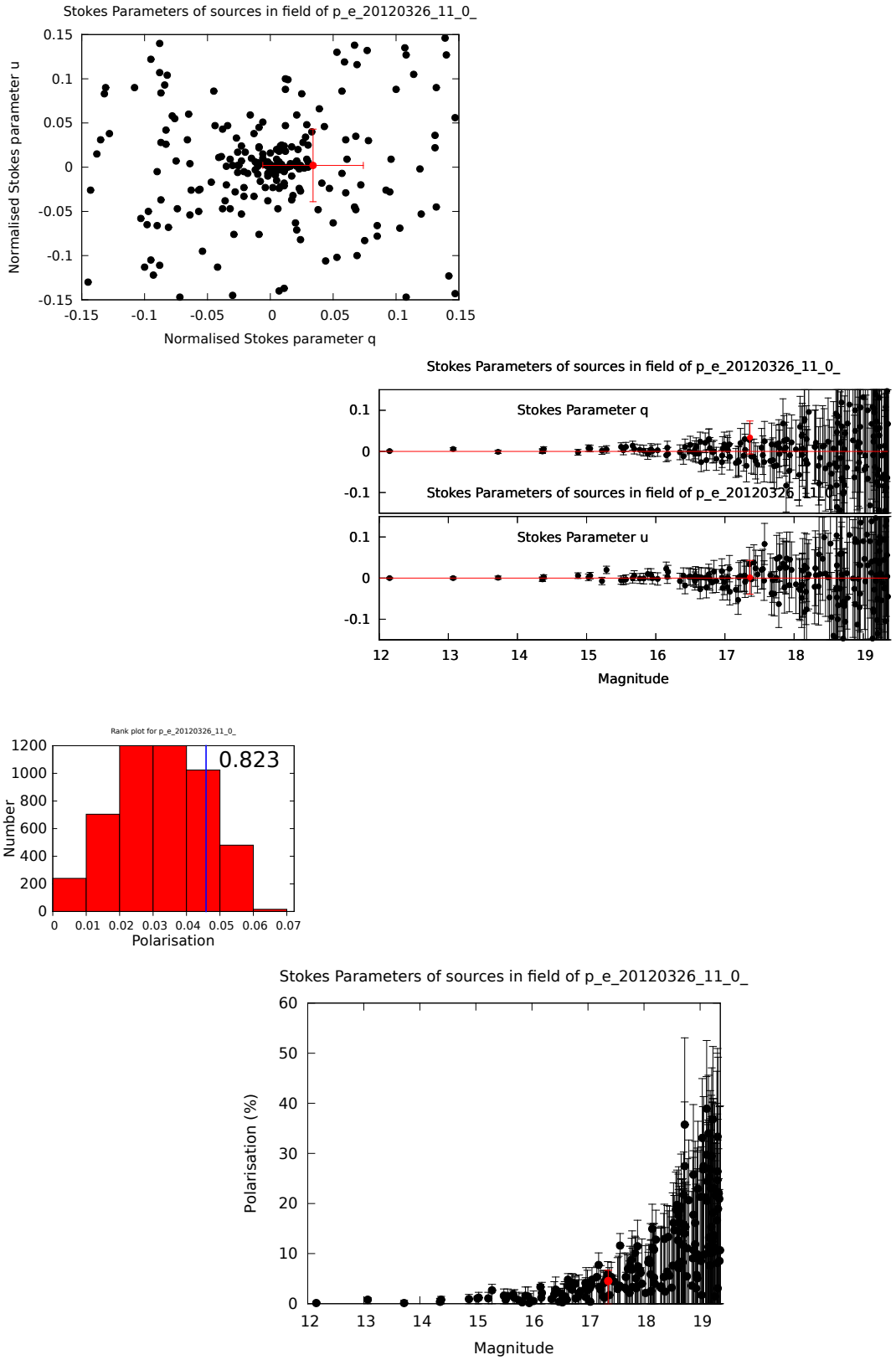


Figure G.12: GRB 120327A polarisation verification plots (Obs 2).

# Bibliography

Arnold, D. M., Steele, I. A., Mottram, C. J., & Smith, R. J. 2012, in Proc. SPIE, Vol. 8446, Ground-based and Airborne Instrumentation for Astronomy

Aslan, Z., Bikmaev, I. F., Vitrichenko, É. A., Gumerov, R. I., Dembo, L. A., Kamus, S. F., Keskin, V., Kiziloglu, U., Pavlinsky, M. N., Panteleev, L. N., Sakhibullin, N. A., Selam, S. O., Sunyaev, R. A., Khamitov, I., & Yaskovich, A. L. 2001, Astronomy Letters, 27, 398

Barrett, P., Hsu, J. C., Hanley, C., Taylor, J., Droettboom, M., Bray, E. M., Hack, W., Greenfield, P., Wyckoff, E., Jedrzejewski, R., De La Pena, M., & Hodge, P. 2012, PyFITS: Python FITS Module, Astrophysics Source Code Library

Barthelmy, S. D., Butterworth, P., Cline, T. L., Gehrels, N., Marshall, F., Takeshima, T., Connaughton, V., Kippen, R. M., Kouveliotou, C., & Robinson, C. R. 1998, in American Institute of Physics Conference Series, Vol. 428, Gamma-Ray Bursts, 4th Hunstville Symposium, ed. C. A. Meegan, R. D. Preece, & T. M. Koshut, 99–103

Basden, A. G. & Haniff, C. A. 2004, MNRAS, 347, 1187

Baumgartner, W. H., Burrows, D. N., Chester, M. M., D'Elia, V., Lien, A. Y., Markwardt, C. B., Page, K. L., Palmer, D. M., & Siegel, M. H. 2012, GRB Coordinates Network, 13017

Benn, C. R. & Ellison, S. L. 1998, New Astronomy Reviews, 42, 503

Bersier, D., McLeod, B., Garnavich, P. M., Holman, M. J., Grav, T., Quinn, J., Kaluzny, J., Challis, P. M., Bower, R. G., Wilman, D. J., Heyl, J. S., Holland, S. T., Hradecky, V., Jha, S., & Stanek, K. Z. 2003, ApJ Let., 583, L63

Bertin, E. & Arnouts, S. 1996, Astronomy and Astrophysics Supplement, 117, 393

Bessell, M. S. 1979, PASP, 91, 589

Beuermann, K., Hessman, F. V., Reinsch, K., Nicklas, H., Vreeswijk, P. M., Galama, T. J., Rol, E., van Paradijs, J., Kouveliotou, C., Frontera, F., Masetti, N., Palazzi, E., & Pian, E. 1999, A&A, 352, L26

Bikmaev, I., Zhuchkov, R., Sakhibullin, N., Burenin, R., Pavlinsky, M., Sunyaev, R., Khamitov, I., Eker, Z., Kiziloglu, U., & Gogus, E. 2012, GRB Coordinates Network, 13029

Bloom, J. 2011, What Are Gamma-Ray Bursts?, Princeton Frontiers in Physics (Princeton University Press)

Bloom, J. S., Kulkarni, S. R., Djorgovski, S. G., Eichelberger, A. C., Côté, P., Blakeslee, J. P., Odewahn, S. C., Harrison, F. A., Frail, D. A., Filippenko, A. V., Leonard, D. C., Riess, A. G., Spinrad, H., Stern, D., Bunker, A., Dey, A., Grossan, B., Perlmutter, S., Knop, R. A., Hook, I. M., & Feroci, M. 1999, Nature, 401, 453

Bradbury, J. W. & Vehrencamp, S. L. 1998, Principles of animal communication (Sinauer Associates)

Burrows, D. N., Hill, J. E., Nousek, J. A., Wells, A. A., Short, A. T., Ambrosi, R. M., Chincarini, G., Citterio, O., & Tagliaferri, G. 2003, in Proc SPIE, Vol. 4851, X-Ray and Gamma-Ray Telescopes and Instruments for Astronomy., ed. J. E. Truemper & H. D. Tananbaum, 1320–1325

Castro-Tirado, A. J., Zapatero-Osorio, M. R., Caon, N., Cairos, L. M., Hjorth, J., Pedersen, H., Andersen, M. I., Gorosabel, J., Bartolini, C., Guarnieri, A., Piccioni, A., Frontera, F., Masetti, N., Palazzi, E., Pian, E., Greiner, J., Hudec, R., Sagar, R., Pandey, A. K., Mohan, V., Yadav, R. K. S., Nilakshi, N., Bjornsson, G., Jakobsson, P., Burud, I., Courbin, F., Valentini, G., Piersimoni, A., Aceituno, J., Montoya, L. M., Pedraz, S., Gredel, R., Claver, C. F., Rector, T. A., Rhoads, J. E., Walter, F., Ott, J., Hippelein, H., Sanchez-Bejar, V., Gutierrez, C., Oscoz, A., Zhu, J., Chen,

J., Zhang, H., Wei, J., Zhou, A., Guziy, S., Shlyapnikov, A., Heise, J., Costa, E., Feroci, M., & Piro, L. 1999, Science, 283, 2069

Clarke, D. & Neumayer, D. 2002, A&A, 383, 360

Coburn, W. & Boggs, S. E. 2003, Nature, 423, 415

Copperwheat, C. M., Steele, I. A., Bates, S. D., Smith, R. J., Bode, M. F., Baker, I., Peacocke, T., & Thomson, K. 2014, in Proc SPIE, Vol. 9145, Ground-based and Airborne Telescopes V, 914511

Coulson, K. L. 1980, Aplied Optics, 19, 3469

Cox, L. J. 1976, MNRAS, 176, 525

Cucchiara, A., Cenko, S. B., Bloom, J. S., Melandri, A., Morgan, A., Kobayashi, S., Smith, R. J., Perley, D. A., Li, W., Hora, J. L., da Silva, R. L., Prochaska, J. X., Milne, P. A., Butler, N. R., Cobb, B., Worseck, G., Mundell, C. G., Steele, I. A., Filippenko, A. V., Fumagalli, M., Klein, C. R., Stephens, A., Bluck, A., & Mason, R. 2011, ApJ, 743, 154

Davis, Jr., L. & Greenstein, J. L. 1951, ApJ, 114, 206

de Juan Ovelar, M. 2013, PhD thesis, Leiden Observatory, Universiteit Leiden, Huygens Laboratory, J.H. Oort Building, Niels Bohrweg 2, NL-2333 CA Leiden, The Netherlands

de Juan Ovelar, M., Diamantopoulou, S., Roelfsema, R., van Werkhoven, T., Snik, F., Pragt, J., & Keller, C. 2012, in Society of Photo-Optical Instrumentation Engineers (SPIE) Conference Series, Vol. 8449, Society of Photo-Optical Instrumentation Engineers (SPIE) Conference Series, 12

de Juan Ovelar, M., Snik, F., & Keller, C. U. 2011, in Society of Photo-Optical Instrumentation Engineers (SPIE) Conference Series, Vol. 8160, Society of Photo-Optical Instrumentation Engineers (SPIE) Conference Series, 0

Denvir, D. J. & Conroy, E. 2003, in Society of Photo-Optical Instrumentation Engineers (SPIE) Conference Series, Vol. 4796, Low-Light-Level and Real-Time Imaging Systems, Components, and Applications, ed. C. B. Johnson, D. Sinha, & P. A. Laplante, 164–174

Eichler, D., Livio, M., Piran, T., & Schramm, D. N. 1989, Nature, 340, 126

Elder, F. R., Gurewitsch, A. M., Langmuir, R. V., & Pollock, H. C. 1947, Physical Review, 71, 829

Fishman, G. J. & Meegan, C. A. 1995, ARA&A, 33, 415

Fitzgibbon, A., Pilu, M., & Fisher, R. B. 1999, Pattern Analysis and Machine Intelligence, IEEE Transactions on, 21, 476

Fraser, S. N. & Steele, I. A. 2002, in Proc SPIE, Vol. 4848, Advanced Telescope and Instrumentation Control Software II, ed. H. Lewis, 443–454

Fukugita, M., Ichikawa, T., Gunn, J. E., Doi, M., Shimasaku, K., & Schneider, D. P. 1996, AJ, 111, 1748

Gehrels, N., Kniffen, D. A., & Ormes, J. F. 1992, in Current Topics in Astrofundamental Physics, ed. N. Sanchez & A. Zichichi, 602

Gehrels, T. 1960, AJ, 65, 466

Ghisellini, G. 2010, in Proc. IAU, Vol. 275, Jets at all scales

Ginzburg, V. L. & Syrovatskii, S. I. 1965, ARA&A, 3, 297

Gisler, G., Akerlof, C. W., Balsano, R. J., Bloch, J. J., Casperson, D. E., Fletcher, S. J., Gisler, G. R., Hills, J. G., Kehoe, R. L., Lee, B. C., Marshall, S. L., McKay, T. A., Miller, R. S., Priedhorsky, W. C., Szymanski, J. J., & Wren, J. A. 1999, in American Institute of Physics Conference Series, Vol. 499, American Institute of Physics Conference Series, ed. S. P. Brumby, 82–89

Gomboc, A., Kobayashi, S., Guidorzi, C., Melandri, A., Mangano, V., Sbarufatti, B., Mundell, C. G., Schady, P., Smith, R. J., Updike, A. C., Kann, D. A., Misra, K., Rol,

E., Pozanenko, A., Castro-Tirado, A. J., Anupama, G. C., Bersier, D., Bode, M. F., Carter, D., Curran, P., Fruchter, A., Graham, J., Hartmann, D. H., Ibrahimov, M., Levan, A., Monfardini, A., Mottram, C. J., O'Brien, P. T., Prema, P., Sahu, D. K., Steele, I. A., Tanvir, N. R., & Wiersema, K. 2008, ApJ, 687, 443

Greiner, J., Bornemann, W., Clemens, C., Deuter, M., Hasinger, G., Honsberg, M., Huber, H., Huber, S., Krauss, M., Krühler, T., Küpcü Yoldaş, A., Mayer-Hasselwander, H., Mican, B., Primak, N., Schrey, F., Steiner, I., Szokoly, G., Thöne, C. C., Yoldaş, A., Klose, S., Laux, U., & Winkler, J. 2008, PASP, 120, 405

Greiner, J., Klose, S., Reinsch, K., Martin Schmid, H., Sari, R., Hartmann, D. H., Kouveliotou, C., Rau, A., Palazzi, E., Straubmeier, C., Stecklum, B., Zharikov, S., Tovmassian, G., Bärnbantner, O., Ries, C., Jehin, E., Henden, A., Kaas, A. A., Grav, T., Hjorth, J., Pedersen, H., Wijers, R. A. M. J., Kaufer, A., Park, H.-S., Williams, G., & Reimer, O. 2003, Nature, 426, 157

Guidorzi, C. & et al. 2006, PASP, 118, 288

Guidorzi, C., Monfardini, A., Gamboc, A., Mundell, C. G., Steele, I. A., Carter, D., Bode, M. F., Smith, R. J., Mottram, C. J., Burgdorf, M. J., Tanvir, N. R., Masetti, N., & Pian, E. 2005, ApJ, 630, L121

Hall, J. S. & Mikesell, A. H. 1949, AJ, 54, 187

—. 1950, Publications of the U.S. Naval Observatory Second Series, 17, 3

Harrington, D. M., Kuhn, J. R., & Hall, S. 2011, PASP, 123, 799

Hey, J. 1983, South African Journal of Science, 79, 310

Hiltner, W. A. 1949, ApJ, 109, 471

Hjorth, J., Bjornsson, G., Andersen, M. I., Caon, N., Cairos, L. M., Castro-Tirado, A. J., Zapatero Osorio, M. R., Pedersen, H., & Costa, E. 1999, Science, 283, 2073

Japelj, J., Kopač, D., Kobayashi, S., Harrison, R., Guidorzi, C., Virgili, F. J., Mundell, C. G., Melandri, A., & Gomboc, A. 2014, ApJ, 785, 84

Jermak, H., Steele, I. A., & Smith, R. J. 2016, in Proc SPIE, Vol. 9908, Society of Photo-Optical Instrumentation Engineers (SPIE) Conference Series, 99084I

Johnson, H. L. & Morgan, W. W. 1953, ApJ, 117, 313

Keller, C. U., Schmid, H. M., Venema, L. B., Hanenburg, H., Jager, R., Kasper, M., Martinez, P., Rigal, F., Rodenhuis, M., Roelfsema, R., Snik, F., Verinaud, C., & Yaitskova, N. 2010, in Society of Photo-Optical Instrumentation Engineers (SPIE) Conference Series, Vol. 7735, Society of Photo-Optical Instrumentation Engineers (SPIE) Conference Series, 6

Kitchin, C. 2003, Astrophysical Techniques, Fourth Edition (Taylor & Francis)

Klebesadel, R. W., Strong, I. B., & Olsen, R. A. 1973, ApJ, 182, L85

Kobayashi, S. 2000, ApJ, 545, 807

Kobayashi, S., Piran, T., & Sari, R. 1999, ApJ, 513, 669

Kobayashi, S. & Zhang, B. 2003, ApJ Let., 582, L75

Kopač, D., Mundell, C. G., Japelj, J., Arnold, D. M., Steele, I. A., Guidorzi, C., Dichiara, S., Kobayashi, S., Gomboc, A., Harrison, R. M., Lamb, G. P., Melandri, A., Smith, R. J., Virgili, F. J., Castro-Tirado, A. J., Gorosabel, J., Järvinen, A., Sánchez-Ramírez, R., Oates, S. R., & Jelínek, M. 2015, ApJ, 813, 1

Kouveliotou, C., Meegan, C. A., Fishman, G. J., Bhat, N. P., Briggs, M. S., Koshut, T. M., Paciesas, W. S., & Pendleton, G. N. 1993, ApJ Let., 413, L101

Landolt, A. U. 1992, AJ, 104, 340

Lang, K. R. 2013, The Life and Death of Stars (Cambridge University Press)

Lin, R. P. 2000, in American Institute of Physics Conference Series, Vol. 528, Acceleration and Transport of Energetic Particles Observed in the Heliosphere, ed. R. A. Mewaldt, J. R. Jokipii, M. A. Lee, E. Möbius, & T. H. Zurbuchen, 201

Lyne, A. G. & Graham-Smith, F. 2006, Pulsar Astronomy (Cambridge Astrophysics Series)

Lyutikov, M. 2009, MNRAS, 396, 1545

Lyutikov, M. & Blandford, R. 2003, in Bulletin of the American Astronomical Society, Vol. 35, AAS/High Energy Astrophysics Division #7, 622

Lyutikov, M., Pariev, V. I., & Blandford, R. D. 2003, ApJ, 597, 998

Marshall, S., Akerlof, C., Kehoe, R., Lee, B., McKay, T., Bloch, J., Casperson, D., Fletcher, S., Gisler, G., Partridge, G., Priedhorsky, W., Roussel-Dupre, D., & Szymanski, J. 1997, in Bulletin of the American Astronomical Society, Vol. 29, American Astronomical Society Meeting Abstracts, 1290

Meegan, C. A., Fishman, G. J., Wilson, R. B., Horack, J. M., Brock, M. N., Paciesas, W. S., Pendleton, G. N., & Kouveliotou, C. 1992, Nature, 355, 143

Mermilliod, J.-C., Weidmann, N., & Hauck, B. 1996, Baltic Astronomy, 5, 413

Mészáros, P. 2002, ARA&A, 40, 137

Mészáros, P. & Rees, M. J. 1994, MNRAS, 269, L41

—. 1999, MNRAS, 306, L39

Mészáros, P., Rees, M. J., & Papathanassiou, H. 1994, ApJ, 432, 181

Mészáros, P., Rees, M. J., & Wijers, R. A. 1999, New Astronomy, 4, 303

Metzger, M. R., Djorgovski, S. G., Kulkarni, S. R., Steidel, C. C., Adelberger, K. L., Frail, D. A., Costa, E., & Frontera, F. 1997, Nature, 387, 878

Meyer-Arendt, J. R. 1989, Englewood Cliffs: Prentice-Hall, 1989, 3rd ed.

Mink, D. J. 1999, in Astronomical Society of the Pacific Conference Series, Vol. 172, Astronomical Data Analysis Software and Systems VIII, ed. D. M. Mehringer, R. L. Plante, & D. A. Roberts, 498

Mirabal, N., Chornock, R., Filippenko, A. V., Halpern, J. P., & Terndrup, D. 2002, in Bulletin of the American Astronomical Society, Vol. 34, American Astronomical Society Meeting Abstracts, 1243

Mochkovitch, R., Hernanz, M., Isern, J., & Martin, X. 1993, Nature, 361, 236

Morales-Rueda, L., Carter, D., Steele, I. A., Charles, P. A., & Worswick, S. 2004, Astronomische Nachrichten, 325, 215

Mundell, C. G., Guidorzi, C., & Steele, I. A. 2010, Advances in Astronomy, 2010, 61

Mundell, C. G., Kopač, D., Arnold, D. M., Steele, I. A., Gomboc, A., Kobayashi, S., Harrison, R. M., Smith, R. J., Guidorzi, C., Virgili, F. J., Melandri, A., & Japelj, J. 2013, Nature, 504, 119

Mundell C.G. et al. 2007, Science, 315, 1822

Munoz-Tunon, C., Vernin, J., & Varela, A. M. 1997, A&AS, 125, 183

Nousek, J., Townsley, L., Broos, P., Horner, S., Mason, K., & Cropper, M. 1999, in Bulletin of the American Astronomical Society, Vol. 31, AAS/High Energy Astrophysics Division #4, 729

Paciesas, W. S., Meegan, C. A., Pendleton, G. N., Briggs, M. S., Kouveliotou, C., Koshut, T. M., Lestrade, J. P., McCollough, M. L., Brainerd, J. J., Hakkila, J., Henze, W., Preece, R. D., Connaughton, V., Kippen, R. M., Mallozzi, R. S., Fishman, G. J., Richardson, G. A., & Sahi, M. 1999, ApJS, 122, 465

Pandey, S. B., Sahu, D. K., Resmi, L., Sagar, R., Anupama, G. C., Bhattacharya, D., Mohan, V., Prabhu, T. P., Bhatt, B. C., Pandey, J. C., Parihar, P., & Castro-Tirado, A. J. 2003, Bulletin of the Astronomical Society of India, 31, 19

Pence, W. 1999, in Astronomical Society of the Pacific Conference Series, Vol. 172, Astronomical Data Analysis Software and Systems VIII, ed. D. M. Mehringer, R. L. Plante, & D. A. Roberts, 487

Pence, W. D., Chiappetti, L., Page, C. G., Shaw, R. A., & Stobie, E. 2010, A&A, 524, A42

Piascik, A. S., Steele, I. A., Bates, S. D., Mottram, C. J., Smith, R. J., Barnsley, R. M., & Bolton, B. 2014, in Society of Photo-Optical Instrumentation Engineers (SPIE) Conference Series, Vol. 9147, Society of Photo-Optical Instrumentation Engineers (SPIE) Conference Series, 8

Piro, L. 1996, Memorie della Societ Astronomia Italiana, 67, 575

Planck, M. 1901, Annalen der Physik, 309, 553

Rautela, B. S., Joshi, G. C., & Pandey, J. C. 2004, Bulletin of the Astronomical Society of India, 32, 159

Reichart, D., Nysewander, M., Moran, J., Bartelme, J., Bayliss, M., Foster, A., Clemens, J. C., Price, P., Evans, C., Salmonson, J., Trammell, S., Carney, B., Keohane, J., & Gotwals, R. 2005, Nuovo Cimento C Geophysics Space Physics C, 28, 767

Reichart, D. E. 1998, ApJ Let., 495, L99

Rhodes, B. C. 2011, PyEphem: Astronomical Ephemeris for Python, Astrophysics Source Code Library

Robbins, M. S. & Hadwen, B. J. 2003, IEEE Transactions on Electron Devices, 50, 1227

Roberge, W. G. 1996, in Astronomical Society of the Pacific Conference Series, Vol. 97, Polarimetry of the Interstellar Medium, ed. W. G. Roberge & D. C. B. Whittet, 401

Roberge, W. G. & Whittet, D. C. B., eds. 1996, Astronomical Society of the Pacific Conference Series, Vol. 97, Polarimetry of the interstellar medium

Sagar, R., Kumar, B., Omar, A., & Joshi, Y. C. 2012, in Astronomical Society of India Conference Series, Vol. 4, Astronomical Society of India Conference Series, 173

Sakamoto, T., Barthelmy, S. D., Baumgartner, W. H., Cummings, J. R., Fenimore, E. E., Gehrels, N., Krimm, H. A., Markwardt, C. B., Palmer, D. M., Stamatikos, M., Sato, G., Tueller, J., & Ukwatta, T. N. 2012, GRB Coordinates Network, 13022

Sari, R., Piran, T., & Narayan, R. 1998, ApJ Let., 497, L17

Schlafly, E. F. & Finkbeiner, D. P. 2011, ApJ, 737, 103

Schlegel, D. J., Finkbeiner, D. P., & Davis, M. 1998, ApJ, 500, 525

Schmidt, G. D., Elston, R., & Lupie, O. L. 1992, Astronomical Journal, 104, 1563

Simmons, J. F. L. & Stewart, B. G. 1985, A&A, 142, 100

Soam, A., Maheswar, G., & Eswaraiah, C. 2014, Ap&SS, 350, 251

Steele, I. A., Bates, S. D., Guidorzi, C., Mottram, C. J., Mundell, C. G., & Smith, R. J. 2004, in Proc. SPIE, Vol. 5492, Ground-based and Airborne Instrumentation for Astronomy, 677–688

Steele, I. A., Bates, S. D., Guidorzi, C., Mottram, C. J., Mundell, C. G., & Smith, R. J. 2010, in Proc. SPIE, Vol. 7735, Ground-based and Airborne Instrumentation for Astronomy III

Steele, I. A., Mundell, C. G., Smith, R. J., Kobayashi, S., & Guidorzi, C. 2009, Nature, 462, 767

Steele, I. A., Smith, R. J., Rees, P. C., Baker, I. P., Bates, S. D., Bode, M. F., Bowman, M. K., Carter, D., Etherton, J., Ford, M. J., Fraser, S. N., Gomboc, A., Lett, R. D. J., Mansfield, A. G., Marchant, J. M., Medrano-Cerda, G. A., Mottram, C. J., Raback, D., Scott, A. B., Tomlinson, M. D., & Zamanov, R. 2004, in Proc SPIE, Vol. 5489, Ground-based Telescopes, ed. J. M. Oschmann, Jr., 679–692

Stetson, P. B. 1987, PASP, 99, 191

Strutt, J. W. 1871, The London, Edinburgh, and Dublin Philosophical Magazine and Journal of Science, 41, 447

Thomas, R. W. L. & Holland, A. C. 1977, in Radiation in the Atmosphere, ed. H.-J. Bolla, 85

Tinbergen, J. 2005, Astronomical Polarimetry (Cambridge)

Tody, D. 1986, in Society of Photo-Optical Instrumentation Engineers (SPIE) Conference Series, Vol. 627, Instrumentation in astronomy VI, ed. D. L. Crawford, 733

Turnshek, D. A., Bohlin, R. C., Williamson, II, R. L., Lupie, O. L., Koornneef, J., & Morgan, D. H. 1990, AJ, 99, 1243

Uehara, T., Toma, K., Kawabata, K. S., Chiyonobu, S., Fukazawa, Y., Ikejiri, Y., Inoue, T., Itoh, R., Komatsu, T., Miyamoto, H., Mizuno, T., Nagae, O., Nakaya, H., Ohsugi, T., Sakimoto, K., Sasada, M., Tanaka, H., Uemura, M., Yamanaka, M., Yamashita, T., Yamazaki, R., & Yoshida, M. 2012, ApJ Let., 752, L6

Velt, C. F. & Tinbergen, J. 1981, A&A, 103, 422

Wang, L. & Wheeler, J. C. 1998, ApJ Let., 504, L87

Wang, X. Y., Dai, Z. G., & Lu, T. 2000, MNRAS, 319, 1159

Waxman, E., Kulkarni, S. R., & Frail, D. A. 1998, ApJ, 497, 288

Wells, A. A. & Gehrels, N. A. 2004, in Proc. SPIE, Vol. 5488, UV and Gamma-Ray Space Telescope Systems, 403–414

Wenger, M., Ochsenbein, F., Egret, D., Dubois, P., Bonnarel, F., Borde, S., Genova, F., Jasniewicz, G., Laloë, S., Lesteven, S., & Monier, R. 2000, A&AS, 143, 9

Westfold, K. C. 1959, ApJ, 130, 241

Wiersema, K., Curran, P. A., Krühler, T., Melandri, A., Rol, E., Starling, R. L. C., Tanvir, N. R., van der Horst, A. J., Covino, S., Fynbo, J. P. U., Goldoni, P., Gorosabel, J., Hjorth, J., Klose, S., Mundell, C. G., O'Brien, P. T., Palazzi, E., Wijers, R. A. M. J., D'Elia, V., Evans, P. A., Filgas, R., Gomboc, A., Greiner, J., Guidorzi, C., Kaper, L., Kobayashi, S., Kouveliotou, C., Levan, A. J., Rossi, A., Rowlinson, A., Steele, I. A., de Ugarte Postigo, A., & Vergani, S. D. 2012, MNRAS, 426, 2

Wigger, C., Hajdas, W., Arzner, K., Güdel, M., & Zehnder, A. 2005, Nuovo Cimento C Geophysics Space Physics C, 28, 265

Woosley, S. E. 1993, ApJ, 405, 273

Woosley, S. E. & Bloom, J. S. 2006, ARA&A, 44, 507

Zhang, B. & Kobayashi, S. 2005, ApJ, 628, 315

Zhang, B., Kobayashi, S., & Mészáros, P. 2003, ApJ, 595, 950